

Controlling Molecular Motion



UNSW
SYDNEY

Thomas Stuart Charles MacDonald

A thesis in fulfilment of the requirements for the degree of
Doctor of Philosophy

School of Chemistry, Faculty of Science
UNSW Sydney
May, 2020



Australia's
Global
University

THESIS/DISSERTATION SHEET

Surname/Family Name	:	MacDonald
Given Name/s	:	Thomas Stuart Charles
Abbreviation for degree as give in the University calendar	:	PhD
Faculty	:	Science
School	:	Chemistry
Thesis Title	:	Controlling Molecular Motion

This thesis explores spatial control over chemical processes. The goal was to influence the diffusion of small molecules in solution, which could lead towards control over spatial distributions and the ability to create concentration gradients. The primary tool used to investigate this behaviour was diffusion NMR spectroscopy. It is widely recognised that major advances in chemistry arrive as a result of new tools, and here the development and application of new tools to measure diffusion is conducted in parallel.

Chapter 2 describes the development of new techniques for acquiring and processing time-resolved diffusion NMR data with high time resolution. These methods are used repeatedly throughout this work to follow chemical processes through time-dependent changes in diffusion coefficients. This chapter also presents a new temperature-independent method of gradient calibration using methanol, simplifying the process of obtaining calibrated absolute measurements of diffusion by NMR spectroscopy.

Chapter 3 investigates the controversial phenomenon of 'enhanced diffusion' of active catalysts as a means towards driving translational motion at the molecular scale. Using two model reactions, key results from the literature are reproduced experimentally but found to be caused by convection, not enhanced diffusion as had been reported. These results have wider implications for ongoing research into enhanced diffusion.

Chapter 4 describes a different approach towards influencing the diffusion rates of small molecules by combining photoswitchable anion binding with antielectrostatic self-assembly of phosphate anions in solution. Contrary to the chemical intuition that like charges repel, the dihydrogen phosphate anion is found to self-associate to a remarkable extent in a polar solvent. These surprising findings reveal the complex solution state self-association of a common anion., and the polyanionic phosphate clusters formed in solution allow much greater control over the diffusive properties of the photoswitchable host than could be achieved otherwise.

Chapter 5 contains a proposal for an all-photonic photoswitchable fluorescence feedback system that could amplify information and return an output as blue or green light. A theoretical model of this system is presented based on known molecular properties, and numerical modelling is used to illustrate the bifurcating and bistable dynamics of the proposed system. Preliminary experimental work on this topic is also presented.

Declaration relating to disposition of project thesis/dissertation

I hereby grant to the University of New South Wales or its agents a non-exclusive licence to archive and to make available (including to members of the public) my thesis or dissertation in whole or in part in the University libraries in all forms of media, now or here after known. I acknowledge that I retain all intellectual property rights which subsist in my thesis or dissertation, such as copyright and patent rights, subject to applicable law. I also retain the right to use all or part of my thesis or dissertation in future works (such as articles or books).

WITNESS

.....
Signature

.....
Date

The University recognises that there may be exceptional circumstances requiring restrictions on copying or conditions on use. Requests for restriction for a period of up to 2 years can be made when submitting the final copies of your thesis to the UNSW Library. Requests for a longer period of restriction may be considered in exceptional circumstances and require the approval of the Dean of Graduate Research.



UNSW
SYDNEY

Australia's
Global
University

INCLUSION OF PUBLICATIONS STATEMENT

UNSW is supportive of candidates publishing their research results during their candidature as detailed in the UNSW Thesis Examination Procedure.

Publications can be used in their thesis in lieu of a Chapter if:

- The candidate contributed greater than 50% of the content in the publication and is the "primary author", ie. the candidate was responsible primarily for the planning, execution and preparation of the work for publication
- The candidate has approval to include the publication in their thesis in lieu of a Chapter from their supervisor and Postgraduate Coordinator.
- The publication is not subject to any obligations or contractual agreements with a third party that would constrain its inclusion in the thesis

Please indicate whether this thesis contains published material or not:

- This thesis contains no publications, either published or submitted for publication
- Some of the work described in this thesis has been published and it has been documented in the relevant Chapters with acknowledgement
- This thesis has publications (either published or submitted for publication) incorporated into it in lieu of a chapter and the details are presented below

CANDIDATE'S DECLARATION

I declare that:

- I have complied with the UNSW Thesis Examination Procedure
- where I have used a publication in lieu of a Chapter, the listed publication(s) below meet(s) the requirements to be included in the thesis.

Candidate's Name	Signature	Date (dd/mm/yy)
Thomas MacDonald		

Statements

Originality statement

I hereby declare that this submission is my own work and to the best of my knowledge it contains no materials previously published or written by another person, or substantial proportions of material which have been accepted for the award of any other degree or diploma at UNSW or any other educational institution, except where due acknowledgement is made in the thesis. Any contribution made to the research by others, with whom I have worked at UNSW or elsewhere, is explicitly acknowledged in the thesis.

I also declare that the intellectual content of this thesis is the product of my own work, except to the extent that assistance from others in the project's design and conception or in style, presentation and linguistic expression is acknowledged.

Signed:

Thomas S. C. MacDonald

Date:

Copyright statement

I hereby grant the University of New South Wales or its agents a non-exclusive licence to archive and to make available (including to members of the public) my thesis or dissertation in whole or part in the University libraries in all forms of media, now or here after known. I acknowledge that I retain all intellectual property rights which subsist in my thesis or dissertation, such as copyright and patent rights, subject to applicable law. I also retain the right to use all or part of my thesis or dissertation in future works (such as articles or books).

For any substantial portions of copyright material used in this thesis, written permission for use has been obtained, or the copyright material is removed from the final public version of the thesis.

Signed:

Thomas S. C. MacDonald

Date:

Authenticity statement

I certify that the Library deposit digital copy is a direct equivalent of the final officially approved version of my thesis. No emendation of content has occurred and if there are any minor variations in formatting, they are the result of the conversion to digital format.

Signed:

Thomas S. C. MacDonald

Date:

List of included publications

- **Time-Resolved Diffusion NMR Measurements for Transient Processes**
T. S. C. MacDonald, W. S. Price, and J. E. Beves, *ChemPhysChem* **2019**, *20*, 926–930.
- **Enhanced Diffusion of Molecular Catalysts is Due to Convection**
T. S. C. MacDonald, W. S. Price, R. D. Astumian, J. E. Beves, *Angew. Chem. Int. Ed.* **2019**, *58*, 18864–18867.

Abstract

This thesis explores spatial control over chemical processes. The goal was to influence the diffusion of small molecules in solution, which could lead towards control over spatial distributions and the ability to create concentration gradients. The primary tool used to investigate this behaviour was diffusion NMR spectroscopy. It is widely recognised that major advances in chemistry arrive as a result of new tools, and here the development and application of new tools to measure diffusion is conducted in parallel.

Chapter 2 describes the development of new techniques for acquiring and processing time-resolved diffusion NMR data with high time resolution. These methods are used repeatedly throughout this work to follow chemical processes through time-dependent changes in diffusion coefficients. This chapter also presents a new temperature-independent method of gradient calibration using methanol, simplifying the process of obtaining calibrated absolute measurements of diffusion by NMR spectroscopy.

Chapter 3 investigates the controversial phenomenon of ‘enhanced diffusion’ of active catalysts as a means towards driving translational motion at the molecular scale. Using two model reactions, key results from the literature are reproduced experimentally but found to be caused by convection, not enhanced diffusion as had been reported. These results have wider implications for ongoing research into enhanced diffusion.

Chapter 4 describes a different approach towards influencing the diffusion rates of small molecules by combining photoswitchable anion binding with antielectrostatic self-assembly of phosphate anions in solution. Contrary to the chemical intuition that like charges repel, the dihydrogen phosphate anion is found to self-associate to a remarkable extent in a polar solvent. These surprising findings reveal the complex solution state self-association of a common anion., and the polyanionic phosphate clusters formed in solution allow much greater control over the diffusive properties of the photoswitchable host than could be achieved otherwise.

Chapter 5 contains a proposal for an all-photonic photoswitchable fluorescence feedback system that could amplify information and return an output as blue or green light. A theoretical model of this system is presented based on known molecular properties, and numerical modelling is used to illustrate the bifurcating and bistable dynamics of the proposed system. Preliminary experimental work on this topic is also presented.

Acknowledgements

First and foremost, thank you to my supervisor Jon for your ongoing support of my continuously evolving project and for encouraging me to pursue and develop my ideas. I've enjoyed my time at UNSW under your supervision, and I think we can both be proud of the work that we've achieved together. Thank you for your support of my travel (Shanghai and the Netherlands), for your realism, and for your commitment to the centrality of the pub.

To the assorted members of the Beves group, thank you all for your company over the past four years. Aaron, thanks for keeping things upbeat and positive and for your ever-present lab music selections. Ena, thank you for your even-tempered sanity and reliable organisational skills. My four years here would probably have been more chaotic without your influences. Neil, thanks for the lab metal, for your work in getting the various LED setups up and running, and for organising the group camping trips. Hasti, I've always enjoyed our conversations: thanks for being a great labmate, and for giving me some of your photocatalysts during my brief foray into the land of ruthenium. To Laura, Lucy, Ray, and Varsha: from what I've seen, the group is in good hands and I'm looking forward to seeing where your work takes you. Thanks also go to the Colbran-Morris-plus extended pub crew, reliable for a beer at any hour of the morning or night.

To Bill Price, your expertise with diffusion measurements was vital in bringing this project together. Thank you for your support and for your detailed emails sent from taxis all over the world. To Dean Astumian, your ideas are fascinating even if I sometimes feel I've understood less than half of what you've told me. If nothing else, thank your for your evangelism of the Good Word of microscopic reversibility.

This work relied heavily upon NMR experimental evidence, and to that end I thank the MWAC NMR staff: Jim, Adelle, Don, Doug, and Aditya. Jim, thank you for taking a chance and employing me on the basis of an email exchange way back in 2015. I'm not sure if I'd be at UNSW without you. Don, your expert knowledge, ability to play with new pulse sequences, and willingness to let me plug home-made circuitry into the spectrometers have been invaluable over the past few years. Adelle, Doug, and Aditya: thanks for being supportive workmates during my time with the NMR facility, and for helping to keep things running week-in, week-out.

Throughout the past few years I have greatly benefited from conversations with the UNSW Chemistry academics. Palli Thordarson, thank you for your always-insightful conversations on modelling and analysing supramolecular association. It's been great to have access to someone equally comfortable talking about hydrogen bonding or the estimated errors from nonlinear regression. Tim Schmidt, you're another person I might not have ended up at

UNSW without. Thank you for being the first to suggest Jon as a supervisor, for your assistance with maths and modelling, and for your ever-creative ideas over beers. Jason Harper, thank you for your assistance in getting to grips with diffusion, viscosity, and good old Stokes-Einstein-Sutherland.

To the Feringa team in Groningen: we barely spent half a year together, but my PhD wouldn't have been same without it. Thank you all for welcoming me to a beautiful place with your bicycles, boats, and borrels. To Ben Feringa and Sander Wezenberg, thank you for hosting me as a part of your team and for maintaining such a welcome and down-to-earth research environment. To Didi, Dorus, Filippo, Jose, Hugo, Lukas, Ruth, Wojcek, Henrieke and the rest of the C-wing crew: you're a great team, and it was a pleasure to work together and get to know you all. Finally, thank you to Cosima, Max, Daisy, Carlijn, and Yuchen for your friendship, picnics, tandem bicycling, Eurovision enthusiasm, and general lab camaraderie.

To Ruby, thank you so much for being there with me for (most of) this journey. Always patient, always helpful, and such a pleasure to share my life with: this PhD would have been far more challenging without you.

Finally, to my family: Mum, Dad, Molly, and Sarah. Thank you all for your interest and support over the past few years, and for your semi-regular trips to Sydney for Carriageworks brunches and walks along the coast. Now I've made it to the end (and COVID19-permitting), I can't wait to get back down to Tasmania to see you all and spend some time walking and drinking tea together.

List of Abbreviations

AEHB	Antielectrostatic hydrogen bonding
BBFO	Broadband observe with fluorine (a type of NMR probe)
BBO	Broadband observe (a type of NMR probe)
BINAP	2,2-bis(diphenylphosphino)-1,1-binaphthyl
DASA	Donor-acceptor Stenhouse adduct
dba	Dibenzylideneacetone
DCM	Dichloromethane
DDM	Diethyl diallyl malonate
DHP	Dihydrogen phosphate
DIPEA	Diisopropyl ethyl amine
DLS	Dynamic light scattering
DME	Dimethoxy ethane
DMF	Dimethylformamide
DMSO	Dimethyl sulfoxide
DNA	Deoxyribonucleic acid
DTE	Dithienylethene
e.e.	Enantiomeric excess
FCS	Fluorescence correlation spectroscopy
FRET	Förster resonance energy transfer
GCC	Gradient calibration constant
HMBC	Heteronuclear multiple bond correlation spectroscopy
HOMO	Highest occupied molecular orbital
HPLC	High performance liquid chromatography
HSQC	Heteronuclear single quantum correlation spectroscopy
LED	Light emitting diode
LUMO	Lowest unoccupied molecular orbital
NBS	<i>N</i> -bromosuccinimide
NMP	<i>N</i> -methylpyrrolidone
NMR	Nuclear magnetic resonance
NOESY	Nuclear Overhauser effect spectroscopy
PGSE	Pulsed-gradient spin echo
PGSTE	Pulsed-gradient stimulated echo
PSD	Photostationary distribution
PSS	Photostationary state

RNA	Ribonucleic acid
ROESY	Rotating frame nuclear Overhauser effect spectroscopy
SM	Starting material
T3P	Propanephosphonic acid anhydride
TBA	Tetrabutylammonium
TBI	Triple resonance inverse (a type of NMR probe)
TFA	Trifluoroacetic acid
THF	Tetrahydrofuran
TLC	Thin layer chromatography
TXI	Triple resonance inverse (a type of NMR probe)
UV	Ultraviolet
VT	Variable temperature
VT-NMR	Variable temperature NMR

Table of Contents

Statements	vii
List of included publications	ix
Abstract	xi
Acknowledgements	xiii
Table of Contents	xvii
1 Introduction	1
1.1 Molecular machines and devices	2
1.1.1 Energy surfaces and ratchets	3
1.1.2 Microscopic reversibility	4
1.1.3 Photochemistry and nonequilibrium thermodynamics	4
1.2 Non-linear reaction dynamics	5
1.2.1 Chemical feedback: autocatalysis and symmetry breaking	6
1.3 Molecular logic and computing	6
1.3.1 All-photonic autoamplification	7
1.4 Photochromism and switches	8
1.4.1 Photoswitch dynamics	8
1.4.2 Photochromism with visible light	10
1.5 Translational motion at the nanoscale	10
1.5.1 Active motion at low Reynolds number	11
1.5.2 Enhanced diffusion	12
1.6 Experimental measurements of diffusion coefficients	13
1.6.1 Diffusion NMR spectroscopy	13
1.6.2 Diffusion NMR of dynamic processes	14
1.7 Aims and thesis outline	14
1.8 References	15
2 Time-resolved diffusion NMR	25
2.1 Time-resolved diffusion NMR	26
2.1.1 Removing bias with random gradient lists	26
2.2 Improving the time resolution of diffusion measurements	28

2.2.1	Moving-frame processing of continuous data	28
2.2.2	Example data for moving-frame processing	29
2.3	Temperature-insensitive gradient calibration	29
2.3.1	Arrhenius parameters for temperature dependence of methanol diffusion	33
2.3.2	Effect of unknown water content on methanol calibration	33
2.4	Time-resolved diffusion NMR of a living polymerisation	34
2.5	Conclusions and future work	35
2.6	References	36
3	'Enhanced diffusion' of molecular catalysts	39
3.1	Enhanced diffusion of molecular catalysts?	40
3.2	Diffusion study of Grubbs metathesis	40
3.2.1	Time-dependence of T_1 and use of Cr(acac) ₃	40
3.2.2	Time-resolved diffusion measurements of active Grubbs catalyst	44
3.3	Diffusion study of a palladium-catalysed cyclisation	44
3.4	'Enhanced diffusion' or convection?	45
3.4.1	Influence of measurement time Δ on measured diffusion coefficients . .	46
3.4.2	Relationship between reaction rate and measured D	47
3.4.3	Influence of sample geometry on measured D	48
3.4.4	Studies of internal temperature during the reaction	49
3.4.5	Evidence for convection rather than 'enhanced diffusion'	51
3.5	Conclusions	51
3.6	References	52
4	Influencing diffusion by switchable phosphate binding	53
4.1	Introduction	54
4.1.1	Controlling molecular transport	54
4.1.2	Anion binding	54
4.1.3	Antielectrostatic hydrogen bonding in solution	54
4.1.4	Photocontrol of anion binding	55
4.2	Switchable anion binders	56
4.2.1	Towards oxindole-based hemistilbene photoswitches	56
4.2.2	Switchable stiff stilbene anion binders	61
4.3	Anion-binding properties of bis-urea stiff stilbene host	62
4.3.1	Obtaining association constants	62
4.3.2	Obtaining association constants with a self-associating guest	62
4.3.3	Example ^1H NMR titrations with tetrabutylammonium acetate	64
4.3.4	Example ^1H NMR titrations with tetrabutylammonium dihydrogen phosphate	66
4.3.5	Evidence for $[\text{HG}_2]$ binding mode of host Z-4.2	68
4.3.6	Summary of association data for stiff stilbene host	69
4.4	Antielectrostatic oligomerisation of dihydrogen phosphate	69
4.4.1	Viscosity measurements of dihydrogen phosphate solutions	70

4.4.2	Mathematical modelling of oligomer formation	71
4.4.3	Self-association of dihydrogen phosphate in DMSO	74
4.4.4	Control experiments with tetrabutylammonium acetate	75
4.5	Influence of guest-binding on host diffusion	77
4.5.1	Diffusion titrations with isomerically pure host	77
4.5.2	Diffusion titrations with 1:1 mixed host solutions	78
4.5.3	Control experiments with tetrabutylammonium acetate	78
4.5.4	Modelled diffusion coefficients of host during host-guest association	79
4.5.5	Possible complexes formed in solution between H_2PO_4^- and host 4.2	79
4.5.6	Comparison of estimated and measured diffusion coefficients for host-guest assemblies	81
4.6	Time-dependent diffusion with <i>in situ</i> irradiation	82
4.6.1	<i>In situ</i> irradiation causes convection	82
4.6.2	Monitoring temperatures and suppressing convection	82
4.7	Conclusions	85
4.8	References	85
5	Photoswitch-fluorescence feedback: towards a photonic molecular amplifier	89
5.1	Introduction	90
5.1.1	Switchable emission	90
5.1.2	Visible light photoswitching	91
5.2	Modelling the feedback system mathematically	92
5.2.1	Modelling photostationary states	92
5.2.2	Modelling the feedback system	94
5.2.3	List of terms and parameters	96
5.3	Numerical modelling	96
5.3.1	Model spectra	97
5.3.2	Understanding system dynamics with feedback	97
5.3.3	Time-dependent system dynamics	99
5.3.4	Required total absorbance for bifurcation	99
5.3.5	Goldilocks re-absorbance: not too high, and not too low	101
5.4	Binary amplification for non-volatile memory storage	102
5.4.1	A single-bit molecular flip-flop	102
5.4.2	Towards molecular computing?	103
5.5	Attempts to realise the molecular amplifier	104
5.5.1	Accessing the <i>ortho</i> -tetrafluoroazobenzene diacid core	105
5.5.2	Pyrene-functionalised tetrafluoroazobenzene amides	105
5.5.3	Restricted amide bond rotation dynamics of hexylated azobenzene-pyrene conjugate	106
5.5.4	Preliminary fluorescence study of pyrene-azobenzene conjugate	109
5.6	Conclusions and future work	109

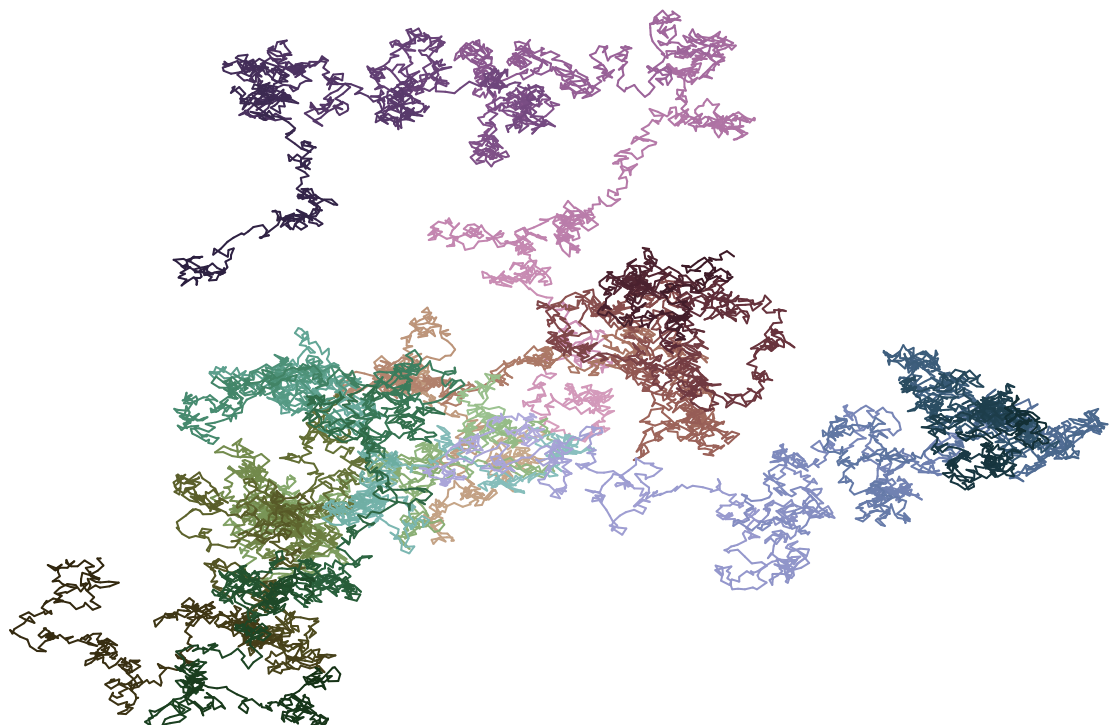
5.7	References	110
6	Conclusions and future work	113
6.1	References	116
7	Appendix for time-resolved diffusion	117
7.1	General experimental	117
7.1.1	Gradient calibration with methanol	117
7.2	Diffusion study of living polymerisation	121
7.3	Python scripts for processing diffusion data	121
7.4	Additional References	125
8	Appendix for ‘enhanced diffusion’ of molecular catalysts	127
8.1	Synthesis	127
8.1.1	Ring-closing metathesis (model reaction 1)	127
8.1.2	Synthesis of substrate for palladium-catalysed cyclisation	128
8.1.3	Palladium-catalysed arylation (model reaction 2)	128
8.2	General NMR experimental, acquisition, and processing	128
8.3	Diffusion data for Grubbs metathesis reaction	129
8.3.1	Agreement of static diffusion coefficients with the literature	129
8.3.2	Standard conditions: 200 mM DDM, 3 mM Grubbs catalyst	131
8.3.3	Reduced catalyst loading: 200 mM DDM, 0.5 mM Grubbs catalyst .	132
8.3.4	Reduced substrate loading: 100 mM DDM, 3 mM Grubbs catalyst .	133
8.3.5	Convection studies: influence of measurement time Δ on measured diffusion	134
8.4	Diffusion data for palladium-catalysed cyclisation	136
8.4.1	Agreement of static diffusion coefficients with the literature	136
8.4.2	Diffusion and concentration plots for palladium-catalysed cyclisation .	137
8.4.3	Convection studies: influence of measurement time Δ on measured diffusion coefficients for Pd-catalysed cyclisation	138
8.5	Influence of sample geometry on measured diffusion	141
8.5.1	Use of a restricted-volume Shigemi tube	141
8.5.2	Data for Grubbs reaction in a narrow 3 mm NMR tube	142
8.5.3	Data for palladium-catalysed reaction in a narrow 3 mm NMR tube .	142
8.6	Python code for processing diffusion data	142
8.7	Additional References	147
9	Appendix for switchable phosphate binding	149
9.1	Acid-base speciation of H_2PO_4^- in DMSO	149
9.1.1	Speciation of phosphate in DMSO	149
9.1.2	Speciation of acetate in DMSO	150
9.2	General experimental	151
9.3	Additional diffusion titration data	152

TABLE OF CONTENTS

9.4	Estimated diffusion coefficients of supramolecular host-guest complexes	154
9.5	Experimental: oxindole-derived hemistilbenes	155
9.5.1	Synthesis	155
9.5.2	Oxindole NMR spectra	159
9.6	Experimental: stiff stilbene anion binders	164
9.6.1	Synthetic details	164
9.6.2	Host NMR spectra	167
9.7	Scripts used for data processing	169
9.8	Additional References	175
10	Appendix for photoswitch-fluorescence feedback	177
10.1	Bifurcation conditions	177
10.2	Reaction experimental	179
10.3	NMR Spectra	182
10.3.1	Pyrenemethyl hexylammonium chloride 5.8	182
10.3.2	Pyrene-azobenzene conjugate 5.9	183
10.4	Additional References	183

Chapter 1

Introduction



Diffusion simulated as a random walk

1.1 Molecular machines and devices

The idea of using artificial molecule-sized devices to perform work is generally attributed to a 1959 talk delivered by Richard Feynman to the American Physical Society, titled ‘There’s Plenty of Room at the Bottom’.^[1] In it, Feynman argued that miniaturisation in manufacturing and design would lead to an inevitable conclusion of control of devices at the molecular level, with functional machines constructed atom by atom. This is clearly an achievable goal: biological systems store information chemically as DNA, retrieve it as RNA, and use that information to program generalised machines such as the ribosome to construct more specialised machines in proteins, each capable of efficiently performing a narrow selection of chemical tasks. While the design of synthetic molecular machines is still in its infancy, significant advances have been made in the previous 10–20 years. This has been recognised by the award of the 2016 Nobel Prize in Chemistry to Ben Feringa, Jean-Pierre Sauvage, and J. Fraser Stoddart for ‘the design and synthesis of molecular machines’.

Within the class of molecular devices, an important distinction can be made between *switches* and *motors*.^[2] Switches can be used to control processes but cannot be used to *drive* processes: if one switching event does thermodynamic work, returning the switch to its starting point undoes any work performed.^[3] Motors use energy to do work, and on return to a starting state (e.g. after a 360° rotation about an axis) any work performed remains. An important way of thinking about this is that the action of a motor has *directionality* through time (meaning that ‘forward’ operation is not the same as ‘reverse’ operation), while a switch does not. This means that for a molecular device to act as a motor, it must be capable of moving through a minimum of three distinct states: the cycle A→B→C→A is distinct from its reverse direction A→C→B→A, while a two-state A→B→A cycle can have no such directionality. Examples are given in Figure 1.1: Feringa’s unidirectional motor **1.1** fulfils this requirement with cyclical procession through 4 states, while azobenzene **1.2** can only access two states and so cannot be used as a motor.

Molecular motors are capable of performing work. From basic thermodynamics, this

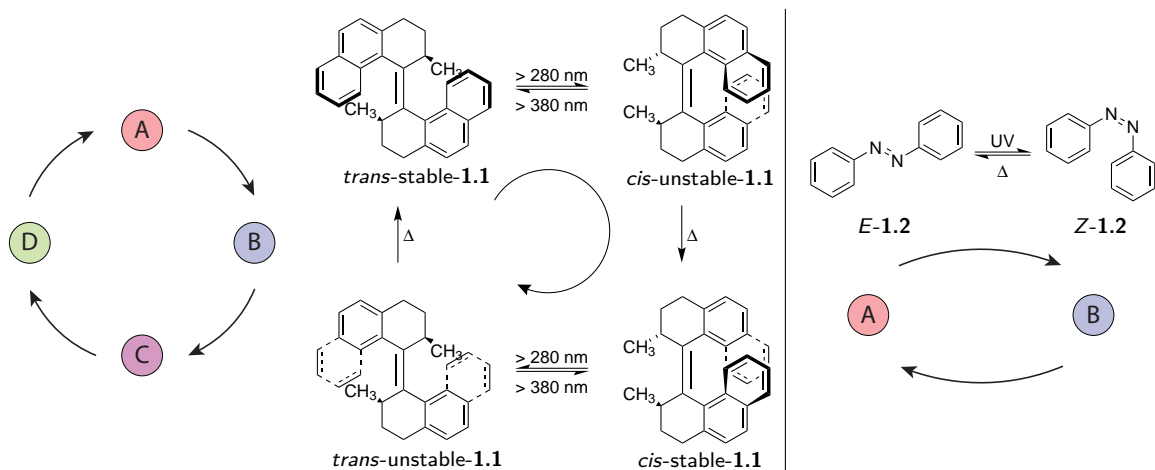


Figure 1.1. With two accessible states, azobenzene **1.2** (left) can function as a switch but not a machine. With four accessible states and directional procession between them, Feringa’s unidirectional motor^[4] **1.1** is a molecular machine and can use an external fuel (light) to do work.

means that they can be used to move a system away from thermodynamic equilibrium. The design of motors to achieve this at the molecular scale is qualitatively different to at the macroscopic scale. With bulk properties such as temperature and pressure meaningless for single molecules, concepts of thermodynamic heat cycles are inapplicable. Adding to this, the forces produced by motions within molecular machines are overshadowed by the buffeting of Brownian motion. Rather than attempting to dominate this random motion with increased force, successful molecular machines allow stochastic motion to occur on an energy surface that changes over time. This is used to create a *Brownian ratchet* that allows the machine to perform work moving away from equilibrium in one direction, while reducing the tendency to run in the reverse direction and undo that work. For the example of a molecular motor attached to an axle, rotation will not occur exclusively in one direction but will sum up over time through the biasing action applied by the ratchet.

1.1.1 Energy surfaces and ratchets

A seemingly plausible example of such a ratchet suggested by Feynman is shown in Figure 1.2.^[5] By coupling a paddle wheel in a box full of gas to a ratchet and pawl mechanism, it is tempting to believe that the random impact of gas molecules on the paddle wheel could be used to rotate the axle in one direction through small but irreversible advances. This could then be used to do work (shown here as lifting a weight against gravity). In reality this is thermodynamically impossible: thermal fluctuations in the ratchet-and-pawl system will always allow slippage and reversal.^[6] A single-molecule realisation of this concept, compound **1.3**, has been shown to exhibit random rotation as expected.^[7]

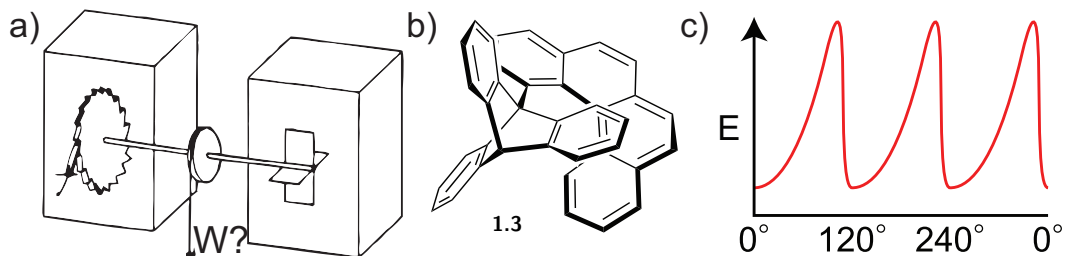


Figure 1.2. a) Feynman's ratchet and pawl.^[5] b) A molecular realisation of this concept,^[7] in which an asymmetric energy barrier c) exists for rotation about an internal axis. As might be expected from basic thermodynamics, in reality neither device rotates directionally or can be used to do work.

Two energy surfaces for functional Brownian ratchets are shown in Figure 1.3 (adapted from Kay *et al*^[3]). The first *energy ratchet* uses periodic changes in an asymmetric energy surface to drive particles from left to right, with work done in the second stroke by raising the average energy of the particles. The second ratchet, Figure 1.3b, changes in response to the location of a particle on its surface: an energy barrier ‘in front’ of the particle is lowered, and raised again when the particle has moved past (this is conceptually similar to Maxwell’s Demon^[3]). As the surface requires knowledge of the particle’s location to function, this is referred to as an *information ratchet*.

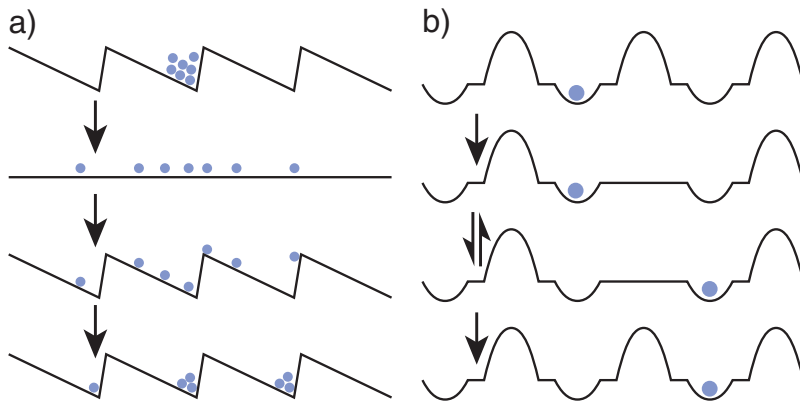


Figure 1.3. Energy surfaces for Brownian ratchets.^[3] a) A *pulsating ratchet* varies periodically, causing a net directional motion of the system. b) An *information ratchet* varies in response to the current state of the system.

1.1.2 Microscopic reversibility

The principle of microscopic reversibility^[8] (also referred to as ‘detailed balance’^[9]) is fundamental to statistical thermodynamics. The IUPAC Gold Book states that ‘*The principle of microscopic reversibility at equilibrium states that, in a system at equilibrium, any molecular process and the reverse of that process occur, on the average, at the same rate*’^[9] and continues to add that ‘...the reaction path in the reverse direction must in every detail be the reverse of the reaction path in the forward direction (provided always that the system is at equilibrium)’.^[9] Understanding this requirement is fundamental for the design of molecular machines and other systems involving nonequilibrium behaviour (such as autocatalysis). Microscopic reversibility has frequently been misunderstood within the context of nonlinear phenomena such as the origins of life, leading to claims of thermodynamically impossible reaction mechanisms.^[8c,10]

1.1.3 Photochemistry and nonequilibrium thermodynamics

Microscopic reversibility does not apply to chemical processes that involve irreversible steps. This is notably the case for photochemical reactions involving access to an excited state energy surface. Considering a model photoisomerisation reaction shown in Figure 1.4, the forward process might involve $S_0 \rightarrow S_1$ photoexcitation, thermal relaxation of the excited state, non-radiative $S_1 \rightarrow S_0$ relaxation to a conical intersection, and finally thermal relaxation to a new ground-state geometry (Figure 1.4a). The clearly unphysical reverse process would involve thermal access to an excited state followed by fluorescence (Figure 1.4b). This escape from microscopic reversibility makes it easier to design cyclic processes that move a system away from equilibrium when one or more of the steps involved is a photochemical step (e.g. Feringa’s motor in Figure 1.1).

The relevance of photophysical processes to nonequilibrium thermodynamics has long been noted.^[11] As photochemical reactions involve access to excited states of molecules, the thermodynamic principle of microscopic reversibility is broken^[8] allowing systems to be maintained indefinitely away from equilibrium. As a result photochemistry has been used to drive

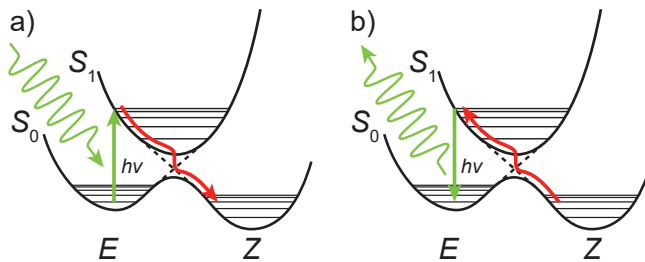


Figure 1.4. Violation of microscopic reversibility by irreversible photochemical processes. a) In this model photoisomerisation, photoexcitation of an *E* isomer from the S_0 to S_1 electronic state is followed by nonradiative cooling and isomerisation to the *Z* isomer *via* a conical intersection. b) The reverse process of this isomerisation, involving thermal access to a high-energy region of the S_1 excited state following by spontaneous fluorescence to return to the S_0 ground state of the *E* photoisomer. This process is clearly unphysical, meaning that the the process depicted in a) is thermally irreversible and the overall reaction does not follow microscopic reversibility.

many non-equilibrium systems including the Briggs-Rauscher,^[12] Belousov-Zhabotinskii,^[13] and Bray-Liebhafsky^[14] oscillating reactions. Nonequilibrium phenomena such as autocatalysis, bifurcation, and bistability can easily result from simple photothermal effects^[15] or photodimerisation/photodissociation^[16] reaction networks due to the inherent non-linearity of light absorption in solution. Autocatalysis is also frequently encountered in photodecomposition pathways,^[17] where photochemical reactions involving decomposition products lead to increasingly rapid destruction of the original substrate.

1.2 Non-linear reaction dynamics

The study of nonlinear reaction dynamics began with the discovery of the first oscillating reaction by Belousov in 1950.^[18] Subsequent research was conducted by Ilya Prigogine amongst others,^[19] who was awarded the 1977 Nobel prize in chemistry ‘...*for his contributions to non-equilibrium thermodynamics, particularly the theory of dissipative structures*’. Here, a ‘dissipative structure’ is a *non-equilibrium* structure or phenomenon that can only be maintained over time through constant input of energy.^[19a,20] Dissipative structures or processes are ubiquitous in living organisms (for example in formation of microtubules^[21]), and have recently been studied for purposes such as self-assembly^[22] or pattern formation.^[23]

In a linear reaction, the concentration of starting material decreases monotonically while the concentration of product increases until eventually a unique stable equilibrium is reached. If the reaction involves intermediates, these species typically increase in concentration to some pseudo-steady state before possibly decreasing at the end of the reaction. As the reaction progresses, the Gibbs free energy ΔG° steadily decreases until it reaches a minimum at equilibrium.

In a nonlinear reaction, at least some of the statements given above are no longer true. For example, in oscillating reactions such as the Belousov-Zhabotinsky reaction^[24] the concentrations of reaction intermediates oscillate periodically upwards and downwards as reagents are converted to products. ΔG° still decreases monotonically over time, but over the course of the reaction properties such as colour or redox potential may oscillate without ever es-

tablishing a pseudo-steady state. These nonlinear reaction systems often feature *bifurcation points*, where reaction dynamics differ qualitatively as a function of subtle combinations of reaction parameters.^[25] A reaction with the potential to oscillate might require some critical reagent concentration for oscillations to develop, while appearing linear for concentrations below that critical point.

1.2.1 Chemical feedback: autocatalysis and symmetry breaking

Non-linear reaction dynamics frequently involve *autocatalytic* reaction mechanisms in which the product of a reaction acts to catalyse its own formation, e.g. A \xrightarrow{B} B where the formation of B from A is catalysed by B.^[26] This introduces the possibility of symmetry-breaking, for example by introducing chirality to an initially racemic solution *via* autocatalytic chiral amplification.^[27] This phenomenon has been proposed as the origin for chiral asymmetry in life,^[28] and it has been suggested that autocatalysis is a *requirement* for the development of life.^[29]

Synthetic systems involving autocatalysis have been studied extensively for the purpose of chiral autoamplification.^[27] In one remarkable example, a pyrimidyl alkanol with an initial enantiomeric excess (e.e.) as low as $5 \times 10^{-5}\%$ was used to establish an e.e. of $>99.5\%$ after three cycles of chiral autoamplification.^[27h] Chiral autocatalysis of this form is a kinetic rather than a thermodynamic phenomenon:^[10] in accordance with microscopic reversibility, a catalyst that asymmetrically catalyses the formation of a chiral R or S product* from a racemic starting material must also asymmetrically catalyse the return of the same chirality product to the racemic starting material (the transition state is lowered for both the forward and back reactions). Chiral autoamplification thus requires both autocatalysis and a non-closed system in which the kinetic product can be removed or the reaction can be halted before the racemic equilibrium is eventually reached.

Autocatalysis has been demonstrated for self-replicating nucleic acids.^[30] More recently the Whitesides group have investigated the nonlinear thermodynamics of complex reaction networks involving autocatalytic steps,^[31] demonstrating the ability of such systems to bifurcate between different stable and dynamic (e.g. oscillating) reaction regimes over time. Autocatalysis has also been used to construct analog DNA-based biochemical circuits^[32] that demonstrate bistable switching and oscillation in response to external stimuli.

1.3 Molecular logic and computing

Non-equilibrium dynamics are important in computing and information processing, where the link between thermodynamics and information theory has long been understood theoretically^[33] and more recently probed experimentally.^[34] While most research in computing is concerned with electronic circuits, alternative computing architectures built from cellular automata,^[35] DNA,^[36] bacteria,^[37] or molecules^[38] have all attracted interest as possible platforms for information processing.

*In an achiral environment, these must have identical Gibbs free energies of formation ΔG° .

Molecular logic involves the use of chemical stimuli or light as inputs and/or outputs for information-processing molecular devices.^[39] Many examples of molecular logic components^[40] have been reported in the literature such as boolean logic gates,^[41] multiplexers and demultiplexers,^[42] and memory devices capable of storing and retrieving information.^[43] Despite these successes in creating individual molecular devices, almost no examples have been reported of linking one logic operator to another, and molecular computing remains a distant prospect as a whole.

Two key problems to be overcome in this regard are *input-output homogeneity*^[39c] and the *amplification of outputs*.^[44] Input-output (in)homogeneity describes whether or not the output of a molecular logic operation is of the same physical form as the input, which is an important requirement for linking logic devices together. For example, a binary AND gate that takes H⁺ and Zn²⁺ ions as inputs and switches on blue fluorescence as an output cannot be linked to another such AND gate without a mechanism of transforming blue light into an increase in H⁺ and/or Zn²⁺ ion concentration. A homogeneous logic system would directly output information in the same physical form as its input.

If a molecular logic system could be designed with homogeneous inputs and outputs, it would still require some form of amplification such that the magnitude of signals could be maintained after many logic operations: a logic device that requires a 10 mM change in H⁺ concentration as an input but can only produce a 1 mM change in H⁺ elsewhere as an output cannot be cascaded to perform more complex operations.

Only after solving these problems of homogeneity and amplification could logic operators be connected together arbitrarily and cascaded to form complex architectures.

1.3.1 All-photonic autoamplification

In an autoamplifying system, a small initial input is increased in magnitude to provide a much larger output. This process of amplification does work, and in doing so requires an external source of energy (chemical, light, electrical, etc). For example, solid-state electronic amplifiers use electrical energy to amplify a small signal voltage to produce a much larger output, while autoamplification of chirality^[27] requires the use of a chemical fuel to produce a chirally enriched product. Of these two examples the electronic amplifier has the advantages of using a general (electricity) rather than specialist fuel source (e.g. ZnⁱPr₂^[27a]) and producing no waste beyond heat. This lack of waste production allows the electronic voltage amplifier to operate continuously, while continuous operation of the chemical chirality amplifier requires the additional process of removing chemical waste products.

Using light as the fuel to power a chemical amplifier avoids this problem of waste buildup. Light can be used by molecular devices to do work without producing any chemical waste, and emitted light (fluorescence or phosphorescence) can be used to couple spatially separated molecular devices together by transmitting energy or information. Finally, light can be delivered to chemical systems with high spatio-temporal precision and does not linger after the light source is turned off. These attributes make light an ideal medium for fuelling and networking molecular devices.^[39a,40b,42,45]

1.4 Photochromism and switches

Some molecules undergo a reversible colour change in response to light, a property known as *photochromism*.^[46] Three well known classes of photochromic molecules are azobenzenes, dithienylethenes, and spiropyrans, as shown in Figure 1.5. The colour change relates to a change in molecular structure between the two accessible *photoisomers*, for example by making or breaking covalent bonds (spiropyrans and dithienylethenes) or from *E/Z* double bond isomerisation (azobenzenes).

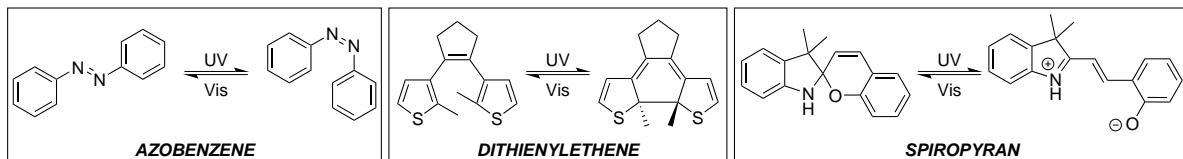


Figure 1.5. Photochromic molecules show structural changes in response to light. Three common classes of photochromic molecules are azobenzenes, dithienylethenes, and spiropyrans.

The ability to reversibly alter molecular structure allows photochromic compounds to be used as molecular *photoswitches* in which molecular properties can be selectively controlled using an external light source. This has led to the incorporation of photochromic molecules into molecular devices designed for applications such as actuating materials,^[47] controlled drug release,^[48] construction of molecular logic gates,^[49] colour tuning fluorescence,^[50] and control of motion within crystalline solids.^[51]

When selecting photochromic molecules to act as components within molecular machines, an important consideration is the amplitude of motion generated by switching.^[52] Each of the example classes shown in Figure 1.5 show different changes on switching. The *E* and *Z* forms of azobenzenes have significantly different geometries, and *para* substituted azobenzenes have been used to further amplify these changes to form molecular pumps,^[53] tweezers^[54] or scissors,^[55] and control rotaxane formation and disassembly.^[56] In contrast, the structural change in dithienylethene (DTE) photoswitching is minor, allowing photoswitching within confined volumes and in the solid phase. The mechanical changes are small enough that single crystals of DTEs are able to photoswitch between the ring-open and ring-closed forms, allowing large changes in electronic structure while maintaining crystalline integrity.^[57]

The development of new classes of photoswitchable molecules is an area of ongoing research, with particular attention given to molecules that achieve new changes in geometry on irradiation or that switch in response to different wavelengths of light. Some recent advances in this field include the development of switches based on hemithioindigos,^[58] bis-imidazolyl radicals,^[59] or hydrazone^[60,61b] photoactive moieties.

1.4.1 Photoswitch dynamics

If a compound can exist in one of two non-degenerate photoisomers, one of these states must necessarily be more thermodynamically stable than the other. Over time the photoswitch can be expected to come to a thermal equilibrium relating to this difference in

energies, but the kinetics of this process vary significantly across different classes of photoswitch. In recent years it has become common to divide photoswitches into two rough classes based on the rate of this thermal equilibration: *P-type* photoswitches which show little thermal switching over the timescale of an experiment, and *T-type* switches which show notable thermal isomerisation over the timescale of an experiment. There is no such thing as a ‘true’ P-type switch which shows *no* thermal reversion: the two classes are divided on a somewhat arbitrary basis of fast *vs* slow kinetics. P-type photoswitches include acylhydrazones,^[61] dithienylethenes,^[62] stilbenes, fulgides,^[63] and tetrafluoroazobenzenes,^[64] while T-type photoswitches include azobenzenes, spiropyrans,^[65] and donor-acceptor Stenhouse adducts (DASAs).^[66]

When a solution of a photoswitch is irradiated with light capable of driving switching, a steady state will eventually be reached involving a mixture of both photoisomers at dynamic equilibrium. For a thermally unstable T-type photoswitch with rates of photoisomerisation comparable to the rate of thermal reversion, the composition of this *photostationary distribution* (PSD) will depend on the intensity of irradiating light as well as its spectral composition. As the forward and backward rates of photoisomerisation increase to eclipse the rate of thermal isomerisation, this steady-state distribution moves towards a *photostationary state* (PSS) with composition governed exclusively by the photophysical properties of the photoswitch and the irradiation wavelength (λ_{irr}). The ratio of photoisomerisation rates to thermal isomerisation rates can be raised by increasing the light intensity I , raising the thermal isomerisation energy barrier ΔG^\ddagger through structural modifications, or by cooling the sample to reduce $k_B T$.

The composition of a PSS results from the absorption spectra (ε) and quantum yields (ϕ^{iso}) of the two photoisomers. In general, achieving a highly selective PSS requires that the photoisomers have separated absorption spectra such that it is possible to select irradiation wavelengths disproportionately absorbed by only one photoisomer. An example of this is shown in Figure 1.6 for diazocine **1.4** and tetrafluoroazobenzene **1.5** where the absorption bands of each photoisomer are separated from those of the other photoisomer, allowing highly selective PSS compositions to be reached under irradiation by suitably chosen wavelengths of light.

Unlike quantum yields for fluorescence or phosphorescence, quantum yields for photoisomerisation may be wavelength dependent.^[68] By Kasha’s rule^[69] it is generally assumed that any photoexcited molecule will quickly cool to the S_1 lowest energy excited state before crossing to a triplet state or returning to the S_0 ground state *via* fluorescence or non-radiative pathways. As a result, quantum yields for processes following photoexcitation would be wavelength-independent. This is not always the case for photoisomerisation, where wavelength-dependent photoisomerisation quantum yields have been reported^[68] and ascribed to a need to traverse energy barriers on the excited state potential energy surface to access the ground state conical intersection required for photoisomerisation.

1.4.2 Photochromism with visible light

As shown in the systems depicted in Figure 1.5, photochromism can often require harsh ultraviolet (UV) light. To avoid this, recent research into photochromic molecules has worked towards using low-energy visible light to drive photochromism, either through the design of new photoswitches^[66a,70] or the modification of known photochromic molecules to enable switching with visible light.^[64a,71] Design strategies to accomplish this include extending π orbital systems to lower the LUMO-HOMO transition energy and the use of two-photon upconversion systems to drive high-energy electronic transitions through the annihilation of two low-energy triplet states.^[72]

Two examples of azobenzene-derived visible light photoswitches were shown in Figure 1.6, diazocine^[67] **1.4** and tetrafluoroazobenzene^[64a,b] **1.5**. The *E* and *Z* photoisomers of either switch have different absorption spectra, allowing access to highly selective photostationary states. With absorption out to near-IR wavelengths (700 nm), diazocine **1.4** can be photoisomerised under *in vivo* conditions where shorter wavelengths of light are unable to penetrate the body.^[73] This property may be useful in the context of the emerging field of photopharmacology, in which photoswitchable drugs are developed that can be switched between active and inactive forms by topical irradiation with light.^[74]

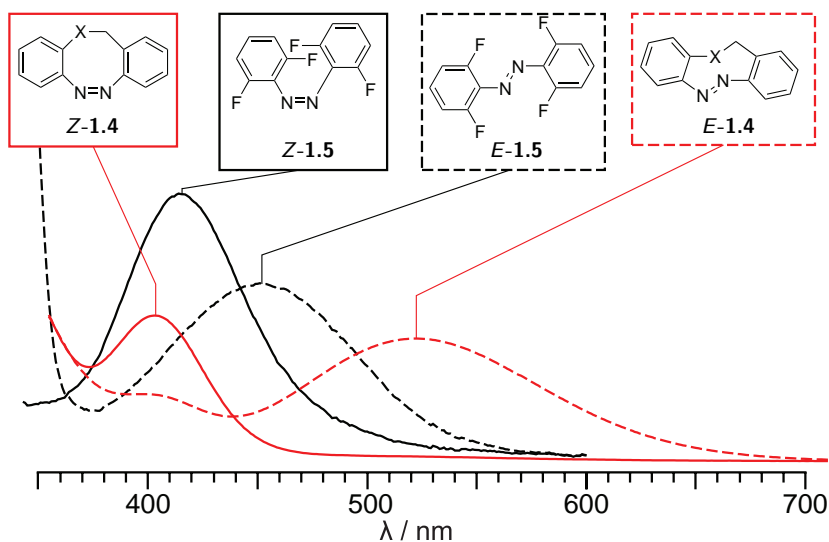


Figure 1.6. Comparison of the visible regions of the absorption spectra of diazocine **1.4**^[67] (red) and *ortho*-tetrafluoroazobenzene **1.5**^[64a,b] (black). Both compounds show separation of the absorption bands of the *Z* (*Z*-**1.4**, *Z*-**1.5**; solid lines) and *E* (*E*-**1.4**, *E*-**1.5**; dashed lines) photoisomers. This separation of absorption bands allows high selectivity (>90%) in switching from one isomer to the other under visible light irradiation.

1.5 Translational motion at the nanoscale

One of the major advantages offered by photocontrol of molecular devices is the ability to achieve spatial control over molecular phenomena using spatially directed light, even if the molecular device in question is distributed homogeneously within a solution. An alternative route towards the same outcome would be to control the translational motion of molecules in

solution, such that concentration gradients could be achieved and maintained as a dissipative structure using a continuously delivered source of energy.

1.5.1 Active motion at low Reynolds number

Synthetic nanoscopic and molecular scale^[2a,3,75] machines, motors, and devices have undergone significant advances in recent years. Small objects have been designed to undergo powered translational motion in solution^[76] with nano-rods,^[77] tubes,^[78] and Janus particles^[79] powered by catalytic decomposition of hydrogen peroxide or ultrasound^[80] among the best known examples.

The motion of particles through fluids at the molecular scale is completely different to the more familiar macroscopic scale. This is due to the balance between the *inertial* and the *viscous* forces acting on a particle as described by the Reynolds number, Re. The Reynolds number is often expressed as $Re = (av\rho)/(\eta)$ for a particle of length a and velocity v in a fluid of density ρ and viscosity η . For macroscopic objects, Re is large (> 1) and inertial forces dominate: objects put into motion will follow ballistic trajectories while viscous drag gradually slows them down. For microscopic objects at extremely low Reynolds number ($\ll 1$), viscosity completely overwhelms inertial forces and the equations of motion become *time independent*. In this regime, the motion of a particle at a point in time can be described completely by the forces acting on it in that moment, with no reference to forces that acted on it previously.^[81] Achieving constructive motion in the low Re regime is therefore qualitatively different to achieving motion at high Re.^[82]

Three simple designs for low-Reynolds swimming are given in Figure 1.7.^[82a] As with the molecular motors discussed earlier, all of these ‘swimmers’ achieve motion through a series of conformational changes that is not symmetric over time. In the absence of inertial forces, this is a requirement for achieving motion in the low-Re regime. The fourth ‘swimmer’ (d) is representative of the two-state reciprocal swimming motion of a macroscopic scallop, which can only ‘swim’ at high Re and does not function at microscopic scales.^[81] Interestingly, a single molecule realisation of swimmer a) has been proposed previously^[3] but does not appear to have been synthesised.

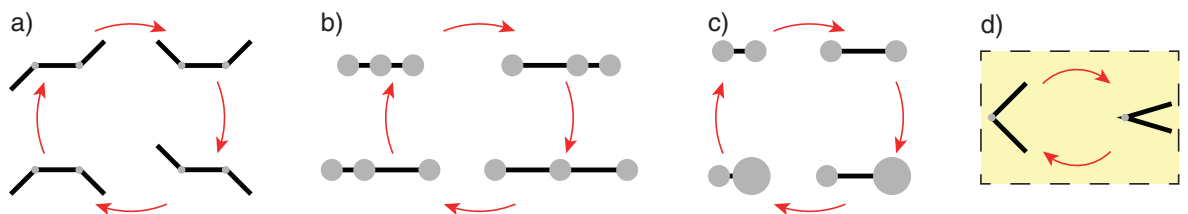


Figure 1.7. Minimal low-Reynolds number swimmers with two degrees of freedom. Two possible shape changes occur: a) linker angle changes; b) linker length changes; c) one linker length change and one size change. As with the machines in Figure 1.1, these changes must occur as a time-irreversible cycle to work against thermodynamic equilibrium and achieve motion: simple reciprocal motion as shown in d) is time reversible (the ‘forward’ cycle, as shown by the red arrows, is identical to the ‘reverse’ cycle), and so cannot be used to do work.^[81,82a]

Many microbiological systems are capable of ‘swimming’ at very low Reynolds numbers, propelled by mechanisms including cilia and flagella^[83] or the beating of a flexible tail.^[89b]

A number of artificial swimmers with sizes comparable to bacteria have been designed^[84] and built,^[85] but most of these are based on metallic nanorods, nanotubes, or nanospheres. In these devices, propulsion is generally achieved using metal-catalysed decomposition of hydrogen peroxide fuel. In contrast, there is surprising lack of research into swimmers at the molecular scale. One previous study claims to show swimming of a device based on Feringa's motor^[90b] (measured as an increase in the rate of diffusion), and another reports that the diffusion rate of Grubbs' catalyst increases significantly in the presence of olefinic 'fuel'.^[86]

While reciprocal motion is incapable of driving swimming at low Re , it may be able to increase rates of diffusion of single molecules.^[87] This is a result of the rapid rotation of molecular-scale objects in solution: if orientation is completely scrambled between the forward and reverse strokes of a reciprocal cycle, it is highly unlikely that the return stroke will undo *all* of the translational motion achieved by the forward stroke. Unlike the ballistic motion of bacteria or nanorods discussed earlier, this random-walk motion is diffusive and described by a diffusion coefficient D with units $[D] = \text{m}^2 \text{s}^{-1}$, not a velocity v with units $[v] = \text{m s}^{-1}$. The difference between the time-dependent translational behaviour of ballistic and diffusive particles is shown below: ballistic motion is *directional* with a distance travelled \vec{x} that increases linearly with time (Equation 1.1), while diffusive motion is *directionless* with a statistical expected distance from the starting point $\langle x \rangle$ that increases with $t^{1/2}$ (Equation 1.2).

$$\vec{x}(t) = \vec{v} \cdot t \quad (1.1)$$

$$\langle x \rangle(t) = \sqrt{D \cdot t} \quad (1.2)$$

1.5.2 Enhanced diffusion

Natural enzymes have been shown to undergo chemotactic^[88] movement towards higher substrate concentrations or anti-chemotactic^[88j] movement away from higher substrate concentration behaviour in solution. Despite the broad differences between fluid dynamics at macroscopic high Reynolds number regimes and microscopic low-Reynolds regimes being well understood,^[81,89] the underlying mechanism of this motion remains unclear. The short rotational correlation times of small molecules in solution would appear to rule out ballistic motion, suggesting that active propulsion of small molecules (if possible) would be observed as an increased diffusion coefficient rather than as a linear velocity. This increase in diffusion coefficient is referred to as *enhanced diffusion*.^[88a] There have been multiple reports of enhanced diffusion in active enzymes,^[88] with most measurements performed using optical techniques such as fluorescence correlation spectroscopy (FCS).^[88d,90] These results have been subject to recent questions regarding the possible dissociation of enzymes at the low substrate concentrations needed for FCS,^[90e] and some experiments using alternative measurement approaches such as dynamic light scattering^[91] (DLS) or diffusion NMR spectroscopy^[92] have been unable to replicate the microscopy results. The theoretical framework surrounding the observed enhanced diffusion remains an open question with multiple proposed models^[88d,h,93] drawing links between enhanced diffusion and reaction rates, binding-unbinding rates, and reaction thermodynamics, with conclusions ranging from new possibilities in targeted molec-

ular transport^[93d] to scepticism of enhanced diffusion in sub-nanometre objects.^[94] While proposed models focus on enhanced diffusion in enzymes, their findings should in principle also be applicable to small molecules.

1.6 Experimental measurements of diffusion coefficients

The ability to measure the rates of diffusion of molecular species in solution is a valuable tool for monitoring many types of chemical processes.^[95] Such processes include the self-assembly of supramolecular structures,^[96] the synthesis^[97] and dynamics^[98] of polymeric materials, crystallization,^[99] aggregation,^[100] ion mobility in electrolytes,^[101] molecular behaviour in confined environments,^[102] monitoring of dynamic material properties,^[103] measuring binding events,^[104] monitoring drug release,^[105] and other biological processes.^[106] One way to measure diffusion rates is by using NMR spectroscopy.

1.6.1 Diffusion NMR spectroscopy

Diffusion NMR spectroscopy is an effective approach for measuring the diffusion coefficients of small-to-medium sized molecules in solution as it can be performed on any NMR-active molecular species without the need for chemical modifications. Diffusion NMR experiments are also typically conducted on solutions containing chemically-relevant mM to M concentrations of a substrate, in contrast to FCS or radiolabelled diffusion measurements typically conducted at extremely low substrate concentrations (<1 nM). NMR measurements of diffusion can be acquired relatively quickly over timescales of minutes to tens of minutes and are well suited to investigate dynamic changes of diffusion over reaction timescales.

The diffusion NMR experiment involves the acquisition of a series of echo spectra using pulsed gradient spin-echo (PGSE) or pulsed gradient stimulated-echo (PGSTE) sequences of the type shown in Figure 1.8. In these experiments, the amplitude of a magnetic gradient field pulse (g) is varied over a number of acquisitions, resulting in a series of spectra with signal intensities decreasing with higher gradient pulse amplitudes. The measured intensities of the NMR resonances are then fitted to the Stejskal-Tanner equation^[107] (Equation 1.3) where I is the echo intensity, γ the gyromagnetic ratio of the nucleus, δ is the length of the (effective rectangular) gradient pulse, Δ is the delay between gradient pulses, and I_0 is the echo intensity in the absence of gradient pulses.

$$\begin{aligned} \frac{I}{I_0} &= \exp \left[-D\gamma^2 g^2 \delta^2 \left(\Delta - \frac{\delta}{3} \right) \right] \\ &= \exp (-bD) \end{aligned} \quad (1.3)$$

It is convenient to define a parameter $b = g^2 \delta^2 \gamma^2 (\Delta - \delta/3)$, as shown. The diffusion coefficient D can then be obtained through a non-linear exponential regression of the measured peak intensity I against b , giving the diffusion coefficients of the corresponding molecular species.

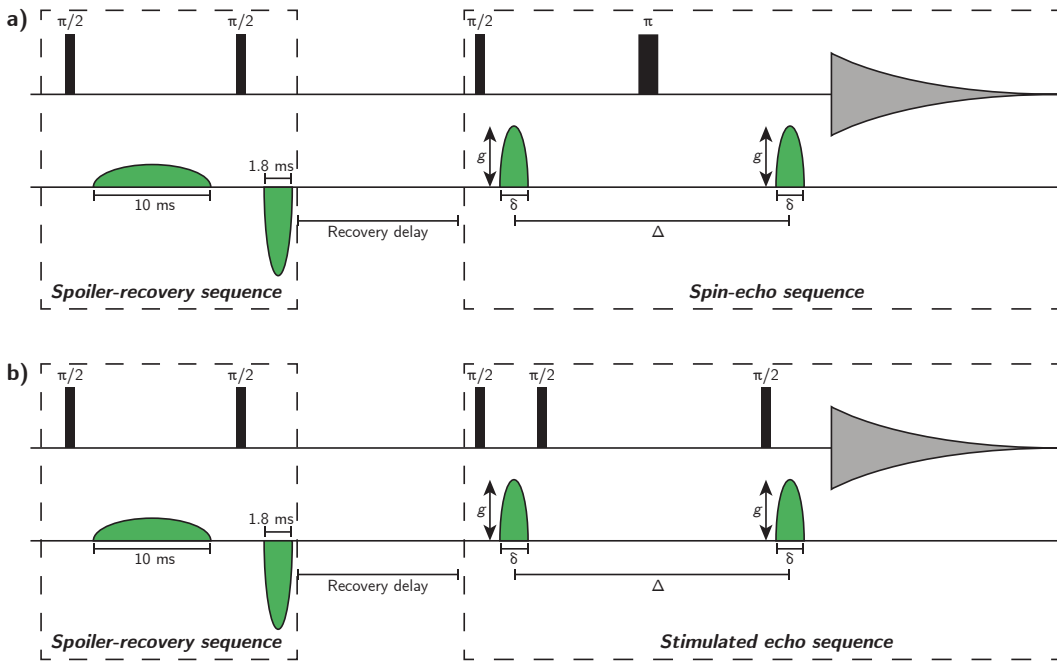


Figure 1.8. Pulse sequences used for gradient-echo diffusion NMR experiments. a) Pulsed gradient spin-echo (PGSE) or b) pulsed-gradient stimulated echo (PGSTE) sequences are the most common methods of measuring diffusion by NMR. Spoiler-recovery sequences consisting of two mismatched gradient pulses of +33% and -90% g_{max} can be used to destroy residual magnetisation between experiments, allowing faster repetition rates.

1.6.2 Diffusion NMR of dynamic processes

Performing an NMR measurement of a diffusion coefficient using standard techniques requires the acquisition of a series of gradient echo experiments using a list of typically 8–16 gradients. Each of these experiments typically involves a phase cycle of at least 8 transients, meaning that a complete diffusion measurement will require collecting a minimum of 64–128 acquisitions over perhaps 10 minutes. Incorporating additional components into the diffusion experiment, for example convection suppression sequences,^[108] may increase the required phase cycle to 16 or 32 steps and lead to experiments requiring hundreds of acquisitions even in the presence of high substrate concentrations and good signal to noise. As a result of these limitations, diffusion NMR experiments are generally restricted to studies of static systems where acquisition times of tens of minutes are considered acceptable. Time-dependent diffusion NMR studies of active processes do exist,^[86] but the inherently low time resolution of standard diffusion NMR experiments makes real-time observation of dynamic processes challenging.

1.7 Aims and thesis outline

This thesis explores spatial control over chemical processes by selectively addressing switchable molecular devices. The goal was to influence the translational diffusion of small molecules in solution, which could lead towards control over spatial distributions and the ability to create concentration gradients. The primary tool used to investigate this behaviour was diffusion

NMR spectroscopy. It is widely recognised that major advances in chemistry arrive as a result of new tools:^[109] in this work, the development and application of new tools to measure diffusion is conducted in parallel.

Chapter 2 describes the development of new techniques for acquiring and processing accurate time-resolved diffusion NMR data with high time resolution. These techniques are used repeatedly throughout this work to follow chemical processes through time-dependent changes in diffusion coefficients. In addition, this chapter presents a new temperature-independent method of gradient calibration for diffusion NMR measurements using methanol, simplifying the process of obtaining calibrated absolute measurements of diffusion by NMR spectroscopy.

Chapter 3 investigates the controversial phenomenon of ‘enhanced diffusion’ of active catalysts as a means towards driving translational motion at the molecular scale. Using two model reactions, key results from the literature are reproduced experimentally but found to result from convection and not enhanced diffusion as had been reported. These results have wider implications for ongoing research into enhanced diffusion.

Chapter 4 describes a different approach towards influencing the diffusion rates of small molecules by combining photoswitchable anion binding with antielectrostatic self-assembly of phosphate anions in solution. Contrary to the chemical intuition that like charges repel, the dihydrogen phosphate anion is found to self-associate to a remarkable extent in a polar solvent. These surprising findings reveal the complex solution state self-association of a common anion. The polyanionic phosphate clusters formed in solution allow much greater control over the diffusive properties of the photoswitchable host than could be achieved otherwise.

Chapter 5 contains a proposal for an all-photonic photoswitchable fluorescence feedback system that could amplify information and return an output as blue or green light. A theoretical model of this system is presented based on known molecular properties, and numerical modelling is used to illustrate the bifurcating and bistable dynamics of the proposed system. Preliminary experimental work on this topic is also presented.

Chapter 6 provides an outlook beyond the work described in this thesis, and proposes some directions of future work that would continue from the results presented here.

1.8 References

- [1] R. P. Feynman, *Caltech Eng. Sci.* **1960**, *23*, 22–36.
- [2] (a) S. Erbas-Cakmak, D. A. Leigh, C. T. McTernan, A. L. Nussbaumer, *Chem. Rev.* **2015**, *115*, 10081–10206; (b) E. R. Kay, D. A. Leigh, *Angew. Chem. Int. Ed.* **2015**, *54*, 10080–10088.
- [3] E. R. Kay, D. A. Leigh, F. Zerbetto, *Angew. Chem. Int. Ed.* **2007**, *46*, 72–191.
- [4] N. Koumura, R. W. J. Zijlstra, R. A. van Delden, N. Harada, B. L. Feringa, *Nature* **1999**, *401*, 152–155.

- [5] *The Feynman Lectures on Physics*, Definitive ed., (Eds.: R. P. Feynman, R. B. Leighton, M. Sands, M. A. Gottlieb, R. Leighton), Pearson, Addison-Wesley, San Francisco, Calif., **2006**.
- [6] J. M. R. Parrondo, P. EspaÑol, *Am. J. Phys.* **1996**, *64*, 1125–1130.
- [7] T. R. Kelly, J. P. Sestelo, I. Tellitu, *J. Org. Chem.* **1998**, *63*, 3655–3665.
- [8] (a) R. C. Tolman, *Proc. Natl. Acad. Sci.* **1925**, *11*, 436–439; (b) R. C. Tolman, *The Principles of Statistical Mechanics*, Dover Publications, New York, **1979**, 660 pp.; (c) R. D. Astumian, *Nat. Nanotechnol.* **2012**, *7*, 684–688.
- [9] *IUPAC Compendium of Chemical Terminology: Gold Book*, 2.1.0, (Eds.: M. Nič, J. Jirát, B. Košata, A. Jenkins, A. McNaught), IUPAC, Research Triangle Park, NC, **2009**.
- [10] D. G. Blackmond, *Angew. Chem. Int. Ed.* **2009**, *48*, 2648–2654.
- [11] (a) B. Borderie, D. Lavabre, G. Levy, J. C. Micheau, J. P. Laplante, *Int. J. Chem. Kinet.* **1992**, *24*, 309–317; (b) P. L. Gentili, J.-C. Micheau, *J. Photochem. Photobiol. C Photochem. Rev.* **2019**, 100321.
- [12] (a) E. Dulos, P. De Kepper, *Biophys. Chem.* **1983**, *18*, 211–223; (b) P. K. Srivastava, Y. Mori, I. Hanazaki, *Chem. Phys. Lett.* **1992**, *190*, 279–284.
- [13] (a) Y. Mori, Y. Nakamichi, T. Sekiguchi, N. Okazaki, T. Matsumura, I. Hanazaki, *Chem. Phys. Lett.* **1993**, *211*, 421–424; (b) M. Jinguji, M. Ishihara, T. Nakazawa, *J. Phys. Chem.* **1992**, *96*, 4279–4281.
- [14] (a) K. R. Sharma, R. M. Noyes, *J. Am. Chem. Soc.* **1975**, *97*, 202–204; (b) S. Kéki, G. Székely, M. T. Beck, *J. Phys. Chem. A* **2003**, *107*, 73–75.
- [15] (a) A. Nitzan, J. Ross, *J. Chem. Phys.* **1973**, *59*, 241–250; (b) A. Nitzan, P. Ortoleva, J. Ross, *J. Chem. Phys.* **1974**, *60*, 3134–3143.
- [16] (a) C. L. Creel, J. Ross, *J. Chem. Phys.* **1976**, *65*, 3779–3789; (b) J. Kramer, J. Reiter, J. Ross, *J. Chem. Phys.* **1986**, *84*, 1492–1499.
- [17] B. Borderie, D. Lavabre, J. C. Micheau, J. P. Laplante, *J. Phys. Chem.* **1992**, *96*, 2953–2961.
- [18] A. T. Winfree, *J. Chem. Educ.* **1984**, *61*, 661.
- [19] (a) G. Nicolis, I. Prigogine, *Self-Organization in Nonequilibrium Systems: From Dissipative Structures to Order through Fluctuations*, Wiley, New York, **1977**, 491 pp.; (b) D. Kondepudi, I. Prigogine, *Modern Thermodynamics: From Heat Engines to Dissipative Structures*, Second edition, John Wiley & Sons Inc, Chichester, West Sussex, **2015**, 1 p.; (c) I. Prigogine, *Non-Equilibrium Statistical Mechanics*, Dover edition, Dover Publications, Inc, Mineola, New York, **2017**, 319 pp.
- [20] (a) G. Lebon, D. Jou, J. Casas-Vázquez, *Understanding Non-Equilibrium Thermodynamics: Foundations, Applications, Frontiers*, Springer, Berlin, **2008**, 325 pp.; (b) S. A. P. van Rossum, M. Tena-Solsona, J. H. van Esch, R. Eelkema, J. Boekhoven, *Chem. Soc. Rev.* **2017**, *46*, 5519–5535.

- [21] G. M. Cooper, *The Cell: A Molecular Approach*, Eighth edition, Sinauer Associates, an imprint of Oxford University Press, Oxford ; New York, **2019**.
- [22] (a) J. Boekhoven, A. M. Brizard, K. N. K. Kowlgi, G. J. M. Koper, R. Eelkema, J. H. van Esch, *Angew. Chem. Int. Ed.* **2010**, *49*, 4825–4828; (b) J. Boekhoven, W. E. Hendriksen, G. J. M. Koper, R. Eelkema, J. H. van Esch, *Science* **2015**, *349*, 1075–1079; (c) J. H. van Esch, R. Klajn, S. Otto, *Chem. Soc. Rev.* **2017**, *46*, 5474–5475.
- [23] J. J. D. de Jong, P. R. Hania, A. Pugžlys, L. N. Lucas, M. de Loos, R. M. Kellogg, B. L. Feringa, K. Duppen, J. H. van Esch, *Angew. Chem. Int. Ed.* **2005**, *44*, 2373–2376.
- [24] A. M. Zhabotinsky, *Dokl. Akad. Nauk USSR* **1964**, *157*, 392–395.
- [25] A. H. Nayfeh, D. T. Mook, *Nonlinear Oscillations*, Wiley classics library ed, Wiley, New York, **1995**, 704 pp.
- [26] A. J. Bissette, S. P. Fletcher, *Angew. Chem. Int. Ed.* **2013**, *52*, 12800–12826.
- [27] (a) K. Soai, S. Niwa, H. Hori, *J. Chem. Soc. Chem. Commun.* **1990**, 982–983; (b) K. Soai, T. Shibata, H. Morioka, K. Choji, *Nature* **1995**, *378*, 767–768; (c) K. Soai, T. Shibata, I. Sato, *Acc. Chem. Res.* **2000**, *33*, 382–390; (d) D. K. Kondepudi, K. Asakura, *Acc. Chem. Res.* **2001**, *34*, 946–954; (e) D. A. Singleton, L. K. Vo, *J. Am. Chem. Soc.* **2002**, *124*, 10010–10011; (f) I. D. Gridnev, J. M. Serafimov, H. Quiney, J. M. Brown, *Org. Biomol. Chem.* **2003**, *1*, 3811–3819; (g) K. Soai, I. Sato, T. Shibata, S. Komiya, M. Hayashi, Y. Matsueda, H. Imamura, T. Hayase, H. Morioka, H. Tabira, J. Yamamoto, Y. Kowata, *Tetrahedron Asymmetry* **2003**, *14*, 185–188; (h) I. Sato, H. Urabe, S. Ishiguro, T. Shibata, K. Soai, *Angew. Chem. Int. Ed.* **2003**, *42*, 315–317.
- [28] F. C. Frank, *Biochim. Biophys. Acta* **1953**, *11*, 459–463.
- [29] (a) V. Vasas, C. Fernando, M. Santos, S. Kauffman, E. Szathmáry, *Biol. Direct* **2012**, *7*, 1; (b) A. J. Surman, M. Rodriguez-Garcia, Y. M. Abul-Haija, G. J. T. Cooper, P. S. Gromski, R. Turk-MacLeod, M. Mullin, C. Mathis, S. I. Walker, L. Cronin, *Proc. Natl. Acad. Sci.* **2019**, *116*, 5387–5392.
- [30] T. Tjivikua, P. Ballester, J. Rebek, *J. Am. Chem. Soc.* **1990**, *112*, 1249–1250.
- [31] (a) S. N. Semenov, L. J. Kraft, A. Ainla, M. Zhao, M. Baghbanzadeh, V. E. Campbell, K. Kang, J. M. Fox, G. M. Whitesides, *Nature* **2016**, *537*, 656–660; (b) B. J. Cafferty, A. S. Y. Wong, S. N. Semenov, L. Belding, S. Gmüür, W. T. S. Huck, G. M. Whitesides, *J. Am. Chem. Soc.* **2019**, *141*, 8289–8295.
- [32] A. J. Genot, A. Baccouche, R. Sieskind, N. Aubert-Kato, N. Bredeche, J. F. Bartolo, V. Taly, T. Fujii, Y. Rondelez, *Nat. Chem.* **2016**, *8*, 760–767.
- [33] C. E. Shannon, *Bell Syst. Tech. J.* **1948**, *27*, 379–423.
- [34] (a) S. Toyabe, T. Sagawa, M. Ueda, E. Muneyuki, M. Sano, *Nat. Phys.* **2010**, *6*, 988–992; (b) A. Bérut, A. Arakelyan, A. Petrosyan, S. Ciliberto, R. Dillenschneider, E. Lutz, *Nature* **2012**, *483*, 187–189; (c) J. M. R. Parrondo, J. M. Horowitz, T. Sagawa, *Nat. Phys.* **2015**, *11*, 131–139.

- [35] J. Mazoyer, J.-B. Yunès in *Handbook of Natural Computing*, (Eds.: G. Rozenberg, T. Bäck, J. N. Kok), Springer, Berlin, Heidelberg, **2012**, pp. 159–188.
- [36] L. Kari, S. Seki, P. Sosik in *Handbook of Natural Computing*, (Eds.: G. Rozenberg, T. Bäck, J. N. Kok), Springer, Berlin, Heidelberg, **2012**, pp. 1073–1127.
- [37] Y. Sakakibara, S. Hiyama in *Handbook of Natural Computing*, (Eds.: G. Rozenberg, T. Bäck, J. N. Kok), Springer, Berlin, Heidelberg, **2012**, pp. 1203–1232.
- [38] M. Hagiya, S. Kobayashi, K. Komiya, F. Tanaka, T. Yokomori in *Handbook of Natural Computing*, (Eds.: G. Rozenberg, T. Bäck, J. N. Kok), Springer, Berlin, Heidelberg, **2012**, pp. 1129–1184.
- [39] (a) J. Andréasson, U. Pischel, S. D. Straight, T. A. Moore, A. L. Moore, D. Gust, *J. Am. Chem. Soc.* **2011**, *133*, 11641–11648; (b) U. Pischel, J. Andréasson, D. Gust, V. F. Pais, *ChemPhysChem* **2013**, *14*, 28–46; (c) J. Andréasson, U. Pischel, *Chem. Soc. Rev.* **2015**, *44*, 1053–1069.
- [40] (a) U. Pischel, *Angew. Chem. Int. Ed.* **2007**, *46*, 4026–4040; (b) S. Silvi, E. C. Constable, C. E. Housecroft, J. E. Beves, E. L. Dunphy, M. Tomasulo, F. M. Raymo, A. Credi, *Chem. Eur. J.* **2009**, *15*, 178–185; (c) S. Silvi, M. Venturi, A. Credi, *Chem. Commun.* **2011**, *47*, 2483–2489.
- [41] (a) P. A. de Silva, N. H. Q. Gunaratne, C. P. McCoy, *Nature* **1993**, *364*, 42–44; (b) V. Balzani, M. Venturi, A. Credi, *Molecular Devices and Machines: A Journey into the Nano World*, Wiley-VCH, Weinheim, **2003**, 494 pp.; (c) A. P. de Silva, N. D. McClenaghan, *Chem. Eur. J.* **2004**, *10*, 574–586; (d) J. Andréasson, Y. Terazono, B. Albinsson, T. A. Moore, A. L. Moore, D. Gust, *Angew. Chem. Int. Ed.* **2005**, *44*, 7591–7594; (e) K. Szacilowski, W. Macyk, G. Stochel, *J. Am. Chem. Soc.* **2006**, *128*, 4550–4551; (f) P. Remón, M. Bälter, S. Li, J. Andréasson, U. Pischel, *J. Am. Chem. Soc.* **2011**, *133*, 20742–20745.
- [42] M. Amelia, M. Baroncini, A. Credi, *Angew. Chem. Int. Ed.* **2008**, *47*, 6240–6243.
- [43] (a) S. Silvi, A. Arduini, A. Pochini, A. Secchi, M. Tomasulo, F. M. Raymo, M. Baroncini, A. Credi, *J. Am. Chem. Soc.* **2007**, *129*, 13378–13379; (b) T. Avellini, H. Li, A. Coskun, G. Barin, A. Trabolsi, A. N. Basuray, S. K. Dey, A. Credi, S. Silvi, J. F. Stoddart, M. Venturi, *Angew. Chem. Int. Ed.* **2012**, *51*, 1611–1615.
- [44] M. Baroncini, M. Semeraro, A. Credi, *ChemPhysChem* **2017**, *18*, 1755–1759.
- [45] (a) J. Andréasson, G. Kodis, Y. Terazono, P. A. Liddell, S. Bandyopadhyay, R. H. Mitchell, T. A. Moore, A. L. Moore, D. Gust, *J. Am. Chem. Soc.* **2004**, *126*, 15926–15927; (b) A. Credi, *Angew. Chem. Int. Ed.* **2007**, *46*, 5472–5475; (c) V. Balzani, A. Credi, M. Venturi, *ChemSusChem* **2008**, *1*, 26–58; (d) J. Kärnbratt, M. Hammarson, S. Li, H. L. Anderson, B. Albinsson, J. Andréasson, *Angew. Chem. Int. Ed.* **2010**, *49*, 1854–1857; (e) M. Bälter, S. Li, J. R. Nilsson, J. Andréasson, U. Pischel, *J. Am. Chem. Soc.* **2013**, *135*, 10230–10233.
- [46] *Photochromism: Molecules and Systems*, Rev. ed, (Eds.: H. Dürr, H. Bouas-Laurent), Elsevier, Amsterdam ; Boston, **2003**, 1044 pp.

- [47] K. Kumar, C. Knie, D. Bléger, M. A. Peletier, H. Friedrich, S. Hecht, D. J. Broer, M. G. Debije, A. P. H. J. Schenning, *Nat. Commun.* **2016**, *7*, 11975.
- [48] (a) S. O. Poelma, S. S. Oh, S. Helmy, A. S. Knight, G. L. Burnett, H. T. Soh, C. J. Hawker, J. Read de Alaniz, *Chem. Commun.* **2016**, *52*, 10525–10528; (b) J. Olejniczak, C.-J. Carling, A. Almutairi, *J. Controlled Release*, Drug Delivery Research in North America – Part I **2015**, *219*, 18–30.
- [49] T. Sendler, K. Luka-Guth, M. Wieser, Lokamani, J. Wolf, M. Helm, S. Gemming, J. Kerbusch, E. Scheer, T. Huhn, A. Erbe, *Adv. Sci.* **2015**, *2*, 1500017.
- [50] M. Bälter, S. Li, M. Morimoto, S. Tang, J. Hernando, G. Guirado, M. Irie, F. M. Raymo, J. Andréasson, *Chem. Sci.* **2016**, *7*, 5867–5871.
- [51] P. Commins, M. A. Garcia-Garibay, *J. Org. Chem.* **2014**, *79*, 1611–1619.
- [52] D. Bléger, *Macromol. Chem. Phys.* **2016**, *217*, 189–198.
- [53] (a) M. Baroncini, S. Silvi, M. Venturi, A. Credi, *Angew. Chem. Int. Ed.* **2012**, *51*, 4223–4226; (b) G. Ragazzon, M. Baroncini, S. Silvi, M. Venturi, A. Credi, *Beilstein J. Nanotechnol.* **2015**, *6*, 2096–2104.
- [54] E. Marchi, M. Baroncini, G. Bergamini, J. Van Heyst, F. Vögtle, P. Ceroni, *J. Am. Chem. Soc.* **2012**, *134*, 15277–15280.
- [55] T. Muraoka, K. Kinbara, Y. Kobayashi, T. Aida, *J. Am. Chem. Soc.* **2003**, *125*, 5612–5613.
- [56] (a) M. Asakawa, P. R. Ashton, V. Balzani, C. L. Brown, A. Credi, O. A. Matthews, S. P. Newton, F. M. Raymo, A. N. Shipway, N. Spencer, A. Quick, J. F. Stoddart, A. J. P. White, D. J. Williams, *Chem. Eur. J.* **1999**, *5*, 860–875; (b) V. Balzani, A. Credi, F. Marchioni, J. F. Stoddart, *Chem. Commun.* **2001**, 1860–1861; (c) Y. Inoue, P. Kuad, Y. Okumura, Y. Takashima, H. Yamaguchi, A. Harada, *J. Am. Chem. Soc.* **2007**, *129*, 6396–6397; (d) S. Angelos, Y.-W. Yang, N. M. Khashab, J. F. Stoddart, J. I. Zink, *J. Am. Chem. Soc.* **2009**, *131*, 11344–11346; (e) D. P. Ferris, Y.-L. Zhao, N. M. Khashab, H. A. Khatib, J. F. Stoddart, J. I. Zink, *J. Am. Chem. Soc.* **2009**, *131*, 1686–1688; (f) Y.-L. Zhao, J. F. Stoddart, *Langmuir* **2009**, *25*, 8442–8446.
- [57] S. Kobatake, S. Takami, H. Muto, T. Ishikawa, M. Irie, *Nature* **2007**, *446*, 778–781.
- [58] (a) S. Wiedbrauk, H. Dube, *Tetrahedron Lett.* **2015**, *56*, 4266–4274; (b) C. Petermayer, H. Dube, *Acc. Chem. Res.* **2018**, *51*, 1153–1163.
- [59] (a) Y. Kishimoto, J. Abe, *J. Am. Chem. Soc.* **2009**, *131*, 4227–4229; (b) T. Yamaguchi, M. F. Hilbers, P. P. Reinders, Y. Kobayashi, A. M. Brouwer, J. Abe, *Chem. Commun.* **2014**, *51*, 1375–1378; (c) T. Yamaguchi, Y. Kobayashi, J. Abe, *J. Am. Chem. Soc.* **2016**, *138*, 906–913.
- [60] L. A. Tatum, X. Su, I. Aprahamian, *Acc. Chem. Res.* **2014**, *47*, 2141–2149.
- [61] (a) D. J. van Dijken, P. Kovaříček, S. P. Ihrig, S. Hecht, *J. Am. Chem. Soc.* **2015**, *137*, 14982–14991; (b) X. Su, I. Aprahamian, *Chem. Soc. Rev.* **2014**, *43*, 1963–1981.

- [62] M. Irie, *Chem. Rev.* **2000**, *100*, 1685–1716.
- [63] Y. Yokoyama, *Chem. Rev.* **2000**, *100*, 1717–1740.
- [64] (a) D. Bléger, J. Schwarz, A. M. Brouwer, S. Hecht, *J. Am. Chem. Soc.* **2012**, *134*, 20597–20600; (b) C. Knie, M. Utecht, F. Zhao, H. Kulla, S. Kovalenko, A. M. Brouwer, P. Saalfrank, S. Hecht, D. Bléger, *Chem. Eur. J.* **2014**, *20*, 16492–16501.
- [65] G. Berkovic, V. Krongauz, V. Weiss, *Chem. Rev.* **2000**, *100*, 1741–1754.
- [66] (a) S. Helmy, S. Oh, F. A. Leibfarth, C. J. Hawker, J. Read de Alaniz, *J. Org. Chem.* **2014**, *79*, 11316–11329; (b) N. Mallo, P. T. Brown, H. Iranmanesh, T. S. C. MacDonald, M. J. Teusner, J. B. Harper, G. E. Ball, J. E. Beves, *Chem. Commun.* **2016**, *52*, 13576–13579; (c) M. M. Lerch, W. Szymański, B. L. Feringa, *Chem. Soc. Rev.* **2018**, *47*, 1910–1937.
- [67] M. Hammerich, C. Schütt, C. Stähler, P. Lentes, F. Röhricht, R. Höppner, R. Herges, *J. Am. Chem. Soc.* **2016**, *138*, 13111–13114.
- [68] T. Sumi, Y. Takagi, A. Yagi, M. Morimoto, M. Irie, *Chem. Commun.* **2014**, *50*, 3928–3930.
- [69] M. Kasha, *Discuss. Faraday Soc.* **1950**, *9*, 14–19.
- [70] S. Helmy, F. A. Leibfarth, S. Oh, J. E. Poelma, C. J. Hawker, J. Read de Alaniz, *J. Am. Chem. Soc.* **2014**, *136*, 8169–8172.
- [71] (a) R. Siewertsen, H. Neumann, B. Buchheim-Stehn, R. Herges, C. Näther, F. Renth, F. Temps, *J. Am. Chem. Soc.* **2009**, *131*, 15594–15595; (b) S. Samanta, A. A. Beharry, O. Sadovski, T. M. McCormick, A. Babalhavaeji, V. Tropepe, G. A. Woolley, *J. Am. Chem. Soc.* **2013**, *135*, 9777–9784; (c) E. A. Dragu, A. E. Ion, S. Shova, D. Bala, C. Mihailciuc, M. Voicescu, S. Ionescu, S. Nica, *RSC Adv.* **2015**, *5*, 63282–63286.
- [72] D. Bléger, S. Hecht, *Angew. Chem. Int. Ed.* **2015**, *54*, 11338–11349.
- [73] G. Cabré, A. Garrido-Charles, À. González-Lafont, W. Moormann, D. Langbehn, D. Egea, J. M. Lluch, R. Herges, R. Alibés, F. Busqué, P. Gorostiza, J. Hernando, *Org. Lett.* **2019**, *21*, 3780–3784.
- [74] (a) W. A. Velema, W. Szymanski, B. L. Feringa, *J. Am. Chem. Soc.* **2014**, *136*, 2178–2191; (b) J. Broichhagen, J. A. Frank, D. Trauner, *Acc. Chem. Res.* **2015**, *48*, 1947–1960; (c) M. Dong, A. Babalhavaeji, S. Samanta, A. A. Beharry, G. A. Woolley, *Acc. Chem. Res.* **2015**, *48*, 2662–2670; (d) M. M. Lerch, M. J. Hansen, G. M. van Dam, W. Szymanski, B. L. Feringa, *Angew. Chem. Int. Ed.* **2016**, *55*, 10978–10999.
- [75] (a) W. R. Browne, B. L. Feringa, *Nat. Nanotechnol.* **2006**, *1*, 25–35; (b) J. M. Abendroth, O. S. Bushuyev, P. S. Weiss, C. J. Barrett, *ACS Nano* **2015**, *9*, 7746–7768; (c) M. R. Wilson, J. Solà, A. Carloni, S. M. Goldup, N. Lebrasseur, D. A. Leigh, *Nature* **2016**, *534*, 235–240.

- [76] (a) W. F. Paxton, S. Sundararajan, T. E. Mallouk, A. Sen, *Angew. Chem. Int. Ed.* **2006**, *45*, 5420–5429; (b) R. A. Pavlick, S. Sengupta, T. McFadden, H. Zhang, A. Sen, *Angew. Chem. Int. Ed.* **2011**, *50*, 9374–9377; (c) S. Sengupta, M. E. Ibele, A. Sen, *Angew. Chem. Int. Ed.* **2012**, *51*, 8434–8445; (d) S. Sanchez, L. Soler, J. Katuri, *Angew. Chem. Int. Ed.* **2015**, *54*, 1414–1444; (e) R. Guha, F. Mohajerani, M. Collins, S. Ghosh, A. Sen, D. Velegol, *J. Am. Chem. Soc.* **2017**, *139*, 15588–15591; (f) J. Agudo-Canalejo, T. Adeleke-Larodo, P. Illien, R. Golestanian, *Acc. Chem. Res.* **2018**, *50*, 2365–2372; (g) K. K. Dey, *Angew. Chem. Int. Ed.* **2019**, *58*, 2208–2228.
- [77] (a) W. F. Paxton, K. C. Kistler, C. C. Olmeda, A. Sen, S. K. St. Angelo, Y. Cao, T. E. Mallouk, P. E. Lammert, V. H. Crespi, *J. Am. Chem. Soc.* **2004**, *126*, 13424–13431; (b) S. Fournier-Bidoz, A. C. Arsenault, I. Manners, G. A. Ozin, *Chem. Commun.* **2005**, 441–443; (c) T. R. Kline, W. F. Paxton, T. E. Mallouk, A. Sen, *Angew. Chem. Int. Ed.* **2005**, *44*, 744–746; (d) Y. Hong, N. M. K. Blackman, N. D. Kopp, A. Sen, D. Velegol, *Phys. Rev. Lett.* **2007**, *99*, 178103; (e) Z. Wu, Y. Wu, W. He, X. Lin, J. Sun, Q. He, *Angew. Chem. Int. Ed.* **2013**, *52*, 7000–7003.
- [78] (a) A. A. Solovev, Y. Mei, E. Bermúdez Ureña, G. Huang, O. G. Schmidt, *Small* **2009**, *5*, 1688–1692; (b) W. Gao, S. Sattayasamitsathit, J. Orozco, J. Wang, *J. Am. Chem. Soc.* **2011**, *133*, 11862–11864; (c) S. Naeem, F. Naeem, M. Manjare, F. Liao, V. A. B. Quiñones, G. S. Huang, Y. Li, J. Zhang, A. A. Solovev, Y. F. Mei, *Appl. Phys. Lett.* **2019**, *114*, 033701.
- [79] (a) S. Ebbens, M.-H. Tu, J. R. Howse, R. Golestanian, *Phys. Rev. E* **2012**, *85*, 020401; (b) J. Orozco, B. Jurado-Sanchez, G. Wagner, W. Gao, R. Vazquez-Duhalt, S. Sattayasamitsathit, M. Galarnyk, A. Cortes, D. Saintillan, J. Wang, *Langmuir* **2014**, *30*, 5082–5087; (c) P. H. Colberg, S. Y. Reigh, B. Robertson, R. Kapral, *Acc. Chem. Res.* **2014**, *47*, 3504–3511; (d) L. Ma, R. Baumgartner, Y. Zhang, Z. Song, K. Cai, J. Cheng, *J. Polym. Sci. Part A: Polym. Chem.* **2015**, *53*, 1161–1168; (e) C. Maggi, J. Simmchen, F. Saglimbeni, J. Katuri, M. Dipalo, F. De Angelis, S. Sanchez, R. Di Leonardo, *Small* **2016**, *12*, 446–451; (f) B. Jurado-Sánchez, A. Escarpa, *Electroanalysis* **2017**, *29*, 14–23.
- [80] (a) W. Wang, L. A. Castro, M. Hoyos, T. E. Mallouk, *ACS Nano* **2012**, *6*, 6122–6132; (b) S. Ahmed, D. T. Gentekos, C. A. Fink, T. E. Mallouk, *ACS Nano* **2014**, *8*, 11053–11060; (c) S. Sabrina, M. Tasinkevych, S. Ahmed, A. M. Brooks, M. O. de la Cruz, T. E. Mallouk, K. J. M. Bishop, *ACS Nano* **2018**, *12*, 2939–2947; (d) X. Lu, H. Shen, K. Zhao, Z. Wang, H. Peng, W. Liu, *Chem. Asian J.* **2019**, *14*, 2406–2416.
- [81] E. M. Purcell, *Am. J. Phys.* **1977**, *45*, 3–11.
- [82] (a) E. Lauga, *Soft Matter* **2011**, *7*, 3060–3065; (b) J. Happel, H. Brenner, *Low Reynolds Number Hydrodynamics*, red. by R. J. Moreau, Springer Netherlands, Dordrecht, **1981**.
- [83] J. W. Shaevitz, J. Y. Lee, D. A. Fletcher, *Cell* **2005**, *122*, 941–945.

- [84] (a) F. Alouges, A. DeSimone, A. Lefebvre, *Eur. Phys. J. E* **2009**, *28*, 279–284; (b) D. Walker, M. Kübler, K. I. Morozov, P. Fischer, A. M. Leshansky, *Nano Lett.* **2015**, *15*, 4412–4416; (c) R. Golestanian, *Eur. Phys. J. E* **2008**, *25*, 1–4.
- [85] (a) F. Wong, K. K. Dey, A. Sen, *Annu. Rev. Mater. Res.* **2016**, *46*, 407–432; (b) K. E. Peyer, S. Tottori, F. Qiu, L. Zhang, B. J. Nelson, *Chem. Eur. J.* **2013**, *19*, 28–38; (c) J. R. Howse, R. A. L. Jones, A. J. Ryan, T. Gough, R. Vafabakhsh, R. Golestanian, *Phys. Rev. Lett.* **2007**, *99*, 048102; (d) R. Golestanian, *Phys. Rev. Lett.* **2010**, *105*, 018103.
- [86] K. K. Dey, F. Y. Pong, J. Breffke, R. Pavlick, E. Hatzakis, C. Pacheco, A. Sen, *Angew. Chem. Int. Ed.* **2016**, *55*, 1113–1117.
- [87] E. Lauga, *Phys. Rev. Lett.* **2011**, *106*, 178101.
- [88] (a) H. S. Muddana, S. Sengupta, T. E. Mallouk, A. Sen, P. J. Butler, *J. Am. Chem. Soc.* **2010**, *132*, 2110–2111; (b) S. Sengupta, K. K. Dey, H. S. Muddana, T. Tabouillot, M. E. Ibele, P. J. Butler, A. Sen, *J. Am. Chem. Soc.* **2013**, *135*, 1406–1414; (c) S. Sengupta, M. M. Spiering, K. K. Dey, W. Duan, D. Patra, P. J. Butler, R. D. Astumian, S. J. Benkovic, A. Sen, *ACS Nano* **2014**, *8*, 2410–2418; (d) C. Riedel, R. Gabizon, C. A. M. Wilson, K. Hamadani, K. Tsekouras, S. Marqusee, S. Presse, C. Bustamante, *Nature* **2015**, *517*, 227–U288; (e) I. Ortiz-Rivera, H. Shum, A. Agrawal, A. Sen, A. C. Balazs, *Proc. Natl. Acad. Sci. U. S. A.* **2016**, *113*, 2585–2590; (f) X. Zhao, K. K. Dey, S. Jeganathan, P. J. Butler, U. M. Córdova-Figueroa, A. Sen, *Nano Lett.* **2017**, *17*, 4807–4812; (g) X. Zhao, K. Gentile, F. Mohajerani, A. Sen, *Acc. Chem. Res.* **2018**, *51*, 2373–2381; (h) C. Weistuch, S. Pressé, *J. Phys. Chem. B* **2018**, *122*, 5286–5290; (i) A.-Y. Jee, S. Dutta, Y.-K. Cho, T. Tlusty, S. Granick, *Proc. Natl. Acad. Sci.* **2018**, *115*, 14–18; (j) A.-Y. Jee, Y.-K. Cho, S. Granick, T. Tlusty, *Proc. Natl. Acad. Sci.* **2018**, *115*, E10812–E10821.
- [89] (a) R. D. Astumian, P. Hänggi, *Phys. Today* **2002**, *55*, 33–39; (b) E. Lauga, T. R. Powers, *Rep. Prog. Phys.* **2009**, *72*, 096601; (c) P. Hänggi, F. Marchesoni, *Rev. Mod. Phys.* **2009**, *81*, 387–442.
- [90] (a) J. Enderlein, I. Gregor, D. Patra, T. Dertinger, U. B. Kaupp, *ChemPhysChem* **2005**, *6*, 2324–2336; (b) V. García-López, P.-T. Chiang, F. Chen, G. Ruan, A. A. Martí, A. B. Kolomeisky, G. Wang, J. M. Tour, *Nano Lett.* **2015**, *15*, 8229–8239; (c) V. Garcia-Lopez, J. Jeffet, S. Kuwahara, A. A. Marti, Y. Ebenstein, J. M. Tour, *Org. Lett.* **2016**, *18*, 2343–2346; (d) P. Illien, T. Adeleke-Larodo, R. Golestanian, *EPL* **2017**, *119*, 40002; (e) J.-P. Günther, M. Börsch, P. Fischer, *Acc. Chem. Res.* **2018**, *51*, 1911–1920.
- [91] Y. Zhang, M. J. Armstrong, N. M. Bassir Kazeruni, H. Hess, *Nano Lett.* **2018**, *18*, 8025–8029.
- [92] J.-P. Günther, G. Majer, P. Fischer, *J. Chem. Phys.* **2019**, *150*, 124201.

- [93] (a) R. D. Astumian, *ACS Nano* **2014**, *8*, 11917–11924; (b) M. Dennison, R. Kapral, H. Stark, *Soft Matter* **2017**, *13*, 3741–3749; (c) F. Mohajerani, X. Zhao, A. Somasundar, D. Velegol, A. Sen, *Biochemistry* **2018**, *57*, 6256–6263; (d) J. Agudo-Canalejo, P. Illien, R. Golestanian, *Nano Lett.* **2018**, *18*, 2711–2717; (e) P. Gaspard, R. Kapral, *Adv. Phys. X* **2019**, *4*, 1602480.
- [94] (a) Y. Zhang, H. Hess, *ACS Cent. Sci.* **2019**, *5*, 939–948; (b) M. Feng, M. K. Gilson, *Biophys. J.* **2019**, *116*, 1898–1906; (c) R. P. Sear, *Phys. Rev. Lett.* **2019**, *122*, 128101.
- [95] E. L. Cussler, *Diffusion: Mass Transfer in Fluid Systems*, Cambridge University Press, **2009**, 655 pp.
- [96] (a) Y. Cohen, L. Avram, L. Frish, *Angew. Chem. Int. Ed.* **2005**, *44*, 520–554; (b) L. Avram, Y. Cohen, *Chem. Soc. Rev.* **2015**, *44*, 586–602.
- [97] P. G. Clark, E. N. Guidry, W. Y. Chan, W. E. Steinmetz, R. H. Grubbs, *J. Am. Chem. Soc.* **2010**, *132*, 3405–3412.
- [98] (a) L. Dorđević, T. Marangoni, T. Miletić, J. Rubio-Magnieto, J. Mohanraj, H. Amenitsch, D. Pasini, N. Liaros, S. Couris, N. Armaroli, M. Surin, D. Bonifazi, *J. Am. Chem. Soc.* **2015**, *137*, 8150–8160; (b) T. S. Fischer, D. Schulze-Sünninghausen, B. Luy, O. Altintas, C. Barner-Kowollik, *Angew. Chem. Int. Ed.* **2016**, *55*, 11276–11280.
- [99] W. S. Price, F. Tsuchiya, Y. Arata, *Biophys. J.* **2001**, *80*, 1585–1590.
- [100] (a) M. Petryk, A. Troć, B. Gierczyk, W. Danikiewicz, M. Kwit, *Chem. Eur. J.* **2015**, *21*, 10318–10321; (b) S. Bachmann, R. Neufeld, M. Dzemski, D. Stalke, *Chem. Eur. J.* **2016**, *22*, 8462–8465.
- [101] M. Forsyth, H. Yoon, F. Chen, H. Zhu, D. R. MacFarlane, M. Armand, P. C. Howlett, *J. Phys. Chem. C* **2016**, *120*, 4276–4286.
- [102] E. Chiavazzo, M. Fasano, P. Asinari, P. Decuzzi, *Nat. Commun.* **2014**, *5*, 3565.
- [103] S. Tang, M. Wang, B. D. Olsen, *J. Am. Chem. Soc.* **2015**, *137*, 3946–3957.
- [104] (a) L. Fielding, *Tetrahedron* **2000**, *56*, 6151–6170; (b) B. Meyer, T. Peters, *Angew. Chem. Int. Ed.* **2003**, *42*, 864–890.
- [105] L. Serra, J. Doménech, N. A. Peppas, *Biomaterials* **2006**, *27*, 5440–5451.
- [106] C. Di Rienzo, V. Piazza, E. Gratton, F. Beltram, F. Cardarelli, *Nat. Commun.* **2014**, *5*, 5891.
- [107] (a) W. S. Price, *Concepts Magn. Reson.* **1997**, *9*, 299–336; (b) S.-G. Timothy, T. Allan, Z. Mikhail, A. W. Scott, Z. Gang, S. P. William, *Curr. Org. Chem.* **2018**, *22*, 758–768; (c) E. O. Stejskal, J. E. Tanner, *J. Chem. Phys.* **1965**, *42*, 288–292.
- [108] (a) K. I. Momot, P. W. Kuchel, *J. Magn. Reson.* **2004**, *169*, 92–101; (b) G. Zheng, W. S. Price, *J. Biomol. NMR* **2009**, *45*, 295.
- [109] F. J. Dyson, *Science* **2012**, *338*, 1426–1427.

Chapter 2

Time-resolved diffusion NMR



This chapter is based on work published as:

T. S. C. MacDonald, W. S. Price, J. E. Beves, *ChemPhysChem* **2019**, *20*, 926–930.

I performed all experimental work and analysis. All authors contributed towards project design and paper writing.

Summary:

A general procedure for measurement of time-resolved diffusion coefficients of molecular species by NMR is described, including the use of methanol for fast temperature-independent gradient calibration.

2.1 Time-resolved diffusion NMR

Diffusion NMR experiments are typically slow, with a complete measurement taking on the order of 10 minutes. Various methods have been developed to reduce the time required for collecting diffusion data,^[1] including **difftrain** pulse sequences^[1b,d,i] and methods with the number of scans matched to gradient strengths.^[1k] These approaches are applicable to determining diffusion coefficients in static systems where the diffusion coefficient of each species is independent of time or changing more slowly than the experimental time scale. However, new approaches are required for studying systems where chemical processes result in changes in diffusion and/or concentrations at time scales comparable to that of the NMR experiment.

In this chapter, I present a new methodology for acquiring time-dependent diffusion NMR data of evolving processes.

2.1.1 Removing bias with random gradient lists

In a standard diffusion NMR measurement, a series of gradient echo experiments are acquired using a series of gradient pulse amplitudes g taken from a gradient list. The intensities of the acquired NMR signals decrease as gradient pulse strengths increase, and diffusion coefficients (D) can then be calculated by fitting the Stejskal-Tanner equation (1.3) to signal intensities as a function of g . Chemical species with a higher diffusion coefficient show a greater signal attenuation as the gradient pulse strength g is increased, while species with a lower diffusion coefficient show a slower decrease in signal intensity with increasing g . An example of this is shown in Figure 2.1 for a mixture of water and methanol: here, water has a higher diffusion coefficient than methanol and therefore the water signal at 4.35 ppm attenuates more rapidly than the methanol signals.

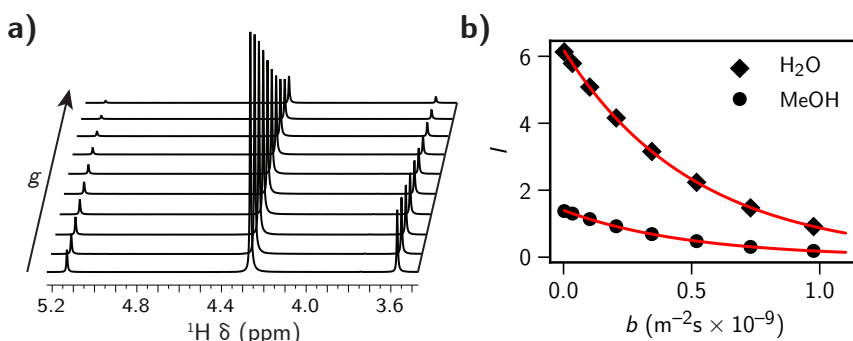


Figure 2.1. Measurement of the diffusion coefficient of methanol (^1H NMR 400 MHz, 298 K). a) A pulsed-gradient stimulated echo (PGSE) experiment acquired with increasing values of the gradient strength g , resulting in an attenuation of signal intensities. b) Diffusion coefficients determined by non-linear fitting of the Stejskal-Tanner equation Equation 1.3 to the echo signal attenuation. See key reviews^[2,3] for details.

In an NMR diffusion experiment, it is assumed that changes in acquired signal intensities over the duration of the experiment are solely caused by changes in the gradient pulse strength g . If the *concentration* of a chemical species changes appreciably over the measurement time (for example, as a result of a chemical reaction), this will *also* cause a change in the received

2.1. TIME-RESOLVED DIFFUSION NMR

signal intensities and may lead to an erroneous measured diffusion coefficient D . This is demonstrated below.

Simulated data of a chemical reaction where compound X reacts to form compound Y over an arbitrary timescale are shown in Figure 2.2. The diffusion coefficients D of X and Y were each set to $1.0 \times 10^{-9} \text{ m}^2 \text{s}^{-1}$ and the echo attenuations were simulated for eight linearly incremented g values chosen to give 10 to 99% attenuation. The simulated data and the corresponding fits for compounds X and Y are shown in Figure 2.2b and Figure 2.2c, respectively. In the case of compound X, which has a decreasing concentration over time, the determined diffusion coefficient ($D = (1.27 \pm 0.04) \times 10^{-9} \text{ m}^2 \text{s}^{-1}$) is well above the real diffusion coefficient. Similarly, for compound Y which has an increasing concentration over time, the fitted diffusion value ($D = (0.72 \pm 0.06) \times 10^{-9} \text{ m}^2 \text{s}^{-1}$) is lower than the real value. Figure 2.2d and Figure 2.2e show the data for the same process, except where the same gradient list has been *randomly re-ordered*. This removes the correlation between concentration changes and the values in the gradient list. The result is the diffusion coefficients for both compound X

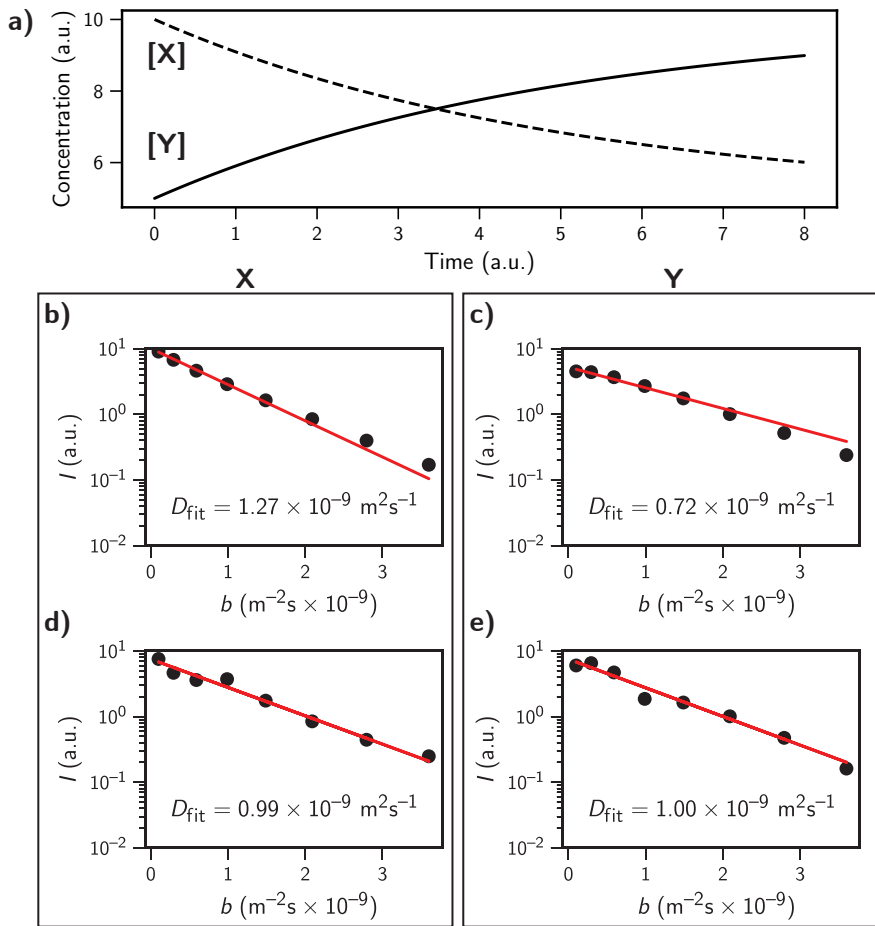


Figure 2.2. Simulated diffusion experiments on species with changing concentrations. a) Concentrations of X and Y over time, each with a diffusion coefficient of $1 \times 10^{-9} \text{ m}^2 \text{s}^{-1}$. When diffusion values are measured using a linearly increasing gradient list for species with decreasing concentration ((b), [X]) or species with increasing concentration ((c), [Y]) over the course of the experiment, the diffusion coefficient obtained by fitting the Stejskal-Tanner equation (Equation 1.3) is erroneously higher or lower, respectively. Randomizing the order of the gradient list reduces this distortion, as shown in (d) and (e). All data fits by non-linear least squares regression.

($D = (0.99 \pm 0.17) \times 10^{-9} \text{ m}^2 \text{ s}^{-1}$) and compound Y ($D = (1.00 \pm 0.16) \times 10^{-9} \text{ m}^2 \text{ s}^{-1}$) are more accurately determined, despite these species undergoing concentration changes during the diffusion measurement.

2.2 Improving the time resolution of diffusion measurements

We are also concerned with chemical systems where diffusion coefficients themselves are changing over time. As a typical NMR diffusion measurement requires a series of ^1H NMR spectra (e.g. Figure 2.1a) one approach to measuring changes in diffusion would be to acquire a set of 8–16 spectra using a range of (randomly shuffled) gradient amplitudes, fit a single diffusion coefficient across the set, and then repeat this process until the end of the experiment.^[4] This would limit time resolution of the diffusion measurement to the time taken to collect a complete series of spectra (generally in the range of 5–20 minutes). Instead, the use of random gradient pulse amplitude allows diffusion coefficients to be fitted over a *moving subset* of data taken from a long continuously-acquired experiment using many randomly distributed gradient pulse strengths, improving time resolution without loss of signal-to-noise.

2.2.1 Moving-frame processing of continuous data

Time-resolved diffusion data were continuously acquired using experiments set up with long gradient lists of 500–2000 gradient points. All time-resolved diffusion data were processed using a moving-average approach to solve the Stejskal-Tanner equation (Equation 1.3).

Diffusion rates for each point in time were calculated using a moving regression analysis over a number of (I, b) points centred on that point in time. Diffusion coefficients and signal intensities D and I_0 at each time point t_i were calculated by non-linear regression of points $I_{i-n} \dots I_{i+n}$ against $b_{i-n} \dots b_{i+n}$ (slices of $2n+1$ points, centred on time t_i) using Equation 1.3. The number of points used for the regression was chosen arbitrarily: a larger n improves the precision of measured average D , but at the expense of time resolution. An example of this is shown in Table 2.1.

Table 2.1. Time-resolved diffusion measurements of methanol using a moving fit of the integral of the methyl ^1H NMR signal. A diffusion coefficient $D(t)$ for each timepoint t is calculated in this example using a non-linear fit of I against b for a sample of five data points centred about time t (highlighted), allowing simultaneous measurement of concentration and diffusion data. $b = \gamma^2 \delta^2 g^2 (\Delta - \delta/3)$.

t min	$b \times 10^7 \text{ m}^{-2} \text{ s}$	$I_{t=0.5}$	$I_{t=0.67}$	$I_{t=0.75}$
0.17	3.86	3663.9	3663.9	3663.9
0.33	19.66	2657.5	2657.5	2657.5
0.50	18.03	2752.7	2752.7	2752.7
0.67	93.62	595.0	595.0	595.0
0.83	10.33	3211.3	3211.3	3211.3
1.0	26.50	2315.4	2315.4	2315.4
1.17	53.99	1326.5	1326.5	1326.5
$D \times 10^{-9} \text{ m}^2 \text{ s}^{-1}$		2.025	2.024	2.025
I_0		3961	3959	3961

2.2.2 Example data for moving-frame processing

An application of continuous acquisition and moving-frame data processing is shown in Figure 2.3, which contains experimental ^1H NMR data for neat methanol measured over 5 minutes. During this data acquisition the temperature was increased after 2 minutes, generating a change in the diffusion coefficient during the measurement. Figure 2.3a shows the raw data of the ^1H signal intensity of the methyl signal (red) against the random gradient strength used (b , black). By selecting eight consecutive data points the diffusion coefficient can be fitted over that time period (Figure 2.3b). For example, at $t = 1.5$ min the fitted diffusion coefficient is $(2.32 \pm 0.01) \times 10^{-9} \text{ m}^2 \text{s}^{-1}$, which changes to $(2.40 \pm 0.01) \times 10^{-9} \text{ m}^2 \text{s}^{-1}$ at $t = 3.5$ min after the temperature change. Such a fitting method can be used with a continually moving frame of eight spectra to give time resolution down to the experiment time of a single spectrum, as shown in Figure 2.3c.

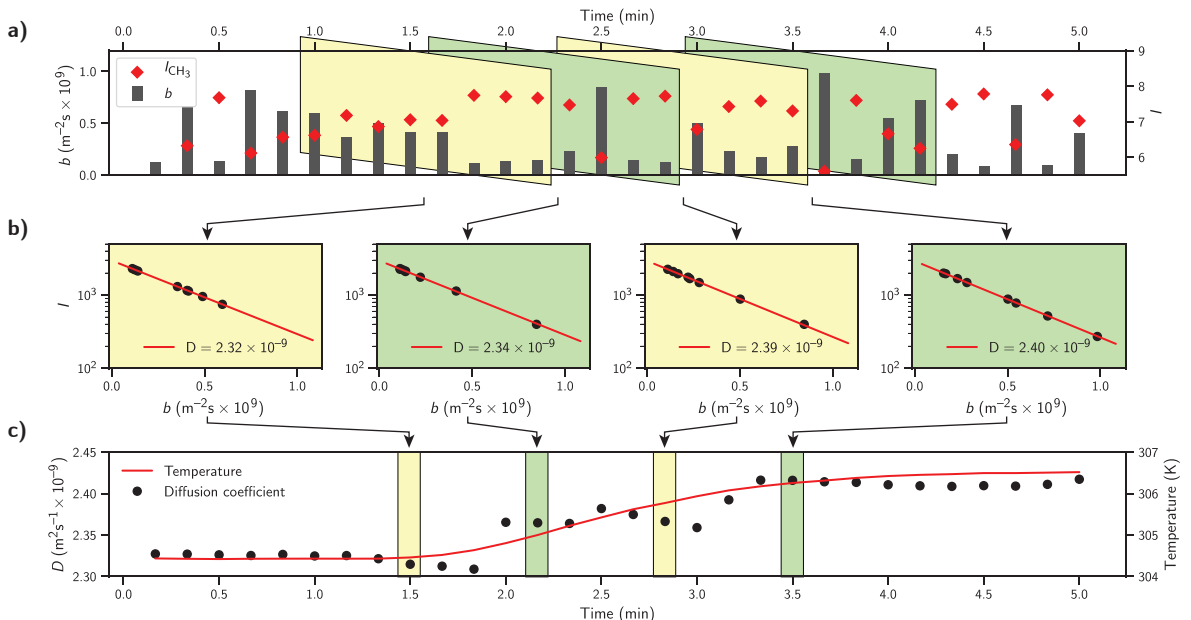


Figure 2.3. Moving average analysis of time-resolved diffusion NMR data. a) Continuous rapid acquisition of spectra using a random gradient list (black) generates an array of NMR spectra over time from which peaks can be integrated (red). Diffusion coefficients are then obtained by fitting the Stejskal-Tanner equation (Equation 1.3) to a moving subset of $[I, b]$ points (8 points here) centred about time t . b) Time-dependent diffusion information $D(t)$ is obtained by advancing this fit over the dataset as a series of non-linear fits, allowing c) changes in diffusion (black) induced by temperature changes (red) to be followed over sub-minute timescales. ^1H PGSE ($\delta = 1.2 \text{ ms}$, $\Delta = 45 \text{ ms}$, $ns = 2, 5$ s repetition time), methanol capillary placed in DMSO-d_6 , $304.5\text{--}306.5 \text{ K}$, 500 MHz .

2.3 Temperature-insensitive gradient calibration

Small changes in temperature can lead to dramatic changes in diffusion coefficients, making diffusion measurements of non-equilibrium systems challenging: a transient change in measured D could be the result of either a non-thermal change in D , or a simple fluctuation in sample temperature. Diffusion measurements of exothermic or endothermic reactions are particularly vulnerable to this sort of confusion. An NMR experiment that provides simultaneous

measurement of the temperature of the solution along with concentrations and diffusion rates of individual species would allow discrimination between thermal and non-thermal changes in measured diffusion.

There are many compounds with well-characterised temperature-dependent changes in chemical shifts.^[5] For ¹H NMR, the chemical shift difference ($\Delta\delta$) between the OH and alkyl protons of methanol or ethylene glycol are known to allow the temperature to be measured within ± 0.5 K over the ranges 175–330 K and 270–415 K, respectively.^[5d] In this work, methanol was selected as a thermometer due to its ready availability and good sensitivity for temperatures close to room temperature. Adding a flame-sealed capillary filled with methanol to the NMR sample allows the internal temperature of the sample to be monitored over the course of the diffusion measurement to detect any temperature transients that may occur, which is how the temperature in Figure 2.3c was determined. The relationship we have used for temperature determination with methanol is given in Equation 2.1:^[5d]

$$T = 409.0 - 36.54(\Delta\delta) - 21.85(\Delta\delta)^2 \quad (2.1)$$

Accurate NMR diffusion measurement also requires the gradient pulse amplitude g to be precisely calibrated. This is generally performed using a diffusion calibrant of known D , such as pure water,^[5e,6,7a] which can be complicated by the strong dependence of D on the temperature of water:^[7] at 298 K, a 1 K change in temperature corresponds to a 2.5% change in the diffusion coefficient of water.^[8] It is therefore clear that accurate calibration of gradients with a reference sample also requires an accurate knowledge of sample temperature, and that it would be desirable to develop a *temperature insensitive* method of gradient calibration to address this concern. One approach to this problem would be to perform the gradient calibration using a known temperature-dependent diffusion coefficient of a species that could act as its own thermometer, such as methanol. While there is no single model that can generally describe the temperature dependence of the diffusion coefficient of molecular liquids and solutions, it has long been recognised^[9] that the temperature dependence of diffusion $D(t)$ can often be empirically approximated using the Arrhenius-like relationship shown in Equation 2.2:

$$D(t) = D_0 \exp \left[\frac{-A}{T} \right] \quad (2.2)$$

This Arrhenian relationship approximates molecular liquids as hard spheres, and can accurately describe the self-diffusion of weakly interacting solvents (eg alkanes) over wide temperature ranges.^[5g] Unfortunately, the hard sphere approximation fails to describe the complex temperature-dependent changes of the well-ordered solution structure present in hydrogen-bonding solvents such as water, or to a lesser extent methanol, and these solvents are known to display non-Arrhenian behavior over larger temperature ranges.^[5g] This is an unavoidable consequence of the value of methanol as an NMR thermometer: the temperature-dependent hydrogen bonding which results in the chemical shift differences used to measure temperature is the same phenomenon that leads to a non-Arrhenian diffusion-temperature relationship. If a single calibration probe is to be used, this complication is unavoidable.

Despite the hydrogen bonding behaviour of methanol, the diffusion coefficient can be approximated by the Arrhenius equation over limited temperature ranges^[10] and it was hoped that this would be sufficient to use methanol as a temperature-insensitive gradient calibrant.

To establish the temperature dependence of the diffusion coefficient of methanol, a standard sample was prepared containing flame-sealed water and methanol capillaries in a regular NMR tube of DMSO-d₆. Continuous diffusion experiments were then performed while incrementally increasing and or decreasing the sample temperature, typically by 3 °C every 15 minutes. An example of the data acquired from one of these experiments is shown in Figure 2.4.

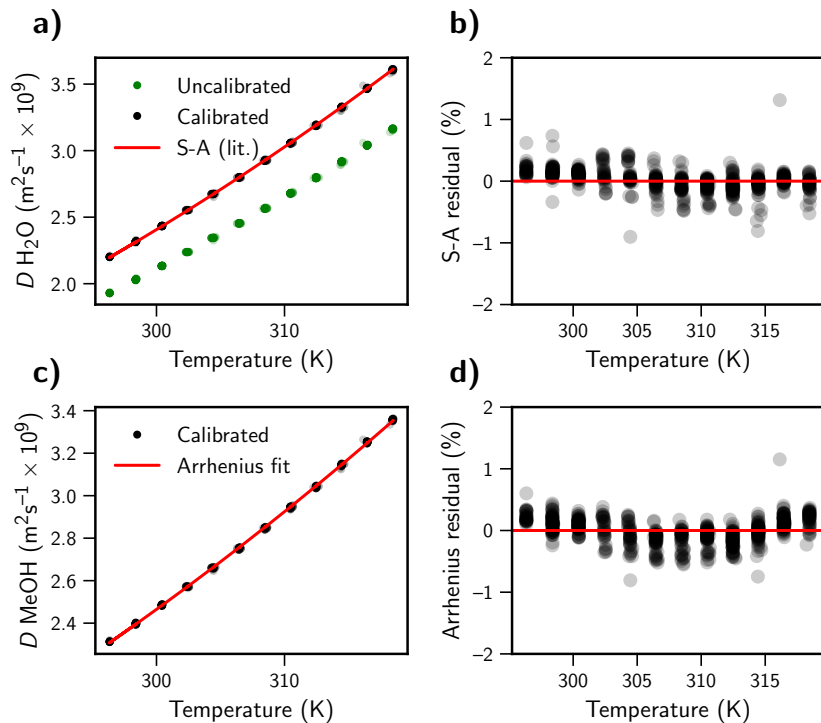


Figure 2.4. Temperature-insensitive gradient calibration with methanol. a) Measured temperature-dependent diffusion of water (green) can be used to calibrate gradient pulse strength by fitting against a literature diffusion-temperature curve (red),^[5g] with calibrated values shown in black. b) Residuals of the gradient calibration with water show no systematic variation over the temperature range studied, and agree well with literature values (<0.5%). c) The diffusion of methanol over temperature modelled with an Arrhenius relationship. d) The residuals of the Arrhenius fit show some systematic error but agree with measured values to <0.5% over the temperature range studied. Data was collected using water and methanol in separate sealed glass capillaries in an NMR tube of DMSO-d₆ solution and measured by ¹H NMR (PGSE, 500 MHz, δ = 1.1 ms, Δ = 45 ms). Data for other instruments is included in subsection 7.1.1.

The measured diffusion rate of water was used to calibrate the experiment: while the temperature dependence of the diffusion coefficient of water (Figure 2.4a) is known to be non-Arrhenian,^[8a,11] it can be described by the empirical Speedy-Angell function shown in Equation 2.3.^[5g] This equation allows the measured diffusion coefficient of water to be used as an internal calibrant in combination with the sample temperature measured by the methanol chemical shift thermometer.

$$D = D_0 \left[\frac{T}{T_S} - 1 \right]^\gamma \quad (2.3)$$

For water, parameters for Equation 2.3 have been reported^[5g] as follows:

$$D_0 = (1.635 \pm 0.002) \times 10^{-8} \text{ m}^2 \text{ s}^{-1}$$

$$T_S = (215.0 \pm 1.2) \text{ K}$$

$$\gamma = 2.064 \pm 0.051$$

Multiple variable temperature diffusion experiments were performed, with the combined data shown in Figure 2.5. The temperature dependence of the self-diffusion coefficient of methanol (Figure 2.5a; Figure 2.4c) was found to display largely Arrhenian behaviour over the range of temperatures studied, and while some deviation was observed (Figure 2.4d; Figure 2.5b) the fit was deemed acceptable for use as a calibration standard over the 295–335 K temperature range shown. The parameters for this Arrhenius model of temperature-dependent diffusion are shown in Equation 2.4.

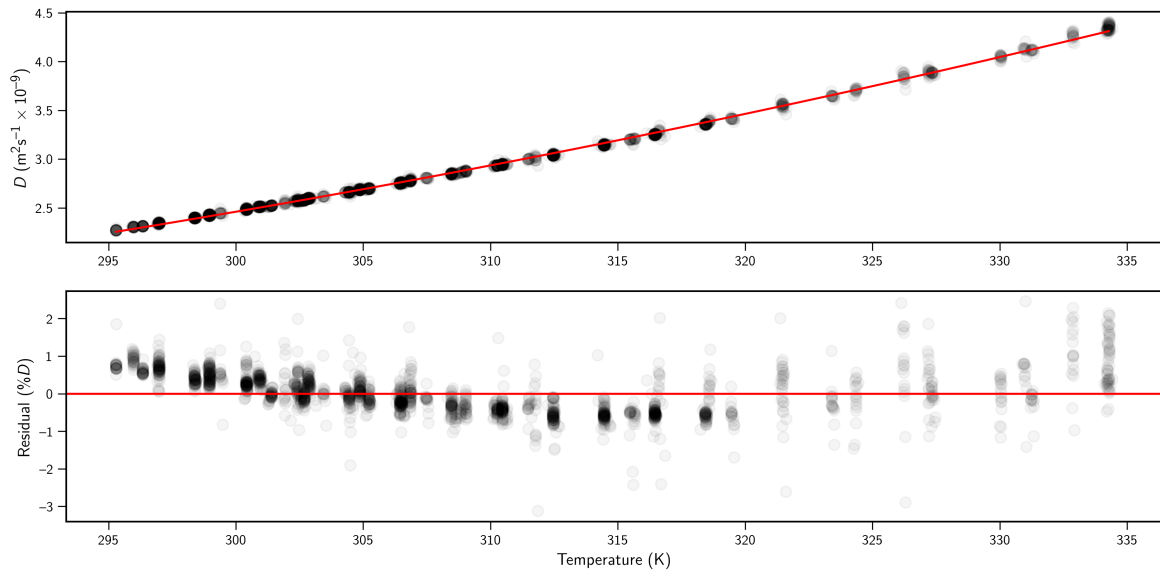


Figure 2.5. a) Arrhenius fit over combined $D(T)$ points for methanol from all experiments (see appendix subsection 7.1.1). b) While the residuals show a clear systemic deviation from the Arrhenius model, the low error of < 1% is acceptable over the 295–335 K temperatures studied. Points are plotted with partial transparency to aid visualisation.

$$D(T) = \left((5.847 \pm 0.023) \times 10^{-7} \right) \exp \left[\frac{-1641 \pm 3}{T} \right] \quad (2.4)$$

Combining Equation 2.4 and Equation 2.1 allows temperature-independent gradient calibration using methanol from *the chemical shift separation alone* over the calibrated range of 295–335 K, as shown in Equation 2.5 where $\delta\Delta$ is the chemical shift separation between the OH and CH₃ peaks of CH₃OH in ppm.

$$D(\Delta\delta) = (5.847 \pm 0.023) \times 10^{-7} \exp \left[\frac{-1641 \pm 1.3}{409.0 - 36.54(\Delta\delta) - 21.85(\Delta\delta)^2} \right] \quad (2.5)$$

2.3.1 Arrhenius parameters for temperature dependence of methanol diffusion

The Arrhenius parameters for all six calibration experiments (see appendix subsection 7.1.1) are shown in Table 2.2. All calibrated methanol $D(T)$ points were plotted simultaneously (Figure 2.5) and used to fit a single non-linear Arrhenius curve, obtaining the parameters given previously in Equation 2.4 and shown at the bottom of Table 2.2. As can be seen in the residuals for the fit plotted in Figure 2.5, the Arrhenius approximation does not fully capture the temperature dependence of the self-diffusion coefficient of methanol but the variance of < 1% over the examined range of 295–335 K was judged as acceptable for our purposes.

Table 2.2. Arrhenius parameters for the temperature dependence of the self-diffusion coefficient of methanol, measured over the range 295–335 K.

Instrument, probe (corresponding data)	$\alpha^{[a]}$	$A / \text{K}^{[b]}$	$D_0 / 10^{-7} \text{ m}^2 \text{s}^{-1}^{[c]}$
400 MHz ‘Gauss’, Cryo-BBO (Figure 7.1) (Figure 7.2)	0.908 0.905	1568 ± 2 1667 ± 5	4.61 ± 0.04 6.4 ± 0.01
500 MHz ‘Hertz’, TCI (Figure 7.3) (Figure 7.4)	1.138 1.14	1583 ± 6 1592 ± 1	4.84 ± 0.09 4.97 ± 0.02
(Figure 7.5)	1.14	1620 ± 3	5.46 ± 0.05
600 MHz ‘Tesla’, BBFO (Figure 7.6)	1.16	1594 ± 2	5.00 ± 0.04
Combined (Figure 2.5)		1641 ± 1	5.84 ± 0.02

[a] α = instrument-specific scaling factor for gradient calibration, as discussed in subsection 7.1.1

[b] A = Arrhenius exponential factor in Equation 2.2

[c] D_0 = Arrhenius pre-exponential factor in Equation 2.2

2.3.2 Effect of unknown water content on methanol calibration

The use of methanol as a calibration standard is not without its problems. The most obvious of these is the water content of the standard. Using long relaxation delays (at least $5 \times T_1$), the relative water content of the methanol sample can be measured directly by ^1H NMR peak integration, and in our hands, flame-sealed capillaries with less than 0.1% water content can be readily prepared using standard commercially available anhydrous methanol. We considered the “worst case” scenario of up to 1% water content. The diffusion coefficients of methanol at room temperature in 90:10 methanol/water mixtures are known,^[12] from which we estimate a 1.4 % decrease in the diffusion coefficient of methanol containing 1% water (linear interpolation). Similarly, the ^1H NMR peak separation of the methyl and exchangeable OH signals of pure methanol and 99% methanol/water allow the uncertainty in temperature to be estimated as less than 0.4 K for 1% water near 298 K (Figure 2.6).^[13] These conservative estimates suggest the inherent errors in measured diffusion values of 1–2% will be larger than those introduced by these small differences from minimal water content.

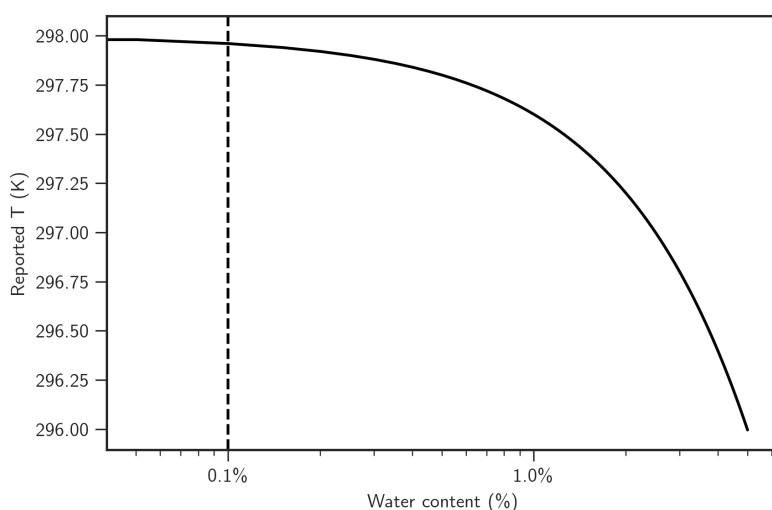
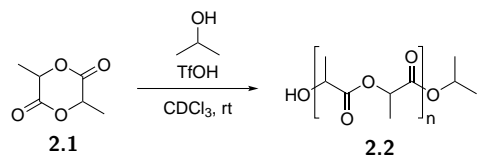


Figure 2.6. Predicted effects of water concentration on temperature measured by methanol chemical shift thermometer 298 K. Linear interpolation of literature values^[13] for the chemical shift separation of methanol with 0% and 10% water was used in combination with Equation 2.1 to show that the influence of trace water impurities on the measured temperature will be small (<0.5 K) for a ‘worst case’ scenario of methanol contaminated by 1% water.

2.4 Time-resolved diffusion NMR of a living polymerisation

As a practical demonstration of the use of these techniques to monitor changes in diffusion over time, we selected the simple cationic living polymerization reaction shown in Scheme 2.1.^[14]



Scheme 2.1 Living polymerisation of DL-lactide to form polylactide. Trifluoromethanesulfonic acid acts to catalyse the ring-opening polymerisation of DL-lactide **2.1**, with the final molecular weight of polymer **2.2** determined by the ratio of monomer to isopropanol. Here, a large decrease in the diffusion coefficient of the growing polymer was observed over time along with a smaller decrease in the diffusion coefficient of the monomer, which we ascribe to increasing solution viscosity.

The data presented in Figure 2.7 show that kinetics can be followed over 8 hours while simultaneously measuring the average diffusion coefficients of species in solution, and accurately monitoring temperature change with a time resolution of 40 seconds per gradient slice. The measured average diffusion coefficient for the polymer decreases steadily over time, consistent with the decreasing rate of diffusion expected as the chain length grows during the living polymerisation. A decrease in D over time is also observed for the residual solvent signal and the monomer signal: the source of this change in D is less readily apparent, but we ascribe it to an increase in effective solvent viscosity as the concentration and chain length of polymer grows over time.

The large (approximately sevenfold) decrease in D measured for the polymer over the course of the reaction from $7 \times 10^{-10} \text{ m}^2 \text{s}^{-1}$ to $1 \times 10^{-10} \text{ m}^2 \text{s}^{-1}$ demonstrates the growth in average polymer chain lengths over time, while simultaneous monitoring of the sample

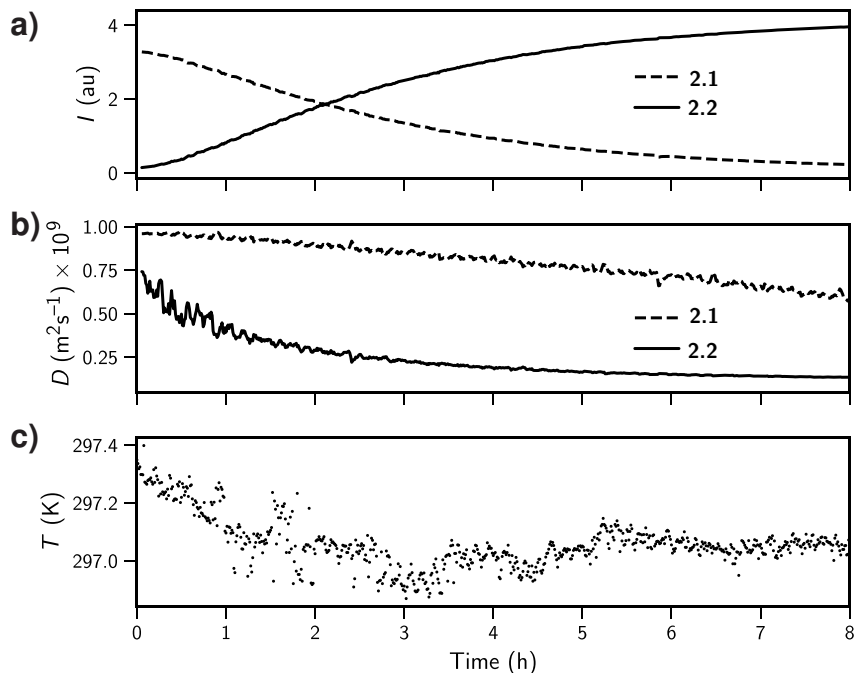


Figure 2.7. *In situ* monitoring of diffusion coefficients during the model living polymerisation reaction shown in Scheme 2.1, observed by ^1H NMR (600 MHz, CDCl_3 , see 7.2 for reaction details). a) Relative concentrations and b) measured diffusion coefficients of the monomer **2.1** and polymer **2.2** over time, determined from methyl ^1H NMR signals and with internal gradient calibration from methanol. c) Sample temperature, measured simultaneously using a methanol capillary.

temperature through use of a methanol capillary shows that temperatures remained relatively stable to within 0.3 K.

2.5 Conclusions and future work

In summary, the use of random gradient amplitudes removes bias for systems where concentrations are changing during the diffusion measurement and allows high time resolution (minutes) for diffusion data measured by NMR. We also show that methanol capillaries can be conveniently added to NMR samples for simultaneous calibration of temperature and gradient strength during the ^1H NMR diffusion experiment, allowing diffusion changes resulting from chemical changes to be discriminated from those resulting from changes in temperature. This may also allow diffusion measurements to be made even where temperature changes are occurring. We anticipate this methodology will be applicable for studying dynamic systems, such as for simultaneous kinetics and diffusion measurements of chemical reactions, with one illustrative example presented.

Future work on this topic could expand upon the use of time-resolved diffusion NMR for quantitative measurements of reaction properties. For example, the diffusion data presented here for a living polymerisation model reaction demonstrated a qualitative increase in polymer size over time. Building upon this to gain a *quantitative* understanding of chain growth could allow diffusion NMR to become a powerful technique for following the time-dependent kinetics of any reactions involving large changes in size or shape, particularly those involving

polymers, other macromolecules, or discrete self-assembled systems.

2.6 References

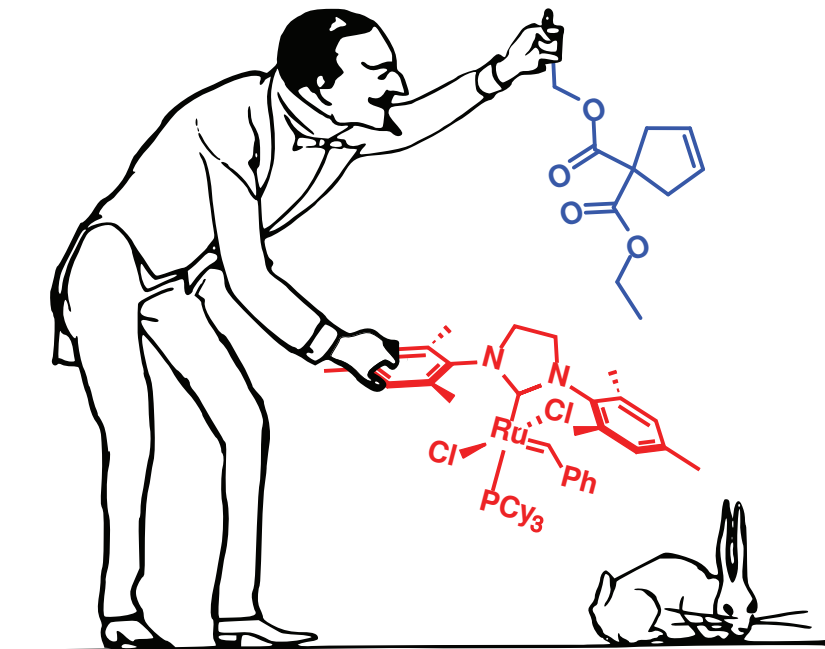
- [1] (a) P. Loureiro de Sousa, D. Abergel, J.-Y. Lallemand, *Chem. Phys. Lett.* **2001**, *342*, 45–50; (b) J. P. Stamps, B. Ottink, J. M. Visser, J. P. M. van Duynhoven, R. Hulst, *J. Magn. Reson.* **2001**, *151*, 28–31; (c) M. D. Pelta, G. A. Morris, M. J. Stchedroff, S. J. Hammond, *Magn. Reson. Chem.* **2002**, *40*, S147–S152; (d) C. Buckley, K. G. Hollingsworth, A. J. Sederman, D. J. Holland, M. L. Johns, L. F. Gladden, *J. Magn. Reson.* **2003**, *161*, 112–117; (e) M. J. Thriplleton, N. M. Loening, J. Keeler, *Magn. Reson. Chem.* **2003**, *41*, 441–447; (f) Y.-Q. Song, X. Tang, *J. Magn. Reson.* **2004**, *170*, 136–148; (g) T. Stait-Gardner, P. G. Anil Kumar, W. S. Price, *Chem. Phys. Lett.* **2008**, *462*, 331–336; (h) Y. Shrot, L. Frydman, *J. Magn. Reson.* **2008**, *195*, 226–231; (i) J. Mitchell, M. L. Johns, *Concepts Magn. Reson.* **2009**, *34A*, 1–15; (j) S. Ahola, O. Mankinen, V.-V. Telkki, *Magn. Reson. Chem.* **2017**, *55*, 341–347; (k) R. Masuda, A. Gupta, T. Stait-Gardner, G. Zheng, A. Torres, W. S. Price, *Magn. Reson. Chem.* **2018**, *56*, 847–851.
- [2] W. S. Price, *Concepts Magn. Reson.* **1997**, *9*, 299–336.
- [3] W. S. Price, *Concepts Magn. Reson.* **1998**, *10*, 197–237.
- [4] M. Oikonomou, J. Asencio-Hernández, A. H. Velders, M.-A. Delsuc, *J. Magn. Reson.* **2015**, *258*, 12–16.
- [5] (a) A. L. Van Geet, *Anal. Chem.* **1970**, *42*, 679–680; (b) D. S. Raiford, C. L. Fisk, E. D. Becker, *Anal. Chem.* **1979**, *51*, 2050–2051; (c) G. C. Levy, J. Terry Bailey, D. A. Wright, *J. Magn. Reson.* **1980**, *37*, 353–356; (d) C. Ammann, P. Meier, A. Merbach, *J. Magn. Reson.* **1982**, *46*, 319–321; (e) M. Holz, H. Weingärtner, *J. Magn. Reson.* **1991**, *92*, 115–125; (f) W. H. Sikorski, A. W. Sanders, H. J. Reich, *Magn. Reson. Chem.* **1999**, *36*, S118–S124; (g) M. Holz, S. R. Heil, A. Sacco, *Phys. Chem. Chem. Phys.* **2000**, *2*, 4740–4742; (h) M. Findeisen, T. Brand, S. Berger, *Magn. Reson. Chem.* **2006**, *45*, 175–178.
- [6] H. Weingärtner, *Z. Phys. Chem.* **1982**, *132*, 129–149.
- [7] (a) R. Mills, *J. Phys. Chem.* **1973**, *77*, 685–688; (b) R. J. Speedy, F. X. Prielmeier, T. Vardag, E. W. Lang, H. D. Lüdemann, *Mol. Phys.* **1989**, *66*, 577–590; (c) H. Liu, C. M. Silva, E. A. Macedo, *Chem. Eng. Sci.* **1998**, *53*, 2403–2422.
- [8] (a) W. S. Price, F. Tsuchiya, Y. Arata, *J. Am. Chem. Soc.* **1999**, *121*, 11503–11512; (b) W. S. Price, H. Ide, Y. Arata, O. Söderman, *J. Phys. Chem. B* **2000**, *104*, 5874–5876.
- [9] M. H. Cohen, D. Turnbull, *J. Chem. Phys.* **1959**, *31*, 1164–1169.
- [10] (a) M. Petrowsky, R. Frech, *J. Phys. Chem. B* **2010**, *114*, 8600–8605; (b) M. Petrowsky, A. M. Fleshman, R. Frech, *J. Phys. Chem. B* **2013**, *117*, 2971–2978.

2.6. REFERENCES

- [11] (a) K. T. Gillen, D. C. Douglass, M. J. R. Hoch, *J. Chem. Phys.* **1972**, *57*, 5117–5119;
 (b) C. A. Angell, E. D. Finch, P. Bach, *J. Chem. Phys.* **1976**, *65*, 3063–3066.
- [12] Z. J. Derlacki, A. J. Easteal, A. V. J. Edge, L. A. Woolf, Z. Roksandic, *J. Phys. Chem.* **1985**, *89*, 5318–5322.
- [13] W. S. Price, H. Ide, Y. Arata, *J. Phys. Chem. A* **2003**, *107*, 4784–4789.
- [14] D. Bourissou, B. Martin-Vaca, A. Dumitrescu, M. Graullier, F. Lacombe, *Macromolecules* **2005**, *38*, 9993–9998.

Chapter 3

‘Enhanced diffusion’ of molecular catalysts



This chapter is based on work published as:

T. S. C. MacDonald, W. S. Price, R. D. Astumian, J. E. Beves, *Angew. Chem. Int. Ed.* **2019**, *58*, 18864–18867

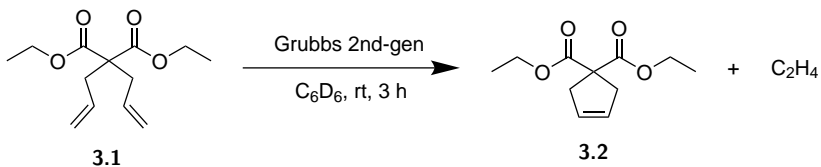
I performed all experimental work and analysis. All authors contributed towards project design and paper writing.

Summary:

Intriguing reports of enhanced diffusion in enzymes and molecular catalysts have spurred significant interest in experimental and theoretical investigations of this phenomenon, the mechanism of which is an ongoing topic of lively debate. Here we use time-resolved diffusion NMR methods to measure the diffusion coefficients of small molecule species involved in chemical reactions with high temporal resolution. I show the enhanced diffusion of small molecules cannot be explained by reaction velocity, and that apparent measurements of enhanced diffusion by small molecules appear to be caused by bulk fluid flow processes such as convection.

3.1 Enhanced diffusion of molecular catalysts?

A single example of the enhanced diffusion of an active small-molecular catalyst has been reported, in which 2nd generation Grubbs catalyst was used to drive an intramolecular ring-closing reaction of diethyl diallyl malonate (DDM) **3.1** to form cyclised product **3.2** by extrusion of ethylene (Scheme 3.1).^[1] Herein I use recently developed time-resolved diffusion NMR techniques^[2] (Chapter 2) to study two mechanistically distinct metal-catalysed intramolecular ring-closing reactions, beginning with the previously reported example shown in Scheme 3.1. All time-resolved diffusion data were processed using scripts written in Python which are provided in appendix section 8.6.



Scheme 3.1 Ring-closing metathesis (RCM) of diethyl diallyl malonate **3.1** (DDM) using Grubbs 2nd generation catalyst. The ring closing of **3.1** to give cyclic **3.2** is reversible, but the reaction is driven to completion by the loss of ethylene gas.

3.2 Diffusion study of Grubbs metathesis

Time-resolved diffusion NMR^[2] allows simultaneous measurement of concentration and diffusion coefficients for all species in solution over time scales of minutes and gives access to finely resolved time-dependent information. The self-diffusion* data obtained (Figure 3.1) are in reasonable agreement[†] with those previously reported at low time resolution, except now we can reveal data about the early stages of the reaction. The results are not as expected. As shown in Figure 3.1, the measured diffusion coefficients for each species are higher in the early stages of the reaction than at the end (consistent with previous reports^[1b]), but more complicated behaviour is seen over time than the previously suggested strictly exponentially decrease in D .

3.2.1 Time-dependence of T_1 and use of $\text{Cr}(\text{acac})_3$

One of the major advantages of diffusion NMR spectroscopy in studying systems with time-varying diffusion is the ability to simultaneously observe the concentrations of all species present. However, early experiments following the Grubbs ring-closing metathesis showed anomalous changes in measured concentrations. The sum total of starting material and product varied over the course of the reaction while it should have remained constant, and

*Self-diffusion and mutual diffusion are not strictly identical: see reference [3, Chapter 4].

[†]Previous reports of diffusion enhancement during this reaction^[1b] appear to have used uncalibrated gradients during the NMR experiment, leading to incorrect measured absolute diffusion coefficients. For example, the quoted D for benzene of $2.68 \times 10^{-10} \text{ m}^2 \text{s}^{-1}$ does not agree with the literature value of $2.21 \times 10^{-10} \text{ m}^2 \text{s}^{-1}$.^[4] As miscalibrated gradient pulses distort measured D by a constant scaling factor, relative D/D_0 values can still be compared as shown here.

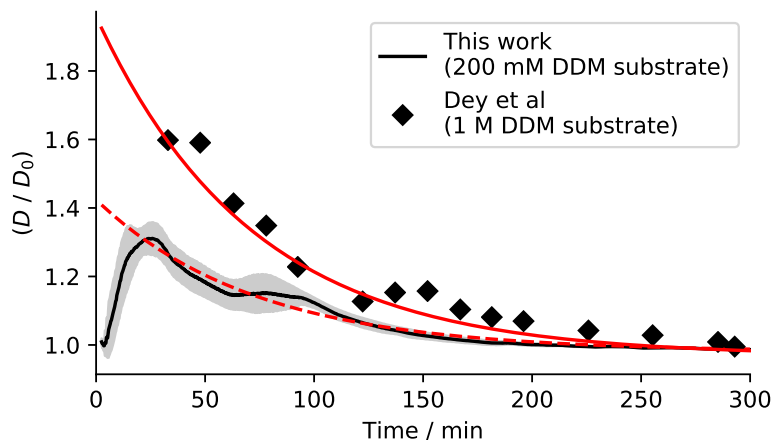


Figure 3.1. Time-dependent diffusion measurements of benzene during Grubbs metathesis, measured by us (black line and shaded area showing mean and error over eight experiments) and as previously reported^[1b] (black diamonds). Enhanced diffusion has been proposed to follow reaction kinetics, described here by an exponential function (solid red line). We find enhanced diffusion to follow a more complex profile of rising and falling that cannot be adequately explained by single-order exponential kinetics (red dashed line). See 8.2 for details of NMR experiments.

most notably the measured intensity of the residual solvent signal was reduced by half over the course of the experiment. In the absence of explanation, these clearly unphysical experimental artefacts risked undermining the validity of the experimental technique in measuring time-dependent diffusion coefficients.

Accurate quantitative NMR measurements require that the experimental repetition time be significantly longer than the T_1 longitudinal relaxation time, with repetition times $> 5T_1$ typically recommended. If the experimental repetition time is comparable to or less than T_1 , saturation occurs and the measured intensity of the signal is reduced.

It was suspected that the incorrect concentration measurements might be caused by the combination of fast 5 s repetition rates used for NMR experiments and changes in T_1 over the course of the experiment, perhaps due to some sort of ‘self-sparging’ effect caused by generated C₂H₄ gas[†]. This was confirmed through time-dependent T_1 measurements recorded during a Grubbs reaction under the standard conditions used in this study. The time-dependent T_1 data was acquired and processed using a time-dependent inversion-recovery pulse sequence implemented using the same concepts of continuous acquisition and moving-fit processing as used in our time-dependent diffusion experiments (see subsection 2.2.1), demonstrating the versatility of the moving-frame approach to data analysis described in Chapter 2 in what may be one of the first examples of a time-resolved T_1 measurement. The results are shown in Figure 3.2. A clear trend is visible: T_1 times increase by up to 50% over the course of the reaction (from $t = 0$ to $t \approx 250$ min), before gradually returning towards initial values over the next 6 hours. For a diffusion-monitoring experiment acquired with a 5 s repetition rate, these large and changing T_1 relaxation times make quantitative measurement impossible.

[†] T_1 times are dramatically shortened by the presence of paramagnetic species, and so are highly dependent on the concentration of dissolved molecular oxygen. Sparging with argon or nitrogen is a common technique used to increase T_1 relaxation times by lowering the concentration of dissolved O₂.

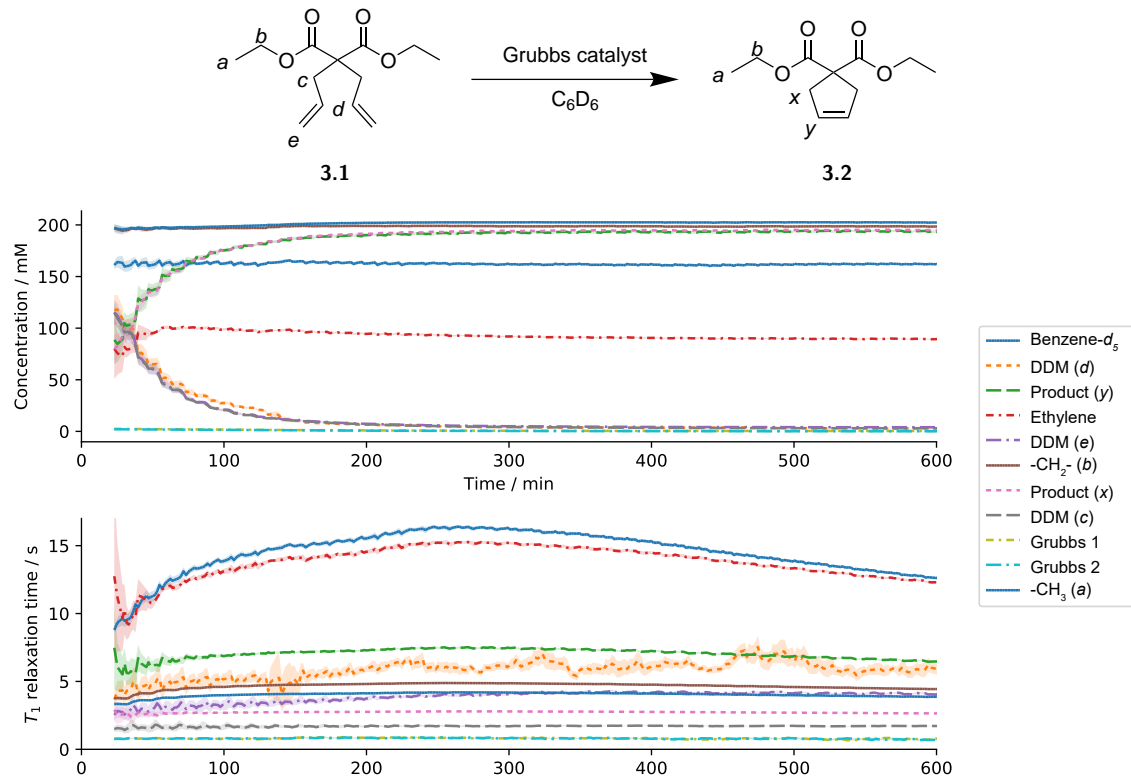


Figure 3.2. Changes in concentration (top plot) and T_1 longitudinal relaxation times (bottom plot) of NMR signals during Grubbs metathesis. Relaxation times can be seen to increase significantly over the course of the experiment, perhaps driven by a ‘self-sparging’ effect where generated ethylene removes paramagnetic dissolved oxygen from the system, before slowly returning to initial values once the experiment is complete. Concentrations have been normalised by spin multiplicities and scaled to the ethyl peaks as an internal 200 mM standard.

Use of Cr(acac)₃ as a paramagnetic relaxation agent

Chromium(III) acetylacetone (Cr(acac)₃) is a paramagnetic species soluble in nonpolar organic solvents and capable of dramatically shortening T_1 relaxation times.^[5] As such, it was hoped that the addition of a small quantity of Cr(acac)₃ to the Grubbs reaction system would cause acceptable relaxation over short repetition rates, and regain the ability to make quantitative measurements of concentration. T_1 measurements of a 200 mM solution of **3.1** in C₆D₆ with 0.1, 1, and 10 mM dissolved Cr(acac)₃ showed favourable relaxation times of 1–2 s

Table 3.1. T_1 relaxation times of benzene and **3.1** with varying concentrations of paramagnetic Cr(acac)₃. In the presence of 1 mM relaxation agent, relaxation was found to occur with ideal T_1 times of 1–2 s. 200 mM DDM in C₆D₆, 500 MHz.

3.1	[Cr(acac) ₃] / mM	T_1 / s				
		C ₆ HD ₅	H ^a	H ^b	H ^c	H ^d
	10 mM	0.27	0.26	0.23	0.31	0.30
	1 mM	2.00	1.42	1.37	1.08	1.72
	0.1 mM	6.10	2.65	2.85	1.47	3.48
	0 (as-prepared)	8.82	3.12	3.48	1.60	4.24
	0 (sparged with argon)	26.5	4.37	5.06	1.86	6.86
						3.81

3.2. DIFFUSION STUDY OF GRUBBS METATHESIS

at 1 mM Cr(acac)₃ (Table 3.1). This corresponds to approximately 92–99% signal recovery over a 5 s repetition rate for standard diffusion experiments, with 5–2.5% signal loss over the $\Delta = 50$ ms diffusion measuring time. As a result of these measurements, 1 mM of Cr(acac)₃ was used as an additive for all Grubbs metathesis reactions to allow the acquisition of near-quantitative data despite fast experimental repetition times.

For the Pd-catalysed cyclisation reaction discussed in the next section, no concentration abnormalities were observed under standard reaction conditions and thus no paramagnetic additive was used. As Cr(acac)₃ is unstable under the strongly acidic reaction conditions, a different paramagnetic species would have been needed if required for quantitative kinetics.

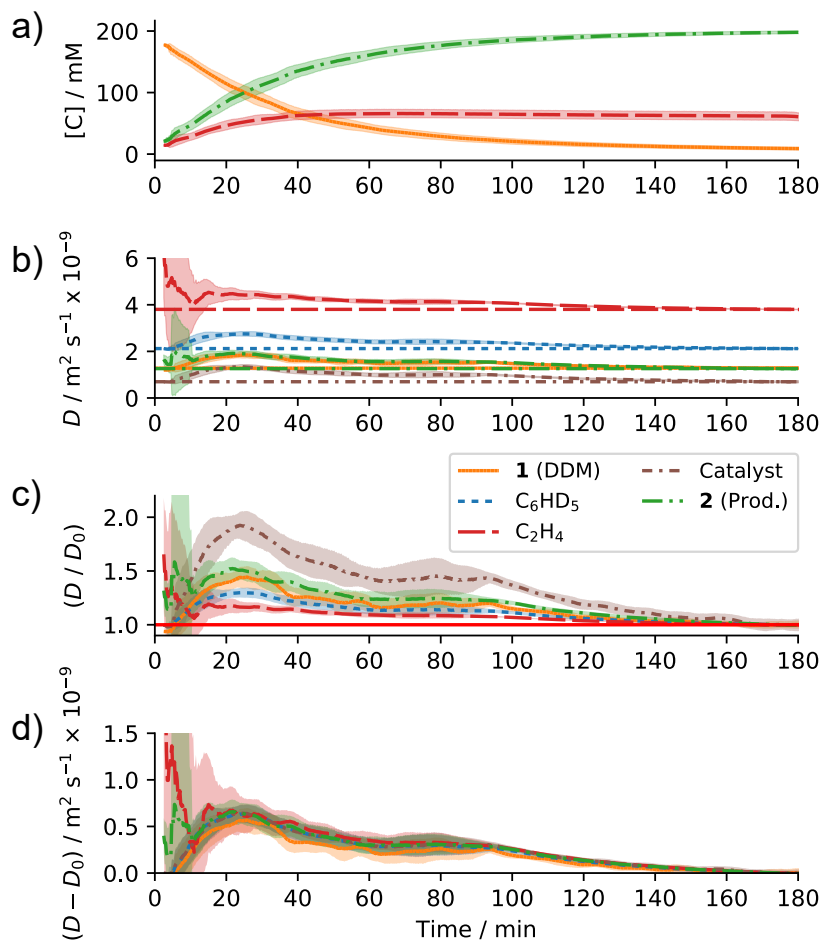


Figure 3.3. Measured concentrations (a) and diffusion coefficients (b) of species present in the reaction shown in Scheme 3.1 over time. (c) The Grubbs catalyst appear to show greater *relative* enhancement than the other molecular species, but I believe this to be coincidental as *absolute* changes in measured diffusion coefficients (d) are uniform for all species. Each line and associated uncertainties (shaded areas) is from the combined results of eight separate experiments; see 8.3 for data, 8.6 for processing. Horizontal lines indicate the measured final diffusion coefficients of each species on reaction completion. 200 mM **3.1** and 3 mM Grubbs 2nd generation catalyst in C₆D₆ with 1 mM Cr(acac)₃ as a paramagnetic relaxation agent^[5] to allow quantitative kinetics.

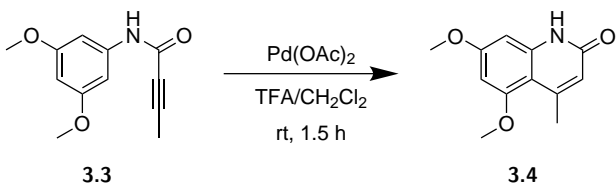
3.2.2 Time-resolved diffusion measurements of active Grubbs catalyst

The time-resolved data shown in Figure 3.3 reveals that rates of diffusion for all species do not reach a maximum until approximately 25 min into the reaction. This delayed increase in measured diffusion indicates that, in contrast to theoretical explanations,^[6] the degree of diffusion enhancement is not directly proportional to the strictly decreasing reaction velocity or to the rate of catalyst binding/unbinding events. Similar data were observed at reduced catalyst loadings (appendix subsection 8.3.3).

Figure 3.3c shows the enhanced diffusion for all chemical species present relative to their final diffusion coefficients, D_0 . The maximum relative enhanced diffusion of each species is in agreement with that previously reported under the same conditions.^[1b] The large relative increase in D seen for the active catalyst compared to the low relative increase observed for the non-reacting benzene solvent has been viewed as supportive of enhanced diffusion being driven by the active catalyst, but we believe that this ordering is coincidental. By comparing the absolute increase in diffusion of each species (Figure 3.3d) it is clear each species has an identical profile over the reaction. For example, at the point of maximum measured diffusion (25 min) each species has a diffusion coefficient approximately $0.7 \times 10^{-9} \text{ m}^2 \text{ s}^{-1}$ greater than that at the end of the reaction (see appendix 8.3.1 for at-rest diffusion coefficients). This additive increase to measured diffusion is suggestive of directional bulk transport such as convection, rather than increased diffusive motion. In the presence of bulk transport, the seemingly high relative diffusion enhancement of the Grubbs catalyst relative to other species present is a consequence of its low thermodynamic diffusion coefficient (i.e. its large size).

3.3 Diffusion study of a palladium-catalysed cyclisation

To investigate a possible link between enhanced diffusion and gas generation and to discover whether enhanced diffusion could be similarly observed for other catalysed reactions, we selected a known^[7] palladium-catalysed intramolecular cyclisation reaction that does not generate any form of by-product (Scheme 3.2). This reaction has favourable kinetics for NMR monitoring over a few hours and the mechanism of palladium-mediated C-C bond formation is well known.^[8]



Scheme 3.2 Model synthesis of quinolinone **3.4** *via* room-temperature palladium-catalysed intramolecular ring closure of alkyne **3.3**. Unlike the Grubbs metathesis, this ring closure generates no chemical by-product. All data presented here involved the reaction of **3.3** (200 mM) and Pd(OAc)₂ (3 mM) in 1:3 TFA:CD₂Cl₂.

The measured diffusion coefficients of the starting material **3.3**, product **3.4**, and acidic protons[§] are shown in Figure 3.4. As with the ring-closing metathesis reaction, an initial

[§]As trifluoroacetic acid contains no covalently bound protons, the broad exchangeable CF₃CO₂H/H₂O/H⁺

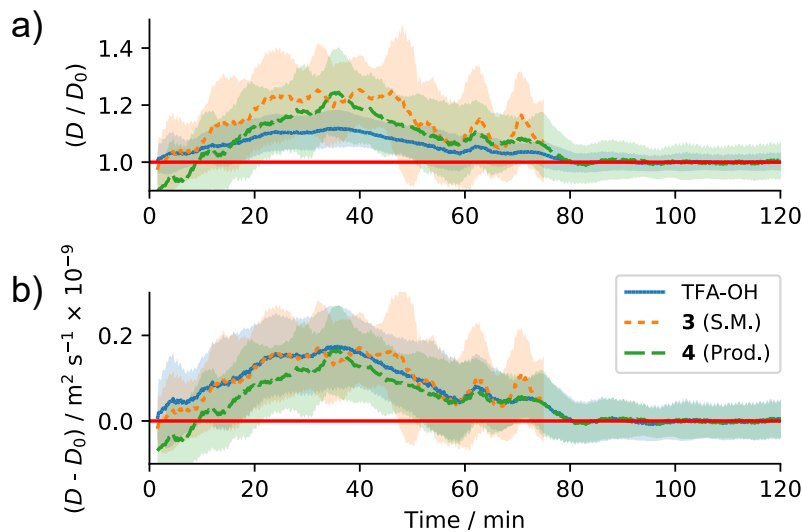


Figure 3.4. Diffusion enhancement during the palladium-catalysed intramolecular arylation reaction shown in Scheme 3.2. Data are averaged from six independent experiments, with standard errors shown as shaded areas. a) Relative changes in diffusion of starting material **3.3**, product **3.4**, and acidic protons; b) Absolute changes in measured diffusion of the same species. Note: diffusion-time curves for **3.3** have been truncated at $t = 75$ min due to the decreasing concentration making diffusion measurements difficult beyond this point.

increase in measured diffusion reaching a maximum at 30–40 min is followed by a gradual decrease to a stable D matching that of the isolated species in solution (appendix 8.4.1 for measurements of D at rest). Again, the absolute increase in diffusion coefficients (Figure 3.4b) are in good agreement for all species, suggesting the measured increases in diffusion coefficients are caused by bulk transport.

3.4 ‘Enhanced diffusion’ or convection?

Convection is a bulk flow phenomenon resulting from density variations within a fluid. When a denser fluid is positioned above less-dense fluid, a system becomes unstable and convective flows can act to dissipate the instability.^[9] These variations in density are frequently a result of temperature inhomogeneities: as density generally decreases with increasing temperatures, convection can result from any phenomenon that causes a temperature gradient to form across a fluid volume. For the tall and slender columns of liquid used in solution NMR experiments, two forms of convection are commonly encountered:^[10]

1. Rayleigh-Bénard convection, resulting from a negative vertical temperature gradient where colder/more dense liquid sits above warmer/less dense liquid. This is a *critical phenomenon*, with convection occurring only when the temperature gradient exceeds some critical value determined by experimental factors such as dynamic viscosity, sample geometry, and the coefficient of thermal expansion. Importantly, Rayleigh-Bénard convection requires that the vertical temperature gradient be negative (cooler fluid

signal was used for all measurements

above warmer fluid). A positive temperature gradient of warmer fluid above cooler fluid cannot drive this form of convection.

2. Hadley convection, resulting from horizontal temperature gradients. This is not a critical phenomenon: any lateral temperature gradient will drive Hadley convection, regardless of magnitude or direction.

The temperature inside an NMR probe is regulated by a constant flow of gas (the ‘VT gas’). This gas flow enters the probe below and offset to the sample and travels upwards over the interior of the probe and the exterior of the sample. As temperature is regulated from below, Rayleigh-Bénard convection can only occur as a result of a) performing experiments at above-ambient temperature with the VT gas heating the sample from below, or b) bulk cooling within the sample volume such as from an endothermic reaction. Even in these cases, the critical nature of Rayleigh-Bénard convection means that convection can be eliminated using a reduced volume sample such as a narrow or Shigemi-type NMR tube.

In contrast, the non-axisymmetric nature of the probe and gas flow means that *any* change in temperature away from ambient will cause some level of Hadley convection.^[10] Reducing the sample volume can be helpful in reducing Hadley convection to the point of not interfering with diffusion measurements, but given any lateral temperature gradient Hadley convection cannot be eliminated.^[12b]

3.4.1 Influence of measurement time Δ on measured diffusion coefficients

Diffusion NMR experiments involve a fixed measurement time Δ of typically 30–200 ms where diffusion is allowed to evolve. In the absence of directional flow the diffusion coefficient D does not depend on Δ , but in the presence of convection measured D shows a roughly linear increase proportional to increasing Δ .^[10,11] As shown in Figure 3.5, the measured diffusion coefficient of Grubbs’ catalyst at $t = 30$ minutes (approximately where D is highest) varies

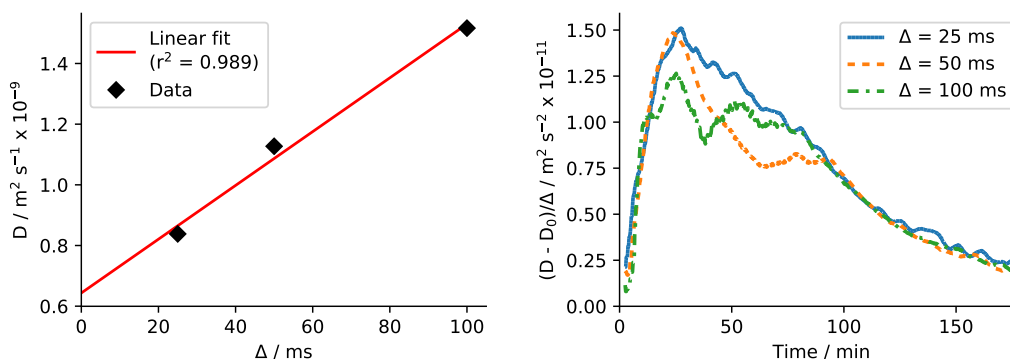


Figure 3.5. Influence of diffusion measurement time Δ on measured D for Grubbs catalyst. Left: measured D at $t = 30$ minutes (where D is highest) increases linearly with increasing Δ . Extrapolating this to $\Delta = 0$ gives a D of approximately $6.5 \times 10^{-10} \text{ m}^2 \text{s}^{-1}$ in the absence of convection, the same value measured for the reaction product at reaction completion.^[12a] Right: plotting the absolute increase in measured D of product **3.2** divided by the value of Δ $((D - D_0)/\Delta)$ shows good agreement between the curves over time, consistent with bulk motion and inconsistent with diffusion. See Figure 8.6, Figure 8.3, Figure 8.7 for full data at each Δ measurement time.

linearly with increasing Δ . An extrapolation of this trend to $\Delta = 0$ gives an implied D of $(6.5 \pm 0.4) \times 10^{-10} \text{ m}^2 \text{ s}^{-1}$ in the absence of convection, equal to the diffusion coefficient of $6.5 \times 10^{-10} \text{ m}^2 \text{ s}^{-1}$ measured for Grubbs’ catalyst in C₆D₆ (Appendix subsection 8.3.1). This indicates that measured ‘enhanced diffusion’ of this reaction is a bulk transport phenomenon, and that the rate of molecular self-diffusion does not increase during this reaction.^[12] Plotting the measured absolute increase in D divided by the measurement time Δ (*i.e.* $(D - D_0)/\Delta$; Figure 3.5b) shows similar curves for experiments performed with $\Delta = 25, 50$, or 100 ms, indicating that the measured time-dependent diffusion coefficients D are proportional to increasing Δ and that there is no Δ -independent component present that cannot be explained by convection alone.

A similar relationship between Δ and D was observed for the palladium-catalysed cyclisation, with data shown in Figure 3.6.

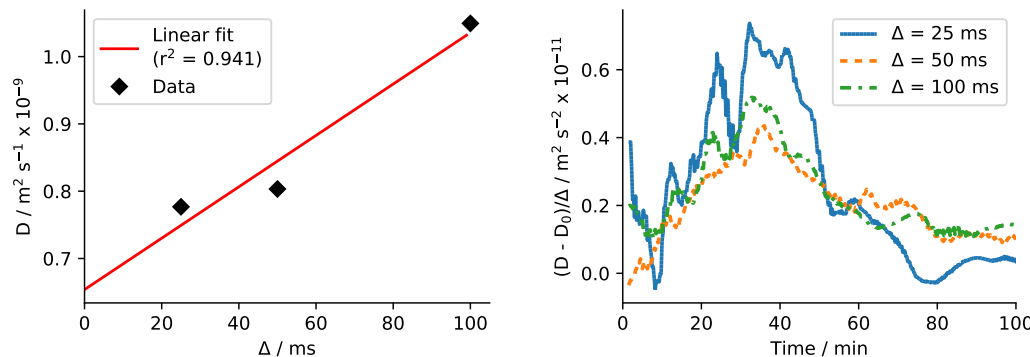


Figure 3.6. Influence of diffusion measurement time Δ on measured D for Pd-catalysed cyclisation product **3.4**. Left: measured D at $t = 40$ minutes (where D is highest) increases approximately linearly with increasing Δ . Extrapolating this to $\Delta = 0$ gives a D of approximately $6.5 \times 10^{-10} \text{ m}^2 \text{ s}^{-1}$ in the absence of convection, the same value measured for the reaction product at reaction completion. Right: absolute increase in the measured diffusion coefficient of cyclised product divided by the value of Δ $((D - D_0)/\Delta)$. This plot shows moderate agreement between curves over time, consistent with bulk motion and inconsistent with diffusion.

3.4.2 Relationship between reaction rate and measured D

It has previously been proposed that the ‘enhanced diffusion’ of active enzymes may be tied to reaction rates or rates of substrate binding/unbinding.^[13,14] From the time-dependent diffusion data shown in Figure 3.1 and Figure 3.3, this explanation is incompatible with our experimental data. Most visibly we observe an increasing D in the early stages of both reactions, while the reaction rates are strictly decreasing with time. Figure 3.7 shows the reaction rate over time, calculated from a monoexponential fit to the measured concentration of Grubbs starting material **3.1**.[¶] The measured D decreases proportionally to the reaction rate past $t \approx 60$ minutes, but before this point there is no agreement between measured D and the measured reaction rate. This data is incompatible with current theories linking

[¶]Used as a rough approximation, despite the data deviating slightly from first-order kinetics. This may be due to the metathesis reaction first moving towards equilibrium between starting material and product before slowly moving further to completion as volatile ethylene is lost from the system.

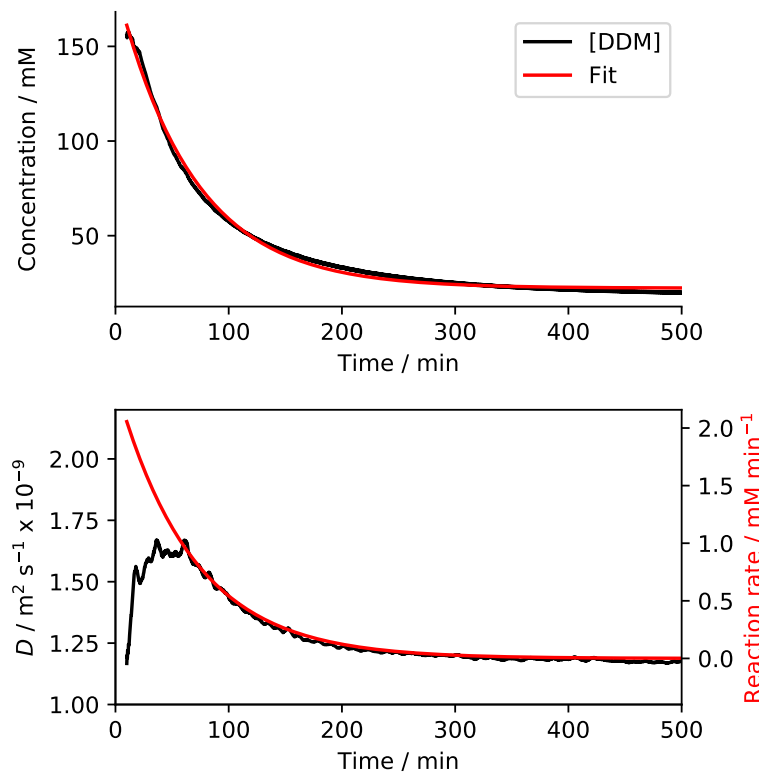


Figure 3.7. Relationship between measured D and reaction rate. Top: measured concentration of DDM (black) and fitted first-order kinetics plot (red) during the Grubbs reaction (200 mM DDM, 0.5 mM Grubbs catalyst), averaged from three independent experiments. Bottom: measured D (black line) and calculated reaction rate (red line). The measured diffusion coefficient decreases in proportion to the reaction rate past $t = 60$ min, but early in the reaction the rate and D clearly diverge. C₆D₆; ¹H, 500 MHz, $\delta = 1.3$ ms, $\Delta = 50$ ms. Concentrations calibrated from the ethyl protons as an internal standard at assumed 200 mM concentration.

‘enhanced diffusion’ to the turnover rate of the active catalyst, but can be explained by convective flow taking some time to establish under forcing conditions before decreasing with decreasing reaction rate as that forcing diminishes.

3.4.3 Influence of sample geometry on measured D

Unlike diffusion, convection is a bulk flow phenomenon and strongly affected by the geometry of a system. It has previously been reported that the presence of convection can be dramatically reduced by using narrow NMR tubes.^[12] Figure 3.8 shows data for the Pd-catalysed cyclisation where the standard 5 mm NMR tube has been replaced with a narrower 3 mm NMR tube (appendix subsection 8.5.3; see subsection 8.5.1 for additional data using a Shigemi restricted-volume NMR tube).

The change in tube diameter has a clear impact on the time-dependent diffusion coefficient, with no transient increase in diffusion observed for the reaction conducted in a narrow 3 mm NMR tube. A similar result is obtained for the Grubbs metathesis reaction: when conducted in a 3 mm NMR, the transient increase in D observed previously disappears almost entirely (Appendix subsection 8.5.2).

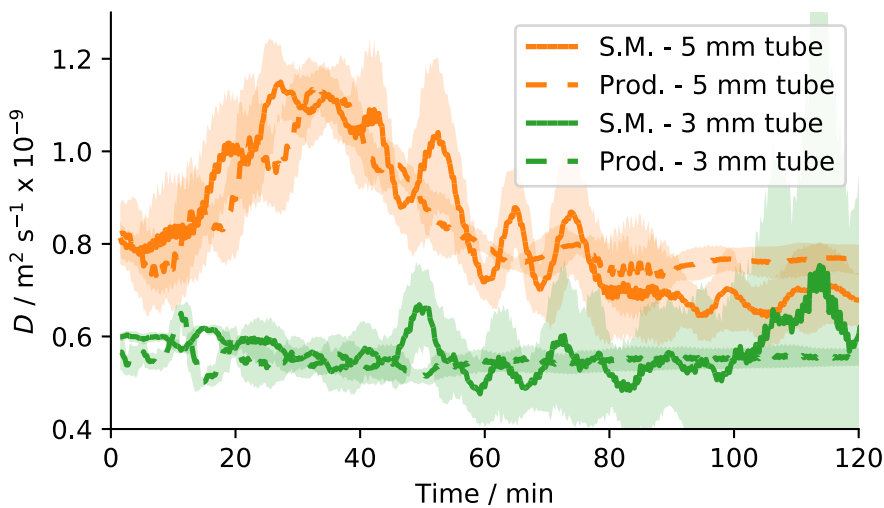


Figure 3.8. No increase in measured D is observed when the palladium-catalysed cyclisation reaction shown in Scheme 3.2 is conducted in a narrow 3 mm NMR tube. Lines show measured diffusion coefficients for starting material and reaction products averaged over three experiments, $\Delta = 100$ ms, see 8.5.3 for details. See 8.5.2 for the related comparison for the Grubbs catalysed reaction.

3.4.4 Studies of internal temperature during the reaction

Convection occurs when a fluid contains density inhomogeneities, with more-dense fluid placed above less-dense fluid. In both systems studied here convection was somehow driven by the activity of the chemical reaction. The exact mechanism by which the reactions generated a density gradient was not conclusively determined. Two proposed potential sources of convection are gas generation during ring-closing metathesis or generation of temperature gradients during the reactions. The generation of ethylene gas during Grubbs ring-closing metathesis could drive convection either through bubble formation (a phenomenon familiar to anyone who has ever enjoyed a pint of stout^[15]), or by producing a gradient in dissolved ethylene concentration through losses to the atmosphere at the air-liquid interface. If ethylene-depleted reaction mixture is more dense than ethylene-rich reaction mixture, this would drive Rayleigh-Bénard convection. Alternatively, internal heating or cooling of the reaction mixture could create a temperature gradient to the (assumed constant) temperature of the tube surface.

To investigate the possibility of reaction-induced temperature inhomogeneities, experiments were performed with a methanol chemical-shift thermometer (present as a flame-sealed capillary) placed inside the NMR sample. For the Grubbs metathesis reaction, temperatures were stable to within ± 0.1 °C over typical experimental run times (Figure 3.9). In contrast, measured temperatures during Pd-catalysed cyclisation (Figure 3.10) increase by approximately 1.5 °C and appear to be correlated with the transient increase in D observed during this reaction. These measurements over average temperature over the sample volume do not directly provide any information regarding internal temperature gradients, but the existence of a measurable change in temperature suggests that such gradients do indeed exist for the Pd-catalysed reaction (as discussed in section 3.4). Similarly, the absence of a measured

change in sample average temperature during the Grubbs reaction does *not* rule out the formation of temperature gradients.

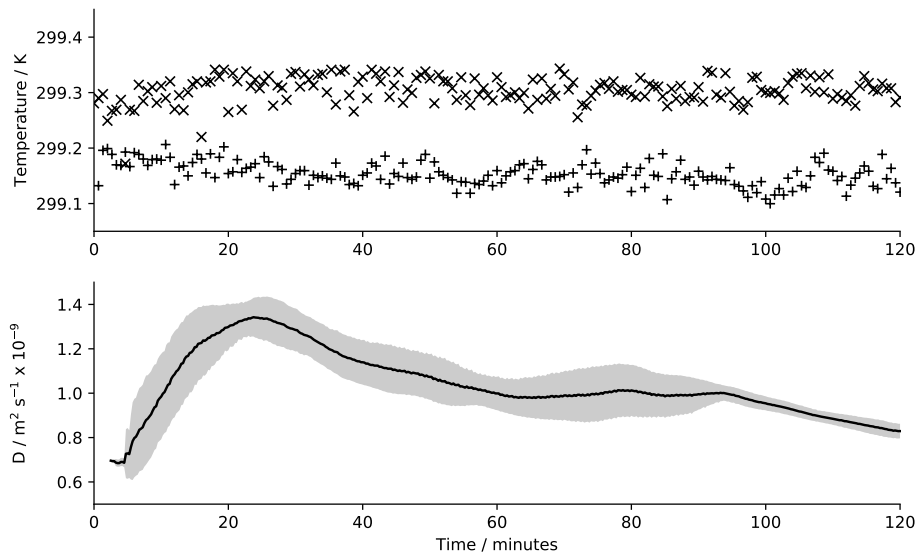


Figure 3.9. Measured temperature (top) of the Grubbs reaction over time (x and + points represent two separate experiments), using a flame-sealed methanol capillary. No correlation can be seen between the increased diffusion coefficient (bottom) and the reaction temperature (top), which is stable to $\pm 0.1^\circ\text{C}$. As this technique can only give a sample-averaged measurement, this does not rule out temperature inhomogeneities over the course of the experiment.

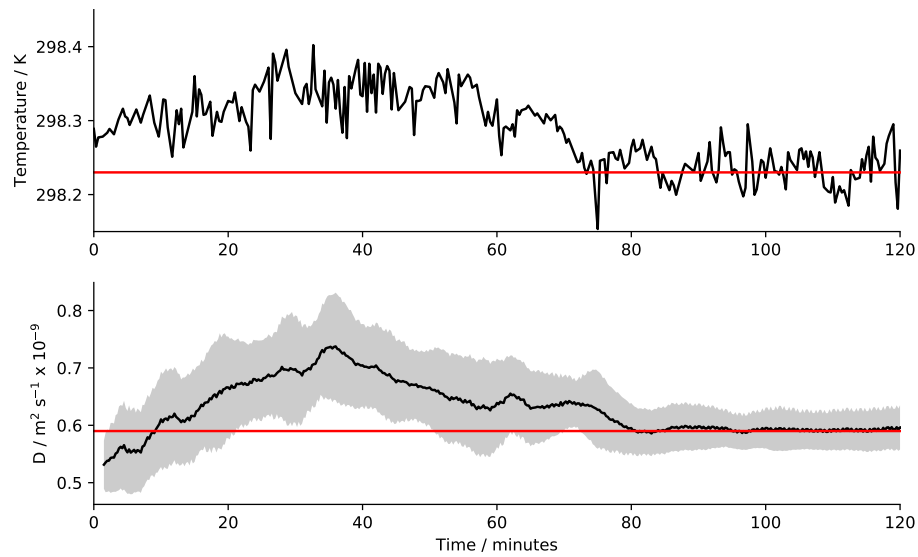


Figure 3.10. Measured temperature of the Pd-catalysed cyclisation reaction over time, using a flame-sealed methanol capillary. A small change in temperature (top) of approximately $\pm 0.15^\circ\text{C}$ can be observed to rise and fall with a similar profile to the measured diffusion coefficient (bottom). It has previously been shown than internal changes in the temperature of NMR samples will invariably generate lateral temperature gradients and drive Hadley convection.^[10]

3.4.5 Evidence for convection rather than ‘enhanced diffusion’

As summarised in Table 3.2, the sum of the evidence collected supports the claim that enhanced diffusion as-claimed^[1b] is in fact misinterpreted convection.

Table 3.2. Summary of evidence for reaction-induced convection vs enhanced diffusion.

Factor	Results	Supports enhanced diffusion?	Supports convection?
Echo time Δ	Measured D increases $\propto \Delta$	No: measured D should be invariant to Δ	Yes: measured D increases approximately linearly with Δ .
Reaction rate	D does not follow rate	No: D does not strictly decrease following reaction rate	Yes: convective flow takes some time to establish under forcing
Geometry	The transient increase in D is sharply reduced in a narrow tube	No: diffusion is a microscopic phenomenon, independent of macroscopic sample geometry	Yes: convection is a bulk phenomenon, strongly affected by macroscopic sample geometry

3.5 Conclusions

From several key observations we have shown that the only reported example of enhanced diffusion driven by a small molecule catalyst is likely caused by convection. Measured diffusion coefficients are seen to increase early in reactions in contrast to the strictly decreasing reaction velocity, inconsistent with rapidly established microscopic interactions but consistent with the slow formation of convection currents. Measured diffusion coefficients were found to increase by the same absolute value for all species in the reaction mixture and vary linearly with Δ . Finally, no increase in measured diffusion was observed for reactions conducted in a narrow NMR tube. These observations cannot be explained by any proposed model of enhanced diffusion but are entirely consistent with induced convection.

The cause of this convection is less clear. I hypothesise that convection could originate from the following scenarios:

1. The small temperature increase of 0.15 K averaged over the detection volume in the Pd-catalysed reaction (see Figure 3.10), correlating with changes in measured diffusion and suggestive of temperature inhomogeneity;
2. The gaseous product formed during the Grubbs reaction.^[15] No temperature change was detected during the Grubbs reaction ($\Delta T < 0.1$ K, see Figure 3.9); however, temperature inhomogeneity is still conceivable over the averaged detection volume.

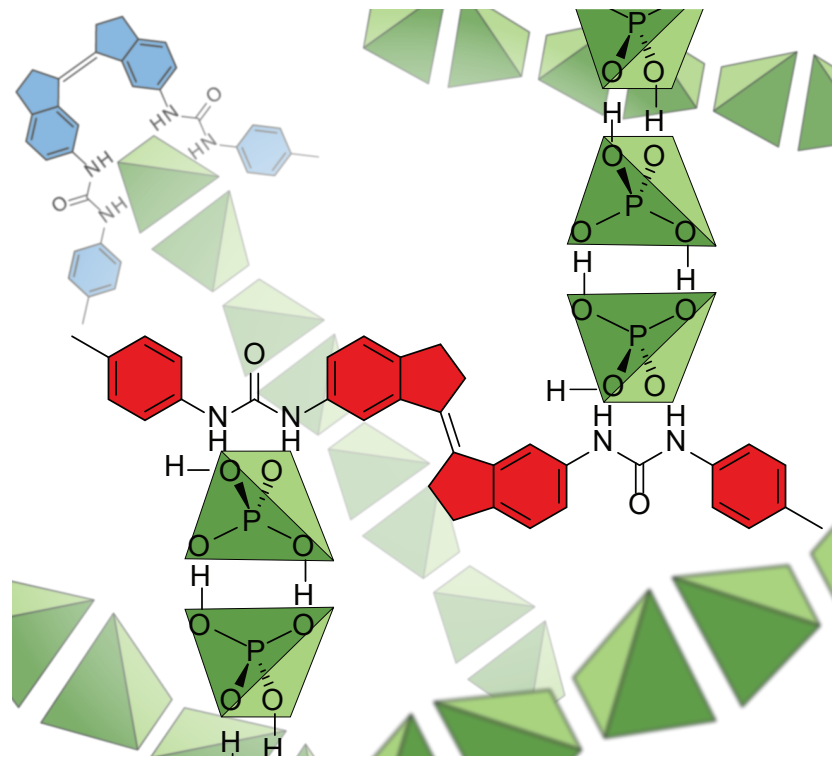
This could be further investigated by measuring transient concentration gradients that may form during the reaction. These findings provide experimental evidence that challenge the concept of enhanced diffusion in molecular systems and may also have implications for enzymatic systems.

3.6 References

- [1] (a) R. A. Pavlick, K. K. Dey, A. Sirjoosinhg, A. Benesi, A. Sen, *Nanoscale* **2013**, *5*, 1301–1304; (b) K. K. Dey, F. Y. Pong, J. Breffke, R. Pavlick, E. Hatzakis, C. Pacheco, A. Sen, *Angew. Chem. Int. Ed.* **2016**, *55*, 1113–1117.
- [2] (a) M. Urbańczyk, D. Bernin, A. Czuroń, K. Kazimierczuk, *Analyst* **2016**, *141*, 1745–1752; (b) T. S. C. MacDonald, W. S. Price, J. E. Beves, *ChemPhysChem* **2019**, *20*, 926–930.
- [3] *Modern NMR Techniques for Synthetic Chemistry*, (Ed.: J. Fisher), CRC Press/Taylor & Francis Group, Boca Raton, **2015**, 341 pp.
- [4] A. F. Collings, R. Mills, *Trans. Faraday Soc.* **1970**, *66*, 2761–2766.
- [5] O. A. Gansow, A. R. Burke, G. N. L. Mar, *J. Chem. Soc. Chem. Commun.* **1972**, 456–457.
- [6] P. Illien, X. Zhao, K. K. Dey, P. J. Butler, A. Sen, R. Golestanian, *Nano Lett.* **2017**, *17*, 4415–4420.
- [7] C. Jia, D. Piao, T. Kitamura, Y. Fujiwara, *J. Org. Chem.* **2000**, *65*, 7516–7522.
- [8] (a) C. Jia, D. Piao, J. Oyamada, W. Lu, T. Kitamura, Y. Fujiwara, *Science* **2000**, *287*, 1992–1995; (b) J. Wencel-Delord, T. Dröge, F. Liu, F. Glorius, *Chem. Soc. Rev.* **2011**, *40*, 4740–4761.
- [9] M. Lappa, *Thermal Convection: Patterns, Evolution and Stability*, Wiley, Chichester, UK, **2010**, 670 pp.
- [10] I. Swan, M. Reid, P. W. A. Howe, M. A. Connell, M. Nilsson, M. A. Moore, G. A. Morris, *J. Magn. Reson.* **2015**, *252*, 120–129.
- [11] W. S. Price, *NMR Studies of Translational Motion Principles and Applications*, Cambridge University Press, Cambridge, **2009**.
- [12] (a) N. Hedin, T. Y. Yu, I. Furó, *Langmuir* **2000**, *16*, 7548–7550; (b) T. M. Barbosa, R. Rittner, C. F. Tormena, G. A. Morris, M. Nilsson, *RSC Adv.* **2016**, *6*, 95173–95176.
- [13] J. Agudo-Canalejo, T. Adeleke-Larodo, P. Illien, R. Golestanian, *Acc. Chem. Res.* **2018**, *50*, 2365–2372.
- [14] J. Agudo-Canalejo, P. Illien, R. Golestanian, *Nano Lett.* **2018**, *18*, 2711–2717.
- [15] E. S. Benilov, C. P. Cummins, W. T. Lee, *Am. J. Phys.* **2013**, *81*, 88–91.

Chapter 4

Influencing diffusion by switchable phosphate binding



Summary:

Dihydrogen phosphate anions are found to spontaneously associate into anti-electrostatic assemblies via hydrogen bonding interactions at millimolar concentrations in DMSO. Diffusion NMR measurements were used to characterise these assemblies, which can be bound by photoswitchable anion receptors to form large bridged assemblies of approximately three times the volume of the free host. Photoisomeriation of the receptor-bound complex causes a decrease in diffusion coefficient of up to 16%, corresponding to a 70% increase in effective volume. This new approach to controlling diffusion may have applications in controlling molecular transport.

4.1 Introduction

This work was conducted in collaboration with Dr. Sander Wezenberg and Prof. Ben Feringa at the University of Groningen in the Netherlands. The synthetic work and initial characterisations were carried out during a research exchange to the University of Groningen.

4.1.1 Controlling molecular transport

Active control over molecular transport by synthetic systems is a topic of ongoing interest.^[1] Recent progress has shown that motors, enzymes, or other energy consuming nanostructures can effectively drive molecular transport in solution.^[2] Despite these recent advances, controlling transport of molecules in solution remains a challenging goal. One way to control transport is by controlling the diffusion rate of species in solution, as previously explored in Chapter 3. Various theoretical proposals and experimental data have shown that increasing or decreasing the rate of diffusion can lead to directional transport when coupled with, for example, concentration gradients.^[3] Molecular photoswitches can control supramolecular self-assembly into discrete structures^[4] or polymers,^[4b,d,5] influencing diffusion rates.^[4d,e,5b] While diffusion NMR^[6] measurements are a known approach for characterizing supramolecular assembly,^[7] the use of switchable host-guest interactions to control diffusive transport is relatively unexplored.

4.1.2 Anion binding

Many small molecular hosts have been developed to selectively bind anions.^[8] Such binding would be expected to result in changes to the size of the host and could therefore represent a means to influence the rate of diffusion, if this binding could be switched on and off by external stimuli. Most anions (e.g. Cl⁻, F⁻, NO₃⁻...) are relatively small compared to anion-binding hosts, so in the absence of other effects the change in host diffusion on guest-binding would be expected to be quite small. Larger changes in host diffusion could be achieved by binding larger anionic guests. One anion commonly studied in anion binding assays is dihydrogen phosphate, H₂PO₄⁻. H₂PO₄⁻ is a particularly attractive anion for influencing diffusion rates of an anion-binding host due to its potential to form large structures in solution *via* antielectrostatic hydrogen bonding.^[9]

4.1.3 Antielectrostatic hydrogen bonding in solution

In contrast to the chemical intuition that like charges repel, some anions are known to associate through hydrogen-bonds and form polyanionic species.^[10] This antielectrostatic hydrogen bonding (AEHB) is common in the solid state^[11] for oxoanions such as HCO₃⁻, HSO₄⁻, and H₂PO₄⁻ (Figure 4.1). While AEHB interactions have been identified in solid-state crystal structures, detection of unchaperoned anion dimers or oligomers in solution is challenging due to limited spectroscopic signatures, weak anion-anion bonds, labile protons and rapidly exchanging bound species. These difficulties can be attenuated by the use of an anion-binding host to template AEHB interactions,^[12] leading to reports of HSO₄⁻ dimers^[13]

and H_2PO_4^- dimers^[14] and oligomers^[15] in solution. Conductimetric and spectroscopic techniques have been used to establish the formation of discrete structures from HCO_3^- and H_2PO_4^- in water^[16] and DMSO^[13c] by AEHB and have suggested the possibility of higher-order oligomers.^[16c] However, to our knowledge the unassisted formation of AEHB oxoanion oligomers in solution has yet to be conclusively established. The formation of such structures could provide a means to substantially alter the diffusion coefficients of bound anion receptors.

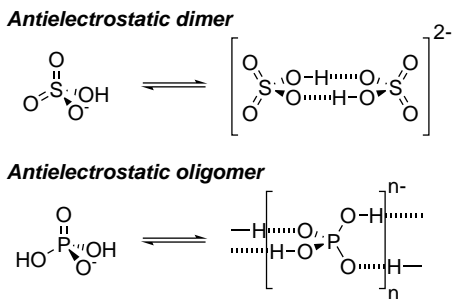


Figure 4.1. Antielectrostatic hydrogen-bonding of anions. Anions with a single hydrogen bond donor/acceptor pair (e.g. HSO_4^-) may form dimers^[13a] while anions with multiple donor/acceptors (e.g. H_2PO_4^-) can form oligomers in the solid state.^[15b]

4.1.4 Photocontrol of anion binding

Molecular photoswitches^[17] have been recently combined with anion receptors to allow binding properties to be controlled by light.^[18] Recently, the first photoswitchable receptor **4.1** exhibiting strong dihydrogen phosphate binding was developed by the Feringa group, based on photoswitchable stiff stilbenes^[4d,5b] and bis-urea anion binders (Figure 4.2).^[17] This compound can be converted from the weakly guest-binding *E*-**4.1** to a strongly binding *Z*-**4.1** form using near-UV light. The combination of this type of photoswitchable anion receptor with dihydrogen phosphate AEHB oligomers might allow substantial changes in diffusion to be controlled by light. However, the requirement of UV light for photocontrol over this system imposes a significant drawback: it would be preferable to develop a photoswitchable anion binding system capable of responding to visible light, which is less harmful and less prone to causing photodegradation in solution.

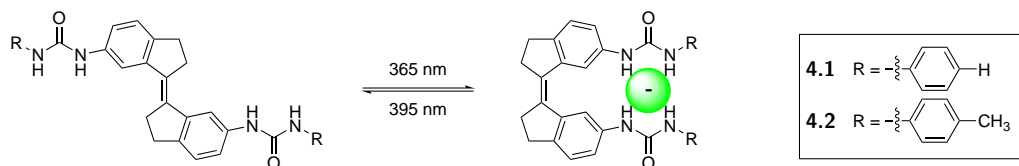


Figure 4.2. Previously reported bis-urea photoswitchable anion binder **4.1**^[24a] and analogous tollylurea compound **4.2** used in this study. The *E* and *Z* photoisomers exhibit different binding properties, with the association constant of *Z*-**4.1** for anions approximately an order of magnitude greater than that of *E*-**4.1**. This change was ascribed to the cooperative/chelate-like positioning of the urea receptor groups. The photoisomers can be interconverted by irradiation with near-UV light.

Herein I report quantitative self-association data for the antielectrostatic oligomerization of dihydrogen phosphate in DMSO at millimolar concentrations and a photoswitchable an-

ion receptor that allows reversible binding to the oligo-H₂PO₄⁻ to control rates of diffusive transport.

4.2 Switchable anion binders

4.2.1 Towards oxindole-based hemistilbene photoswitches

The photochromic properties of oxindole-based hemistilbene molecules (Figure 4.3) have been known for some time,^[19] but the potential of these compounds as visible light photoswitches has only recently been examined^[20] and remains underexplored. These compounds are attractive due to the relative ease of installing the central C=C double bond *via* acid-catalysed Knoevenagel condensation. In collaboration with Dr Sander Wezenberg and Prof. Ben Feringa at the University of Groningen, I attempted to synthesise a new photoswitchable anion binder analogous to those previously reported^[24a] but based on an oxindole core. This work was ultimately abandoned due to synthetic difficulties, but early results are presented here with synthetic details and characterisations given in appendix section 9.5.

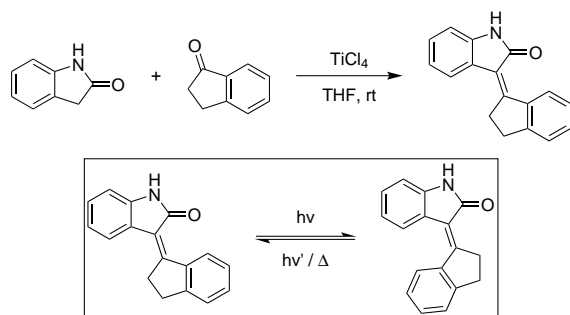


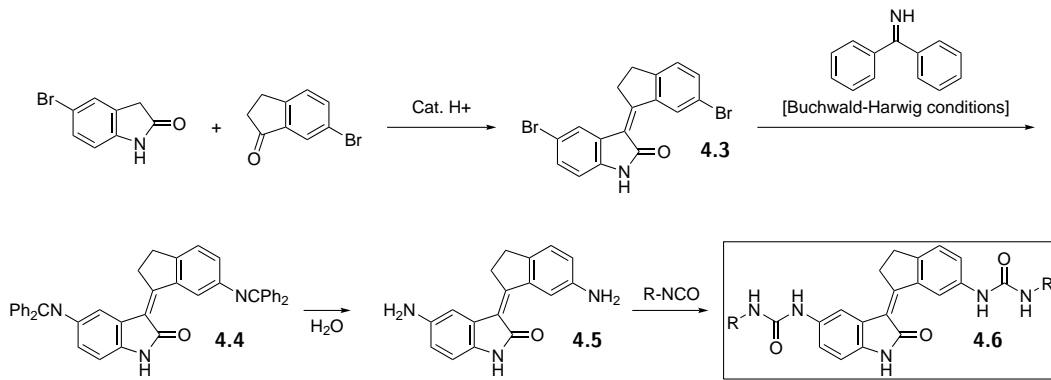
Figure 4.3. The oxindole-derived hemistilbene core can be accessed through a simple Knoevenagel condensation between an oxindole and an aryl ketone or aldehyde (e.g. indanone, shown here). Double-bond isomerisation of the central C=C bond occurs upon irradiation of the core with blue light.

Synthesis

The planned synthetic route towards oxindole-based photoswitchable anion binders is shown in Scheme 4.1. My synthetic strategy was to access dibromo oxindole-based photoswitch **4.7** *via* an acid-catalysed condensation reaction, which would then be transformed into diamine compound **4.5** *via* Buchwald-Hartwig coupling with benzophenone imine as an ammonia surrogate. This diamine core could then be reacted with commercially available aryl isocyanates to give the desired bis-urea anion binders.

Synthesis of the oxindole-based hemistilbene core

One of the appealing aspects of oxindole-based photoswitches is the relative ease of forming the tetrasubstituted C=C double-bond by mixed condensation of an oxindole and an indanone under basic or acidic conditions. This Knoevenagel-like condensation has previously been accomplished in the Feringa group using Brønsted acid catalysis with *p*-toluenesulfonic acid



Scheme 4.1 Planned route towards bis-urea anion binders based around oxindole photoswitch cores. Dibromo hemistilbene **4.3** would be obtained *via* Knoevenagel condensation of commercial oxindole and bromoindanone. **4.3** would then be coupled with benzophenone imine under Buchwald-Hartwig conditions to access diimine **4.4**, which would then be hydrolysed to diamine **4.5**. Bis-urea host **4.6** would be obtained from diamine **4.5** by reaction with aryl isocyanates.

(TsOH), with products obtained in low yield (10–30%). This condensation reaction was found to be surprisingly challenging and resulted in only low yields of coupled product under the various reaction conditions shown in Table 4.1 (entries 1–4). The oxindole-based switches obtained also had limited solubility in organic solvents other than DMSO or acetone making synthetic handling and characterisation challenging.

Reaction yields were dramatically improved to 50–90% by replacing Brønsted acid catalysis with a $Ti(O^iPr)_4$ -mediated Knoevenagel procedure from the literature^[21] in which $Ti(O^iPr)_4$ reacts with the oxindole to give an amide enolate that reacts readily with the electrophilic carbonyl (Table 4.1; entries 6–7). Excess $Ti(O^iPr)_4$ in the reaction may also scavenge traces

Table 4.1. Development of conditions to access hemistilbene photoswitch cores by condensation of oxindoles and 6-bromoindanone. The condensation seems to be thermodynamically unfavourable: equilibrium yields were low in dry solvents, and no product was obtained in wet solvents. A $Ti(O^iPr)_4$ -based procedure improved yields, and the use of more soluble *N*-methyloxindoles gave access to mono- and dibromo switches **4.8** and **4.9** in good yields.

Entry	Cmpd.	X	R	Conditions	Outcome
<i>Brønsted acid-catalysed condensation with TsOH</i>					
1	4.10	NH	H	15 mol% TsOH, 'wet' toluene, overnight reflux	0%
2		NH	H	15 mol% TsOH, dry (SPS) toluene, overnight reflux	10–30%
3		NH	H	15 mol% TsOH, dry (SPS) toluene, 150 °C (MW) 1 h	15%
4	4.3	NH	Br	15 mol% TsOH, dry (SPS) toluene, overnight reflux	0%
<i>Piperidine-catalysed Knoevenagel</i>					
5	4.10	NH	H	2 eq piperidine, dry MeOH, overnight reflux	15%
<i>Ti(O<i>i</i>Pr)₄-mediated Knoevenagel</i>					
6	4.10	NH	H	3 eq $Ti(O^iPr)_4$, 2 eq pyridine, dry THF, rt overnight	50–90%
7	4.3	NH	Br	3 eq $Ti(O^iPr)_4$, 2 eq pyridine, dry THF, rt overnight	2%
<i>Improving solubility with N-methyloxindole</i>					
8	4.8	NCH ₃	H	4 eq $Ti(O^iPr)_4$, 3 eq pyridine, dry THF, rt overnight	90%
9	4.9	NCH ₃	Br	4 eq $Ti(O^iPr)_4$, 3 eq pyridine, dry THF, rt overnight	40–60%

of water and prevent hydrolysis back to the starting materials. The poor solubility of compound **4.10** and **4.3** became a limiting factor: separation of the barely soluble product from stoichiometric TiO_2 byproduct complicated the workup procedure and limited reaction scale. The sparingly soluble monobromo switch **4.10** could be prepared in hundred-milligram scale using this procedure, but only traces of the less soluble dibromo switch **4.3** could be recovered from the TiO_2 byproduct *via* repeated washing with hot acetone.

It was suspected that the presence of a free amine functionality contributed to the poor solubility of oxindole hemistilbenes **4.10** and **4.3** through intermolecular hydrogen bonding in the solid state. If this were the case, solubility could be improved by replacing oxindole with an alkylated oxindole and thus removing the ability to form hydrogen bonds. This was achieved by replacing oxindole (with an unprotected NH) with commercially available *N*-methyloxindole. Solubility and ease of workup were improved, with monobromo *N*-methyloxindole switch **4.8** obtained in 90% yield (Table 4.1, entry 8). As before, dibromo compound **4.9** was less soluble but could still be obtained in good yield (40–60%; Table 4.1, entry 8)). Monobromo and dibromo switches were both easily recrystallised from hot toluene, affording pure crystalline product without chromatography.

Buchwald-Hartwig amination of brominated oxindole switches

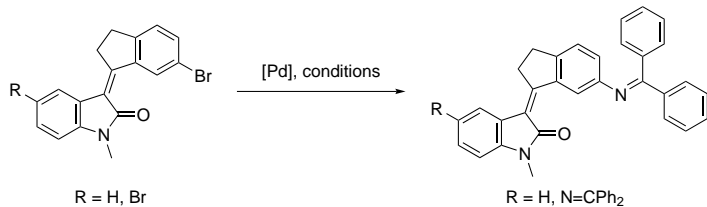
Buchwald-Hartwig palladium catalysed cross-couplings are a powerful tool for installing heteroatomic substituents on aryl groups, but finding and optimising successful reaction conditions can be challenging. Successful amination can require harsh conditions that may be incompatible with fragile moieties: conditions used previously in the Feringa group for similar aminations^[24a] involve strongly basic sodium tert-butoxide at 90 °C. Given the instability of the hemistilbene core towards hydrolysis, it was anticipated that amination without degradation could be challenging.

The installation of primary amine or aniline functionalities under Buchwald-Hartwig conditions is more difficult than the installation of substituted amine nucleophiles, because direct couplings with ammonia as a nitrogen source are generally impractical under standard pressures and temperatures. Instead, masked ‘ammonia surrogates’ such as benzophenone imine^[22] or tert-butyl carbamate^[23] can be first used as coupling partners and subsequently deprotected to expose the desired primary amine product.

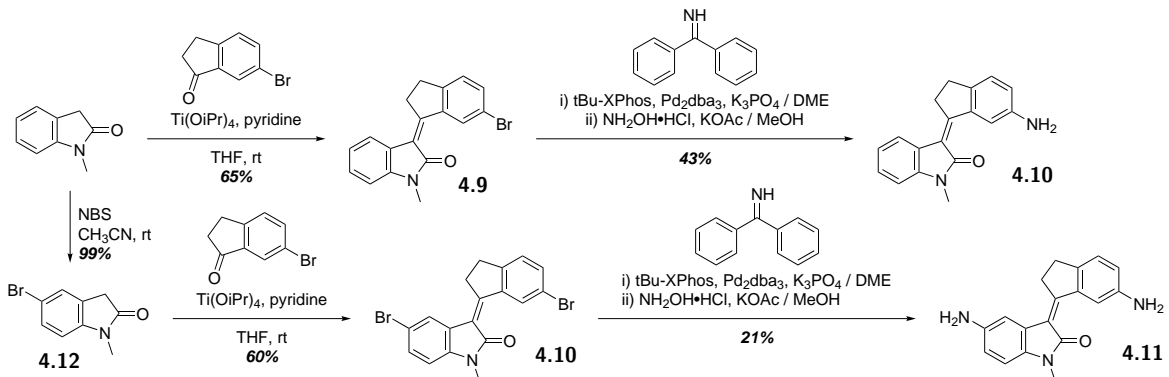
Buchwald-Hartwig coupling conditions trialled are summarised in Table 4.2. Initial attempts to couple *N*-methylated monobromo switch **4.8** with benzophenone imine under standard conditions^[24a] ($\text{Pd}(\text{dpf})\text{Cl}_2$ and NaO^tBu , toluene, 90 °C) led to decomposition and no evidence of product formation. Shorter reaction times or lower temperatures allowed some recovery of starting material, but still without any product formation. Replacing the $\text{Pd}(\text{dpf})\text{Cl}_2$ catalyst with more active $\text{Pd}_2\text{dba}_3/\text{BINAP}$ or $\text{Pd}_2\text{dba}_3/\text{XantPhos}$ systems in dioxane with Cs_2CO_3 as a weaker base also led to decomposition. Finally, a mild procedure^[23] using Pd_2dba_3 , $t^{\text{Bu}}\text{Xphos}$, and K_3PO_4 in dimethoxyethane at room temperature was found to give the desired monoimine product **4.11** in low to moderate yield (20–60%). These conditions were successful in producing diimine **4.12** from dibromo **4.9** in 20–30% yield, but this reaction proved challenging to replicate.

To avoid hydrolysing the photoswitch core, the benzophenone iminated coupling products **4.11** and **4.12** were deprotected by transamination with hydroxylamine^[23] rather than with the aq. HCl procedure used previously,^[24a] giving amine **4.13** and diamine **4.14**. The overall routes to *N*-methyloxindole compounds **4.13** and **4.14** are shown in Scheme 4.2.

Table 4.2. Accessing oxindole-switch benzophenone imines *via* Buchwald-Hartwig imination. The oxindole core seems unstable towards strong bases and at high temperature, but room-temperature coupling in dimethoxyethane with a Pd₂dba₃/^tBuXPhos/K₃PO₄ system gave the desired product with minimal decomposition.



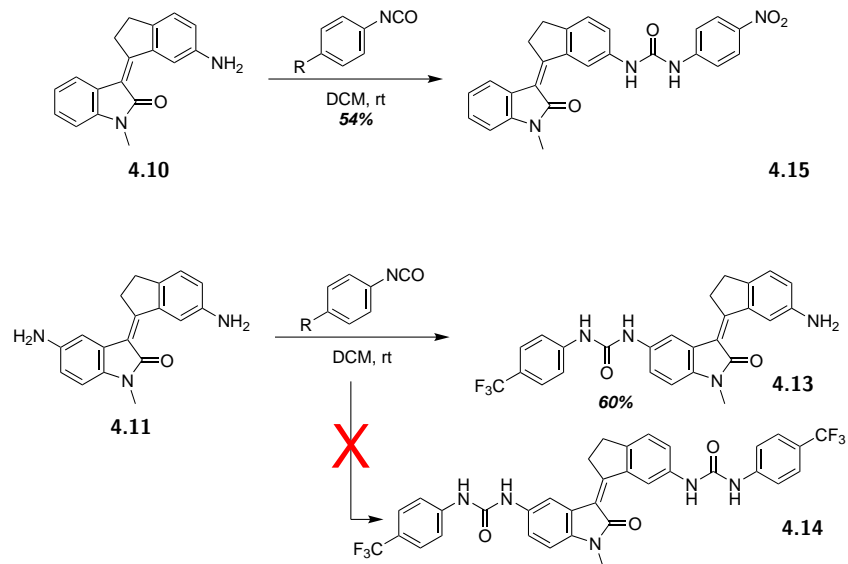
Entry	S.M.	R	Conditions	Prod.	Outcome
1	4.8	H	Pd(dppf)Cl ₂ , NaO ^t Bu, toluene, 90 °C 3 days	4.11	Decomp.
2		H	Pd(dppf)Cl ₂ , NaO ^t Bu, toluene, 150 °C 15 min		Decomp.
3		H	Pd(dppf)Cl ₂ , NaO ^t Bu, toluene, 50 °C 3 days		Decomp.
4		H	Pd ₂ dba ₃ , BINAP, Cs ₂ CO ₃ , dioxane, 90 °C 20 h		Decomp.
5		H	Pd ₂ dba ₃ , XantPhos, Cs ₂ CO ₃ , dioxane, 90 °C 20 h		Decomp.
6		H	Pd ₂ dba ₃ , ^t BuXPhos, K ₃ PO ₄ , dimethoxyethane, 48 h at rt.	20–60%	
7	4.9	Br	Pd ₂ dba ₃ , ^t BuXPhos, K ₃ PO ₄ , dimethoxyethane, 48 h at rt.	4.12	20–30%, then failed.



Scheme 4.2 Synthesis of mono- and di-bromo *N*-methyloxindole switches **4.13** and **4.14**. The Buchwald-Hartwig conditions used to couple brominated compounds **4.8** and **4.9** was highly sensitive, and stopped working after early successes.

N-methyloxindole hemistilbene ureas

Two oxindole-based ureas were synthesised by reaction of amines **4.13** and **4.14** with aryl isocyanates in dichloromethane at room temperature, as shown in Scheme 4.3. Disappointingly, an attempt to prepare a bis-urea from diamine **4.14** gave monourea **4.16**, rather than desired bis-urea **4.17**. This is likely due to the poor solubility of the monourea in dichloromethane.



Scheme 4.3 Ureas synthesised from oxindole-based hemistilbene switches. Coupling of diamine **4.14** and 4-trifluoromethylphenyl isocyanate gave only monourea **4.16**, with the lack of bisurea **4.17** ascribed to the insolubility of **4.16**.

Preliminary switching studies

Preliminary UV-vis absorption studies were performed on 4-nitrophenyl urea hemistilbene **4.18** in DMSO. This compound was soluble in DMSO and sparingly soluble in toluene or acetonitrile, and showed limited switching in response to 340–500 nm light sources (Figure 4.4). Spectra show a solvent dependence, with absorption in DMSO red-shifted by approximately 25 nm relative to absorption in toluene. Limited photoswitching is possible in DMSO using 405 nm and 505 nm visible light sources, but is accompanied by decomposition: absorption at λ_{max} (360 nm) increases and decreases semi-reversibly, but absorption at longer wavelengths (450 nm) decreases on irradiation with either source. The DMSO used for these experiments had been sparged with N₂ but not dried, so this decomposition may well be related to the hydrolysis of the double bond seen previously.

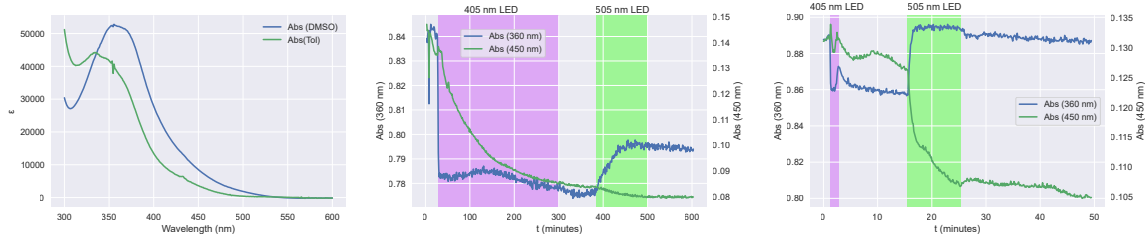


Figure 4.4. Left: absorption spectra of **4.18** in DMSO (blue) and toluene (green). The absorption profile is redshifted by approximately 25 nm in the more polar solvent. Centre and right: switching of 4-nitrophenylurea compound **4.18** in DMSO, followed by UV-vis absorption at 360 nm and 450 nm. Some switching clearly occurs (360 nm absorption can be decreased or increased), but decomposition can also be seen (450 nm absorption decreases under irradiation by either wavelength).

In light of the challenging synthesis and less-than-ideal switching properties, research efforts turned to the stiff stilbene bis-urea anion binders.

4.2.2 Switchable stiff stilbene anion binders

The stiff stilbene host targeted for this study is shown in Figure 4.5. This compound is based on the known class of stiff stilbene anion receptors.^[24]

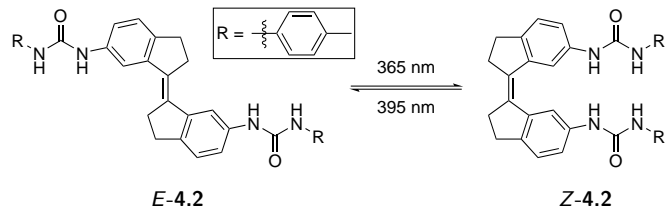
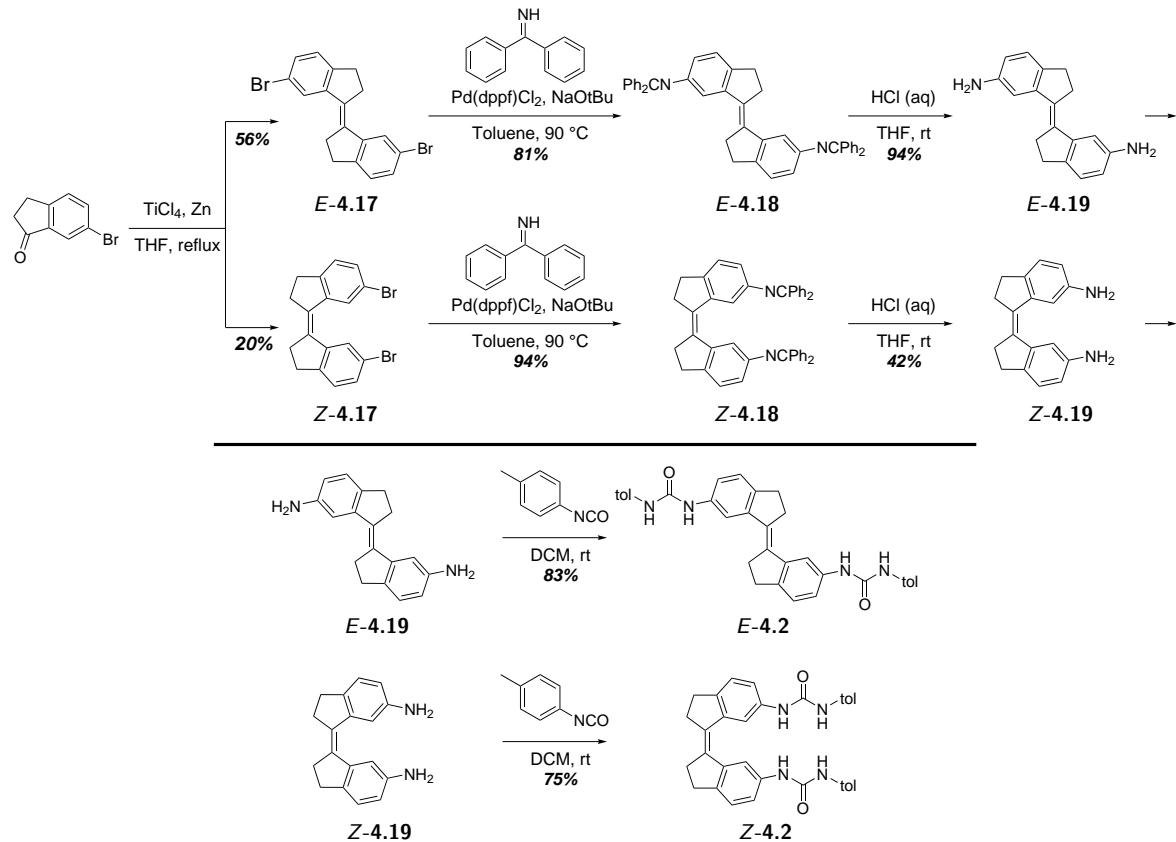


Figure 4.5. Bis-urea anion binding photoswitch **4.2**, based on previously reported^[24a] compound **4.1**.

These hosts can be converted from a weakly guest-binding *E* to a strongly binding *Z* form using near-UV light.^[4d,5c] We selected a bis-tolyl host **4.2** (Figure 4.5) for our host-guest diffusion studies to make use of the convenient ¹H NMR signal of the methyl groups for diffusion NMR experiments. Stiff stilbene hosts *E*-**4.2** and *Z*-**4.2** were prepared according to the previously reported^[24a] synthetic scheme shown in Scheme 4.4.



Scheme 4.4 Synthetic route to photoswitchable anion binders *E*-**4.2** and *Z*-**4.2**. All reaction conditions used were adapted from the literature.^[24a]

4.3 Anion-binding properties of bis-urea stiff stilbene host

The binding constants of host **4.2** for anions H_2PO_4^- and OAc^- were measured by NMR titrations in DMSO with 0.5% added H_2O . Chemical shift data obtained was fitted to 1:2 $[\text{HG}_2]$ binding models, and the results were comparable to those previously reported^[24a] over the same guest concentration range. The water was added to minimise the effect of variable water content in the DMSO- d_6 and for consistency with previous studies on this system.^[17]

4.3.1 Obtaining association constants

Standard mathematical models were used to obtain host-guest association constants, K .^[25] Dilution-corrected NMR titrations were performed by adding aliquots of the guest + 5 mM host to 5 mM solutions of host in DMSO- d_6 with 0.5% added water. The obtained chemical shift data were used to fit curves and obtain association constants using the processing routines given in Script 9.1. In all cases, 1:2 H:G binding models were used for fitting.^[25] Two association constants were fitted, K_1 and K_2 , respectively defined as:

$$K_1 = \frac{[\text{HG}]}{[\text{H}][\text{G}]} \quad (4.1)$$

$$K_2 = \frac{[\text{HG}_2]}{[\text{HG}][\text{G}]} \quad (4.2)$$

In practice, curve-fitting was used to obtain K_1 and cooperativity parameter α , which is defined as:^[25]

$$\alpha = \frac{K_1}{4K_2} \quad (4.3)$$

For *E*-**4.2**, a noncooperative ($\alpha = 1$) model was used to reflect the spatially and electronically isolated urea binding sites. For *Z*-**4.2**, a cooperative model with floating α was used to reflect intramolecular interactions across the adjacent urea binding sites.

4.3.2 Obtaining association constants with a self-associating guest

The self-association of H_2PO_4^- described in the following sections makes determination of host-guest binding challenging. Considering a minimal case of host-guest binding with a 1:1 stoichiometry and no self-association for either host or guest, the concentration of free guest [G] can be found by solving the quadratic:^[25]

$$0 = [\text{G}]^2 - [\text{G}] \left([\text{G}]_0 - [\text{H}]_0 - \frac{1}{K_a} \right) - \frac{[\text{G}]_0}{K_a} \quad (4.4)$$

where $[\text{G}]_0$ and $[\text{H}]_0$ are respectively the total concentration of guest and host, and K_a is the association constant. This quadratic derives from the definition of an association constant

4.3. ANION-BINDING PROPERTIES OF BIS-UREA STIFF STILBENE HOST

and the mass balance equations for host and guest, as shown below:

$$K_a = \frac{[\text{HG}]}{[\text{H}][\text{G}]} \quad (4.5)$$

$$[\text{G}]_0 = [\text{G}] + [\text{HG}] \quad (4.6)$$

$$[\text{H}]_0 = [\text{H}] + [\text{HG}] \quad (4.7)$$

If the guest is capable of indefinite self-association, constructing such a model for host-guest binding becomes more challenging. With infinite oligo-guest species present in solution, if the host binding site is capable of binding not only monomeric G but also G₂ dimers, G₃ trimers, G₄ tetramers *etc* there is no longer a single ‘guest’ for the host to bind to nor a single host-guest association constant, K_a , capable of reflecting the infinite possible host-guest interactions in solution. The mass balance equations for such a system are also complex:

$$[\text{G}]_0 = \sum_{n=1}^{\infty} n[\text{G}_n] + \sum_{n=1}^{\infty} n[\text{HG}_n] \quad (4.8)$$

$$[\text{H}]_0 = [\text{H}] + \sum_{n=1}^{\infty} [\text{HG}_n] \quad (4.9)$$

Modelling association constants for such loosely-defined systems would be challenging. Doing so would involve answering questions such as whether or not a host molecule can bind a G₂ dimer as readily as it binds monomeric G, or if the guest bound in an [HG] complex is able to bind a subsequent guest to form [HG₂] (and if so, how this compares to the dimerisation of 2 G to form [G₂]).

While understanding this system in such detail would be an interesting problem in its own right, it is beyond the scope of this work. Instead we continue to use standard equations of host-guest binding^[25] that assume that the guest can only exist in free or host-bound forms and that all host-guest complexes are either [HG] or [HG₂] in form, while noting the inadequacy of such standard models when faced with self-associating species.

4.3.3 Example ^1H NMR titrations with tetrabutylammonium acetate

Before considering the more complicated case of binding to H_2PO_4^- , control titration experiments were conducted against tetrabutylammonium acetate. As the acetate anion is incapable of forming extended hydrogen-bonding oligomers, standard methods of determining host-guest binding constants by NMR titration are successful and fitted parameters have relatively low errors (errors estimated as the square of the diagonal elements of the covariance matrix, σ_{xx}^2) demonstrating that standard approaches^[25] are adequate to obtain good association data, as summarised in Table 4.3.

Acetate binding of *E-4.2*

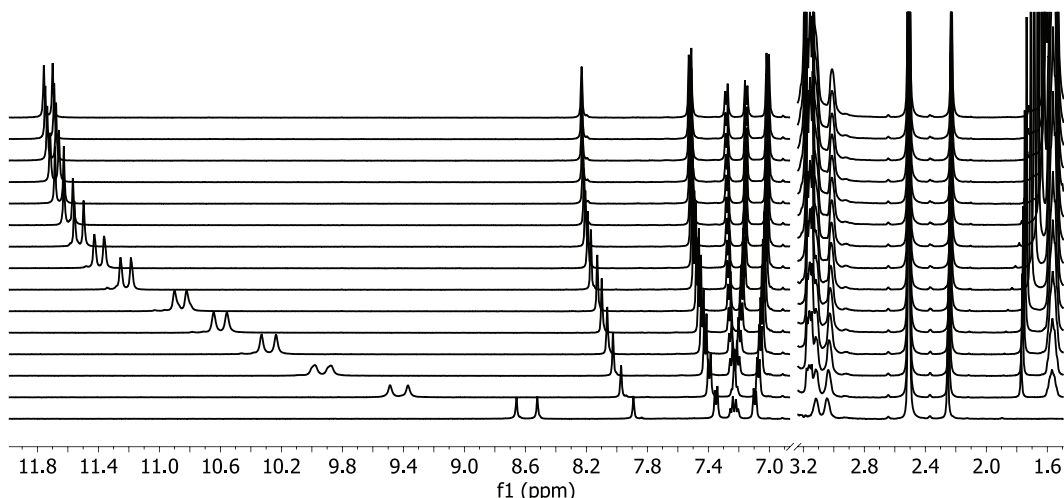


Figure 4.6. Representative NMR titration of 50 mM TBA-OAc into 5 mM of *E-4.2*. 500 MHz, $\text{DMSO}-d_6 + 0.5\% \text{H}_2\text{O}$. $[\text{OAc}^-]$ increases from bottom to top.

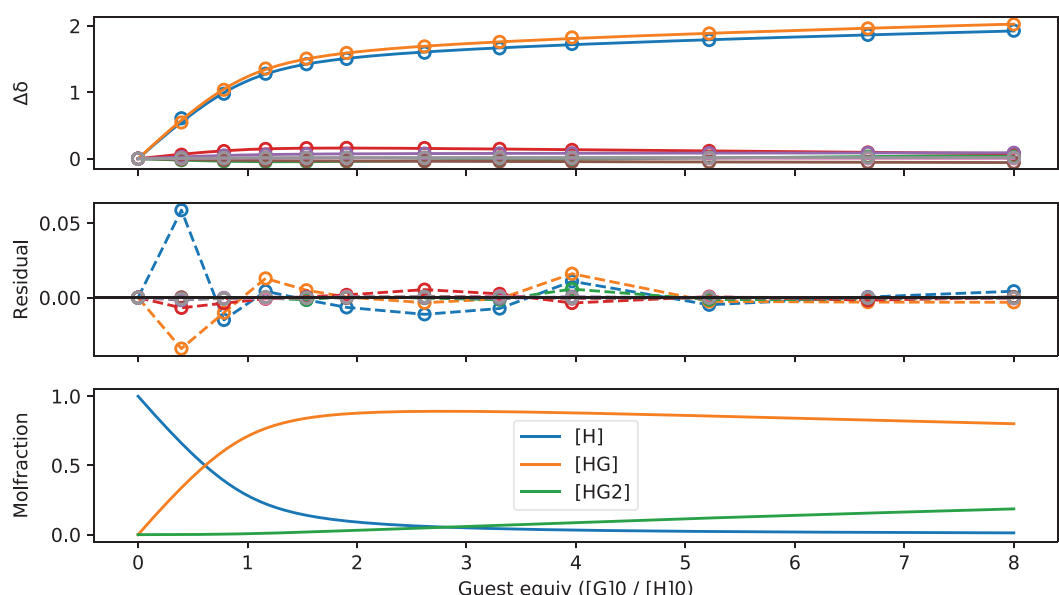


Figure 4.7. Data from Figure 4.6 fitted to a 1:2 host:guest association model. $K_1 = (350 \pm 90) \text{ M}^{-1}$, $\alpha = 1$ (forced), $K_2 = 87 \text{ M}^{-1}$.

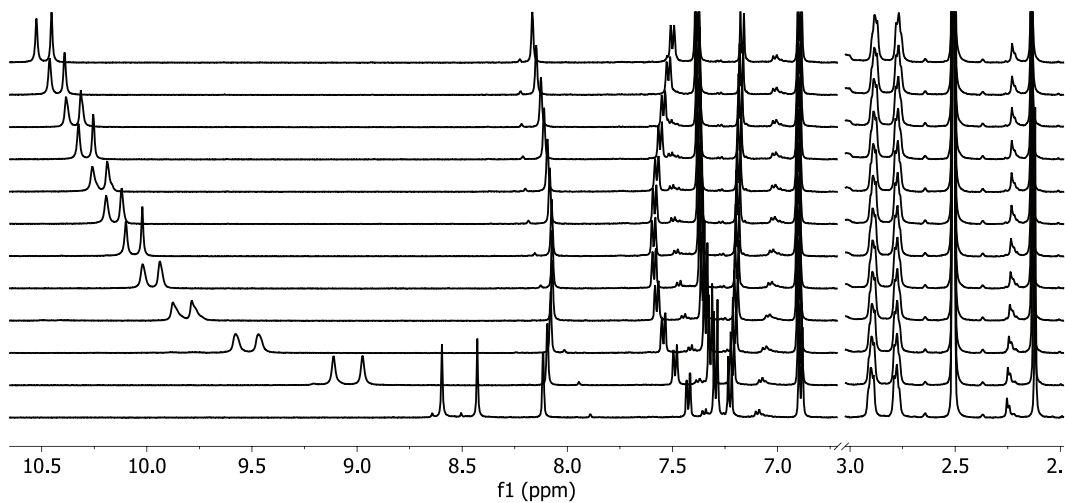
Acetate binding of Z-4.2

Figure 4.8. Representative NMR titration of 50 mM TBA-OAc into 5 mM of **Z-4.2**. 400 MHz, $\text{DMSO}-d_6 + 0.5\% \text{H}_2\text{O}$. $[\text{OAc}^-]$ increases from bottom to top.

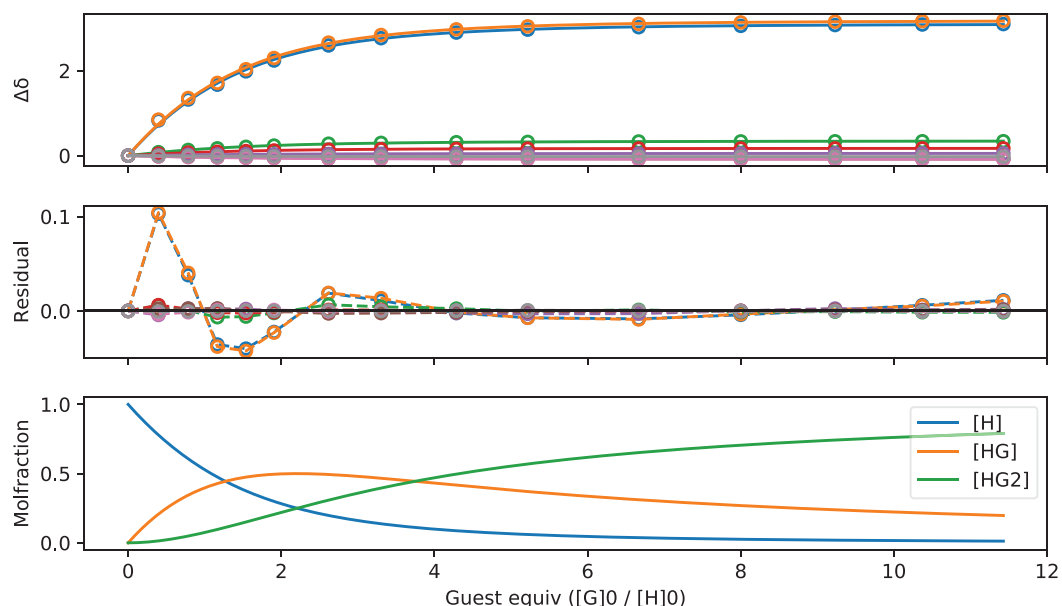


Figure 4.9. Data from Figure 4.8 fitted to a 1:2 host:guest association model. $K_1 = (1.8 \pm 0.2) \times 10^3 \text{ M}^{-1}$, $\alpha = 0.01 \pm 0.01$, $K_2 = 7 \text{ M}^{-1}$.

4.3.4 Example ^1H NMR titrations with tetrabutylammonium dihydrogen phosphate

We now consider the binding of H_2PO_4^- by host **4.2**. Obtaining association constants for H_2PO_4^- binding is difficult for the reasons discussed in subsection 4.3.2, and the inadequacy of the non-competitive 1:2 host:guest binding model used can be seen from the large errors obtained from curve fitting (errors estimated as the square of the diagonal elements of the covariance matrix, eg σ_{xx}^2).

Dihydrogen phosphate binding of *E*-**4.2**

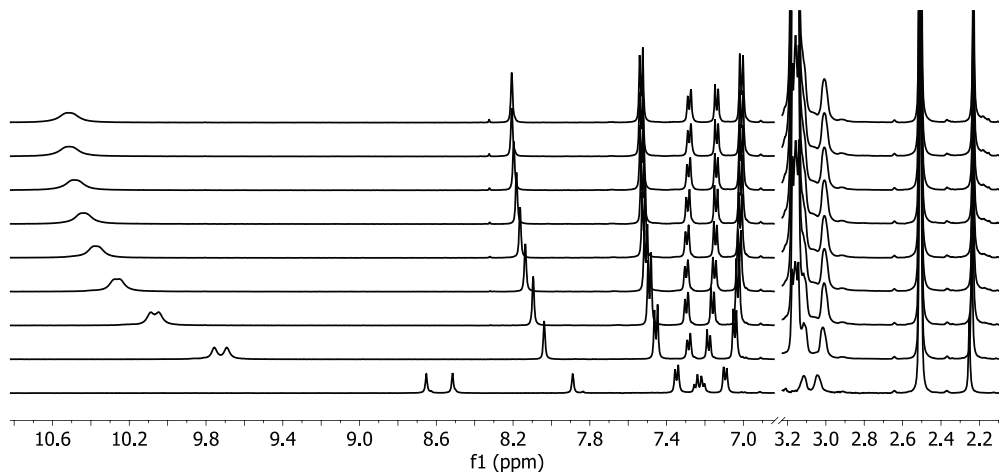


Figure 4.10. Representative NMR titration of 50 mM [TBA] $[\text{H}_2\text{PO}_4]$ into 5 mM of *E*-**4.2**, to 18 mM total guest concentration. 500 MHz, $\text{DMSO}-d_6 + 0.5\%$ H_2O . $[\text{H}_2\text{PO}_4^-]$ increases from 0 mM at the bottom to 18 mM at the top.

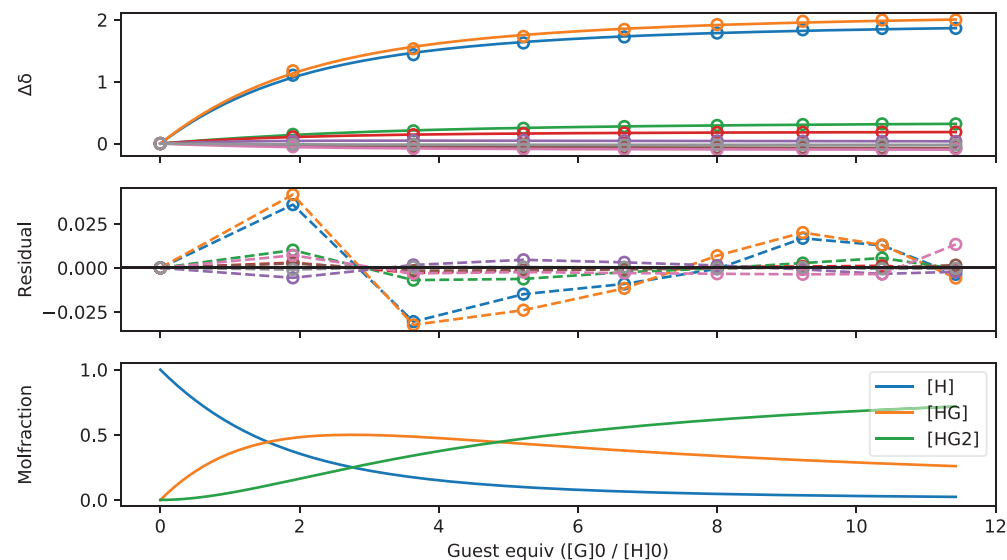


Figure 4.11. Data from Figure 4.10 fitted to a 1:2 host:guest association model. $K_1 = (230 \pm 140) \text{ M}^{-1}$, $\alpha = 1$ (forced), $K_2 = 57 \text{ M}^{-1}$.

Dihydrogen phosphate binding of Z-4.2

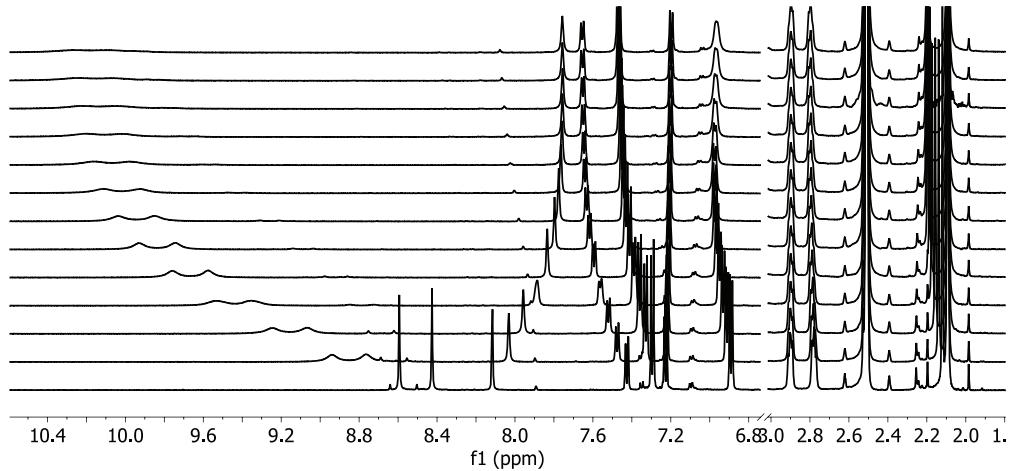


Figure 4.12. Representative NMR titration of 50 mM [TBA] $\text{[H}_2\text{PO}_4^-$] into 5 mM of **Z-4.2**, to 9.7 mM total guest concentration. 400 MHz, $\text{DMSO}-d_6 + 0.5\%$ H_2O . $[\text{H}_2\text{PO}_4^-]$ increases from 0 mM at the bottom to 9.7 mM at the top.

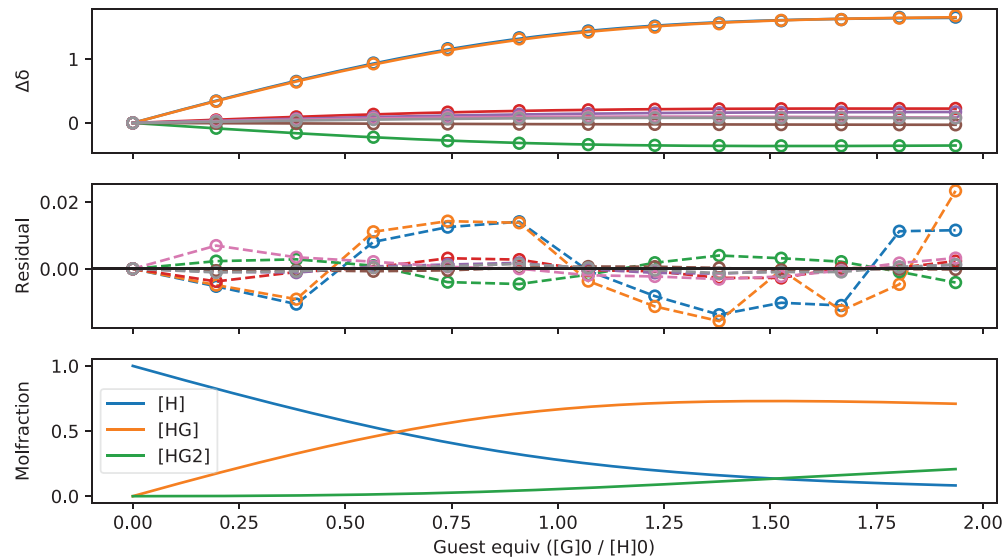


Figure 4.13. Data from Figure 4.12 fitted to a 1:2 host:guest association model. $K_1 = 2.1 \times 10^3 \text{ M}^{-1}$, $\alpha = 0.14 \pm 0.33$, $K_2 = 7 \times 10^1 \text{ M}^{-1}$.

4.3.5 Evidence for $[HG_2]$ binding mode of host Z-4.2

In previous work^[24a] studying analogous host **4.2**, it has been assumed that the *Z*-**4.2** isomer can only bind one molecule of guest. However, we observe clear evidence for a two-step binding process from the movement of peaks shown in Figure 4.14, where some host peaks are seen to first move in one direction and then in the other on addition of $H_2PO_4^-$. The changes in peak chemical shifts relative to those of free *Z*-**4.2** are shown in Figure 4.15, and are consistent with the shielding and deshielding caused by the urea carbonyl on rotation of the aryl-urea C–N bond, as required for formation of the HG_2 complex.

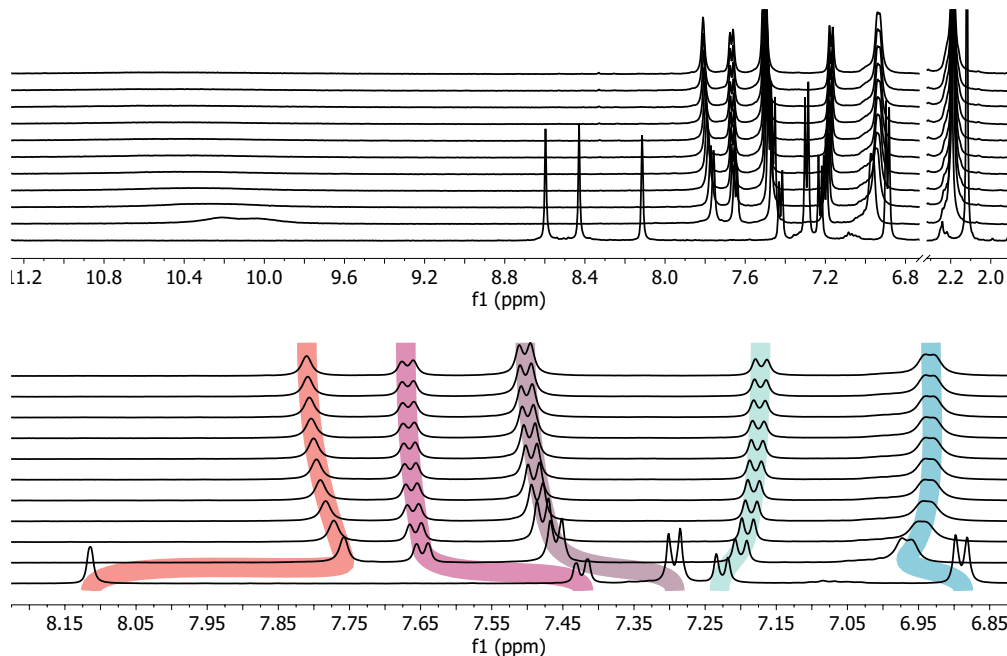


Figure 4.14. Titration of 200 mM [TBA] $[H_2PO_4^-]$ into 5 mM of *Z*-**4.2** to 66.7 mM guest concentration. 500 MHz, $DMSO-d_6 + 0.5\% H_2O$. Bottom: the same spectrum, zoomed to focus on the aromatic region and exclude the coalesced urea NH peaks. A clear two-step process can be seen in the movements of the peaks, particularly the peaks initially at 8.1 and 6.9 ppm.

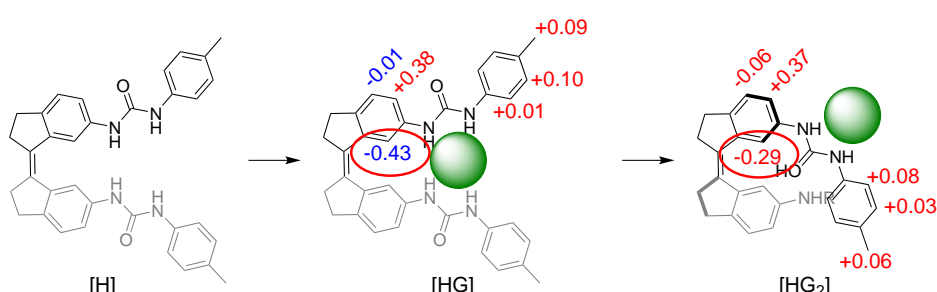


Figure 4.15. Changes in 1H NMR chemical shifts of *Z*-**4.2** (ppm, relative to those of free host) support the two-step binding fit proposed for the *Z* isomer in Figure 4.13. Most notably, the inner aryl proton (circled) is first shielded and then deshielded by the two steps of binding. This is consistent with the expected chemical shift induced by the carbonyl group magnetic anisotropy for the geometries drawn for the $[HG]$ and $[HG_2]$ complexes.

4.3.6 Summary of association data for stiff stilbene host

The measured association constants for **E-4.2** and **Z-4.2** binding acetate and dihydrogen phosphate are shown in Table 4.3 and Table 4.4 respectively. Binding data for studied di-tolylurea host **4.2** is also compared to literature^[24a] binding constants for analogous di-phenylurea host **4.1** under the same conditions. Binding studies at higher concentrations of H_2PO_4^- resulted in slightly different association constants than those previously reported. The self-association of H_2PO_4^- makes titration experiments necessarily competition experiments, which complicates models for calculating association constants.^[25] For example, a recent report of H_2PO_4^- binding^[26] found different binding constants and stoichiometries when measured at different concentrations by UV-vis absorption or NMR spectroscopy, likely due to H_2PO_4^- aggregation.

Table 4.3. Summary of data for host **4.2** binding acetate (as TBA-OAc); DMSO-*d*₆ + 0.5% H₂O).

	<i>E-4.2</i> ^[a]	<i>E-4.2</i> ^[a]	<i>E-4.1</i> ^[b]	<i>Z-4.2</i> ^[a]	<i>Z-4.2</i> ^[a]	<i>Z-4.1</i> ^[b]
Endpoint / mM	57	8.6	-	40	57	-
K_1 / M ⁻¹	330 ± 35	350 ± 90	210	1800 ± 200	1500 ± 200	1400
K_2 / M ⁻¹	83	87	50	7	5	-
α	<i>Forced as 1</i>	0.01 ± 0.01	0.01 ± 0.01

^[a] Measured association constants from compound **4.2**

^[b] Literature association constants for analogous compound **4.1**

Table 4.4. Summary of data for host **4.2** binding dihydrogen phosphate (as [TBA][H₂PO₄]); DMSO-*d*₆ + 0.5% H₂O).

	<i>E-4.2</i> ^[a]	<i>E-4.2</i> ^[a]	<i>E-4.1</i> ^[b]	<i>Z-4.2</i> ^[a]	<i>Z-4.2</i> ^[a]	<i>Z-4.2</i> ^[a]	<i>Z-4.1</i> ^[b]
Endpoint / mM	18	58	-	9.8	15.5	67	-
K_1 / M ⁻¹	360 ± 320	230 ± 320	154	2100 ± 2100	3500 ± 1100	13000 ± 8000	1400
K_2 / M ⁻¹	90	60	40	70	110	72	-
α	<i>Forced as 1</i>	0.14 ± 0.33	0.13 ± 0.08	0.02 ± 0.02	-

^[a] Measured association constants from compound **4.2**

^[b] Literature association constants^[24a] for analogous compound **4.1**

4.4 Antielectrostatic oligomerisation of dihydrogen phosphate

Before considering the changes in diffusion of host **4.2** on binding H₂PO₄⁻, it was necessary to study the self-associating properties of H₂PO₄ in the absence of host. Diffusion coefficients of NBu₄⁺ (TBA) and H₂PO₄⁻ were conducted respectively using ¹H (TBA) and ³¹P (H₂PO₄⁻) diffusion NMR in DMSO-d₆ with 0.5% added water. Our initial diffusion studies of tetrabutylammonium dihydrogen phosphate ([TBA][H₂PO₄]) solutions revealed a surprising decrease in the diffusion coefficient of the H₂PO₄⁻ anion ($D_{\text{H}_2\text{PO}_4^-}$) at sub-molar concentrations, while the diffusion coefficient of the TBA counterion (D_{TBA}) remained relatively constant (Figure 4.16).

Most significantly, I found that at 20 mM the relative order of the diffusion coefficients of TBA and H₂PO₄⁻ reverse: below 20 mM TBA diffuses more slowly than H₂PO₄⁻, while above 20 mM H₂PO₄⁻ diffuses more slowly than TBA. This suggests that as concentration

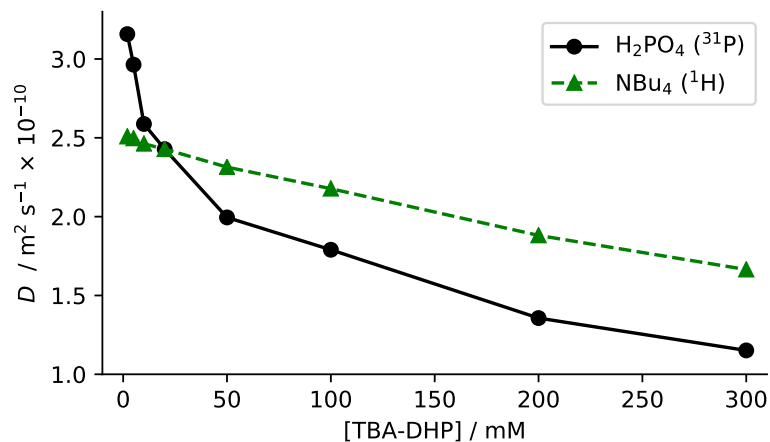


Figure 4.16. Measured diffusion coefficients of tetrabutylammonium dihydrogen phosphate ($[\text{TBA}][\text{H}_2\text{PO}_4]$) measured by ^1H or ^{31}P NMR. 500 MHz ^1H NMR PGSTE, $\delta = 3\text{ ms}$, $\Delta = 50\text{ ms}$, $g = 0\text{--}53.45\text{ g cm}^{-1}$; 202 MHz ^{31}P NMR PGSTE, $\delta = 7\text{ ms}$, $\Delta = 100\text{ ms}$, $0\text{--}53.45\text{ g cm}^{-1}$; $\text{DMSO}-d_6$ with 0.5% added water.

increases, the effective size of the H_2PO_4^- anion (MW = 97) also increases until it becomes larger than the TBA cation (MW = 243). This behaviour cannot be explained by changes in ion pairing or viscosity which would affect the diffusion coefficients of both species equally, and appears suggestive of antielectrostatic hydrogen bonding.

The Stokes-Einstein-Sutherland equation describes the diffusion coefficient of a hard spherical particle as

$$D = \frac{k_B T}{6\pi\eta R_H} \quad (4.10)$$

where k_B is the Boltzmann constant, T is the temperature, η is the dynamic viscosity of the solution, and R_H is the hydrodynamic radius of the particle. If we assume that a molecular particle is roughly spherical, it follows that the diffusion coefficient will be approximately proportional to the inverse cube root of molecular volume, $D \propto V^{-1/3}$.^[27] The >50% decrease in $D_{\text{H}_2\text{PO}_4^-}$ as the H_2PO_4^- concentration is increased from 2–300 mM therefore suggests a greater than *eight-fold increase* in effective volume over this concentration range. As this is too great a change in volume to be explained by the formation of H_2PO_4^- dimers, I propose this decrease in $D_{\text{H}_2\text{PO}_4^-}$ results from the formation of antielectrostatic hydrogen bonded oligomers of H_2PO_4^- in solution.

4.4.1 Viscosity measurements of dihydrogen phosphate solutions

From the Stokes-Einstein-Sutherland equation (Equation 4.10), D is affected by changes in the particle hydrodynamic radius R_H and in the solution viscosity η . This means that any change in measured D for a molecular species can be a result of changes in both η and R . With the intention of comparing R_H for H_2PO_4^- at different concentrations, it was thus necessary for us to measure any changes in viscosity η that might occur over the same range of concentrations.

We measured η directly for solutions of $[\text{TBA}][\text{H}_2\text{PO}_4]$ in $\text{DMSO}-d_6$ by falling ball vis-

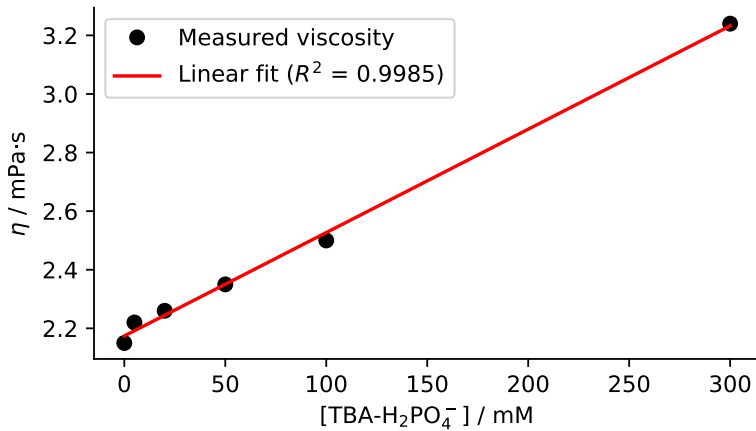


Figure 4.17. Concentration dependence of the measured viscosity of tetrabutylammonium dihydrogen phosphate solutions in DMSO-*d*₆ with 0.5% added water. Linear fit: $\eta = 2.17 + 3.53 \times [\text{TBA}-\text{H}_2\text{PO}_4^-] / \text{mM}$. For calibrating diffusion measurements, it is convenient to express this in relative form: $\frac{\eta}{\eta_0} = 1 + 1.63 \times [\text{TBA}][\text{H}_2\text{PO}_4] / \text{mM}$

cometry. In these experiments, a small stainless steel ball is dropped through a capillary containing a liquid solution, with the viscosity η obtainable from the time taken for the ball to fall a given distance. The results are given in Figure 4.17, and show an approximately linear relationship between viscosity η and $[\text{TBA}][\text{H}_2\text{PO}_4]$ over the 0–300 mM concentration range. This linear relationship between η and $[\text{TBA}][\text{H}_2\text{PO}_4]$ was used to construct a calibration curve, which was used to remove the influence of changing viscosity on D to produce a viscosity-compensated value D' .

4.4.2 Mathematical modelling of oligomer formation

Modelling isodesmic association

The most simple thermodynamic model of supramolecular polymerisation of a monomer A is *isodesmic* association, in which the binding of a monomer A to an oligomeric unit A_n occurs with the same association constant K_i regardless of the size of the oligomer:^[28]

$$K_i = \frac{[A_n]}{[A][A_{n-1}]} \quad (4.11)$$

As species A can exist in oligomers of any length, the total concentration $[A]_0$ will then be given by the mass balance shown in Equation 4.12:

$$[A]_0 = \sum_{n=1}^{\infty} n[A_n] \quad (4.12)$$

It is convenient to define $z = [A]K_i$. We can then construct an expression for $[A_n]$, the concentration of an n -unit oligomer, from Equation 4.11:

$$[A_n] = K_i[A][A_{n-1}] = z[A_{n-i}] \quad (4.13)$$

As $[A_1] = [A]$, by induction:

$$[A_n] = [A]z^{n-1} = \frac{z^n}{K_i} \quad (4.14)$$

By combining Equation 4.12 with Equation 4.14, we can then convert the infinite sum into a closed expression relating z to the total concentration $[A]_0$:

$$[A]_0 = \sum_{n=1}^{\infty} n[A_n] \quad (4.15)$$

$$= \frac{1}{K_i} \sum_{n=1}^{\infty} nz^n \quad (4.16)$$

$$= \frac{z}{K_i(z - 1)^2} \quad (4.17)$$

At this point we wish to solve for z . We can do so by expanding to a quadratic of z , and solving the quadratic:

$$[A]_0 K_i z^2 - (2[A]_0 K_i + 1)z + [A]_0 K_i = 0 \quad (4.18)$$

Defining $L = [A]_0 K_i$ allows us to obtain z as the smallest^[28] root of the quadratic:

$$z = \frac{2L + 1 - \sqrt{4L + 1}}{2L} \quad (4.19)$$

Equation 4.19 allows us to obtain z from total concentration $[A]_0$ and isodesmic association constant K_i , and from z we can find the concentration of unbound monomer as $[A] = \frac{z}{K_i}$. With access to $[A]$, the size distribution of oligomers can be calculated using Equation 4.14 and Equation 4.19.

Modelling the diffusion of oligomers

Fitting an isodesmic association constant to diffusion data also requires a model relating the size of an n -unit A_n oligomer to a diffusion coefficient, D_n . This is challenging for an arbitrarily-shaped oligomer,^[29] but the problem can be simplified by assuming that each n -unit oligomer A_n is a *hard sphere* with a volume V_n equal to nV_0 , where V_0 is the volume of a monomer. The assumption of hard spheres packing perfectly to form larger hard spheres is clearly unrealistic, but the differences between this minimal model and more rigorous treatments has previously been found to be small for a case involving enzymes.^[27] This treatment also assumes that the signal intensity received from an oligomer is strictly proportional to the number of monomer subunits contained. For an NMR study, this means that we neglect potential differences in longitudinal relaxation times T_1 across oligomers of different sizes or between the different sites present within an oligomer.

Under the assumption of perfectly packing spheres, the diffusion coefficient of an n -unit oligomer can be expressed as

$$D_n = n^{-1/3} D_0 \quad (4.20)$$

where D_0 is the diffusion coefficient of the monomer (*i.e.* at infinite dilution).

For a system of oligomers in fast exchange on the NMR timescale, the measured average diffusion coefficient \bar{D} will be the concentration-weighted average of all diffusion coefficients D_n of all oligomers.

$$\bar{D} = \frac{1}{[A]_0} \sum_{n=1}^{\infty} n[A_n]D_n \quad (4.21)$$

By combining previously obtained expressions for D_n (Equation 4.20) and $[A]$ (Equation 4.14), we can then express the measured average diffusion coefficient \bar{D} as:

$$\bar{D} = \frac{D_0}{[A]_0 K_i} \sum_{n=1}^{\infty} n^{2/3} z^n \quad (4.22)$$

There is no closed-form analytic solution to this infinite sum. For numerical modelling and curve-fitting it is convenient to restate it as a polylogarithm, a function available in many numerical computing packages (in this case `mpmath` for Python). The polylogarithm $\text{Li}_s(z)$ is a special function defined^[30] as:

$$\text{Li}_s(z) = \sum_{k=1}^{\infty} \frac{z^k}{k^s}$$

allowing us to re-write Equation 4.22 in a form suitable for curve-fitting as:

$$\bar{D} = \frac{D_0}{[A]_0 K_i} \text{Li}_{(-2/3)}([A]K_i) \quad (4.23)$$

Some example results of this model for the concentration-dependent diffusion of isodesmically self-associating species are shown in Figure 4.18, with the concentration range studied here for H_2PO_4^- (2–300 mM) shaded as a purple box. It is important to note that diffusion measurements at low concentration are necessary to gain a good understanding of D_0 : for example, over the concentration range studied it would difficult to discriminate $K_i = 256$ for a slowly diffusing monomer from $K_i = 1024$ for a monomer with a slightly higher D_0 . As diffusion NMR experiments are practically limited to millimolar or greater concentrations, this approach is likely unsuitable for measuring the association thermodynamics of strongly associating ($K_i > 10^3$) species.

Estimated diffusion of host-guest complexes

Consider a supramolecular complex made up from m host molecules and n guest molecules of the form $[\text{H}_m\text{G}_n]$, where the diffusion coefficients of free host and free guest have been obtained as D_H and D_G . Under the same approximation of perfectly packing hard spheres used previously, we can approximate the diffusion coefficient of the complex as:

$$D(m, n) = (mD_H^{-3} + nD_G^{-3})^{-1/3} \quad (4.24)$$

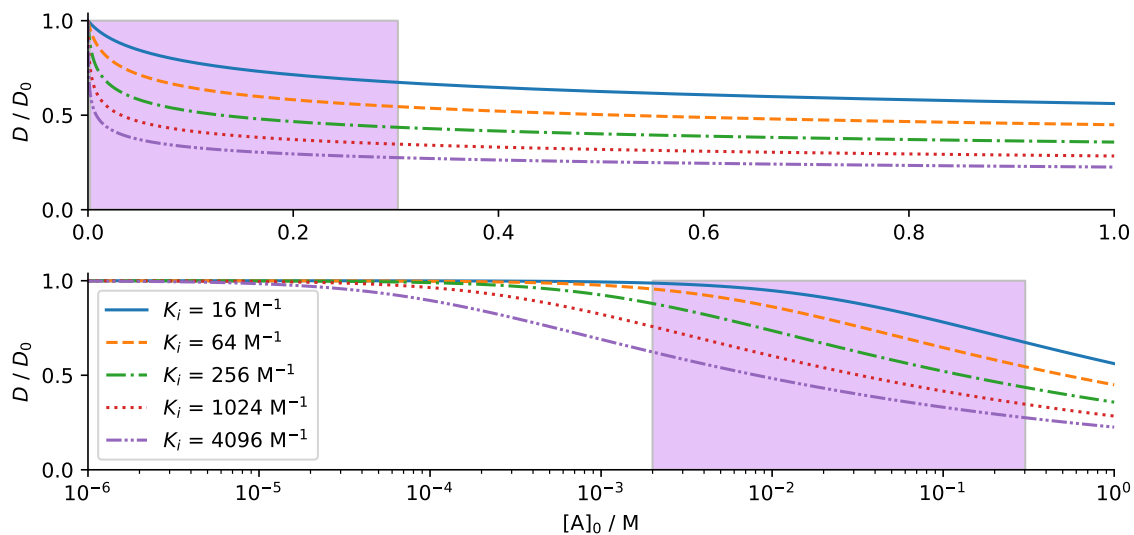


Figure 4.18. Modelled changes in relative diffusion coefficients D/D_0 under conditions of isodesmic self-association (Equation 4.23), for five different association constants K_i over the concentration range $1 \mu\text{M}$ to 1 M . The $2\text{--}300 \text{ mM}$ concentration range studied here has been shaded in purple. Both plots show the same curves, against a linear (top) and log (bottom) concentration scale.

As the hosts and guests will not pack perfectly into hard spherical complexes, the diffusion coefficients of complexes estimated by this method can be considered upper bounds for the actual diffusion coefficients.

Assuming fast exchange of species on the NMR timescale, the diffusion coefficient measured for a host species is a population-weighted average of all $[\text{H}_m\text{G}_n]$ species present:

$$\overline{D_H} = \frac{1}{[\text{H}]_0} \sum_{m=1}^{\infty} \sum_{n=0}^{\infty} m D(m, n) [\text{H}_m\text{G}_n] \quad (4.25)$$

For the case of discrete complexes involving a single host and up to two guests, this evaluates to

$$\overline{D_H} = \frac{1}{[\text{H}]_0} \left([\text{H}] D_H + [\text{HG}] (D_H^{-3} + D_G^{-3})^{-1/3} + [\text{HG}_2] (D_H^{-3} + 2D_G^{-3})^{-1/3} \right) \quad (4.26)$$

As D_H and D_G can be measured directly from dilute solutions of pure host and guest and concentrations $[\text{H}]$, $[\text{HG}]$, and $[\text{HG}_2]$ can be calculated from $[\text{H}]_0$ using association constants obtainable through titration experiments, Equation 4.26 allows the approximate diffusion coefficients of host-guest complexes to be estimated from experimentally obtained parameters.

4.4.3 Self-association of dihydrogen phosphate in DMSO

The concentration-dependent viscosity curve for $[\text{TBA}][\text{H}_2\text{PO}_4^-]$ (subsection 4.4.1) was used to adjust all measured diffusion coefficients D' to compensate for changes in viscosity, with viscosity-corrected diffusion data D' shown in Figure 4.19. It can be seen that D_{TBA} is unchanging with respect to concentration as would be expected for a non-associating cation. Nonlinear regression of Equation 4.23 onto $D'_{\text{H}_2\text{PO}_4^-}$ as a function of $[\text{H}_2\text{PO}_4^-]$ gave isodesmic

association constant $K_i = (120 \pm 32) \text{ M}^{-1}$, remarkably close to the reported dimerisation constant of H_2PO_4^- in DMSO of 180 M^{-1} .^[13c]

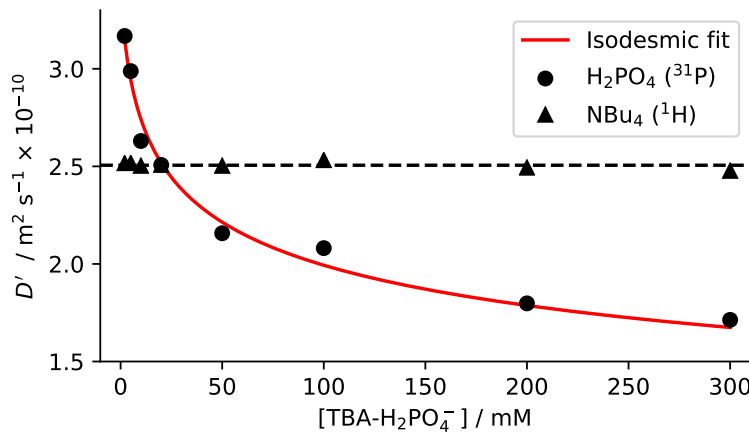


Figure 4.19. Viscosity-corrected diffusion coefficients D' of TBA- H_2PO_4^- measured by ^1H (500 MHz) or ^{31}P (202 MHz) NMR over the 2–300 mM concentration range. See Figure 4.17 for details of viscosity correction. An isodesmic oligomerisation model was fitted to the measured diffusion coefficients of dihydrogen phosphate giving parameters $K_i = (120 \pm 32) \text{ M}^{-1}$ and $D_0 = (3.39 \pm 0.11) \times 10^{-10} \text{ m}^2 \text{ s}^{-1}$. All measurements in DMSO- d_6 with 0.5% added water.

This measured K_i corresponds to median complexes comprised of 4 or 10 H_2PO_4^- subunits at 50 or 300 mM concentrations respectively (Figure 4.20), and I believe this surprisingly strong process in a polar solvent is the first measurement of indefinite AEHB self-association.

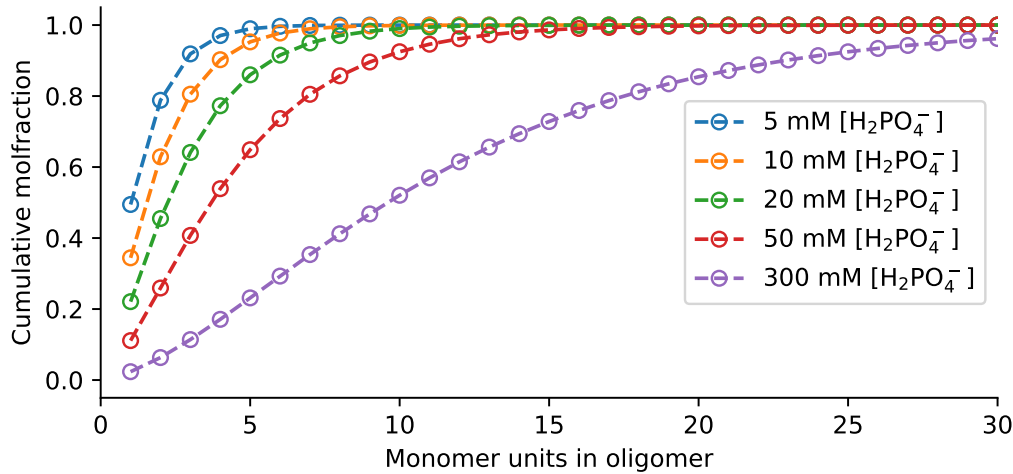


Figure 4.20. Distribution of H_2PO_4^- oligomer sizes under isodesmic association with $K_i = 120 \text{ M}^{-1}$

4.4.4 Control experiments with tetrabutylammonium acetate

Due to the large quantities of DMSO- d_6 required for falling-ball viscometry, no direct viscosities were measured for solutions of tetrabutylammonium acetate (TBA-OAc). Instead, an indirect viscosity calibration was performed from the measured diffusion coefficient of the

DMSO- d_6 solvent residual under the assumption that changes in measured D' for the solvent residual would be primarily a result of changing viscosity, as shown in Figure 4.21. This was used to produce a viscosity calibration curve of $\frac{\eta}{\eta_0} = 1 + 0.521 \times [\text{TBAOAc} / \text{mM}]$.

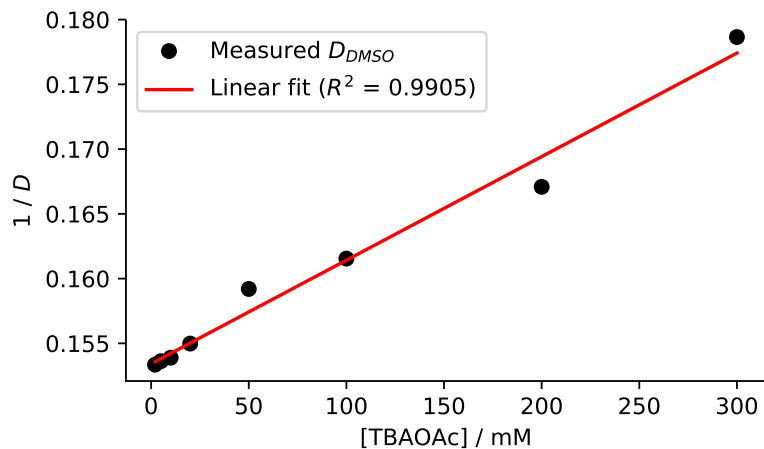


Figure 4.21. Indirect viscosity calibration for tetrabutylammonium acetate, using the diffusion coefficient of the DMSO solvent residual peak. Linear fit for implied relative change in dynamic viscosity: $\frac{\eta}{\eta_0} = 1 + 0.521 \times [\text{TBAOAc} / \text{mM}]$

Control experiments conducted with tetrabutylammonium acetate did not show comparable continuing decreases in diffusion coefficients of either TBA or acetate over the same concentration range as used for [TBA][H₂PO₄⁻] (Figure 4.22), indicating that the formation of AEHB oligomers was unique to H₂PO₄⁻. The diffusion coefficient of acetate does drop over low concentrations (0–20 mM), suggesting the formation of small discrete species such as water-bridged acetate dimers.

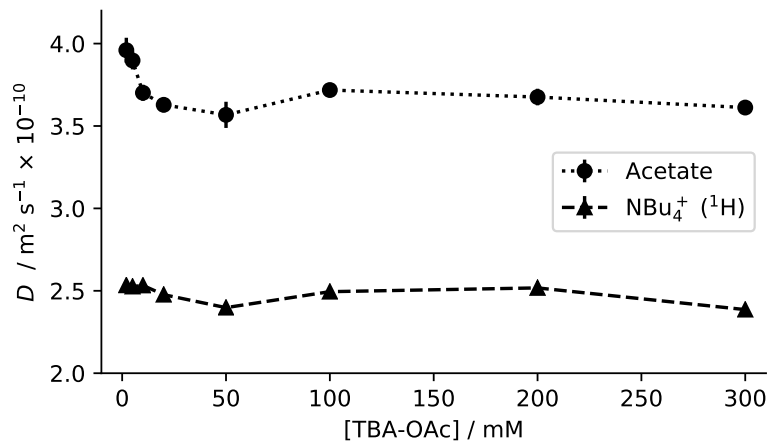


Figure 4.22. Measured diffusion coefficients of tetrabutylammonium acetate over the concentration range 0–300 mM with correction for changes in viscosity (see Figure 4.21). While some acetate self-association appears to occur, the <10% decrease in measured D' is much smaller than seen for dihydrogen phosphate.

4.5 Influence of guest-binding on host diffusion

4.5.1 Diffusion titrations with isomerically pure host

Diffusion NMR experiments were performed during titration of H_2PO_4^- into 5 mM solutions of isomerically pure **E-4.2** or **Z-4.2** in $\text{DMSO}-d_6$ with 0.5% added water as for previous studies,^[24a] with results shown in Figure 4.23. The viscosity-corrected measured diffusion coefficients of **E-4.2** and **Z-4.2** (D'_E and D'_Z) in the presence of 0 or 50 mM H_2PO_4^- are also shown in Table 4.5. In the absence of H_2PO_4^- , the extended **E-4.2** isomer diffuses slightly more slowly (7%) than the more compact **Z-4.2** (Table 4.5; entries 1 vs 2).

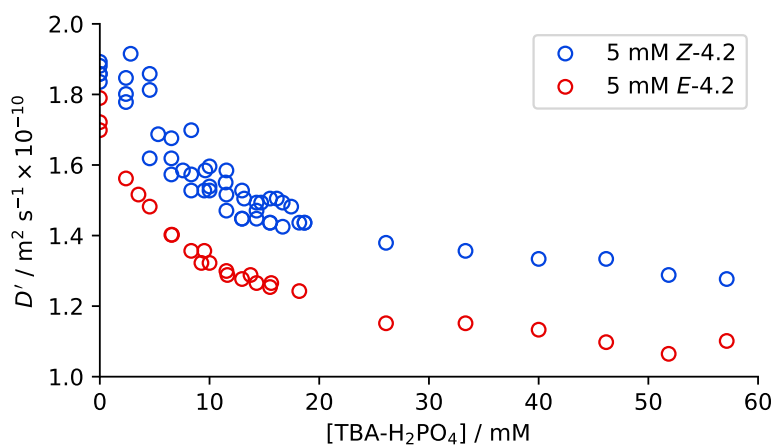


Figure 4.23. Diffusion measurements of pure hosts **E-4.2** or **Z-4.2** under titration with $\text{NBu}_4\text{H}_2\text{PO}_4$, shown on a single axis for ease of comparison. Diffusion coefficients are plotted as D' , the diffusion coefficient corrected for changes in viscosity (see Figure 4.17).

Table 4.5. Changes in diffusion coefficients of chemical species in pure and 1:1 mixed solutions of **E-4.2** and **Z-4.2** in the presence of 50 mM [TBA][H_2PO_4^-].

Entry	$[\text{H}_2\text{PO}_4^-]$ ^[a] / mM	$[\text{E-4.2}]$ ^[a] / mM	$[\text{Z-4.2}]$ ^[a] / mM	$D'_{\text{H}_2\text{PO}_4^-}$ ^[b] / $10^{-10} \text{ m}^2 \text{s}^{-1}$	D'_E ^[c] / $10^{-10} \text{ m}^2 \text{s}^{-1}$	D'_Z ^[c] / $10^{-10} \text{ m}^2 \text{s}^{-1}$	D'_{TBA} ^[c] / $10^{-10} \text{ m}^2 \text{s}^{-1}$
1	-	5	-	-	1.74 ± 0.03	-	-
2	-	-	5	-	-	1.87 ± 0.01	-
3	50	-	-	2.16 ± 0.03	-	-	2.50 ± 0.02
4	50	5	-	1.93 ± 0.04	1.17 ± 0.03	-	2.39 ± 0.01
5	50	-	5	2.01 ± 0.03	-	1.39 ± 0.01	2.37 ± 0.01
6	50	5	5	1.83 ± 0.08	1.12 ± 0.02	1.36 ± 0.01	2.31 ± 0.01
7	50	2.5	2.5	1.97 ± 0.07	1.19 ± 0.01	1.45 ± 0.03	2.44 ± 0.01
8	50	0.5	0.5	2.05 ± 0.02	1.27 ± 0.03	1.57 ± 0.03	2.52 ± 0.02

^[a] $\text{DMSO}-d_6$ with 0.5% added water.

^[b] 202 MHz ^{31}P PGSTE, $\delta = 7 \text{ ms}$, $\Delta = 100 \text{ ms}$, $g = 0\text{--}53.45 \text{ G cm}^{-1}$.

^[c] 500 MHz ^1H PGSTE, $\delta = 4 \text{ ms}$, $\Delta = 50 \text{ ms}$, $g = 0\text{--}53.45 \text{ G cm}^{-1}$.

Given the large difference in size between host **4.2** (MW = 529) and the H_2PO_4^- anion (MW = 97), we might have anticipated a modest decrease in average host diffusion coefficients at guest concentrations where near-complete complexation occurs based on measured binding

constants.* Instead we observe a large decrease in measured D' that continues to decrease at concentrations above those predicted for near-complete complexation (e.g. $[H_2PO_4^-] = 50\text{ mM}$, $[4.2] = 5\text{ mM}$: Table 4.5, entries 4–8; section 9.4). After correcting for $H_2PO_4^-$ -induced viscosity changes (Section 4.4.1) the measured D' of pure *E*-4.2 or *Z*-4.2 in the presence of 50 mM [TBA][H₂PO₄] was found to decrease by respectively 33% (D'_E) and 26% (D'_Z) relative to D' without [TBA][H₂PO₄] (Table 4.5; entries 1 vs 4; 2 vs 5; Figure 4.23 for full H₂PO₄[−]-dependent diffusion data). This suggests greater than 2 or 3-fold increases in effective volumes of the *Z*-4.2 and *E*-4.2 hosts respectively in the presence of 50 mM TBA–H₂PO₄. These substantial decreases in measured D' are too large to be explained by the formation of ditopic [HG₂] complexes^[24a] or even [H(G_n)₂] complexes, where G_n is an oligomeric chain of n hydrogen-bonded H₂PO₄[−] subunits that forms as in the absence of host (Figure 4.27b,c see 9.4 for modelling).

4.5.2 Diffusion titrations with 1:1 mixed host solutions

Diffusion titrations were performed with 1:1 mixed solutions of *E*-4.2:*Z*-4.2 at 1, 5, and 10 mM total concentrations, as shown in Figure 4.24. In all cases the viscosity-corrected diffusion coefficient D' for the host drops sharply on addition of TBA–H₂PO₄. In addition, there appears to be a correlation between host concentration and D' reached with excess H₂PO₄[−] guest: D' is markedly lower at $[4.2] = 10\text{ mM}$ than at $[4.2] = 1\text{ mM}$ for both hosts but particularly for *Z*-4.2 ($D_E = 1.07 \text{ vs } 0.95 \times 10^{-10} \text{ m}^2 \text{ s}^{-1}$; $D_Z = 1.39 \text{ vs } 1.17 \times 10^{-10} \text{ m}^2 \text{ s}^{-1}$).

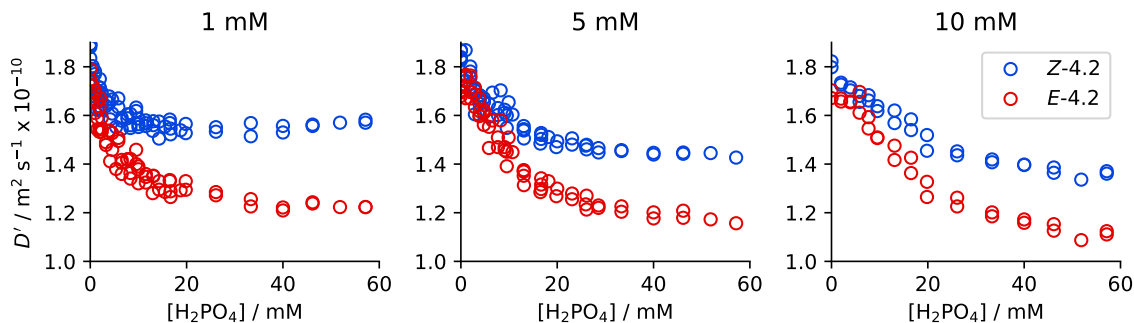


Figure 4.24. Comparison of measured diffusion coefficients of host 4.2 in 1:1 *E*-4.2:*Z*-4.2 mixtures of 1 mM, 5 mM, and 10 mM total concentration (as above). All data corrected for changes in viscosity due to the addition of [TBA][H₂PO₄] (Figure 4.17). Each point represents one diffusion experiment. 500 MHz ¹H, $\Delta = 50\text{ ms}$, $\delta = 4\text{ ms}$, linear ramp of 12 gradients from $g = 0\text{--}53.45\text{ g cm}^{-1}$. See appendix Figure 9.2, Figure 9.3, and Figure 9.4 for larger plots of this data.

4.5.3 Control experiments with tetrabutylammonium acetate

Equivalent experiments using TBA acetate in place of [TBA][H₂PO₄] (Figure 4.25) do not result in similar changes in the measured D' of the host, suggesting that the ability of H₂PO₄[−] to form extended hydrogen-bound chains is critical for the observed changes in measured D' .

*At 5 mM host concentrations used, and with K_1 of 360 and 2100 for *E*-4.2 and *Z*-4.2 respectively, the proportion of unbound host is less than 5% with respectively 5.5 equiv and 2.5 equiv of H₂PO₄[−].

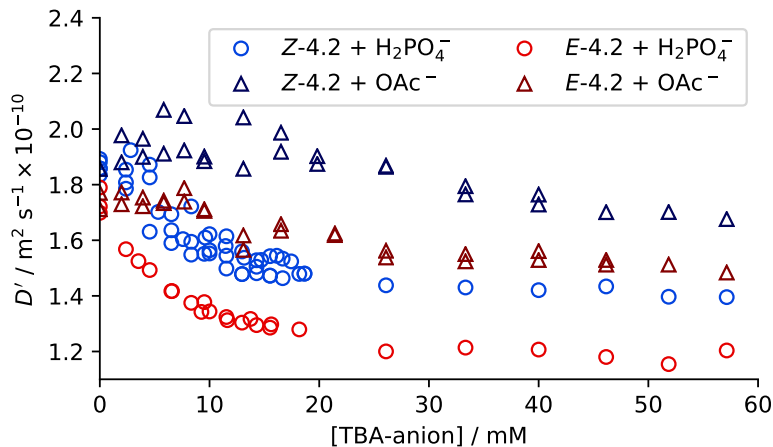


Figure 4.25. Comparison of guest-dependent diffusion for separate 5 mM solutions of pure hosts *E-4.2* or *Z-4.2* in the presence of [TBA][H₂PO₄] or TBA-OAc, presented on a single axis for clarity. Viscosity corrections applied as discussed in Figure 4.17 and Figure 4.21. Each point represents one diffusion experiment. 500 MHz ¹H, $\Delta = 50$ ms, $\delta = 4$ ms, linear ramp of 12 gradients from $g = 0\text{--}53.45\text{ g cm}^{-1}$.

4.5.4 Modelled diffusion coefficients of host during host-guest association

To demonstrate the incompatibility of simple host-guest binding modes with measured host diffusion coefficients, the guest-dependent diffusion coefficients of hosts *E-4.2* and *Z-4.2* binding up to two [H₂PO₄]_n oligomers were modelled using Equation 4.26 and the parameters given in Table 4.6.

Table 4.6. Parameters used for modelling concentration-dependent diffusion coefficients of *E-4.2* and *Z-4.2*.

	$D_0 / \text{m}^2 \text{s}^{-1} \times 10^{-10}$	K_i / M^{-1}	K_1 / M^{-1}	K_2 / M^{-1}
Monomeric DHP	3.39			
5 mM <i>E-4.2</i>	1.74		360	90
5 mM <i>Z-4.2</i>	1.87		2100	70

The results are shown in Figure 4.26. The modelled dependence of D'_E and D'_Z on H₂PO₄⁻ concentration significantly overestimates D' at all concentrations studied, particularly for *E-4.2*, indicating that this model does not accurately reflect the structures formed in solution.

4.5.5 Possible complexes formed in solution between H₂PO₄⁻ and host 4.2

Host *E-4.2* forms larger structures than host *Z-4.2* (Table 4.5; entries 4 vs 5), despite *Z-4.2* binding H₂PO₄⁻ more strongly (Table 4.4). This observation is also supported by changes in the measured diffusion of H₂PO₄⁻, $D'_{\text{H}_2\text{PO}_4}$, (measured by ³¹P NMR), which decreases by 11% or 7% in the presence of 5 mM of **4.23** or *Z-4.2* respectively (Table 4.5; entries 3 vs 4, 5). This indicates that H₂PO₄⁻ is also assembled into larger average structures by *E-4.2* than by *Z-4.2*. Compared to 5 mM solutions of a single isomer, D'_E and D'_Z decrease by just 4% and 2% respectively when an additional 5 mM of the other host is present (Table 4.5; entries 4 vs 6; 5 vs 6), suggesting minimal interactions between the stereoisomers.

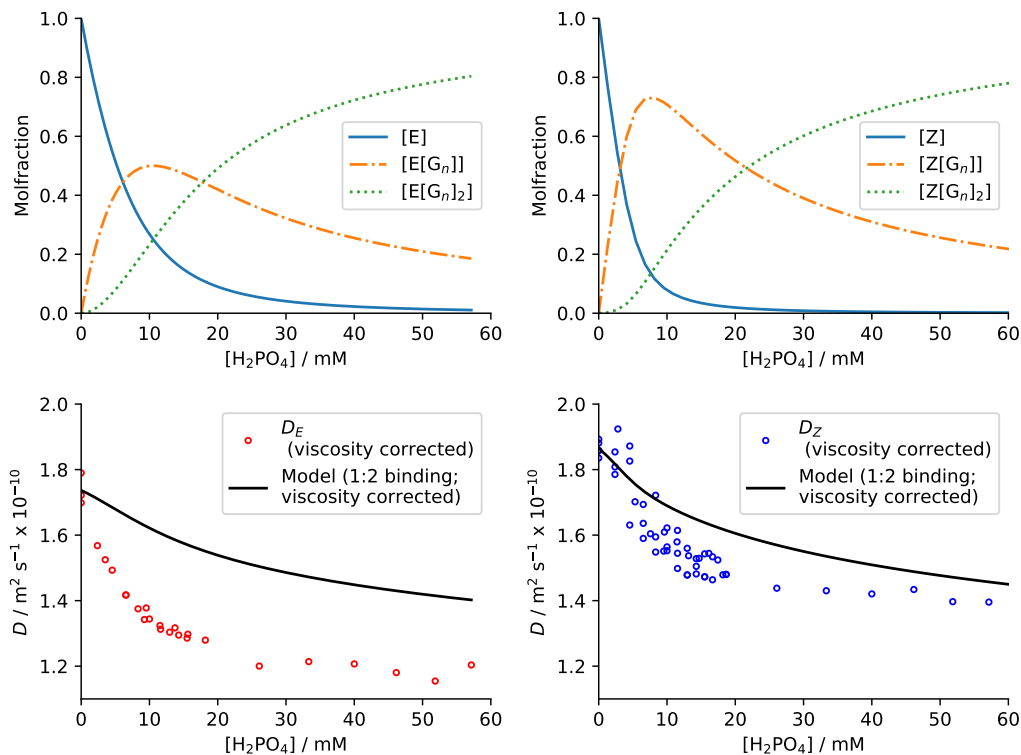


Figure 4.26. Comparison of experimental and modelled H₂PO₄-dependent diffusion coefficients of hosts, using Equation 4.26 and the parameters shown in Table 4.6. Top: speciation of **E-4.2** (left) and **Z-4.2** (right) using a 1:2 host:guest binding model and the association parameters shown in Table 4.6. Bottom: modelled average diffusion coefficients of hosts binding up to 2 H₂PO₄⁻ oligomers (see section 4.4.2, 4.26). This model is clearly insufficient to explain the large decrease in *D* observed on addition of H₂PO₄⁻, particularly for **E-4.2**.

Relative to that of a solution of pure [TBA][H₂PO₄], *D'*_{H₂PO₄} decreases on going from 5 mM of **Z-4.2** ($\Delta D' = -7\%$, Table 4.5, entry 5,) to 5 mM of **E-4.2** ($\Delta D' = -11\%$, entry 4) to 5 mM of each of **Z-4.2** and 5 mM of **E-4.2** ($\Delta D' = -15\%$, entry 6). The measured *D'*_{H₂PO₄} for a solution measured in 2.5 mM **E-4.2** and 2.5 mM **Z-4.2** ($\Delta D' = -9\%$, entry 7) is also the average of those measured for 5 mM solutions of each isomer (entries 4, 5). These results suggest that H₂PO₄⁻ does not experience anything other than a statistical binding by the hosts, with no evidence of cross-linking between different hosts.

Host **4.2** may induce the formation of larger H₂PO₄⁻ oligomers than found in solutions of pure [TBA][H₂PO₄]. If we assume that H₂PO₄⁻ self-association dynamics are unaffected by the addition of **4.2**, the median guest-oligomer present at [H₂PO₄⁻] = 50 mM will incorporate 5 H₂PO₄⁻ units. (Figure 4.20). The near-complete formation of the [H(G_n)₂] complex under these conditions shown in Figure 4.26 would thus result in the incorporation of almost all H₂PO₄⁻ anions present into **4.2**-bound complexes. Increasing the concentration of host would thus reduce the amount of free H₂PO₄⁻ available to each host, with competitive binding resulting in smaller average assemblies and therefore an increase in host *D'*. However, the opposite trend is seen for 1:1 **E-4.2:Z-4.2** mixed solutions of host (Table 4.5; entries 6-8). If H₂PO₄⁻ were bound completely then *D'*_{H₂PO₄} would be comparable to *D'* of the host, but this is also not observed under any conditions measured.

Alternatively, host **4.2** could increase the effective size of polyanionic complexes by increasing ion-pairing to the TBA^+ cation. This would result in a decrease in the measured D'_{TBA} with increasing host concentration. However, only a 5% decrease in D'_{TBA} is observed (Table 4.5, entry 3 vs 4; 3 vs 5). There is also no difference between D'_{TBA} in the presence of *E*-**4.2** or *Z*-**4.2**, despite *E*-**4.2** forming much larger complexes (Table 4.5; entries 4 vs 5). Finally, we consider the formation of extended supramolecular structures involving multiple hosts linking multiple H_2PO_4^- chains (e.g. Figure 4.27d). At a fixed concentration of guest, the formation of structures incorporating multiple hosts may be favoured by increased host concentrations. Titration experiments of H_2PO_4^- into solutions of 1:1 mixtures of *E*-**4.2**:*Z*-**4.2** at 1, 5, and 10 mM total concentrations of host (Figure 4.24) allowed this change in D' to be monitored. A small but observable decrease in D' for both *E*-**4.2** and *Z*-**4.2** was found as the total concentration of the host increases from 1 to 5 to 10 mM (e.g. at 50 mM [TBA][H_2PO_4^-]: Table 4.3, entries 6-8; also Figure 4.24) suggesting that the structures formed do involve multiple hosts.

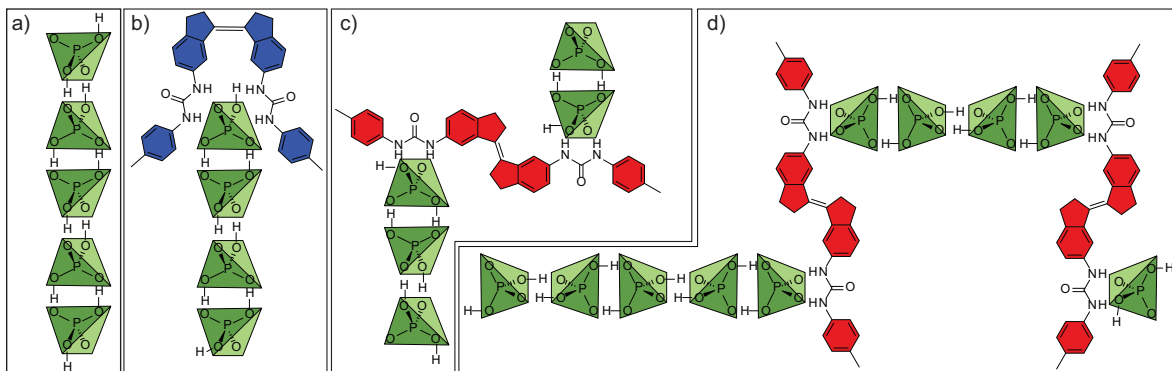


Figure 4.27. Proposed supramolecular assemblies present in solution. (a) Anti-electrostatic dihydrogenphosphate (H_2PO_4^-) oligomers, G_n , form from monomeric phosphates. These oligomers are bound by anion-binding *Z*-**4.2** (b) and *E*-**4.2** (c) bis-urea hosts to form ditopic $[\text{H}(\text{G}_n)]$ or $[\text{H}(\text{G}_n)_2]$ complexes. d) As *E*-**4.2** possesses divergent urea binding sites, larger supramolecular structures can form from H_2PO_4^- chains linked by *E*-**4.2** hosts.

4.5.6 Comparison of estimated and measured diffusion coefficients for host-guest assemblies

From measured diffusion coefficients of free host and oligomeric H_2PO_4^- at 50 mM, I estimate that the measured host D' values are consistent with structures involving 1–2 molecules of **4.2** along with 2–3 chains of oligomeric guest G_n of the same size as forms at 50 mM [TBA][H_2PO_4^-] in the absence of host (Figure 4.27b,c,d; appendix section 9.4 for modelled complex diffusion coefficients). The smaller diffusion coefficients observed for *E*-**4.2** are suggestive of somewhat larger complexes (closer to $\text{H}_2\text{G}(\text{n})_3$), while the smaller *Z*-**4.2**-bound complexes are closer to $\text{H}_1\text{G}(\text{n})_2$ in size. The modelled diffusion coefficients for a number of potential discrete structures present in solution are given in appendix section 9.4. It is important to restate that these estimates are averaged over the entire system and may not be representative of the species actually present in solution. For example, diffusion measurements would be unable to

distinguish complete formation of a small anion-bound complex from incomplete formation of a much large complex.

This analysis does not rely on the accuracy of the isodesmic binding model and fitted parameters: the proposed $[H_{1-2}(G_n)_{2-3}]$ average structure only requires the experimentally measured effective $D'_{H_2PO_4}$. From the modelled size distribution of $H_2PO_4^-$ oligomers at 50 mM (Figure 4.20), this corresponds to complexes incorporating approximately 10 $H_2PO_4^-$ subunits and with average molecular weights of 1.5–2.0 kDa. Together, these results indicate that $H_2PO_4^-$ anions not only form aggregates in polar and hydrogen-bond accepting solvents, but that these structures can associate to form larger assemblies with multiple hosts in solution.

4.6 Time-dependent diffusion with *in situ* irradiation

As **4.2** is a photoswitch, the **E-4.2:Z-4.2** distribution of isomers can be controlled using light. By combining *in situ* irradiation within the NMR spectrometer^[31] with recently developed time-resolved diffusion NMR techniques (chapter 2)^[32] we simultaneously measured changes in concentration and diffusion coefficients of **E-4.2** and **Z-4.2** under 405 nm irradiation.

4.6.1 *In situ* irradiation causes convection

It is well known that NMR diffusion measurements are often disrupted by convection (see Chapter 3), most commonly caused by the presence of temperature gradients within the sample.^[33] Avoiding convection can be challenging under ideal conditions, but here the use of *in situ* irradiation (and inevitable heating) delivered by fibre to the center of the sample can be almost guaranteed to generate temperature gradients during irradiation. This can be seen in the time-dependent diffusion data presented in Figure 4.28. During periods of light irradiation (shaded purple areas), the sample is heated and induced convection leads to sharp increases in measured D .

4.6.2 Monitoring temperatures and suppressing convection

There are many approaches to suppressing convection in diffusion NMR experiments.^[33] We chose the crude but effective method of introducing physical obstructions to the sample to disrupt connective flow. We use glass TLC spotting pipettes broken up into 30–40 mm irregular lengths to pack the sample and restrict flow. These open-ended capillaries were added to the sample around the 1.5 mm quartz optic fibre and flame-sealed methanol capillary used for thermometry (Figure 4.29).

To our pleasant surprise, NMR lineshapes were retained and few difficulties were encountered in shimming after packing our samples with glass and quartz (signal intensity was reduced somewhat by the displacement of liquid from the active volume). The experimental data presented in Figure 4.30 was acquired using a sample similar to that shown in Figure 4.29, with broken glass capillaries added for convection suppression and a flame-sealed methanol capillary for temperature monitoring (see Chapter 2). Using this approach it was

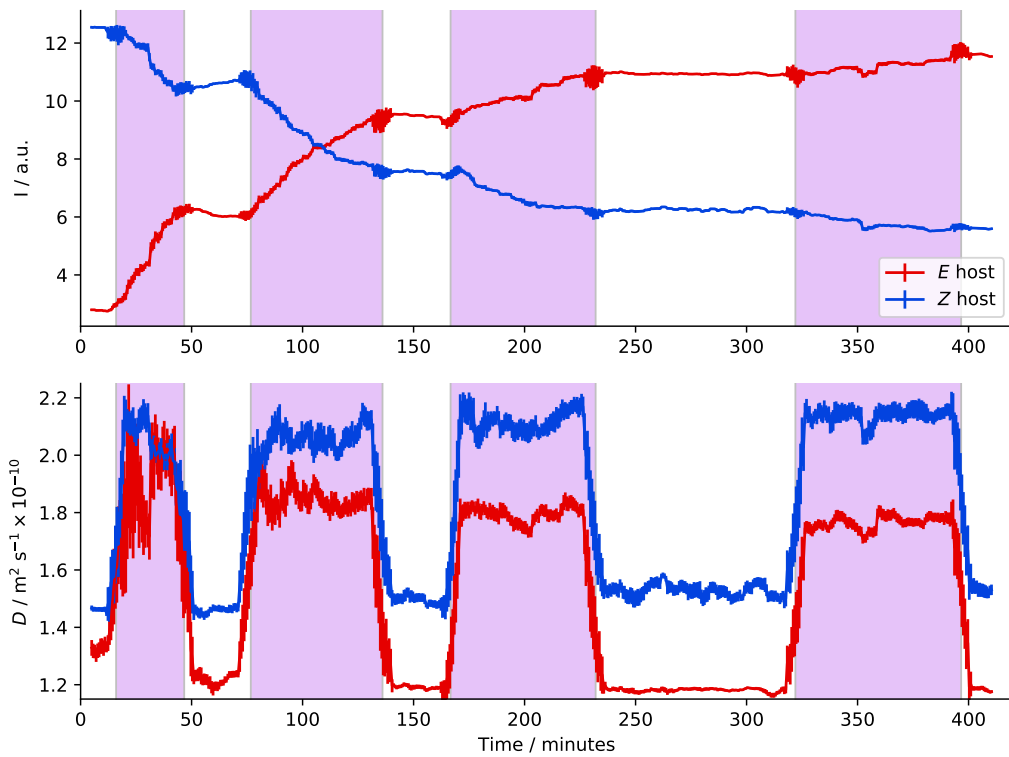


Figure 4.28. Time-resolved diffusion study while photoswitching under *in situ* irradiation (405 nm LED source). 5 mM host (initially 90% Z-4.2) in solution with 50 mM [TBA][H₂PO₄] was irradiated with 405 nm light during the shaded periods of time, while diffusion information was continuously acquired using a long list of random gradients as previously reported.^[32b] Measured diffusion coefficients can be seen to increase sharply under irradiation, but this is convection resulting from temperature gradients caused by uneven sample heating due to light irradiation.

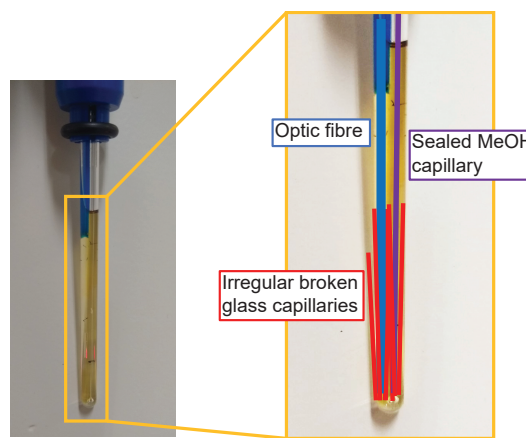


Figure 4.29. NMR sample used for photo-diffusion studies with *in situ* irradiation and temperature measurements. In the expansion the optic fibre (quartz, 1.5 mm diameter), flame-sealed methanol capillary (Sigma-Aldrich, 5 µL capacity glass micropipette), and broken lengths of glass TLC capillaries are highlighted by coloured lines.

possible to suppress the false increase in D caused by light-induced convection previously observed in Figure 4.28.

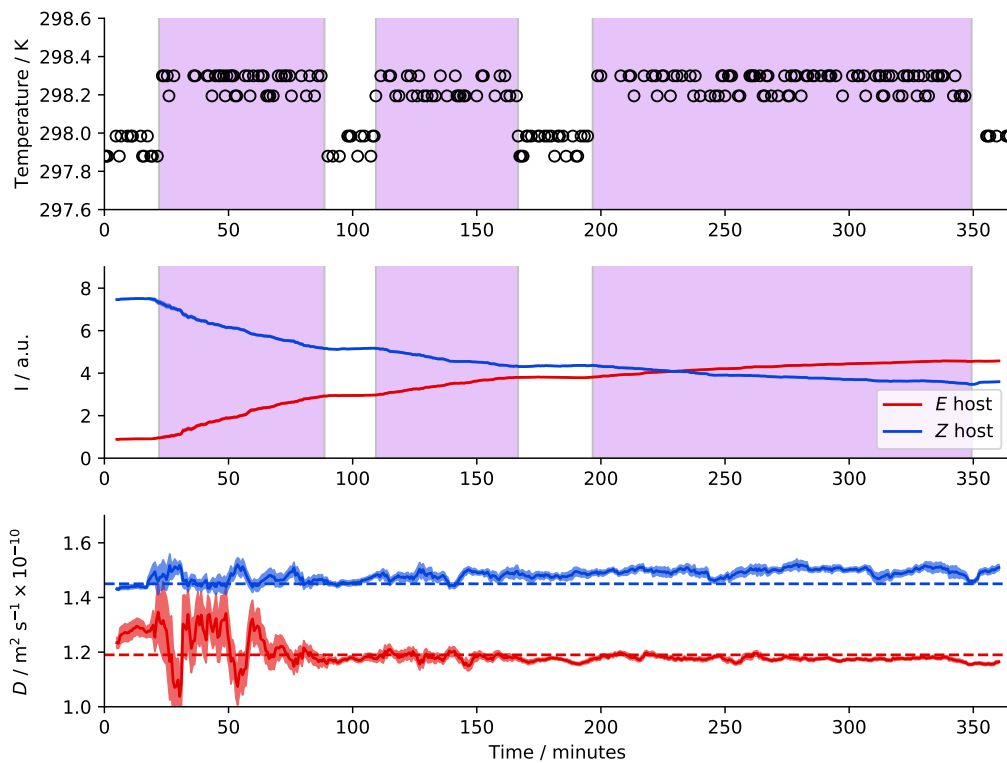


Figure 4.30. Time-resolved diffusion study^[32] while photoswitching under *in situ* irradiation (400 nm LED source), with flame-sealed methanol capillary added for in-situ thermometry and short (30–40 mm) sections of broken glass capillaries added to suppress convection. 5 mM host (initially 90% Z-4.2) in solution with 50 mM TBA-H₂PO₄ was irradiated with 405 nm light during the shaded periods of time, while diffusion information was continuously acquired using a long list of random gradients. Top: temperature measurements taken from the separation of the methanol CH₃ and OH peaks (top) show an increase in sample temperature of approximately 0.35 K while under irradiation.^[32b,34] The apparent quantization of temperature measurements results from the ~0.5 Hz resolution of the NMR spectra. Middle: signal intensity changes of the tolyl peaks of E-4.2 and Z-4.2 during irradiation. Bottom: time-dependent diffusion measurements of the same peaks over time. Measured D for each species taken from measurements of the 1:1 mixture of photoisomers (Table 4.5) are shown as dashed horizontal lines for comparison.

Photoswitching of organic molecules is expected to result in differences in D , but such changes would typically be minor (e.g. the 7% difference between D_E and D_Z in the absence of anion guest (Table 4.5, entries 1 and 2)). Switchable anion binding might give more control over the effective host D , but complexes with small anions (e.g. Cl⁻, OAc⁻, NO₃⁻, HSO₄⁻) might only cause modest changes in host D , as found for control experiments with acetate (8% and 4% decrease respectively in D_E and D_Z at 50 mM TBA-OAc; section 4.5.3). The use of H₂PO₄⁻ oligomers allows greater control over D : switching host 4.2 from Z-4.2 to E-4.2 causes a “molecular gear change” and a 16% decrease in measured D (Table 4.5, entries 4 and 5), suggestive of an approximately 70% increase in average molecular volume. This demonstrates the possibility of achieving substantial control over the diffusion rate of small molecules in bulk solution by coupling photocontrol of guest-binding to the ability of H₂PO₄⁻ to form extended supramolecular structures. Some evidence also suggests that

complexes involving two or more host molecules are selective for the same host isomer (self-sorting). Comparing D_E and D_Z for 5 mM solutions of pure isomers to those for 5 mM of a 1:1 mixture of the isomers, both isomers diffuse faster in the mixed solution (Table 4.5; entries 4, 5, 7). The increase is small (2% for D_E , 4% for D_Z), but a similar trend appears during time-resolved diffusion monitoring of photoswitching hosts (Figure 4.30), where switching **Z-4.2** into **E-4.2** also causes a slight increase in D_Z and decrease in D_E . As **4.2** is a thermally stable ('P-type') photoswitch, these changes in D will persist in the dark.^[4d]

4.7 Conclusions

I sought to use the switchable anion-binding properties of host **4.2** to achieve photocontrol of translational diffusion rates. Diffusion NMR allowed characterization of the thermodynamics of the antielectrostatic self-assembly of the bare dihydrogen phosphate anion in solution, a long-suspected^[16a,b] but previously uncharacterised phenomenon. We obtained a surprisingly high isodesmic association constant of $K_i = (120 \pm 32) \text{ M}^{-1}$ for H_2PO_4^- self-association in DMSO, which corresponds to complexes of a median size of 4 (or 10) H_2PO_4^- subunits at concentrations of 50 mM (or 300 mM). All experiments measuring H_2PO_4^- binding to anion receptors in DMSO therefore also involve competition between host- H_2PO_4^- and anti-electrostatic H_2PO_4^- - H_2PO_4^- interactions, posing problems for measurements under these commonly used conditions (section 4.3.2 for further discussion). This study was conducted exclusively in wet DMSO and it would be reasonable to assume that in less polar solvents such as DMF, acetonitrile, or dichloromethane self-association of H_2PO_4^- may be more significant. Combining the unusual anti-electrostatic oligomerization of H_2PO_4^- with a photo-switchable anion-binding host allowed light to induce a 'gear change' and sharply change the rate of diffusion of a host molecule, equivalent to a 70 % change in effective volume. Can control of diffusion via a spatially selective stimulus (such as light, as demonstrated here) drive directional transport of small molecular species and create concentration gradients? This remains an open question.

4.8 References

- [1] (a) E. R. Kay, D. A. Leigh, F. Zerbetto, *Angew. Chem. Int. Ed.* **2007**, *46*, 72–191; (b) P. Hänggi, F. Marchesoni, *Rev. Mod. Phys.* **2009**, *81*, 387–442; (c) E. Lauga, T. R. Powers, *Rep. Prog. Phys.* **2009**, *72*, 096601; (d) S. Sengupta, M. E. Ibele, A. Sen, *Angew. Chem. Int. Ed.* **2012**, *51*, 8434–8445; (e) R. Kapral, *J. Chem. Phys.* **2013**, *138*, 020901; (f) X. Ma, K. Hahn, S. Sanchez, *J. Am. Chem. Soc.* **2015**, *137*, 4976–4979; (g) S. Sanchez, L. Soler, J. Katuri, *Angew. Chem. Int. Ed.* **2015**, *54*, 1414–1444.
- [2] (a) C. Lozano, B. ten Hagen, H. Löwen, C. Bechinger, *Nat. Commun.* **2016**, *7*, 12828; (b) X. Yao, T. Li, J. Wang, X. Ma, H. Tian, *Adv. Opt. Mater.* **2016**, *4*, 1322–1349; (c) J. Katuri, X. Ma, M. M. Stanton, S. Sánchez, *Acc. Chem. Res.* **2017**, *50*, 2–11; (d) X. Zhao, K. Gentile, F. Mohajerani, A. Sen, *Acc. Chem. Res.* **2018**, *51*, 2373–

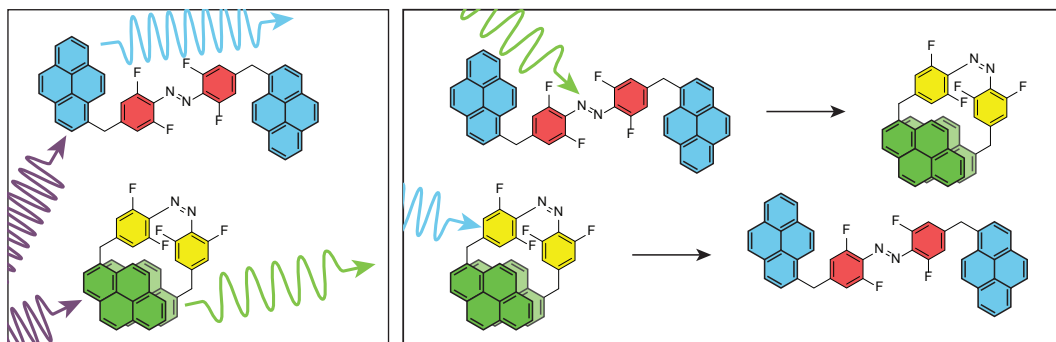
- 2381; (e) M. Fernández-Medina, M. A. Ramos-Docampo, O. Hovorka, V. Salgueiriño, B. Städler, *Adv. Funct. Mater.* **2020**, 1908283.
- [3] (a) J. L. Anderson, D. C. Prieve, *Langmuir* **1991**, *7*, 403–406; (b) R. D. Astumian, *ACS Nano* **2014**, *8*, 11917–11924; (c) J. Agudo-Canalejo, T. Adeleke-Larodo, P. Illien, R. Golestanian, *Acc. Chem. Res.* **2018**, *50*, 2365–2372; (d) C. Weistuch, S. Pressé, *J. Phys. Chem. B* **2018**, *122*, 5286–5290; (e) R. P. Sear, *Phys. Rev. Lett.* **2019**, *122*, 128101.
- [4] (a) S.-S. Sun, J. A. Anspach, A. J. Lees, *Inorg. Chem.* **2002**, *41*, 1862–1869; (b) F. Rakotondradany, M. A. Whitehead, A.-M. Lebuis, H. F. Sleiman, *Chem. Eur. J.* **2003**, *9*, 4771–4780; (c) S. Chen, L.-J. Chen, H.-B. Yang, H. Tian, W. Zhu, *J. Am. Chem. Soc.* **2012**, *134*, 13596–13599; (d) X. Yan, J.-F. Xu, T. R. Cook, F. Huang, Q.-Z. Yang, C.-H. Tung, P. J. Stang, *Proc. Natl. Acad. Sci.* **2014**, *111*, 8717–8722; (e) M. Han, Y. Luo, B. Damaschke, L. Gómez, X. Ribas, A. Jose, P. Peretzki, M. Seibt, G. H. Clever, *Angew. Chem. Int. Ed.* **2016**, *55*, 445–449.
- [5] (a) S. Lee, S. Oh, J. Lee, Y. Malpani, Y.-S. Jung, B. Kang, J. Y. Lee, K. Ozasa, T. Isoshima, S. Y. Lee, M. Hara, D. Hashizume, J.-M. Kim, *Langmuir* **2013**, *29*, 5869–5877; (b) J.-F. Xu, Y.-Z. Chen, D. Wu, L.-Z. Wu, C.-H. Tung, Q.-Z. Yang, *Angew. Chem. Int. Ed.* **2013**, *52*, 9738–9742; (c) J. T. van Herpt, J. Areephong, M. C. A. Stuart, W. R. Browne, B. L. Feringa, *Chem. Eur. J.* **2014**, *20*, 1737–1742; (d) A. J. McConnell, C. S. Wood, P. P. Neelakandan, J. R. Nitschke, *Chem. Rev.* **2015**, *115*, 7729–7793; (e) L. Yang, X. Tan, Z. Wang, X. Zhang, *Chem. Rev.* **2015**, *115*, 7196–7239.
- [6] (a) P. Stilbs, *Prog. Nucl. Magn. Reson. Spectrosc.* **1987**, *19*, 1–45; (b) W. S. Price, *Concepts Magn. Reson.* **1997**, *9*, 299–336; (c) W. S. Price, *Concepts Magn. Reson.* **1998**, *10*, 197–237; (d) C. S. Johnson, *Prog. Nucl. Magn. Reson. Spectrosc.* **1999**, *34*, 203–256; (e) P. T. Callaghan, *Translational Dynamics and Magnetic Resonance: Principles of Pulsed Gradient Spin Echo NMR*, Oxford University Press, **2011**.
- [7] (a) Y. Cohen, L. Avram, L. Frish, *Angew. Chem. Int. Ed.* **2005**, *44*, 520–554; (b) J. M. Zayed, F. Biedermann, U. Rauwald, O. A. Scherman, *Polym. Chem.* **2010**, *1*, 1434–1436; (c) S.-L. Li, T. Xiao, B. Hu, Y. Zhang, F. Zhao, Y. Ji, Y. Yu, C. Lin, L. Wang, *Chem. Commun.* **2011**, *47*, 10755–10757; (d) Y. Liu, Z. Wang, X. Zhang, *Chem. Soc. Rev.* **2012**, *41*, 5922–5932; (e) L. Avram, Y. Cohen, *Chem. Soc. Rev.* **2015**, *44*, 586–602; (f) L. Sian, A. Guerriero, M. Peruzzini, C. Zuccaccia, L. Gonsalvi, A. Macchioni, *Organometallics* **2019**, DOI 10.1021/acs.organomet.9b00703.
- [8] (a) P. A. Gale, E. N. W. Howe, X. Wu, *Chem* **2016**, *1*, 351–422; (b) L. Chen, S. N. Berry, X. Wu, E. N. W. Howe, P. A. Gale, *Chem* **2020**, *6*, 61–141.
- [9] W. Zhao, J. Tropp, B. Qiao, M. Pink, J. D. Azoulay, A. H. Flood, *J. Am. Chem. Soc.* **2020**, *142*, 2579–2591.

- [10] (a) F. Weinhold, R. A. Klein, *Angew. Chem. Int. Ed.* **2014**, *53*, 11214–11217; (b) B. Wu, C. Huo, S. Li, Y. Zhao, X.-J. Yang, *Z. Anorg. Allg. Chem.* **2015**, *641*, 1786–1791; (c) I. Mata, E. Molins, I. Alkorta, E. Espinosa, *J. Phys. Chem. A* **2015**, *119*, 183–194; (d) Y. Liu, A. Sengupta, K. Raghavachari, A. H. Flood, *Chem* **2017**, *3*, 411–427; (e) Q. He, P. Tu, J. L. Sessler, *Chem* **2018**, *4*, 46–93; (f) C. Wang, Y. Fu, L. Zhang, D. Danovich, S. Shaik, Y. Mo, *J. Comput. Chem.* **2018**, *39*, 481–487; (g) F. Weinhold, *Inorg. Chem.* **2018**, *57*, 2035–2044.
- [11] N. G. White, *CrystEngComm* **2019**, *21*, 4855–4858.
- [12] N. Bregović, N. Cindro, L. Frkanec, K. Užarević, V. Tomišić, *Chem. Eur. J.* **2014**, *20*, 15863–15871.
- [13] (a) E. M. Fatila, E. B. Twum, A. Sengupta, M. Pink, J. A. Karty, K. Raghavachari, A. H. Flood, *Angew. Chem. Int. Ed.* **2016**, *55*, 14057–14062; (b) E. M. Fatila, E. B. Twum, J. A. Karty, A. H. Flood, *Chem. Eur. J.* **2017**, *23*, 10652–10662; (c) D. Barišić, V. Tomišić, N. Bregović, *Anal. Chim. Acta* **2019**, *1046*, 77–92.
- [14] (a) Y. Kubo, S. Ishihara, M. Tsukahara, S. Tokita, *J. Chem. Soc. Perkin Trans. 2* **2002**, 1455–1460; (b) V. Amendola, M. Boiocchi, D. Esteban-Gómez, L. Fabbrizzi, E. Monzani, *Org. Biomol. Chem.* **2005**, *3*, 2632–2639; (c) G. Baggi, M. Boiocchi, L. Fabbrizzi, L. Mosca, *Chem. Eur. J.* **2011**, *17*, 9423–9439; (d) D. Mungalpara, H. Kelm, A. Valkonen, K. Rissanen, S. Keller, S. Kubik, *Org. Biomol. Chem.* **2017**, *15*, 102–113; (e) D. M. Gillen, C. S. Hawes, T. Gunnlaugsson, *J. Org. Chem.* **2018**, *83*, 10398–10408; (f) W. Zhao, B. Qiao, J. Tropp, M. Pink, J. D. Azoulay, A. H. Flood, *J. Am. Chem. Soc.* **2019**, *141*, 4980–4989.
- [15] (a) D. Mungalpara, A. Valkonen, K. Rissanen, S. Kubik, *Chem. Sci.* **2017**, *8*, 6005–6013; (b) E. M. Fatila, M. Pink, E. B. Twum, J. A. Karty, A. H. Flood, *Chem. Sci.* **2018**, *9*, 2863–2872.
- [16] (a) R. H. Wood, R. F. Platford, *J. Solut. Chem.* **1975**, *4*, 977–982; (b) F. Rull, A. Del Valle, F. Sobron, S. Veintemillas, *J. Raman Spectrosc.* **1989**, *20*, 625–631; (c) J. M. Shaver, K. A. Christensen, J. A. Pezzuti, M. D. Morris, *Appl. Spectrosc.* **1998**, *52*, 259–264; (d) J. S. McNally, X. P. Wang, C. Hoffmann, A. D. Wilson, *Chem. Commun.* **2017**, *53*, 10934–10937.
- [17] (a) S. J. Wezenberg, B. L. Feringa, *Org. Lett.* **2017**, *19*, 324–327; (b) J. de Jong, B. L. Feringa, S. J. Wezenberg, *ChemPhysChem* **2019**, *20*, 3306–3310.
- [18] (a) M.-M. Russew, S. Hecht, *Adv. Mater.* **2010**, *22*, 3348–3360; (b) C. Brieke, F. Rohrbach, A. Gottschalk, G. Mayer, A. Heckel, *Angew. Chem. Int. Ed.* **2012**, *51*, 8446–8476; (c) J. Zhang, Q. Zou, H. Tian, *Adv. Mater.* **2013**, *25*, 378–399; (d) R. Göstl, A. Senf, S. Hecht, *Chem. Soc. Rev.* **2014**, *43*, 1982–1996; (e) S. Erbas-Cakmak, D. A. Leigh, C. T. McTernan, A. L. Nussbaumer, *Chem. Rev.* **2015**, *115*, 10081–10206; (f) M. P. O'Hagan, S. Haldar, M. Duchi, T. A. A. Oliver, A. J. Mulholland, J. C. Morales, M. C. Galan, *Angew. Chem. Int. Ed.* **2019**, *58*, 4334–4338.
- [19] S. Luňák, P. Horáková, A. Lyčka, *Dyes and Pigments* **2010**, *85*, 171–176.

- [20] D. Roke, M. Sen, W. Danowski, S. J. Wezenberg, B. L. Feringa, *J. Am. Chem. Soc.* **2019**, *141*, 7622–7627.
- [21] H. J. Lee, J. W. Lim, J. Yu, J. N. Kim, *Tetrahedron Lett.* **2014**, *55*, 1183–1187.
- [22] J. P. Wolfe, J. Åhman, J. P. Sadighi, R. A. Singer, S. L. Buchwald, *Tetrahedron Lett.* **1997**, *38*, 6367–6370.
- [23] S. Bhagwanth, G. M. Adjabeng, K. R. Hornberger, *Tetrahedron Lett.* **2009**, *50*, 1582–1585.
- [24] (a) S. J. Wezenberg, B. L. Feringa, *Org. Lett.* **2017**, *19*, 324–327; (b) J. de Jong, B. L. Feringa, S. J. Wezenberg, *ChemPhysChem* **2019**, *20*, 3306–3310.
- [25] P. Thordarson, *Chem. Soc. Rev.* **2011**, *40*, 1305–1323.
- [26] J. Cho, P. Verwilst, M. Kang, J.-L. Pan, A. Sharma, C. S. Hong, J. S. Kim, S. Kim, *Chem. Commun.* **2020**, *56*, 1038–1041.
- [27] W. S. Price, F. Tsuchiya, Y. Arata, *J. Am. Chem. Soc.* **1999**, *121*, 11503–11512.
- [28] R. B. Martin, *Chem. Rev.* **1996**, *96*, 3043–3064.
- [29] (a) J. G. Kirkwood, *J. Polym. Sci.* **1954**, *12*, 1–14; (b) M. H. Cohen, D. Turnbull, *J. Chem. Phys.* **1959**, *31*, 1164–1169; (c) J. G. de la Torre, V. A. Bloomfield, *Q. Rev. Biophys.* **1981**, *14*, 81–139; (d) J. G. D. L. Torre, V. A. Bloomfield, *Biopolymers* **1977**, *16*, 1747–1763.
- [30] L. Lewin, *Polylogarithms and Associated Functions*, North Holland, New York, **1981**, xvii, 359 p.
- [31] C. Feldmeier, H. Bartling, E. Riedle, R. Gschwind, *J. Magn. Reson.* **2013**, *232*, 39–44.
- [32] (a) M. Urbańczyk, D. Bernin, A. Czuroń, K. Kazimierczuk, *Analyst* **2016**, *141*, 1745–1752; (b) T. S. C. MacDonald, W. S. Price, J. E. Beves, *ChemPhysChem* **2019**, *20*, 926–930.
- [33] (a) I. Swan, M. Reid, P. W. A. Howe, M. A. Connell, M. Nilsson, M. A. Moore, G. A. Morris, *J. Magn. Reson.* **2015**, *252*, 120–129; (b) T. M. Barbosa, R. Rittner, C. F. Tormena, G. A. Morris, M. Nilsson, *RSC Adv.* **2016**, *6*, 95173–95176; (c) N. Hedin, T. Y. Yu, I. Furó, *Langmuir* **2000**, *16*, 7548–7550; (d) T. M. Barbosa, R. Rittner, C. F. Tormena, G. A. Morris, M. Nilsson, *RSC Adv.* **2016**, *6*, 95173–95176.
- [34] C. Ammann, P. Meier, A. Merbach, *J. Magn. Reson.* **1982**, *46*, 319–321.

Chapter 5

Photoswitch-fluorescence feedback: towards a photonic molecular amplifier



Summary:

An all-photonic chemical system is proposed that is capable of amplifying small optical inputs into large changes in internal composition, based on a feedback interaction between switchable fluorescence and visible-light photoswitching. This system would demonstrate bifurcating reaction kinetics under irradiation and reach one of two stable photostationary states dependent on the initial composition of the system. This behaviour would allow the system to act as a chemical realisation of the flip-flop circuit, the fundamental element in sequential logic and binary memory storage. While experimental attempts to realise this system were unsuccessful, I use detailed numerical modelling to demonstrate the feasibility of the proposed behaviour based on known molecular phenomena and comment on some of the conditions required to realise this system.

5.1 Introduction

Here I propose an all-photonic molecular amplifier fuelled by light that would be able to amplify small differences in initial concentration into much larger concentration differences, and report the outcome of this amplification through the emission of light. This may be achieved by combining switchable control over emission^[1] and visible light photoswitches^[2] to create a photoswitchable compound that is emissive at *different wavelengths* as either photoisomer, and where the emitted light can be selectively re-absorbed to drive photochromism.

5.1.1 Switchable emission

The feedback system proposed here involves coupling switchable emission to photochromism to create a feedback loop where photoisomerisation results in a change of emissive properties, and emission results in photoisomerisation. This requires a fluorophore that responds to an external stimulus by changing emission energies. There are many approaches to solving this general problem, and for the sake of providing a ‘real’ example I suggest pyrene (Figure 5.1, top). Under UV irradiation dilute pyrene emits blue fluorescence at around 400 nm, but at high concentrations in solution this emission is red-shifted towards 500 nm. The mechanism behind this change is the formation of excimer complexes, where two pyrene molecules aggregate to form a dimer with different emission properties to the free monomer.^[3,4] Pyrene can also be used for intramolecular excimer emission when a molecule contains two pyrene functionalities held close together in space. This property has been applied to chemical sen-

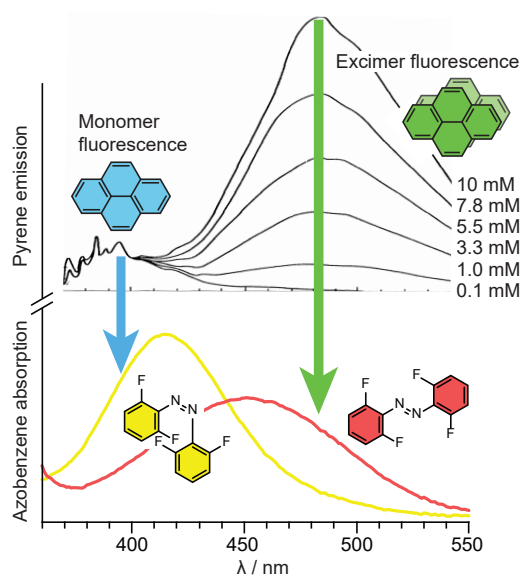


Figure 5.1. Example spectra for the approach towards a fluorescence-photochromism molecular amplifier shown in Figure 5.2. Absorption spectra for tetrafluoro azobenzene^[2b,f] **1.5** were experimentally obtained in acetonitrile, and emission spectra for pyrene are from the literature.^[3] The goal would be to combine these two phenomena by decorating an azobenzene with two pyrene functionalities, such that the *Z* azobenzene (shown here in yellow) could hold the two pyrenes together and force excimer emission (green) while the *E* azobenzene (red) would hold the pyrenes apart and force monomer emission (blue). The monomer and excimer emission spectra of pyrene would then selectively overlap with the absorption spectra of the *Z* and *E* azobenzenes, respectively, and drive feedback.

sors that report a conformational change as a change in luminescence by bringing two pyrene functionalities close together and switching from monomer to excimer emission.^[5]

5.1.2 Visible light photoswitching

In addition to a switchable fluorophore, the feedback system requires a molecular switch that is responsive to the light emitted by the fluorophore. Here I propose the use of *ortho*-tetrafluoroazobenzene,^[2b,f] a visible-light photoswitch with absorption bands that selectively overlap the monomer and excimer emission bands of pyrene (Figure 5.1, bottom). Other photochromic molecules such as diazocines^[2a,6] may also be suitable, with the primary requirement that the absorption bands for the two photoisomers be as selectively matched as possible to the two emission bands of the fluorophore.

The proposed operation of this model *ortho*-tetrafluoroazobenzene-pyrene feedback system under UV irradiation is shown schematically in Figure 5.2. Here, the *E* isomer is labelled ***E*** and the *Z*-isomer is labelled ***Z***. In this example, photoisomerisation from ***E*** to ***Z*** would bring the two pyrene subunits together in space, positioning them to favour excimer emission over monomer emission. This would result in photoisomer ***E*** emitting blue light and *isomerising* on absorption of green light, while isomer ***Z*** emits green light and isomerises on absorption of blue light. Considering light as a reagent, each isomer is thus effectively autocatalytic at the expense of the other isomer (***E*** uses light to produce more ***E*** at the expense of ***Z***).

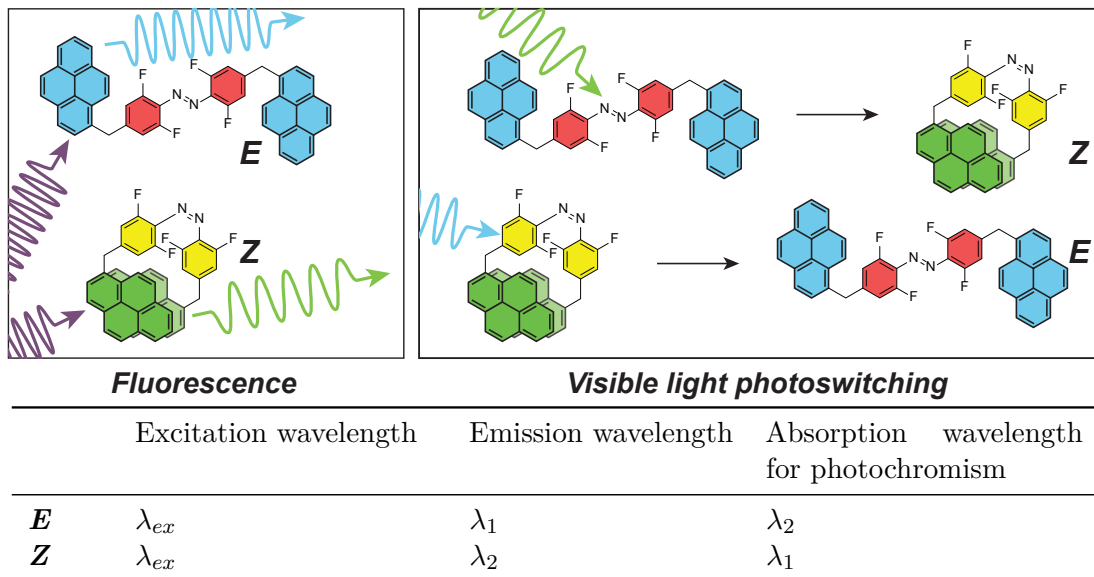


Figure 5.2. General requirements of the molecular amplifier proposal. The compound can exist as one of two photoisomers, here labelled ***E*** and ***Z***. Each isomer is fluorescent in response to UV light with different emission spectra λ_1 and λ_2 . Further, each isomer is a visible light photoswitch that isomerises in response to light of the wavelength emitted by the *other* isomer.

This example ***E-Z*** system is one proposal of how to build an all-photonic feedback system, but it is far from the only one. Alternative approaches might involve photocontrolled self-assembly of fluorescent micelles or pH-sensitive fluorophores coupled to photoacids or

photobases *via* protonation/deprotonation. While these approaches may well be more practical to realise than the all-optical system proposed here, an all-optical two-state (**A**-**B**) feedback system involving only two chemical species is easier to understand and to model and will be the only feedback system considered further in this chapter.

5.2 Modelling the feedback system mathematically

In this section I discuss the behaviour of an all-optical feedback system involve a theoretical compound that can exist as one of two photoisomers, **A** and **B**. In modelling the feedback system proposed here, I make a number of key assumptions throughout:

1. No thermal isomerisation occurs between the isomers. This could be achieved through the use of known thermally bistable photoswitches.^[2b,6a] Alternatively, the model could be adapted relatively easily to include a thermal reversion term.
2. No interactions occur between molecules in solution other than through transmitted and absorbed light. No intermolecular aggregates or associated supramolecular structures are present at any time, and intermolecular energy transfer (e.g. FRET) does not occur except by emission and re-absorption of light. Experimentally, this could be achieved by reducing concentrations (and, if necessary, increasing optical pathlengths to compensate).
3. The electronic systems responsible for photochromism and fluorescence are completely insulated from each other: the fluorescent system excited state can only relax non-radiatively or through fluorescence, and the photochromic excited state can only relax non-radiatively or through photochromism. Achieving this experimentally would likely be the major challenge encountered in realising this proposal.
4. The photoisomerisation quantum yield of the switch is wavelength-independent, ϕ^{iso} . This could also be modelled as a wavelength-dependent quantity for little added complexity, but here I take a minimal approach.

Throughout this section variable quantities that are vectors are denoted in bold and scalars by regular text. For example, the molar absorption *spectrum* of a species would be written $\boldsymbol{\varepsilon}$ while the molar absorbance at a *single wavelength* would be written ε .

5.2.1 Modelling photostationary states

Consider a well-mixed optically dense photochromic **A**-**B** system. We then define molefractions of the two photoisomers x_A and x_B as:

$$x_A = \frac{[\mathbf{A}]}{[\mathbf{A}] + [\mathbf{B}]}$$

$$x_A + x_B = 1$$

If this system is exposed to a light source with spectrum $\mathbf{I}(\lambda)$, the rate of change of composition upon irradiation will follow

$$\frac{d}{dt}x_A = -\frac{\mathbf{I}}{c_0} \cdot \left[\frac{x_A \varepsilon_A \phi_{A \rightarrow B}^{iso} - (1-x_A) \varepsilon_B \phi_{B \rightarrow A}^{iso}}{x_A \varepsilon_A + (1-x_A) \varepsilon_B} \right] \quad (5.1)$$

where x_A and x_B are the mole fractions of **A** and **B**, c_0 is the total concentration, $\varepsilon_A(\lambda)$ and $\varepsilon_B(\lambda)$ the respective molar absorption spectra, and ϕ_A^{iso} and ϕ_B^{iso} are the quantum yields for photoisomerisation. A photostationary state (PSS) occurs where the rate of change of composition as given in Equation 5.1 is equal to zero. For irradiation at a single wavelength (i.e. a monochromatic light source), this can be simplified to:

$$x_A^{PSS} = \frac{\varepsilon_B \phi_{B \rightarrow A}^{iso}}{\varepsilon_A \phi_{A \rightarrow B}^{iso} + \varepsilon_B \phi_{B \rightarrow A}^{iso}} \quad (5.2)$$

With well-characterised or simulated absorption spectra and photoisomerisation quantum yields for species **A** and **B**, Equation 5.1 can be used to model the time-dependent dynamics of a system under irradiation and Equation 5.2 can be used to calculate the stable photostationary state reached upon irradiation at arbitrary wavelength λ_{ex} .

This behaviour is illustrated in Figure 5.3 for a model photoswitch capable of isomerising between two forms, **A** and **B**; i.e. $\text{A} \xrightleftharpoons{h\nu} \text{B}$. The compound is assumed to be a P-type photoswitch with negligible thermal reversion over the timescale of the experiment. The two

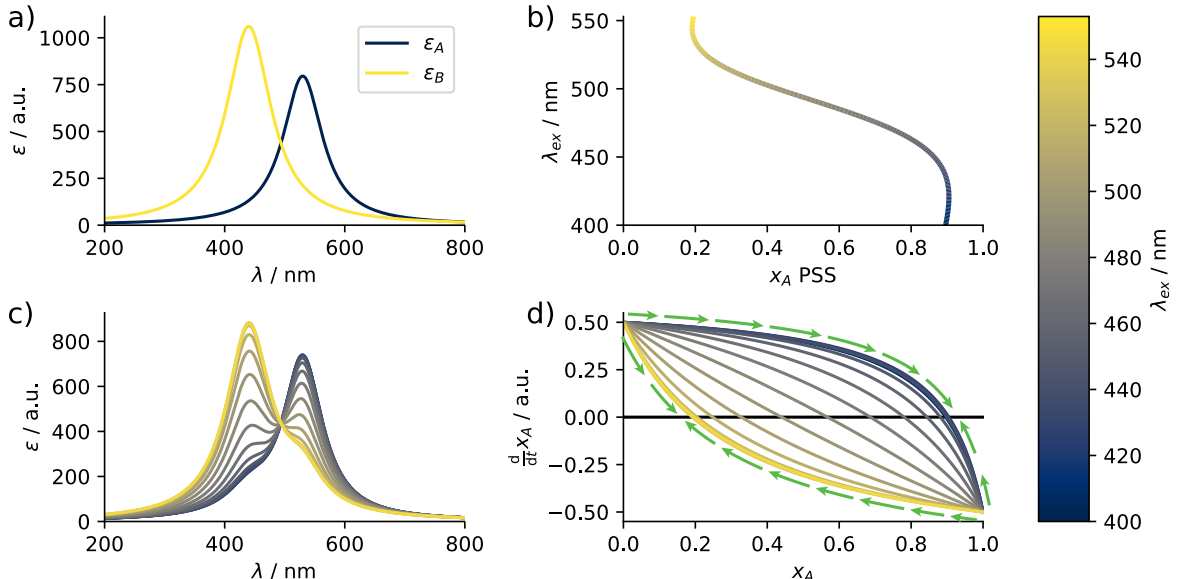


Figure 5.3. Photostationary states under irradiation. A simulated photoswitch can exist in photoisomers **A** or **B**, with absorption spectra shown in a) and photoisomerisation quantum yields $\phi^{iso} = 0.5$ for both isomers. Upon irradiation with visible light at wavelength λ_{ex} , the composition of the photoswitch will change until a steady-state photostationary state (PSS) is reached. The simulated composition x_A of this PSS as a function of λ_{ex} is shown in b), and corresponding absorption spectra are shown in c). d) The photostationary state occurs when $\frac{d}{dt}x_A = 0$. By plotting $\frac{d}{dt}x_A$ as a function of x_A for a range of wavelengths over 400–550 nm, it can be seen that there is a *unique* photostationary state for each irradiation wavelength which is approached (green arrows) regardless of the initial composition.

isomers have different absorption spectra ε : compound **A** absorbs light at longer wavelengths (500–600 nm), and compound **B** absorbs light at shorter wavelengths (400–500 nm). The modelled absorption spectra for both isomers are shown in Figure 5.3a.

On irradiation with a monochromatic light source at wavelength λ_{ex} , a photostationary state is eventually reached with a composition as described by Equation 5.2. The composition of this PSS is a function of λ_{ex} as shown in Figure 5.3b. For the parameters used in this simulation, the most selective PSSs are reached at $\lambda_{ex} = 421$ nm (91% **A**) and $\lambda_{ex} = 545$ nm (81% **B**). Simulated UV-vis spectra for these photostationary states are shown in Figure 5.3c. A less familiar way of representing this same information that will be used repeatedly later in this chapter is to plot the instantaneous *rate of change of composition*, $\frac{d}{dt}x_A$, against compositions x_A as shown in Figure 5.3d. This shows that for any irradiation wavelength λ_{ex} , there is a single stable PSS where $\frac{d}{dt}x_A = 0$ (i.e. the horizontal axis shown). This PSS is approached over time (green arrows) regardless of the initial composition of the system.

5.2.2 Modelling the feedback system

Consider a solution containing compounds **A** and **B** with total concentration c_0 , such that $[\mathbf{A}] + [\mathbf{B}] = c_0$. Each species **A** or **B** has an electronic absorption spectrum $\varepsilon(\lambda)$ made up from two entirely separate electronic systems, one that is fluorescent with absorption spectrum $\varepsilon^F(\lambda)$ and one that can lead to photoisomerisation with absorption spectrum $\varepsilon^{iso}(\lambda)$. The total absorption spectrum, $\varepsilon(\lambda)$, is the sum of these two constituent spectra. For example, the absorption spectrum of isomer **A** is:

$$\varepsilon_A = \varepsilon_A^F + \varepsilon_A^{iso}$$

To simplify this problem mathematically, we will model the system in 1D and with emission \mathbf{I}_{em} occurring from a single point. Consider an infinitesimally thin volume of solution with length r which contains a homogeneous (continuously mixed) solution of compounds **A** and **B**, as shown in Figure 5.4.

A collimated beam of light with spectrum \mathbf{I}_{ex} (measured in $\text{mol} \cdot \text{s}^{-1}$ of photons) is shone across the base of the volume. It encounters a mixture of compounds **A** and **B**, with respective molar absorption coefficients ε_A^F and ε_B^F and fluorescence quantum yield spectra $\phi_A^F(\lambda)$ and $\phi_B^F(\lambda)$. If we assume an optically dense solution (i.e. that all light entering the system is absorbed), the rate of light absorption k_i by isomer i (either **A** or **B**) measured in mol s^{-1} of photons will be:

$$k_i = I_{ex} \cdot \left[\frac{x_i \varepsilon_i^F}{x_A \varepsilon_A^F + x_B \varepsilon_B^F} \right] \quad (5.3)$$

where \cdot is the vector dot product.

The light from \mathbf{I}_{ex} will be absorbed by each isomer at the rate given in Equation 5.3 and re-emitted according to fluorescence spectra normalised for quantum yield ϕ^F . The emission intensities from **A** and **B** respectively will thus be defined as $k_i \phi_i^F$, e.g.:

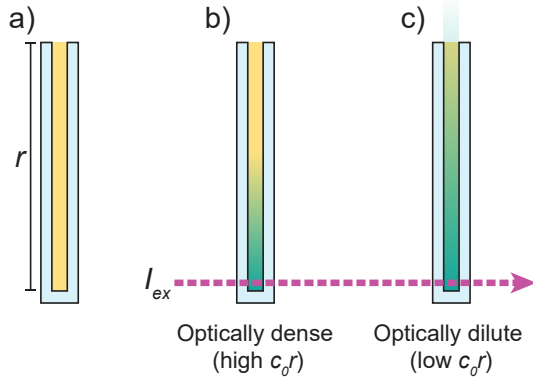


Figure 5.4. Geometry of the modelled system. a) In this minimal approach, the solution is contained within an infinitesimally thin volume of length r and is surrounded by a material that is transmissive for UV light (I_{ex}) and reflective at all other wavelengths. b,c) When the bottom of the volume is irradiated with UV light I_{ex} , fluorescence results in the emission of light with spectrum \mathbf{I}_{em} . This light must travel through the column of solution (length r) if it is to escape the system. If the system is optically dense (b) little to no light will escape, while if it is optically dilute (c) a useful proportion of \mathbf{I}_{em} may be transmitted from the system.

$$\mathbf{I}_{em,A}(\lambda) = \left(I_{ex} \cdot \frac{x_A \epsilon_A^F}{x_A \epsilon_A^F + x_B \epsilon_B^F} \right) \phi_A^F \quad (5.4)$$

$$\mathbf{I}_{em,B}(\lambda) = \left(I_{ex} \cdot \frac{x_B \epsilon_B^F}{x_A \epsilon_A^F + x_B \epsilon_B^F} \right) \phi_B^F \quad (5.5)$$

combining to give a total concentration-weighted emission intensity of

$$\mathbf{I}_{em} = \left(\mathbf{I}_{ex} \cdot \frac{x_A \epsilon_A^F}{x_A \epsilon_A^F + (1-x_A) \epsilon_B^F} \right) \phi_A^F + \left(\mathbf{I}_{ex} \cdot \frac{(1-x_A) \epsilon_B^F}{x_A \epsilon_A^F + (1-x_A) \epsilon_B^F} \right) \phi_B^F \quad (5.6)$$

Assume some perfectly visible light-reflective coating around the volume of solution, such that light can only escape at the opposite end to the source of \mathbf{I}_{em} . This internally emitted fluorescence is then transmitted through the length of the volume and has a probability to be re-absorbed and drive photoisomerisation. The absorption spectra of the photochromic systems are $\epsilon_A^{iso}(\lambda)$ and $\epsilon_B^{iso}(\lambda)$, and we assume that there is no overlap between these absorption spectra and incident light I_{ex} . Some of the emitted light will be transmitted through the system and will escape without re-absorption, with wavelength-dependent transmission spectrum $T(\lambda)$:

$$\mathbf{T}(\lambda) = 10^{-A} = 10^{-rc_0(x_A \epsilon_A + x_B \epsilon_B)} \quad (5.7)$$

but the rest will be re-absorbed and may cause photoisomerisation. If the total rate of photons absorbed by species **A** and **B** is $\mathbf{I}_{em}(1 - \mathbf{T})$ (with \mathbf{T} defined as in Equation 5.7), the rate k_i of photons absorbed per second ($\text{mol} \cdot \text{s}^{-1}$) across all wavelengths by isomer i (either **A** or **B**) will be defined by their relative concentrations and absorption spectra, e.g.:

$$k_i = \mathbf{I}_{em} \cdot \left[\left(\frac{x_i \epsilon_i^{iso}}{x_A \epsilon_A^{iso} + x_B \epsilon_B^{iso}} \right) (1 - \mathbf{T}) \right] \quad (5.8)$$

The rate of concentration change of each isomer will result from losses due to photoisomerisation and gains due to the photoisomerisation of the other photoisomer. If we define quantum yields for photoisomerisation for compounds **A** and **B** as $\phi_{A \rightarrow B}^{iso}$ and $\phi_{B \rightarrow A}^{iso}$ respectively, we can then express rates of concentration change in terms of absorbed photon fluxes and photoisomerisation quantum yields for each isomer:

$$-\frac{d}{dt}x_A = \frac{d}{dt}x_B = k_A \phi_{A \rightarrow B}^{iso} - k_B \phi_{B \rightarrow A}^{iso} \quad (5.9)$$

We can then finally combine Equation 5.9, Equation 5.8, and Equation 5.7 in order to write a differential equation for the rate of change of the concentrations of **A**:

$$-\frac{d}{dt}x_A = \frac{d}{dt}x_B = \mathbf{I}_{em} \cdot \left(\frac{x_A \epsilon_A \phi_{A \rightarrow B}^{iso} - x_B \epsilon_B \phi_{B \rightarrow A}^{iso}}{x_A \epsilon_A^{iso} + x_B \epsilon_B^{iso}} \right) \left(1 - 10^{-rc_0(x_A \epsilon_A^{iso} + x_B \epsilon_B^{iso})} \right) \quad (5.10)$$

where \mathbf{I}_{em} is the spectrum of light emitted by fluorescence as defined in Equation 5.6.

5.2.3 List of terms and parameters

With the differential equation shown in Equation 5.10 it is possible to numerically model the dynamics of this system for arbitrary photophysical parameters, which are summarised in Table 5.1 for convenience.

Table 5.1. Terms and parameters used for modelling the dynamics of the feedback system. Spectra are shown in bold and scalar are shown in regular type, eg \mathbf{I} vs I .

Parameter	Meaning
x_A, x_B	Respective mole fractions of A , B
c_0	Total concentration ($c_0 = [\mathbf{A}] + [\mathbf{B}]$; mol L ⁻¹)
r	Path length for emitted light to escape the solution
I_{ex}	Irradiating light (mol s ⁻¹ of photons)
$\epsilon_A^F(\lambda), \epsilon_B^F(\lambda)$	Molar absorptivity spectra of the fluorescent electronic system of A and B (M ⁻¹ cm ⁻¹)
$\phi_A^F(\lambda), \phi_B^F(\lambda)$	Fluorescence quantum yield spectra of A and B . Defined such that the total quantum yield for fluorescence ϕ^F is equal to the sum of ϕ^F over all wavelengths, i.e. $\phi^F = \int \phi^F d\lambda$.
$\mathbf{I}_{em}(\lambda)$	Light from fluorescence of A and B (mol s ⁻¹ of photons; see Equation 5.6)
$\epsilon_A^{iso}, \epsilon_B^{iso}$	Molar absorptivity spectra of the photochromic electronic systems of A and B (M ⁻¹ cm ⁻¹)
$\phi_{A \rightarrow B}^{iso}, \phi_{B \rightarrow A}^{iso}$	Quantum yields for photoisomerisation of A and B (assumed to be wavelength-independent)

5.3 Numerical modelling

A numerical approach was used to model the dynamics of the feedback system by simulating the parameters listed in Table 5.1 and using these to solve the differential equation shown in Equation 5.10 as a function of x_A . All absorption and emission spectra were modelled as

functions of wavelength (to integer nanometre resolution) over the range 275–800 nm. Note that this is *not* an attempt to model the example molecular structure shown earlier in Figure 5.2, or for that matter any particular structure at all. The parameters used here, while plausible, are chosen to demonstrate the existence and behaviour of competitive autoamplification and bifurcation under irradiation and are not derived from any form of experimental or measured data.

5.3.1 Model spectra

All absorption and emission spectra were modelled as Lorentzian curves for simplicity, using the following form:

$$L(\lambda) = \frac{a}{\pi} \left(\frac{\gamma/2}{(\lambda - \lambda_0)^2 + (\gamma/2)^2} \right) \quad (5.11)$$

The parameters used for the simulated spectra and dynamics in this section are given in Table 5.2. As Lorentzian curves of the form given in Equation 5.11 integrate to a , for emission spectra this parameter was used to set the overall quantum yields for fluorescence to a plausible $\phi_F = 0.9$. Bifurcation does not require a *high* quantum yield, as used here, but rather that the quantum yields of the two isomers are *similar*: see appendix Figure 10.2 for a plot of bifurcation conditions *vs* $\phi_{A \rightarrow B}^{iso}$ and $\phi_{B \rightarrow A}^{iso}$.

Table 5.2. Parameters used for Lorentzian absorption and emission spectra (Equation 5.11). These spectra are plotted graphically in Figure 5.5.

Spectrum	λ_0 / nm	γ / nm	a
ε_A^F	345	20	3500
ε_B^F	355	20	3500
ϕ_A^F	400	20	0.9
ϕ_B^F	550	60	0.9
ε_A^{iso}	530	60	600
ε_B^{iso}	415	20	400

The absorption spectra for the isolated emission and photoisomerisation electronic systems, the total absorption, and the emission spectra for **A** and **B** defined by the parameters given in Table 5.2 are plotted in Figure 5.5 for ease of visualisation. The selective overlap of the emission spectrum (ϕ^F) of each isomer with the photoisomerisation re-absorption spectrum (ε^{iso}) of the other isomer is required for feedback.

5.3.2 Understanding system dynamics with feedback

On irradiation by I_{ex} , light is absorbed by the fluorescent systems of **A** and **B** and is re-emitted *via* fluorescence as \mathbf{I}_{em} , a population-weighted combination of the emission spectra of **A** and **B**. This light can be re-absorbed by the photochromic electronic systems of **A** or **B** to drive photoisomerisation. For a given excitation wavelength I_{ex} , the rate of change of the composition of the system (e.g. $\frac{d}{dt}x_A$) thus depends on the composition of the system.

Using visible-light irradiation at a wavelength λ_{ex} where the fluorophores do not absorb, only direct **A**-**B** photoisomerisation occurs. Under these conditions (Figure 5.6a) there is a single value of x_A for which $\frac{d}{dt}x_A = 0$: this is the photostationary state, and under irradiation

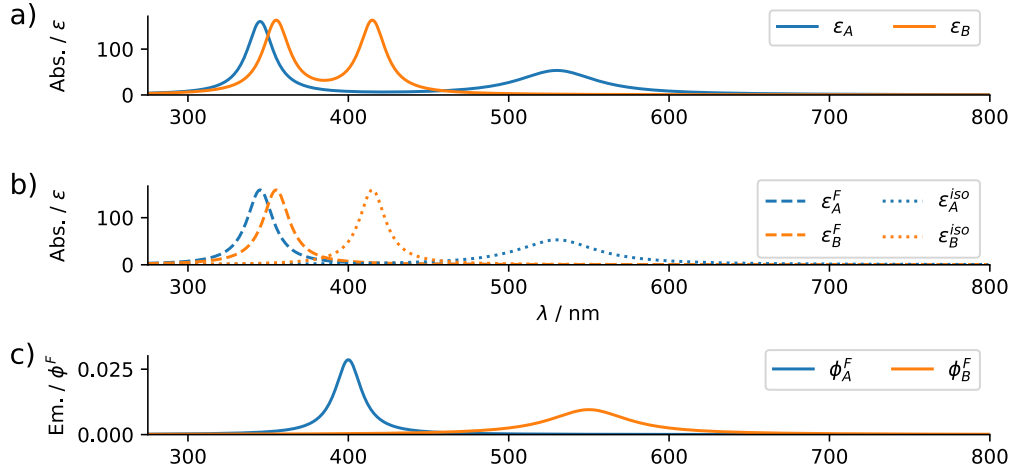


Figure 5.5. Model spectra defined in Table 5.2. a) The absorption spectra of isomers **A** and **B** are each made up from (b) two electronically insulated components, ε^F (dashed lines) which only causes fluorescence and ε^{iso} (dotted lines) which only causes photoisomerisation (i.e., $\varepsilon_A = \varepsilon_A^{iso} + \varepsilon_A^F$). c) The emission spectra of each isomer (ϕ^F) are selectively re-absorbed by ε^{iso} of the *other* isomer.

the system will converge on this composition regardless of the initial mix of photoisomers. Different photostationary states will result from different irradiating wavelengths λ_{ex} , as shown in Figure 5.6a. For the photophysical parameters modelled here, irradiation with 400 nm light leads to a photostationary state containing predominantly **A** while irradiation at 500 nm leads to a photostationary state of predominantly **B**.

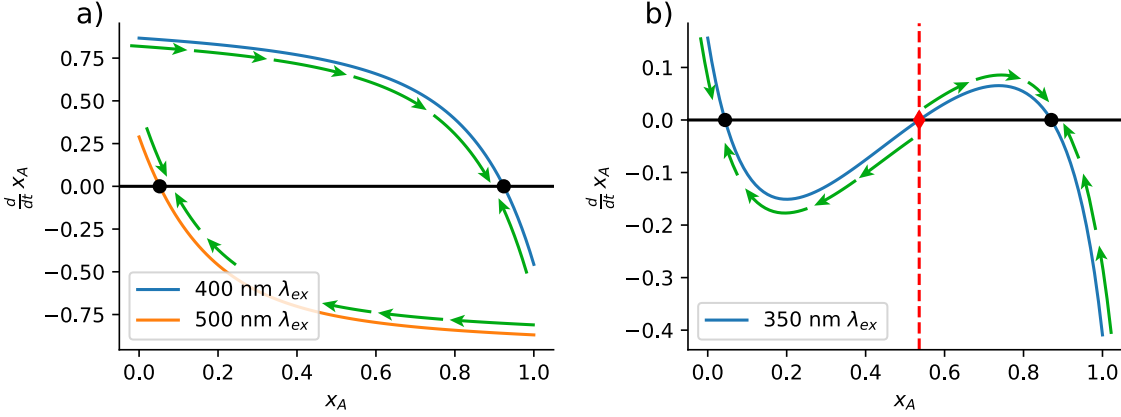


Figure 5.6. Dynamics of the proposed system depicted in Figure 5.5, with absorption and emission spectra as shown in Figure 5.5. a) For standard photochromism without feedback (e.g. visible light irradiation of this system) there is a single wavelength-dependent stable *photostationary state* where $\frac{d}{dt}x_A = 0$. Here, $\frac{d}{dt}x_A$ is shown for irradiation at $\lambda_{ex} = 400$ or 500 nm and photostationary states are highlighted as black circles. b) For a system with self-reinforcing feedback, as proposed here under UV irradiation, there may be *two* stable photostationary states (black circles) separated by an *unstable bifurcation point* x_A^* (red diamond). The photostationary state reached under UV irradiation will depend on whether the initial composition x_A was greater or smaller than the bifurcation point x_A^* . $\frac{d}{dt}x_A$ plotted as solid lines and direction of change shown as green arrows, spectral parameters as Table 5.2, $\phi^{iso} = 0.8$, $c_0r = 1$.

Under irradiation capable of driving emission (here in the UV), the composition-dependence of the response is entirely different: there are *three* different compositions of x_A for which $\frac{d}{dt}x_A = 0$ (Figure 5.6b). Two of these are stable photostationary states (black circles),

but in between there is an unstable *bifurcation point* notated here as x^* (red diamond and dashed vertical line). Under these bistable conditions the photostationary state eventually reached upon irradiation is dependent on whether the initial composition x_A of the system was greater or smaller than x_A^* . For the parameters given in Table 5.2, $x_A^* = 0.54$ and stable photostationary states are reached at $x_A = 0.87$ or $x_A = 0.05$.

5.3.3 Time-dependent system dynamics

The time-dependent dynamics of these systems can be modelled numerically by taking some small time step dt , solving Equation 5.10 for a set of initial conditions, adjusting x_A upwards or downwards by $dx_A = \frac{d}{dt}x dt$, and repeating. An example of this is shown in Figure 5.7 using the same model parameters as Figure 5.6. Depending on whether the initial composition x_A is greater or less than x_A^* , the system eventually converges on either an **A**-rich or **A**-poor photostationary state. The closer the initial composition is to the bifurcation point x^* , the longer it takes for the system to approach one of the two stable photostationary states. This can be partially understood as a thermodynamic requirement: the smaller the initial perturbation away from x^* , the more work must be done to amplify this small compositional imbalance into a larger difference. At a constant rate of power input (irradiation at I_{ex}), this energy requirement manifests as an increased time required to reach a stable PSS (Figure 5.7).*

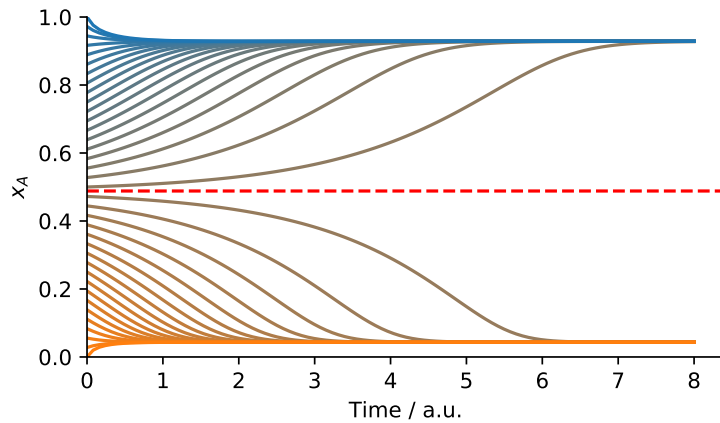


Figure 5.7. Kinetic trajectories of the feedback system over time for a range of initial compositions (spectra as in Table 5.2, $c_0r = 1$). As time increases the system approaches one of two stable photostationary states at either $x_A = 0.04$ or $x_A = 0.87$. In this case bifurcation occurs at approximately $x_A^* = 0.54$ (shown as a dashed red line), with the photostationary state reached depending on whether the initial proportion of **A**, x_A , was larger or smaller than x_A^* .

5.3.4 Required total absorbance for bifurcation

Selective photophysical parameters for re-absorbed emission are necessary but not sufficient for bifurcation. Even when re-absorption of emitted light is selective enough for bifurcation to

*Given the requirement for multiple carefully balanced absorption and emission spectra to amplify information, it is reasonable to say that *many bands make light work*.

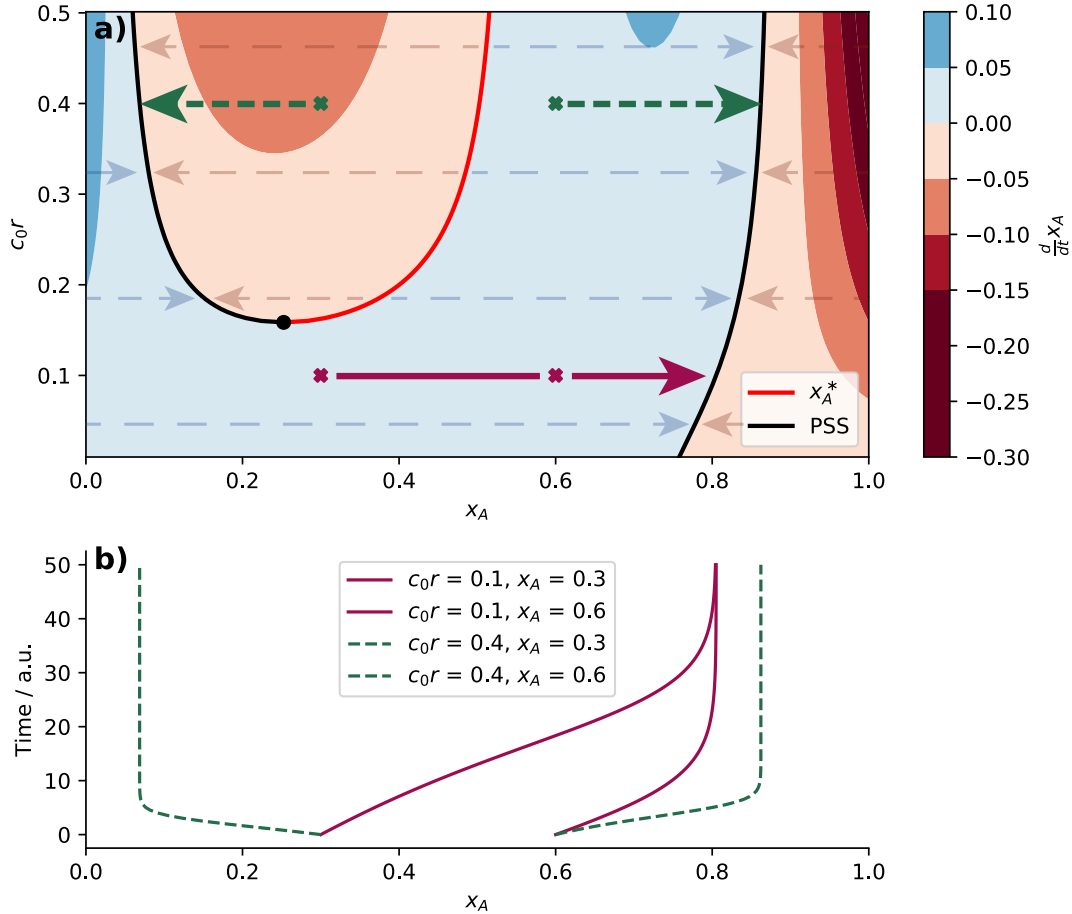


Figure 5.8. Concentration requirements for bifurcation. a) At low c_0r there is a single photostationary state where $\frac{dx_A}{dt} = 0$, shown as a black line. As c_0r increases, bifurcation occurs at a critical value of c_0r (black circle) bringing a second stable photostationary state (black line) and bifurcation point (red line). For the example system with spectra shown in Figure 5.5 and Figure 5.6, this critical value occurs at $c_0r \simeq 0.158$. The location of the bifurcation point x_A^* varies somewhat as a function of c_0r : at the onset of bifurcation $x_A^* = 0.34$, but as c_0r increases to infinity x_A^* increases towards 0.57 (see Figure 10.1 for data to higher values of c_0r). Shading and pale arrows in blue or red represent $\frac{dx_A}{dt} > 0$ and $\frac{dx_A}{dt} < 0$ respectively under irradiation. b) Trajectories are shown for systems initially at $x_A = 0.3$ or 0.6 and $c_0r = 0.1$ or 0.4 under irradiation (marked as crosses on subplot Figure 5.8a). If $c_0r = 0.1$ (maroon points and lines) a single photostationary point is reached regardless of initial x_A , but at $c_0r = 0.4$ (green points and lines) the system bifurcates on irradiation to reach one of two stable photostationary states.

occur, it appears that some minimal optical depth c_0r is required (Figure 5.8). If the concentration c_0 or path length r of the modelled system are too low, a single global photostationary state is reached regardless of initial composition. This behaviour can be seen in Figure 5.8a, where bifurcation only occurs when c_0r is greater than a critical value ($c_0r \simeq 0.158$ for the parameters used here). Below this critical value a single photostationary state (solid black line) is reached regardless of the initial composition of the system (Figure 5.8, purple lines). However, if $c_0r > 0.158$ then the system bifurcates: a second photostationary state (black line) is then separated from the first by a bifurcation point (red line). At the bifurcation point x^* , there is no change in composition upon irradiation ($\frac{dx_A}{dt} = 0$) but the slightest perturbation of composition away from x^* will result in an unstable system that moves *away* from the

bifurcation point and *towards* one of the two photostationary points (Figure 5.8, green lines). This behaviour allows the bifurcating system to amplify small compositional changes (away from x^*) into much larger changes (towards either stable PSS) under UV irradiation. These compositional changes are shown over time in Figure 5.8b for initial compositions $x_A = 0.3$ and $x_A = 0.6$. If $c_0r = 0.1$ (purple crosses and lines), a single global PSS composition is reached upon irradiation. For the same initial compositions but with $c_0r = 0.4$ (green lines), bifurcation occurs and the two compositions diverge to one of two different PSS compositions upon irradiation.

The compositions of the bifurcation point and photostationary states vary somewhat with optical density (see Appendix Figure 10.1 for modelled data to higher concentrations) but eventually converge on stable values at high optical densities.

5.3.5 Goldilocks re-absorbance: not too high, and not too low

While c_0r must be greater than some minimal value for bifurcation to occur, it should not be *too* large. This is because the operation of the amplifier needs to eventually produce some sort of signal in the form of escaping light: if c_0r is very large bifurcation will still occur, but almost none of the emitted light will be transmitted through the solution and escape to the outside world for detection (Equation 5.7) or interaction with other photochromic systems. The system as proposed would still demonstrate non-linear dynamics and bifurcation which could be measured through, for example, absorption or NMR spectroscopy or as other changes in molecular properties.

Ideally c_0r will be selected to fall within a ‘goldilocks region’: large enough for bifurcation and bistability to occur, but small enough for the greatest possible proportion of emitted light (\mathbf{I}_{em} , Equation 5.6) to escape the system. The effects of this are shown in Figure 5.9, where a well-chosen value of c_0r enables bifurcation to occur while also allowing the transmission of a reasonable proportion of emitted light.

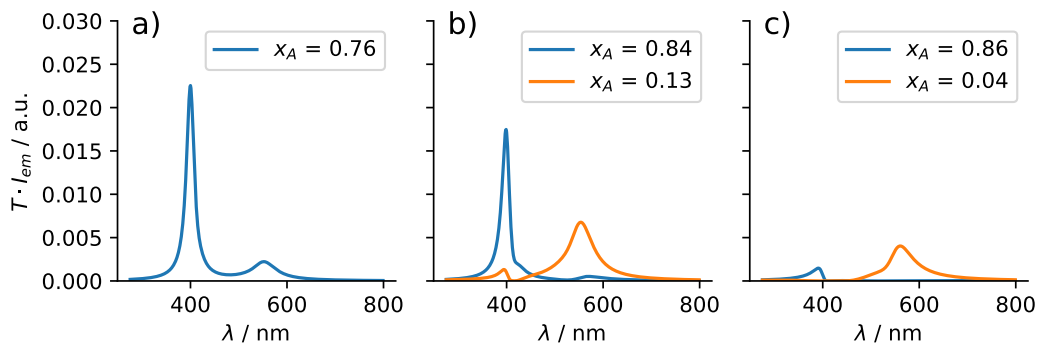


Figure 5.9. Transmission of emitted light at stable photostationary states for $c_0r = 0.02, 0.2$, or 2 . More light can escape at lower values of c_0r , but if c_0r is too small (left) the the system is not bistable. At $c_0r = 0.2$ (middle) bistability occurs and \mathbf{I}_{em} is transmitted through either photostationary state. At $c_0r = 2$ (right), output signals are weak as only a small proportion of \mathbf{I}_{em} can escape the system without re-absorption.

Fortunately, c_0r would be the easiest parameter to adjust in a chemical realisation of the system depicted here. c_0 is simply the concentration, and may be adjusted within the

limits of solubility of compounds **A** and **B**. However, it is likely that in practice experimental concentrations would be kept low to minimise aggregation and intermolecular energy transfer (e.g. FRET). To minimise this, reduced concentrations can be compensated for by increasing the path length r of the system, either through a physical increase in size or by increasing the effective path length with partially reflective surfaces such that light is confined within a smaller physical volume for multiple pathlengths.

5.4 Binary amplification for non-volatile memory storage

The presence of a bifurcation point x^* makes this system capable of amplifying weak perturbations away from x^* into larger binary signals. Crucially, this weak input is the same as the output of the system: a small input flux of blue or green (< 450 or > 450 nm) photons will, after amplification, result in a larger output *also* of blue or green photons. This amplification requires that the system initially be placed in a composition as close to x^* as possible, which can be achieved through direct visible-light photoisomerisation of the system using a wavelength λ_{reset} chosen such that the photostationary state (PSS) is x^* . The existence of such a wavelength λ_{reset} is guaranteed: the system will only be capable of bifurcation if PSSs exist with compositions x_A both greater or smaller than x_A^* , and as the PSS is a continuous function of excitation wavelength it follows that composition x^* must be the PSS for some excitation wavelength. This is shown graphically in Figure 5.10 for the set of model parameters used through this chapter (see subsection 5.2.1 for the function used): here, λ_{reset} occurs at 450 nm.

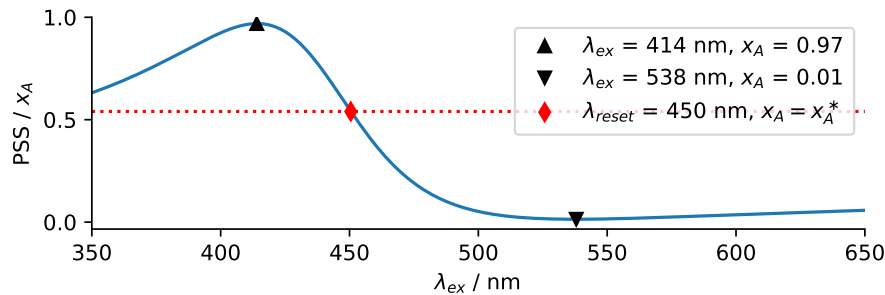


Figure 5.10. Composition of **A** for photostationary states reached for photoisomerisation under direct irradiation (without fluorescence and feedback). For the parameters used here (Table 5.2), photostationary states of 97% and 1% **A** can respectively be reached under 414 or 538 nm irradiation. The bifurcation point x_A^* ($x_A = 0.54$) can be reached under irradiation at a wavelength λ_{reset} somewhere in between, here 450 nm.

The ability to reset the system to x^* using irradiation at λ_{reset} makes it possible to re-use the system indefinitely (in the absence of photodegradation) to amplify small signals of blue (< 450 nm) or green (> 450 nm) light:

5.4.1 A single-bit molecular flip-flop

Each time amplification occurs, a single bit of information ('blue' or 'green') is stored and remains stored until the system is reset by irradiation at λ_{reset} . This memory storage is non-

volatile (it persists in the absence of driving I_{ex}) and can be read at any time by irradiation with UV light (I_{ex}). The behaviour is analogous to a *flip-flop* electronic circuit, also known as a bistable multivibrator or latch.^[7,8] Flip-flops are the fundamental storage element in sequential logic, allowing a bit of information to be stored and later accessed as required. While this is not the first example of an all-photonic molecular flip-flop,^[9] I believe it to be the first proposal to use the same wavelengths of light for inputs and outputs ('input-output homogeneity'^[10]) and to incorporate light-powered amplification, allowing weak signals to be cascaded and 'wired' to further operations without loss of intensity.

Operation of the feedback system as a flip-flop is shown schematically in Figure 5.11. Beginning with the system at the bifurcation point, x^* a binary input signal ('blue' or 'green') can be amplified and read out under irradiation at λ_{ex} (350 nm). The bit of information stored can be retained in the dark for an extended period and read out later as needed. When needed, the bit can be rewritten by a) irradiating at λ_{reset} (450 nm) to reset the system to x^* , followed by b) perturbation with an input and amplification under irradiation by λ_{ex} .



Figure 5.11. Input amplification and non-volatile memory storage using the system proposed here. With the composition set to the bifurcation point x^* , a small input signal of light (< 450 or > 450 nm) can be amplified by UV irradiation at λ_{ex} with the result detectable as a fluorescent output. The internal state of the system (representing one binary bit of memory) is maintained in the absence of UV light, making this an example of nonvolatile memory: irradiation at λ_{ex} can be used to read out the state of the system at any time after amplification has taken place.

5.4.2 Towards molecular computing?

The system proposed here is equivalent to an electronic *flip-flop* circuit that processes binary information as blue (< 450 nm) or green (> 450 nm) light. These are the circuits responsible for solid-state memory storage in computers (e.g. RAM or CPU registers) and are one of the two fundamental components required for computation: flip-flop circuits and logic gates are all that is required to build a fully functional computer.^[11] Constructing an all-photonic molecular computer could be accomplished in principle by combining the flip-flop described here with molecular logic making use of the same blue light/green light binary inputs and outputs.

Molecular logic could be achieved through creation of one of the two 'universal' logic gates, NAND and NOR,^[12] with truth tables as shown in Table 5.3. While a number of examples

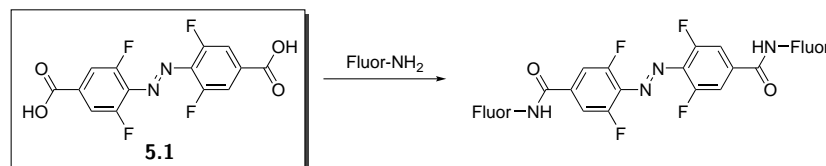
Table 5.3. Photonic molecular logic gates. In addition to the flip-flop proposed here, molecular computing would require either a NAND or NOR logic gate making use of the same blue or green (B/G) light as inputs and outputs.

Photonic NAND gate			Photonic NOR gate		
A	B	Q	A	B	Q
B	B	G	B	B	G
G	B	G	G	B	B
B	G	G	B	G	B
G	G	B	G	G	B

of molecular implementations of Boolean logic have been reported,^[9e,13] true molecular computing under this architecture would require input-output homogeneous logic gates capable of acting on and generating identical input/output signals in the form of blue and green light. With amplification as proposed here, these components could be arbitrarily linked to one another and cascaded to achieve complex operation. This is a challenging problem to address: despite significant research efforts, all-photonic molecular logic with identical inputs and outputs has yet to be achieved practically and it is unclear what such a system might look like.

5.5 Attempts to realise the molecular amplifier

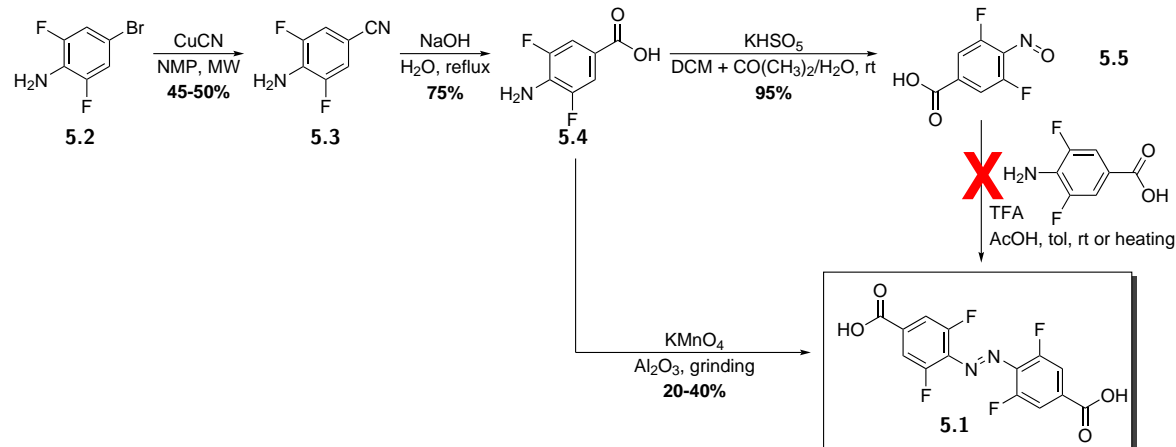
Some progress was made towards the goal of controlling pyrene monomer-excimer emission using an *ortho*-tetrafluoroazobenzene visible-light photoswitch. The targeted compounds were based on the azobenzene dicarboxylic acid core **5.1** shown in Scheme 5.1 for synthetic and photophysical reasons. It is known that the achievable photostationary states of selectivity of *ortho*-tetrafluoroazobenzene become more selective with electron-withdrawing substituents on the 4-position,^[2b,f] so an amide-functionalised azobenzene was anticipated to have good photophysical properties. The reliability of amide coupling reactions combined with the wide variety of commercially available or readily accessed amine-functionalised fluorophores meant that core compound **5.1** could be used to form a wide variety of fluorophore-functionalised azobenzenes.



Scheme 5.1 Planned route towards azobenzene-controlled photoswitchable fluorescence. Azobenzene diacid **5.1** would be coupled with amine-functionalised fluorophores (Fluor-NH₂) to produce azobenzene diamides of the general structure shown.

5.5.1 Accessing the *ortho*-tetrafluoroazobenzene diacid core

A synthetic route to access key fluoroazobenzene dicarboxylic acid **5.1** and fluorophore-photoswitch conjugates is laid out in Scheme 5.2.



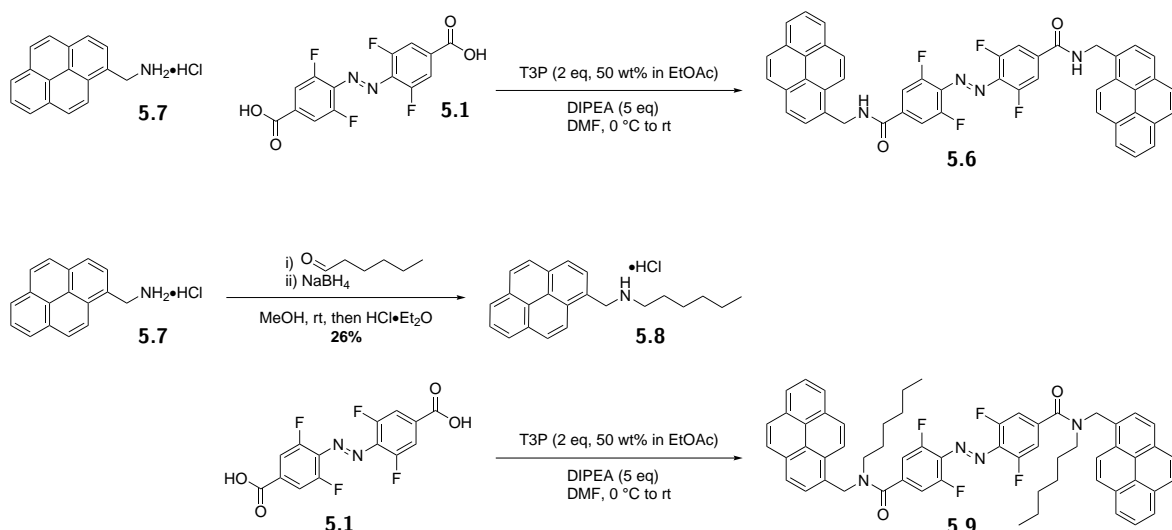
Scheme 5.2 Route to key azobenzene-diacid **5.1**. Difluoroaniline carboxylic acid **5.4** could be synthesised using reported procedures, but attempted Mills coupling between aniline **5.4** and nitroso **5.5** was unsuccessful. Compound **5.1** was eventually acquired as the result of a solid-phase mechanochemical grinding oxidation with KMnO₄ oxidant on an Al₂O₃ substrate.

Starting from commercially available aniline **5.2**, nitrile **5.3** was prepared by reaction with CuCN in *N*-methylpyrrolidone under microwave Rosenmund-von Braun reaction conditions^[14] in moderate yield (50–60%). Nitrile **5.3** was hydrolysed to give aniline-carboxylic acid **5.4** in 75% yield by treatment with aqueous NaOH. The subsequent oxidative coupling of aniline **5.4** to form azobenzene **5.1** was surprisingly challenging. Partial oxidation to nitroso compound **5.5** proceeded in quantitative yield, but Mills coupling to give azobenzene-diacid **5.1** under acidic conditions gave only traces of product. Oxidative coupling of aniline **5.4** using KMnO₄ on FeSO₄ in dichloromethane or chloroform gave no conversion, likely due to the extremely poor solubility of compound **5.4**.

Diacid **5.1** was accessed *via* an unconventional solid-phase mechanochemical oxidation with KMnO₄ on an Al₂O₃ substrate under manual grinding in a pestle and mortar. After 30–60 minutes of grinding oxidation, a colour change of the alumina from purple to red-brown was observed and the azobenzene diacid **5.1** recovered from the solid substrate in low to moderate yield (20–40%) by washing with NaOH, acidification, and re-extraction with ethyl acetate.

5.5.2 Pyrene-functionalised tetrafluoroazobenzene amides

As shown in Scheme 5.3, *ortho*-tetrafluoroazobenzene dicarboxylic acid **5.1** was coupled with pyrene methylamine **5.10** under propylphosphonic anhydride (T3P)-mediated amide coupling conditions. Unfortunately, the resulting bis-pyreneamide azobenzene **5.6** was insoluble in common solvents investigated except DMSO. As excimer formation is disfavoured by polar solvents, this was considered unacceptable.



Scheme 5.3 Pyrene-azobenzene amides. Starting from azobenzene dicarboxylic acid **5.1**, compound **5.6** was prepared by propylphosphonic anhydride (T3P)-mediated amide coupling with pyrenemethylamine **5.7**. Unfortunately, this compound was insoluble in all solvents except DMSO and so was not pursued further. To improve solubility, pyrenemethylamine **5.7** was hexylated *via* reductive amination with hexanal to give secondary amine **5.8**, which was coupling with **5.1** to give solubilised tertiary amide **5.9**. This compound was then used for further studies.

As amide hydrogen bonding was suspected to play a part in the insolubility of **5.6**, pyreneamine **5.7** was hexylated under reductive amination conditions to give hexylamine derivative **5.8**, which was subsequently coupled with diacid **5.1** using the same conditions as before to obtain **5.9** in 91% yield. Compound **5.9** was soluble in apolar solvents, allowing purification by column chromatography (dichloromethane on silica) and making it possible to conduct switching studies in apolar solvents.

5.5.3 Restricted amide bond rotation dynamics of hexylated azobenzene-pyrene conjugate

The signals in the room temperature ^1H NMR spectrum of compound **5.9** were broad, as shown in Figure 5.12. This was suspected to result from slow amide bond rotation on the NMR timescale. Variable temperature NMR was used to study the amide conformers present in solution. ^1H NMR spectra in CDCl_3 from +40 °C to -35 °C are shown in Figure 5.13, and reveal that the spectrum is indeed responsive to temperature. The different conformers do not coalesce at +40 °C, but begin to resolve into multiple sharp peaks as the temperature is lowered to 0 °C. In particular, the azobenzene signals (labelled region II) split from two broad peaks corresponding to the *E* (7.15 ppm) and *Z* (7.05 ppm) isomers at room temperature into 5+ distinct environments at low temperature. Multiple pyrene-methylene peaks in region III are also clearly resolved at -35 °C, but the hexyl signals (IV, V) remain broad and indistinct.

Previous experience in our group has found ^{19}F NMR a valuable technique for analysing tetrafluoroazobenzenes of this type due to *E* and *Z* isomers consistently appearing at $\delta \simeq -117$ and $\delta \simeq -119$, respectively. Low-temperature ^{19}F NMR was able to show that the compound as-synthesised consisted of a mixture of the *E*-**5.9** and *Z*-**5.9** photoisomers in

5.5. ATTEMPTS TO REALISE THE MOLECULAR AMPLIFIER

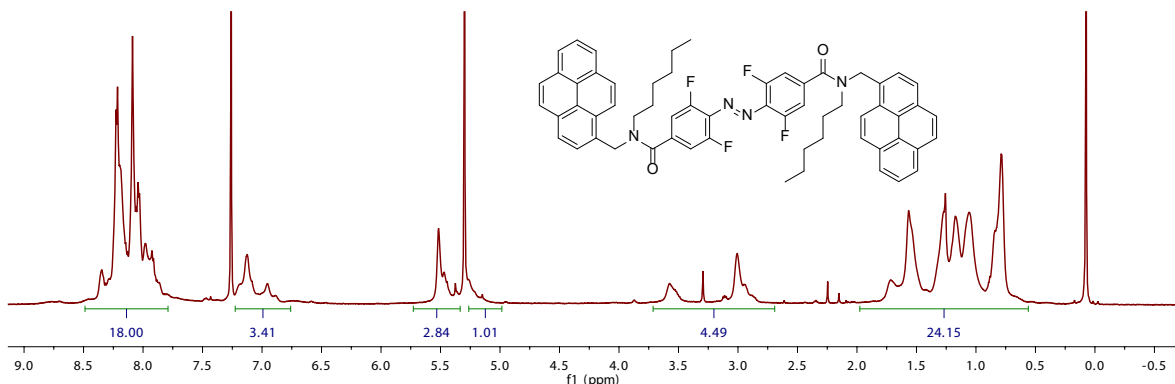


Figure 5.12. ^1H NMR spectrum (500 MHz, CDCl_3) of **5.9** at room temperature after chromatography in dichloromethane. Sharp peaks correspond to CDCl_3 and dichloromethane, and all signals from the pyrene-azobenzene amide are broadened by slow exchange between amide conformers. See Figure 5.13 for assignment of the integrated regions.

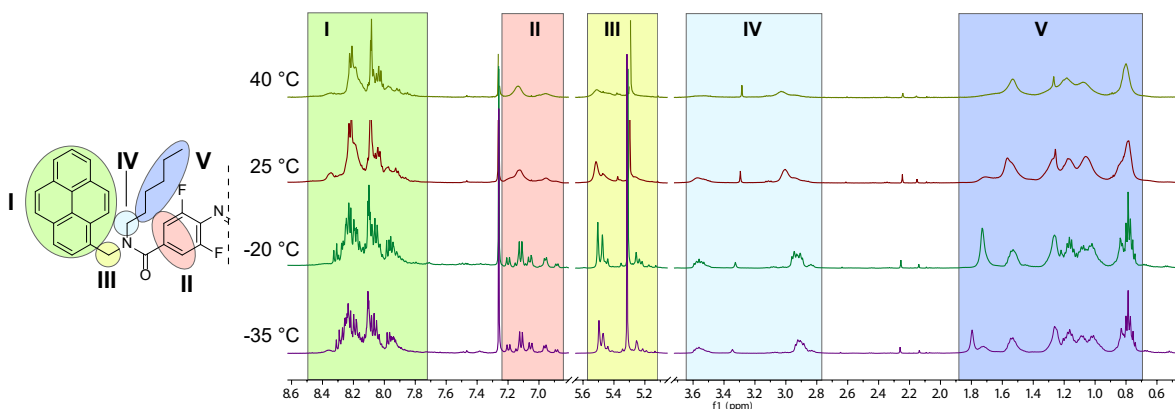


Figure 5.13. VT ^1H spectra (CDCl_3 , 500 MHz) of **5.9** at 40°C , 25°C , -20°C , and -35°C (top to bottom). The spectrum can be broken down into five (labeled) regions: aromatic pyrene (I), fluorine-coupled azobenene (II), pyrene- CH_2-N methylene, $\text{C}_5\text{H}_{11}-\text{CH}_2-\text{N}$ methylene (IV), and aliphatic hexyl (V) proton environments. The broad signals observed at room temperature are well resolved into different amide conformers at -35°C .

approximately 1:2 ratio, as shown in Figure 5.14.

A low-temperature ROESY experiment at -35°C was used to study the conformational dynamics of compound **5.9**, and is shown in Figure 5.15. The *cis* and *trans* amide conformers (as shown on the left) can be distinguished by the correlations between the azobenzene environments (region II) and each of the two methylene areas (regions III and IV): one conformer shows through-space correlations between the pyrene-methylene peaks and both azobenzene and hexyl regions, while the other shows correlations between hexyl methylenes and both azobenzene and pyrene methylene signals but *not* between the pyrene-methylene signals and the azobenzene region. From these correlations, it appears that the major species has the pyrene group *trans* to the azobenzene (i.e. the upper structure, shown in purple). The ratio of this major conformer to the other amide conformer is about 2.5:1, so both species are present in comparable quantities.

The presence of slowly exchanging amide conformers explains the division of methylene signals into two major groups, but does not explain the multiple environments making up each group. This further splitting may be due to restricted rotation about the carbon-carbon

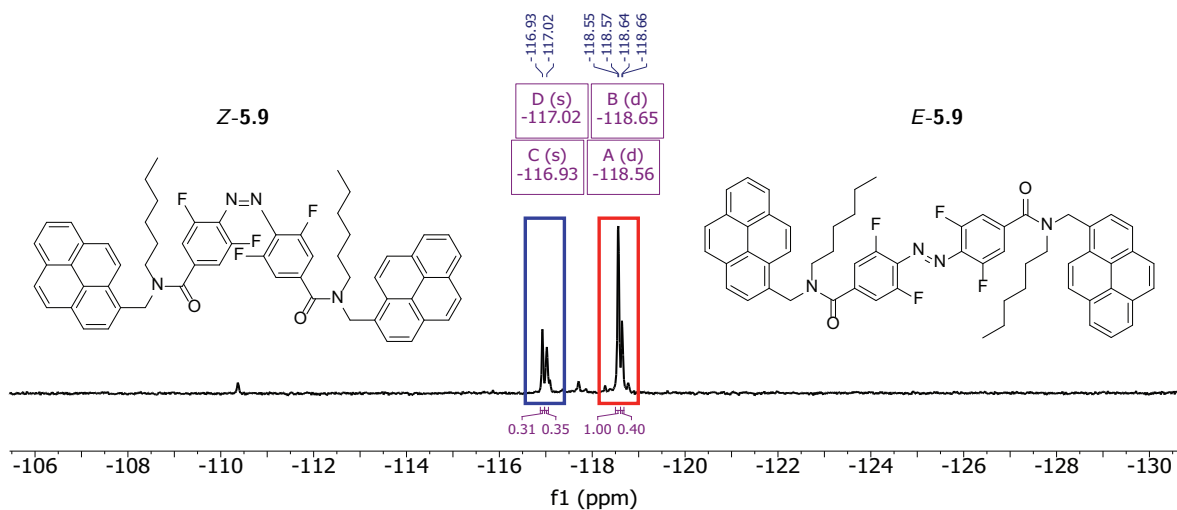


Figure 5.14. Low temperature ^{19}F NMR spectrum (-15°C , CDCl_3 , 565 MHz) of compound **5.9** as a mixture of *E*-**5.9** and *Z*-**5.9**. By analogy with other fluoroazobenzenes studied, the peaks at $\delta \simeq -117$ ppm (blue box) were assigned to *Z*-**5.9** and the peaks at $\delta \simeq -118.5$ ppm (red box) to *E*-**5.9** suggesting an approximately 1:2 ratio of *Z*-**5.9**:*E*-**5.9**.

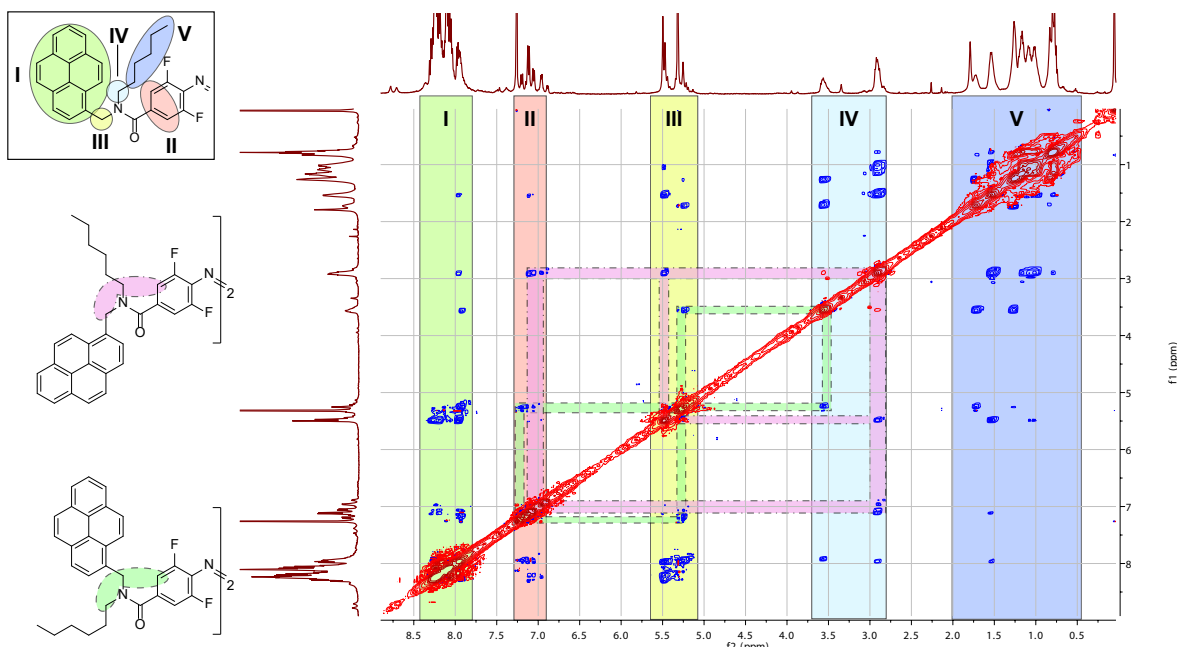


Figure 5.15. ^1H ROESY (CDCl_3 , 500 MHz) at -35°C . The two amide conformers can be separated by the through-space coupling involving the azobenzene protons and each of the $\text{N}-\text{CH}_2-\text{C}$ groups. From this data it appears that the major conformer involves the pyrene group *trans* to the azobenzene-amide, as shown in purple, with an approximately 2.5:1 ratio of the *trans* amide to the *cis* amide.

azobenzene-carbonyl bond breaking the symmetry of each azobenzene proton. The presence of amide conformers may have important implications for the switchable emissive properties of compound **5.9**: for example, it is likely that the monomer/eximer fluorescence selectivity of the *Z* isomer (which should bring the pyrenes closer together in space) will be different depending on whether the pyrene groups are held *cis* or *trans* to the azobenzene core.

5.5.4 Preliminary fluorescence study of pyrene-azobenzene conjugate

Preliminary fluorescence studies of compound **5.9** are shown in Figure 5.16. While there is some limited evidence of monomer-eximer switching of pyrene fluorescence, the selectivity of this switching is small and wholly inadequate for the proposed amplifier. This may result from the amide conformers identified, or from energy transfer between the pyrene fluorophore and the azobenzene switch: as excimer emission requires exciplex formation to occur within the excited state lifetime of monomer pyrene,^[4c] any energy transfer from the pyrene to the azobenzene system would quench excimer emission.

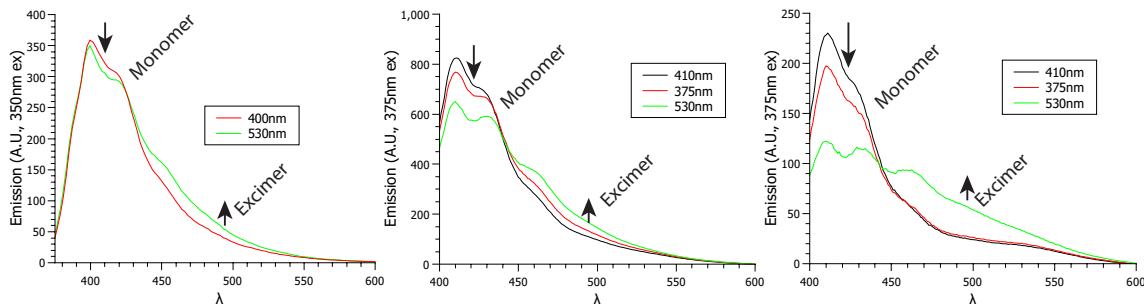


Figure 5.16. Emission spectra of **5.9** in a) cyclohexane, b) CHCl₃, c) CHCl₃ at 3 × higher concentration than before. A decrease in monomer fluorescence (400–430 nm) and increase in excimer fluorescence (450–550 nm) can be seen after 530 nm irradiation and *E* → *Z* isomerisation, but the change in emission is small. In all cases, monomer emission at approximately 400 nm is greater than excimer emission (>450 nm).

5.6 Conclusions and future work

I present a theoretical study of an all-photonic feedback system that is effectively autocatalytic with respect to light. This requires combining the known properties of visible-light photoswitching^[2] and switchable emission^[1] to produce a photoswitchable system involving two states. Each state is fluorescent under UV irradiation with an emission spectrum selectively absorbed by the *other* state, leading to competitive autoamplification of each photoisomer at the expense of the other. Using numerical modelling, I demonstrate that such an auto-amplifying system would be capable of *bifurcation* and *bistability* under irradiation, and could be used to amplify initially small differences in composition. In addition I show that this behaviour is analogous to an electronic flip-flop circuit, the fundamental component of sequential logic and one of the two logic components required to build a computer and process arbitrary information. While molecular flip-flops have been reported previously,^[9] I believe this to be the first proposal of a molecular flip-flop incorporating *amplification* (the output

signal is always the same, regardless of the amplitude of the input) and with *homogeneous inputs and outputs* (binary blue/green inputs result in binary blue/green outputs).

The next stage of work on this subject is clear: to synthesise a molecule (or system of molecules) capable of bifurcation and feedback based on this proposal. Initial synthetic attempts made to achieve this using *ortho*-tetrafluoroazobenzene photoswitches and pyrene fluorophores show only limited control over emissive properties, likely due to the poor formation of pyrene excimers under the conditions studied. This could be improved by replacing the amide linker with a less conformationally restrictive linking group, such as an alkyl chain, and aided by greater understanding of energy transfer pathways using transient absorption spectroscopy. Future work could proceed along these lines, or could turn to modifying previously demonstrated cases of photocontrol over emissive properties^[1] to achieve selective re-absorption of emission as required here. Selective control over the molecular electronics required for this system to function will be challenging to achieve and complications involving unwanted energy transfer pathways can be anticipated in future work aimed at realising this proposal experimentally, but the potential of all-photonic molecular logic devices makes this goal worthwhile.

5.7 References

- [1] (a) C. Li, Y. Zhang, J. Hu, J. Cheng, S. Liu, *Angew. Chem. Int. Ed.* **2010**, *49*, 5120–5124; (b) J. Karpiuk, E. Karolak, J. Nowacki, *Phys. Chem. Chem. Phys.* **2010**, *12*, 8804–8809; (c) S. Kim, S.-J. Yoon, S. Y. Park, *J. Am. Chem. Soc.* **2012**, *134*, 12091–12097; (d) M. Bälter, S. Li, M. Morimoto, S. Tang, J. Hernando, G. Guirado, M. Irie, F. M. Raymo, J. Andréasson, *Chem. Sci.* **2016**, *7*, 5867–5871; (e) G. Naren, C.-W. Hsu, S. Li, M. Morimoto, S. Tang, J. Hernando, G. Guirado, M. Irie, F. M. Raymo, H. Sundén, J. Andréasson, *Nat. Commun.* **2019**, *10*, 1–7.
- [2] (a) R. Siewertsen, H. Neumann, B. Buchheim-Stehn, R. Herges, C. Näther, F. Renth, F. Temps, *J. Am. Chem. Soc.* **2009**, *131*, 15594–15595; (b) D. Bléger, J. Schwarz, A. M. Brouwer, S. Hecht, *J. Am. Chem. Soc.* **2012**, *134*, 20597–20600; (c) S. Samanta, A. A. Beharry, O. Sadovski, T. M. McCormick, A. Babalhavaeji, V. Tropepe, G. A. Woolley, *J. Am. Chem. Soc.* **2013**, *135*, 9777–9784; (d) S. Helmy, S. Oh, F. A. Leibfarth, C. J. Hawker, J. Read de Alaniz, *J. Org. Chem.* **2014**, *79*, 11316–11329; (e) S. Helmy, F. A. Leibfarth, S. Oh, J. E. Poelma, C. J. Hawker, J. Read de Alaniz, *J. Am. Chem. Soc.* **2014**, *136*, 8169–8172; (f) C. Knie, M. Utecht, F. Zhao, H. Kulla, S. Kovalenko, A. M. Brouwer, P. Saalfrank, S. Hecht, D. Bléger, *Chem. Eur. J.* **2014**, *20*, 16492–16501; (g) E. A. Dragu, A. E. Ion, S. Shova, D. Bala, C. Mihailciuc, M. Voicescu, S. Ionescu, S. Nica, *RSC Adv.* **2015**, *5*, 63282–63286.
- [3] J. B. Birks, L. G. Christophorou, *Spectrochim. Acta* **1963**, *19*, 401–410.
- [4] (a) J. B. Birks, D. J. Dyson, I. H. Munro, B. H. Flowers, *Proc. R. Soc. Lond. Ser. Math. Phys. Sci.* **1963**, *275*, 575–588; (b) J. B. Birks, M. D. Lumb, I. H. Munro, B. H.

- Flowers, *Proc. R. Soc. Lond. Ser. Math. Phys. Sci.* **1964**, *280*, 289–297; (c) J. B. Birks, *Rep. Prog. Phys.* **1975**, *38*, 903–974.
- [5] (a) S.-n. Uno, C. Dohno, H. Bittermann, V. L. Malinovskii, R. Häner, K. Nakatani, *Angew. Chem. Int. Ed.* **2009**, *48*, 7362–7365; (b) S. Karuppannan, J.-C. Chambron, *Chem. Asian J.* **2011**, *6*, 964–984; (c) F. G. A. Lister, B. A. F. L. Bailly, S. J. Webb, J. Clayden, *Nat. Chem.* **2017**, *9*, 420–425; (d) F. G. A. Lister, N. Eccles, S. J. Pike, R. A. Brown, G. F. S. Whitehead, J. Raftery, S. J. Webb, J. Clayden, *Chem. Sci.* **2018**, *9*, 6860–6870.
- [6] (a) M. Hammerich, C. Schütt, C. Stähler, P. Lentes, F. Röhricht, R. Höppner, R. Herges, *J. Am. Chem. Soc.* **2016**, *138*, 13111–13114; (b) P. Lentes, E. Stadler, F. Röhricht, A. Brahms, J. Gröbner, F. D. Sönnichsen, G. Gescheidt, R. Herges, *J. Am. Chem. Soc.* **2019**, *141*, 13592–13600; (c) M. S. Maier, K. Hüll, M. Reynders, B. S. Matsuura, P. Leippe, T. Ko, L. Schäffer, D. Trauner, *J. Am. Chem. Soc.* **2019**, *141*, 17295–17304.
- [7] C. E. Shannon, *Bell Syst. Tech. J.* **1948**, *27*, 379–423.
- [8] G. B. Clayton, S. Winder, *Operational Amplifiers*, 5th ed, Newnes, Oxford ; Boston, **2003**, 386 pp.
- [9] (a) R. Baron, A. Onopriyenko, E. Katz, O. Lioubashevski, I. Willner, S. Wang, H. Tian, *Chem. Commun.* **2006**, 2147–2149; (b) G. de Ruiter, L. Motiei, J. Choudhury, N. Oded, M. E. van der Boom, *Angew. Chem. Int. Ed.* **2010**, *49*, 4780–4783; (c) U. Pischel, J. Andréasson, *New J. Chem.* **2010**, *34*, 2701–2703; (d) G. de Ruiter, M. E. van der Boom, *Acc. Chem. Res.* **2011**, *44*, 563–573; (e) P. Remón, M. Bälter, S. Li, J. Andréasson, U. Pischel, *J. Am. Chem. Soc.* **2011**, *133*, 20742–20745.
- [10] J. Andréasson, U. Pischel, *Chem. Soc. Rev.* **2015**, *44*, 1053–1069.
- [11] N. Nisan, S. Schocken, *The Elements of Computing Systems: Building a Modern Computer from First Principles*, MIT Press, Cambridge, Mass, **2005**, 325 pp.
- [12] J. O. Bird, *Engineering Mathematics*, 5th ed, Newnes, Amsterdam ; Boston, **2007**, 576 pp.
- [13] (a) P. A. de Silva, N. H. Q. Gunaratne, C. P. McCoy, *Nature* **1993**, *364*, 42–44; (b) V. Balzani, A. Credi, M. Venturi, *ChemPhysChem* **2003**, *4*, 49–59; (c) A. P. de Silva, N. D. McClenaghan, *Chem. Eur. J.* **2004**, *10*, 574–586; (d) J. Andréasson, Y. Terazono, B. Albinsson, T. A. Moore, A. L. Moore, D. Gust, *Angew. Chem. Int. Ed.* **2005**, *44*, 7591–7594; (e) K. Szaciłowski, W. Macyk, G. Stochel, *J. Am. Chem. Soc.* **2006**, *128*, 4550–4551.
- [14] L. Cai, X. Liu, X. Tao, D. Shen, *Synth. Commun.* **2004**, *34*, 1215–1221.

*CHAPTER 5. PHOTOSWITCH-FLUORESCENCE FEEDBACK: TOWARDS A PHOTONIC
MOLECULAR AMPLIFIER*

Chapter 6

Conclusions and future work

The work in this thesis combines the development and application of new analytical methodology with fundamental studies of the physical chemistry of reaction catalysts, solvated anions, and theoretical modelling of responsive feedback. The common theme linking these topics is the goal of achieving complex and dynamic chemical behaviour using uncomplicated and readily available molecular species.

Biochemistry is able to regulate reaction pathways and communicate between components of dynamic systems using simple molecular species such as Na^+ , K^+ , or Ca^{2+} metal ions, protons, or sugars. The simplicity and ubiquity of these chemical networks makes it relatively feasible to integrate new biomolecular devices with new functionalities into existing architectures and signalling pathways. At its best, supramolecular chemistry takes inspiration from nature to achieve complex system dynamics using readily accessible modular components: examples of this can be seen in the wide range of functionalities achieved with privileged motifs such as azobenzene-cyclodextrin,^[1] ureido-pyrimidones,^[2] or metal-pyridyl^[3] interactions. In contrast, new functionalities resulting from highly specialised molecules accessed via multi-step synthetic tours-de-force are unlikely to be reused or reincorporated into more complex systems. Successful chemical networks involve interactions that are complex, but not complicated. The work presented here looks toward achieving new forms of control over chemical motion using simple and readily available components such as the commercially available Grubbs catalyst and the ubiquitous dihydrogen phosphate anion.

Before studies of the active control of molecular diffusion could begin, it was necessary to develop a method of measuring changes in molecular diffusion rates over time. As discussed in Chapter 2, this was achieved by combining fast diffusion NMR experimental techniques with continuous data acquisition and a new approach of moving-frame data processing. The ability of these experimental techniques to provide minute-resolution time-resolved monitoring of diffusion coefficients was demonstrated by following changes in diffusion over the course of a living polymerisation. By granting access to continuous NMR measurements of diffusion with unprecedented time resolution, this technique represents a powerful tool to follow the dynamics of chemical processes that involve changes to diffusion rates such as polymerisation, guest-binding, or the self-assembly of supramolecular constructs. These processes can be challenging to follow by conventional NMR techniques due to the broad lineshapes associated with large species in chemical exchange with one another, making diffusion measurements

highly complementary to conventional NMR spectroscopic techniques. For example, in the living polymerisation studied here all oligomers shared the same peaks by chemical shift, but growth of the living polymer over time was readily observable as a changing diffusion coefficient. The moving-frame approach demonstrated here can also be adapted to other NMR experiments that obtain data by varying a parameter over a series of spectra, as demonstrated in Chapter 3 for a time-resolved T_1 measurement using an adapted inversion-recovery sequence.

Controlling the motion of small molecules in solution remains a challenge that is of fundamental scientific interest, of obvious applicability, and of unknown possibility. During this study, one approach taken towards actively increasing the translational motion of small molecules in solution was to make use of the reported ‘enhanced diffusion’ of active catalysts as discussed in Chapter 3. The enhanced diffusion of active enzymes has attracted significant study in recent years, but with many mutually contradictory reports the existence and behaviour of this phenomenon continues to be disputed. Our careful study of two metal-catalysed model reactions led to the conclusion that the single reported case of ‘enhanced diffusion’ of an active small molecule resulted from misinterpreted experimental data, leaving the existence of this phenomenon as it relates to small molecules in doubt. It remains unclear whether or not the phenomenon of enhanced diffusion is real or merely illusion, but there is clearly a need for more empirical studies to be conducted in this area. While the low concentrations would prove challenging, the diffusion NMR techniques developed here could be applied to study model reactions that have been widely reported to cause enhanced diffusion under catalysis by enzymes such as urease or aldolase.

The antielectrostatic hydrogen bonding of dihydrogen phosphate described in Chapter 4 represents a new building block for the construction of supramolecular structures. Using diffusion NMR measurements, dihydrogen phosphate was shown to self-assemble into large polyanionic hydrogen-bonded oligomers which could be bound by a photoswitchable anion receptor. The diffusion measurements of the phosphate-bound anion receptor suggested that the complexes formed between the receptor and phosphate oligomers were large, but the structure remains undetermined. Future work on this system would be necessary to establish whether the host-guest species formed in solution are extended oligomers or well-defined discrete complexes.

The work presented in Chapter 4 should be significant to the anion-binding research community, where dihydrogen phosphate has long been recognised as a difficult anion to study. Until now, a physical explanation for the difficulties in applying standard analyses of supramolecular guest-binding to dihydrogen phosphate has been lacking. Here I have demonstrated that any guest-binding study of dihydrogen phosphate is necessarily a competition study, involving host interactions with a condition-dependent sea of phosphate oligomers. These results will change the way people consider a fundamental anion of relevance to both synthetic and biological chemistry.

The self-association of dihydrogen phosphate appears to be surprisingly strong in solution, but more work is needed to confirm and expand upon these results. Analogous studies to the one presented in Chapter 4 should be conducted in other common organic solvents such

as acetonitrile, dimethyl formamide, or chloroform. There is also a possibility of dihydrogen phosphate oligomerisation in water, although the competitive hydrogen bonding nature of water would likely hinder this. If self-assembly does occur in water and under physiological conditions, there may be important implications for the role of dihydrogen phosphate in biological systems.

Having demonstrated the utility of heteronuclear diffusion NMR in probing the self-assembly dynamics of small chemical species in solution, the same techniques could be applied to study the solution dynamics of e.g. HCO_3^- or HSO_4^- dimerisation or mixed heteroanionic systems containing H_2PO_4^- oligomers and chain-terminating HSO_4^- . With the ability to provide electrostatic and hydrogen bonding interactions from a self-assembled oligomeric species of adaptable size, dihydrogen phosphate could also offer fascinating possibilities as a structural motif for well defined self-assembled anion-bound structures in solution, such as coordination cages.^[4]

The final section of work in this thesis, Chapter 5, proposes an approach towards an all-photonic self-amplifying system using known photophysical components. The requirements and general behaviour of the proposed system are modelled numerically, and the properties of the system under irradiation are discussed. This system can be considered a molecular realisation of a flip-flop electronic circuit, one of the fundamental components of molecular logic.

Unfortunately, attempts to synthesise a molecule capable of demonstrating the dynamics proposed here were unsuccessful. Future work on this topic thus has a clear aim: to design, synthesise, and characterise an all-photonic molecular feedback system that is capable of autoamplification as described here. If this can be achieved, future work would involve combining the amplifier with reported fluorescent chemical sensors and photoresponsive molecular devices to create responsive dissipative systems. An example of this would be to combine photonic amplification with fluorescent chemosensors able to detect small quantities of an analyte, report this as a change in chemosensor fluorescence that could perturb the amplifier, and then amplify this output using UV light to obtain a bright blue/green response visible to the naked eye. Alternatively, a solution of photonic amplifier could be mixed with or allowed to transmit light to a physically isolated photoresponsive molecular device (e.g. a photoacid) such that the output of amplification would drive a change of chemical properties (i.e. pH). By linking the proposed molecular amplifier to chemosensors of photoresponsive devices *via* the medium of light, complex functionalities could be developed built around a single core molecular amplifier without any need for chemical modification.

The studies in this thesis depict original approaches towards achieving complex solution-state supramolecular dynamics through both chemical (polyanionic phosphate clusters) and physical (all-photonic feedback) stimuli. I also provide clarifying experimental findings into the subjects of enhanced diffusion and dihydrogen phosphate anion binding that have significant implications for those wider research communities. Above all, the studies presented here are intended to provide tools and conceptual insights to the wider research community that are both generally applicable and practical to implement.

6.1 References

- [1] A. Harada, *Acc. Chem. Res.* **2001**, *34*, 456–464.
- [2] R. P. Sijbesma, F. H. Beijer, L. Brunsved, B. J. B. Folmer, J. H. K. K. Hirschberg, R. F. M. Lange, J. K. L. Lowe, E. W. Meijer, *Science* **1997**, *278*, 1601–1604.
- [3] (a) J. P. Sauvage, J. P. Collin, J. C. Chambron, S. Guillerez, C. Coudret, V. Balzani, F. Barigelli, L. De Cola, L. Flamigni, *Chem. Rev.* **1994**, *94*, 993–1019; (b) J.-P. Sauvage, *Acc. Chem. Res.* **1998**, *31*, 611–619.
- [4] Z. Wu, Y. Wu, W. He, X. Lin, J. Sun, Q. He, *Angew. Chem. Int. Ed.* **2013**, *52*, 7000–7003.

Chapter 7

Appendix for time-resolved diffusion

7.1 General experimental

Methanol capillary inserts were prepared from glass melting point sample tubes and HPLC grade methanol. Water inserts were prepared from deionised water. Capillaries were filled with water or methanol, frozen in liquid N₂, evacuated, and flame-sealed under vacuum. ¹H NMR PGSE diffusion experiments were performed using 400, 500, or 600 MHz Bruker Avance III spectrometers equipped with TXI, BBFO, or cryo-BBO probes and standard high-resolution gradient systems. PGSE experiments were performed using the Bruker **diffSe** pulse sequence, with spoiler pulses (1500 ms recovery time) used to destroy residual magnetization between acquisitions. For a typical diffusion experiment δ was set to 1.0 ms, Δ to 50 ms, and sine gradient pulses of 5–50 G cm⁻¹ strength were used. Equation 1.3 was corrected for the use of sine shaped gradient pulses in the calculations,^[1] *viz.* $b = -\delta^2 g^2 \Delta^2 (4\Delta - \delta)/\pi^2$.

7.1.1 Gradient calibration with methanol

To obtain accurate estimates of D the amplitude of the gradient pulse, g , must be precisely calibrated. This is related to an accurately-measured delivered electrical current by an empirical gradient calibration constant (GCC). If the GCC is set incorrectly it will cause the measured diffusion value D_{expt} to deviate from the correct value D by some scaling factor α (eg, $D = \alpha D_{expt}$). If the true value of D is known, the GCC can then be corrected with a factor of $1/\sqrt{\alpha}$ (equivalent to a factor of $\sqrt{D_{expt}/D}$).

Gradients were calibrated by conducting diffusion experiments on a sample containing methanol and water samples in flamed sealed capillaries at a range of temperatures. The diffusion coefficients of methanol (D_{MeOH}) and water (D_{H_2O}) were measured over a range of temperatures by ¹H NMR, while the internal sample temperature was determined using the methanol OH-CH₃ ¹H NMR chemical shift separation and Equation 2.1. The scaling factor α was then obtained by linear regression of $D_{H_2O}(T)$ against the Speedy-Angell curve shown in Equation 2.3 with the intercept fixed at zero. This calibration factor was used to correct the measured methanol diffusion coefficient data points. Plotted temperature-dependent diffusion data for the six calibration experiments run are shown in Figure 7.1, Figure 7.2, Figure 7.3, Figure 7.4, Figure 7.5, and Figure 7.6.

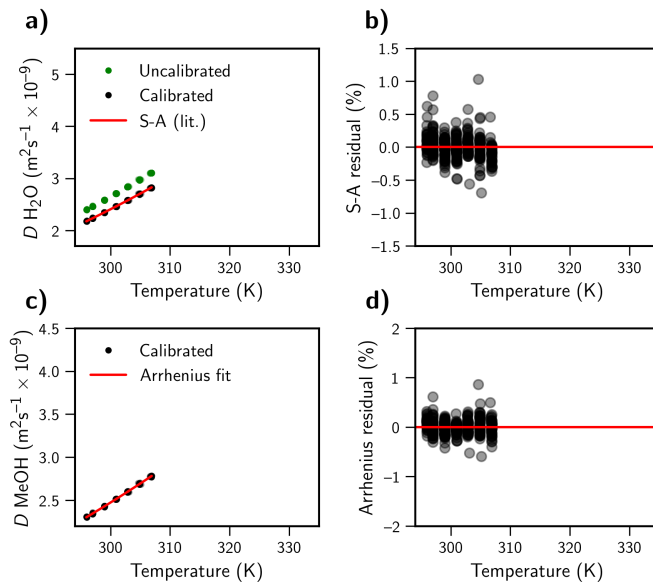


Figure 7.1. Diffusion-temperature measurements of water and methanol in separate sealed glass capillaries in an NMR tube of DMSO-d₆ solution (for locking and shimming), measured by ¹H NMR (PGSE, 400 MHz, $\delta = 1.1$ ms, $\Delta = 45$ ms). a) Gradient calibration by fitting the measured self-diffusion coefficient of water (green) to a literature diffusion-temperature curve (red). Calibrated measurements shown in black. b) Residual plot of measured water diffusion after calibration. c) Calibrated diffusion-temperature measurements of methanol (black) with a fitted Arrhenius curve (Equation 2.2) with constants $D_0 = (4.61 \pm 0.04) \times 10^{-7} \text{ m}^2 \text{s}^{-1}$, $A = (1568 \pm 2) \text{ K}$ (red). d) Residual plot of measured methanol diffusion against Arrhenius fit.

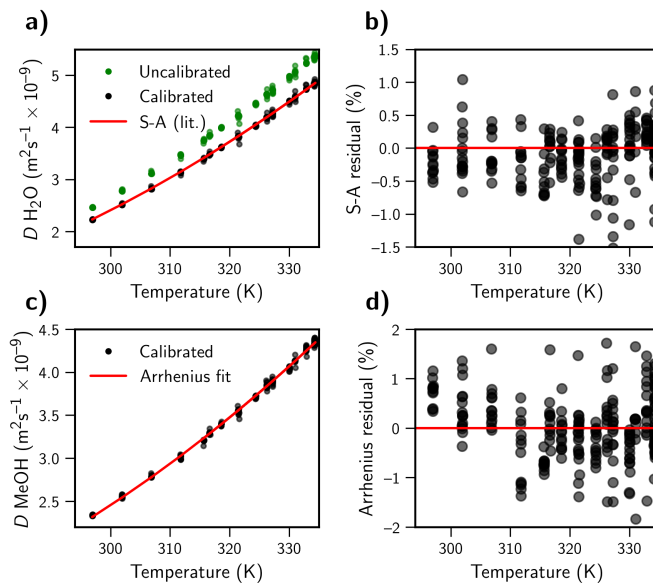


Figure 7.2. Diffusion-temperature measurements of water and methanol in separate sealed glass capillaries in an NMR tube of DMSO-d₆ solution (for locking and shimming), measured by ¹H NMR (PGSE, 400 MHz, $\delta = 1.0$ ms, $\Delta = 50$ ms). a) Gradient calibration by fitting the measured self-diffusion coefficient of water (green) to a literature diffusion-temperature curve (red). Calibrated measurements shown in black. b) Residual plot of measured water diffusion after calibration. c) Calibrated diffusion-temperature measurements of methanol (black) with a fitted Arrhenius curve (Equation 2.2) with constants $D_0 = (6.4 \pm 0.1) \times 10^{-7} \text{ m}^2 \text{s}^{-1}$, $A = (1667 \pm 5) \text{ K}$ (red). d) Residual plot of measured methanol diffusion against Arrhenius fit.

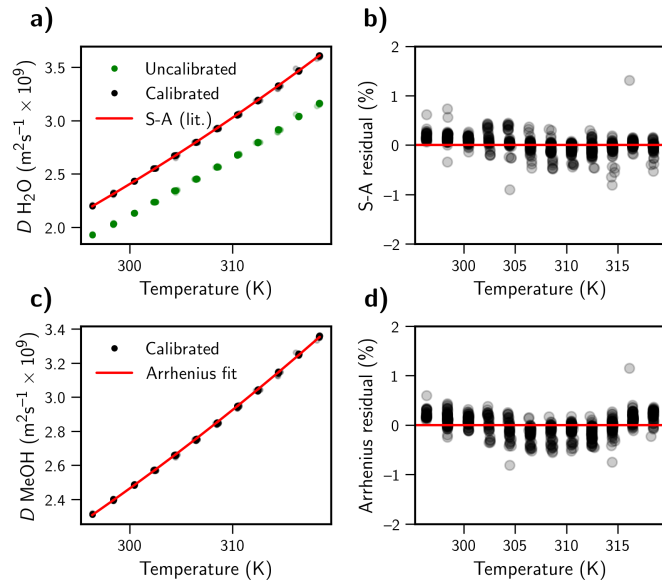


Figure 7.3. Diffusion-temperature measurements of water and methanol in separate sealed glass capillaries in an NMR tube of DMSO-d₆ solution (for locking and shimming), measured by ¹H NMR (PGSE, 500 MHz, δ = 1 ms, Δ = 50 ms). a) Gradient calibration by fitting the measured self-diffusion coefficient of water (green) to a literature diffusion-temperature curve (red). Calibrated measurements shown in black. b) Residual plot of measured water diffusion after calibration. c) Calibrated diffusion-temperature measurements of methanol (black) with a fitted Arrhenius curve (Equation 2.2) with constants $D_0 = (4.84 \pm 0.09) \times 10^{-7} \text{ m}^2 \text{s}^{-1}$, A = $(1583 \pm 6) \text{ K}$ (red). d) Residual plot of measured methanol diffusion against Arrhenius fit.

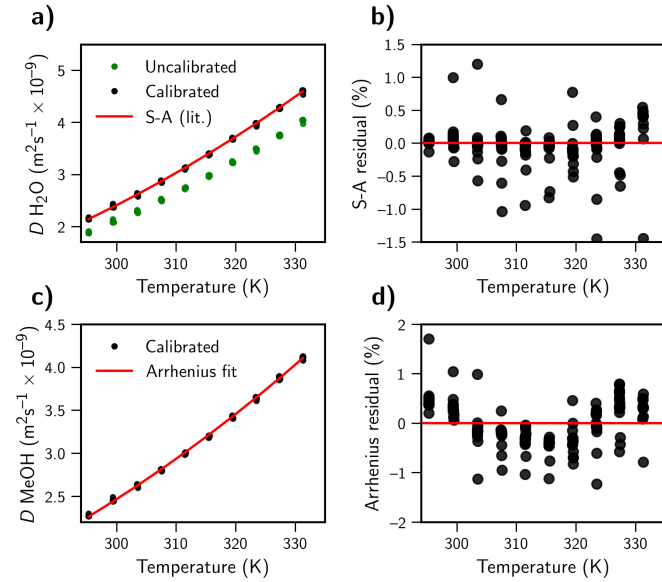


Figure 7.4. Diffusion-temperature measurements of water and methanol in separate sealed glass capillaries in an NMR tube of DMSO-d₆ solution (for locking and shimming), measured by ¹H NMR (PGSE, 500 MHz, δ = 1.1 ms, Δ = 45 ms). a) Gradient calibration by fitting the measured self-diffusion coefficient of water (green) to a literature diffusion-temperature curve (red). Calibrated measurements shown in black. b) Residual plot of measured water diffusion after calibration. c) Calibrated diffusion-temperature measurements of methanol (black) with a fitted Arrhenius curve (Equation 2.2) with constants $D_0 = (4.970 \pm 0.016) \times 10^{-7} \text{ m}^2 \text{s}^{-1}$, A = $(1592 \pm 1) \text{ K}$ (red). d) Residual plot of measured methanol diffusion against Arrhenius fit.

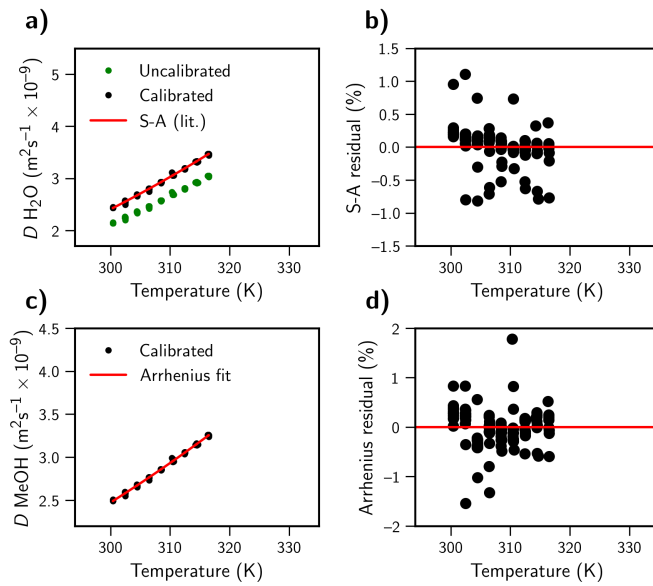


Figure 7.5. Diffusion-temperature measurements of water and methanol in separate sealed glass capillaries in an NMR tube of DMSO-d₆ solution (for locking and shimming), measured by ¹H NMR (PGSTE, 500 MHz, δ = 1.25 ms, Δ = 30 ms). a) Gradient calibration by fitting the measured self-diffusion coefficient of water (green) to a literature diffusion-temperature curve (red). Calibrated measurements shown in black. b) Residual plot of measured water diffusion after calibration. c) Calibrated diffusion-temperature measurements of methanol (black) with a fitted Arrhenius curve (Equation 2.2) with constants $D_0 = (5.46 \pm 0.05) \times 10^{-7} \text{ m}^2 \text{s}^{-1}$, A = (1620 ± 3) K (red). d) Residual plot of measured methanol diffusion against Arrhenius fit.

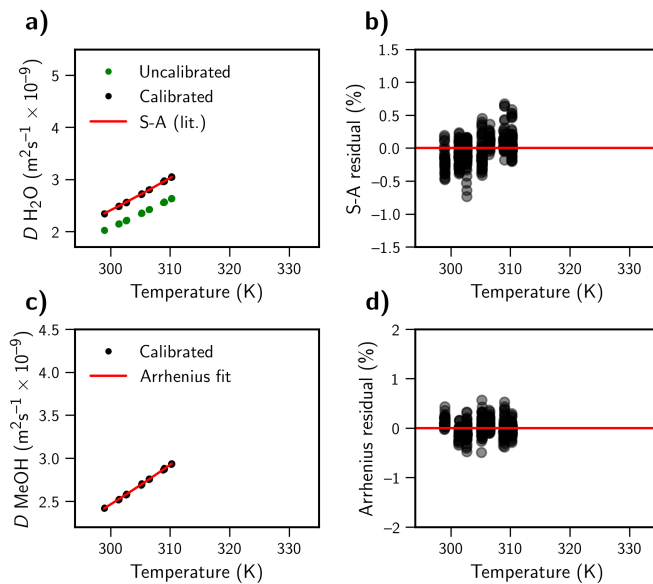
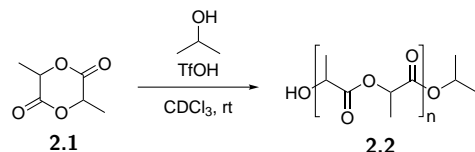


Figure 7.6. Diffusion-temperature measurements of water and methanol in separate sealed glass capillaries in an NMR tube of DMSO-d₆ solution (for locking and shimming), measured by ¹H NMR (PGSE, 600 MHz, δ = 1.1 ms, Δ = 45 ms). a) Gradient calibration by fitting the measured self-diffusion coefficient of water (green) to a literature diffusion-temperature curve (red). Calibrated measurements shown in black. b) Residual plot of measured water diffusion after calibration. c) Calibrated diffusion-temperature measurements of methanol (black) with a fitted Arrhenius curve (Equation 2.2) with constants $D_0 = (5.00 \pm 0.04) \times 10^{-7} \text{ m}^2 \text{s}^{-1}$, A = (1594 ± 2) K (red). d) Residual plot of measured methanol diffusion against Arrhenius fit.

7.2 Diffusion study of living polymerisation



As described in the literature,^[2] DL-Lactide (72 mg, 0.5 mmol, 20 eq) **2.1** dissolved in 500 µl CDCl_3 . Trifluoromethanesulfonic acid (2.2 µl, 25 µmol, 1 eq) and isopropanol (1.9 µl, 25 µmol, 1 eq) were added before transferring the reaction mixture into an NMR tube containing a flame-sealed methanol capillary (HPLC grade methanol in Sigma-Aldrich 5 µl TLC spotting pipette, for approximately 2–3 µL of methanol within the active volume of the NMR probe). Reaction completion and diffusion coefficients of monomer **2.1** and polymerising oligomer **2.2** were then monitored by NMR, with results shown in Figure 7.7, Figure 7.8, and Figure 7.9. Temperature monitoring with the methanol capillary (Figure 7.8 and Figure 7.9) reveals that internal sample temperature varies by less than 0.5 K over the duration of the experiment.

Diffusion results for cationic living polymerisation

NMR experiments were performed using Bruker Avance III HD spectrometers with ^1H frequencies of 500 or 600 MHz. Diffusion experiments were run using the **diffSte** stimulated-echo pulse program implemented through Topspin's **diff5** utility ($\text{ns} = 8$, $\delta = 1.3$ ms, $\Delta = 50$ ms, $\text{td} = 16\text{k}$, 5 s repetition time, hard spoiler gradient used with 1.5 s recovery delay). Three separate experiments were performed, with results presented in Figure 7.7, Figure 7.8, and Figure 7.9. Concentrations and diffusion measurements were determined by integrating the areas of the methyl signals of the monomer and polymer.

7.3 Python scripts for processing diffusion data

After integration of peaks in MestreNova, moving-fit diffusion coefficients were calculated with simple Python scripts (Python 3.6), making use of the **numpy**, **pandas**, and **lmfit** modules. The scripts used are shown in Script 7.1.

Script 7.1 Python scripts for fitting of diffusion data. Functions included are used for processing diffusion data, calculating temperatures from methanol peak chemical shift separations in ppm, and calculating the expected diffusion coefficient of methanol for a given methanol chemical shift separation in ppm.

```

1  '''Module for global fitting of (time-dependent) diffusion NMR data,
2  maintained at: https://github.com/tscmacdonald/diffusion-fits.
3  This module provides the following functions:
4
5  GlobalDiff(data)
6      Global nonlinear fitting of the S-T equation for an arbitrary number of gradients and chemical shift
    environments.
7      Returns an lmfit parameters object containing fitted 1D intensities for all peaks, as well as a
    single globally fitted D value.

```

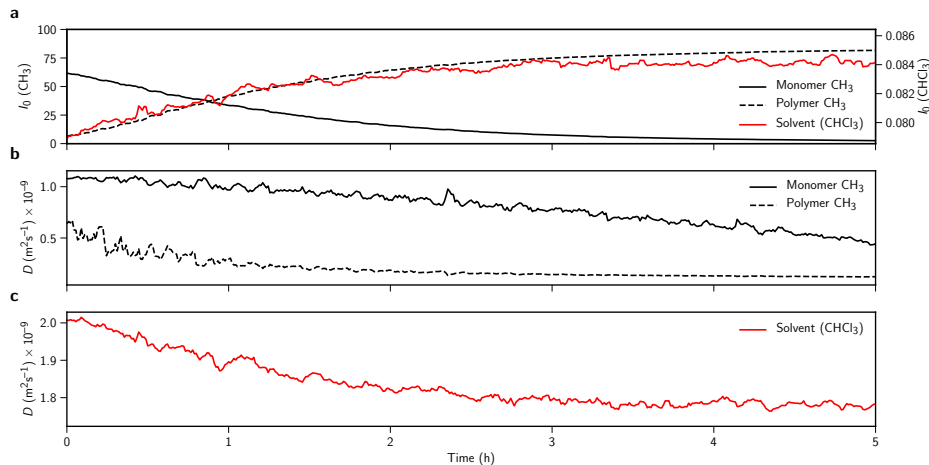


Figure 7.7. a) Relative integrals of the ^1H NMR (500 MHz, CDCl_3) methyl signals of the monomer and polymer (black lines; left axis) and residual chloroform solvent signal (red line; right axis). Integrals are calculated from the curve fitting of the diffusion data. The integral of the residual solvent peak increases over time as the viscosity of the solvent increases, lowering the T_1 time. b) Measured diffusion coefficients of the monomer and polymer over time. c) The measured diffusion coefficient of the residual chloroform signal over time, changing as the viscosity of the solvent increases upon polymer formation.

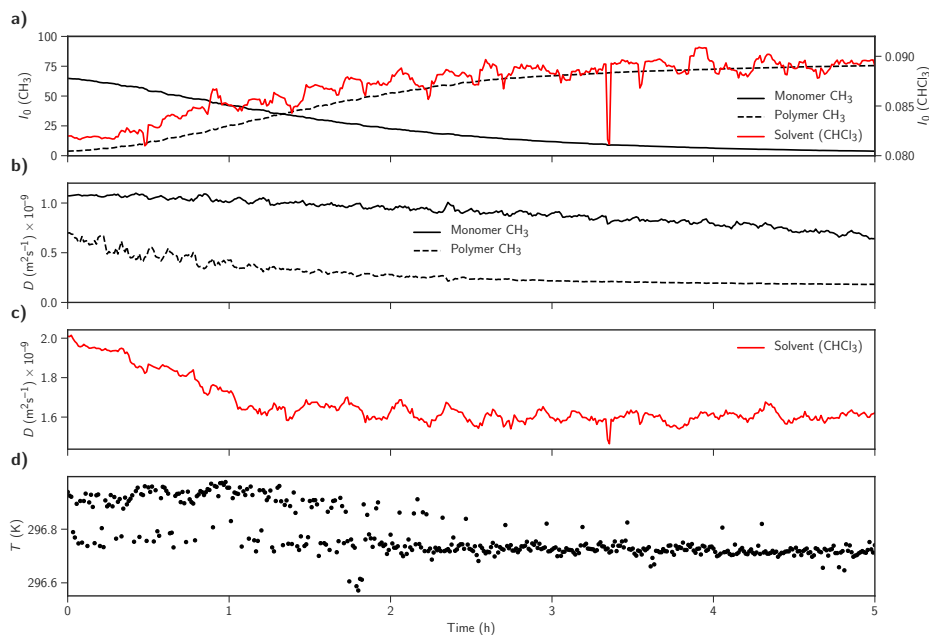


Figure 7.8. a) Relative integrals of the ^1H NMR (500 MHz, CDCl_3) methyl signals of the monomer and polymer (black lines; left axis) and residual chloroform solvent signal (red line; right axis). Integrals are calculated from the curve fitting of the diffusion data. The integral of the residual solvent peak increases over time as the viscosity of the solvent increases, lowering the T_1 time. b) Measured diffusion coefficients of the monomer and polymer over time. c) The measured diffusion coefficient of the residual chloroform signal over time, changing as the viscosity of the solvent increases upon polymer formation. d) The temperature as measured with a methanol capillary and Equation 2.1.

7.3. PYTHON SCRIPTS FOR PROCESSING DIFFUSION DATA

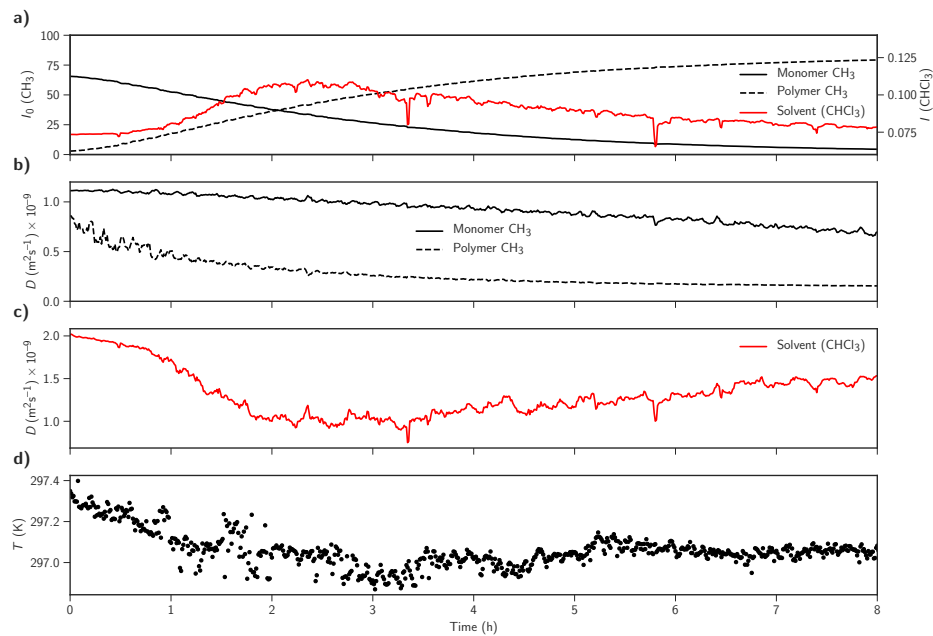


Figure 7.9. a) Relative integrals of the ^1H NMR (600 MHz, CDCl_3) methyl signals of the monomer and polymer (black lines; left axis) and residual chloroform solvent signal (red line; right axis). Integrals are calculated from the curve fitting of the diffusion data. The integral of the residual solvent peak increases over time as the viscosity of the solvent increases, lowering the T_1 time. b) Measured diffusion coefficients of the monomer and polymer over time. c) The measured diffusion coefficient of the residual chloroform signal over time, changing as the viscosity of the solvent increases upon polymer formation. d) The temperature as measured with a methanol capillary and Equation 2.1.

```

8  MovingDiff(data,slicelength=10)
9      Moving average fit for diffusion, using GlobalDiff to obtain a D value for each time point.
10     Takes as input a pandas dataframe with the first column containing B values, and subsequent columns
11     containing integrals for the peaks of interest. Slicelength sets the number of experiments used for
12     each D(time) point.
13     Returns (Dpoints, I0points): two numpy arrays.
14  MovingDiff_csv(fname,slicelength=10)
15      A wrapper for MovingDiff to act on a similarly formatted .csv file.
16  SeparateMovingDiffusion(data,slicelength=10)
17      Generates a pair of pandas dataframes [D,I] containing calculation time-dependent diffusion
18      coefficients and unattenuated integrals.
19      Acts on a pandas dataframe.
20  SeparateMovingDiffusion_csv(fname,slicelength=10)
21      Generates a pair of pandas dataframes [D,I] containing calculation time-dependent diffusion
22      coefficients and unattenuated integrals.
23      Acts on a .csv file with the first column containing B-values, and each subsequent column containing
24      the corresponding integrals
25      for a particular chemical shift.
26  MeOHTemp(dDelta)
27      Calculates temperature from methanol OH-CH3 chemical shift separation (in ppm).
28  MeOHdiff(dDelta)
29      Calculates expected diffusion coefficient from methanol OH-CH3 chemical shift separation (in ppm)
30  ...
31  def GlobalDiff(data):
32      '''Function to globally fit a single diffusion coefficient to data from a list of peaks.
33      Input: a pandas dataframe consisting of:
34          B_0 I0_0 I1_0 ... In_0
35          B_1 I0_1 I1_1 ... In_1

```

```

32 ...
33 B_m IO_m I1_m ... In_m
34 where B is the list of B-parameters for all experiments, and each column In_ contains the integrals
35 ↵ measured for a single peak.
36 The function returns a single lmfit Parameters object.
37 '''
38
39 import numpy as np
40 import pandas as pd
41 from lmfit import minimize, Parameters, report_fit
42
43 def STEExp(B,IO,D):
44     IO,B,D = np.asarray(IO), np.asarray(B), np.asarray(D)
45     return IO*np.exp(-B*D)
46 def STEExp_dataset(B,params,i):
47     IO = params['IO_%i' % (i+1)].value
48     D = params['D_%i' % (i+1)].value
49     return STEExp(B,IO,D)
50 def objective(params,B,data):
51     dataT = np.array(data.T[1:])
52     ndata, nx = dataT.shape
53     resid = 0.0*dataT[:,]
54     #Residual per data set:
55     for i in range(ndata):
56         resid[i,:] = dataT[i,:]-STEExp_dataset(B,params,i)
57     #Flatten to a 1d array as required by lmfit
58     return resid.flatten()
59
60 B = data.iloc[:,0]
61 dataT = np.array(data.T[1:])
62 fit_params = Parameters()
63 for iy, y in enumerate(dataT):
64     fit_params.add('D_%i' % (iy+1), value = 1e-9, min = 1e-12, max = 1e-8)
65     fit_params.add('IO_%i' % (iy+1), value = 100, min = 1, max = 1e8)
66 for iy in range(2,len(dataT)+1):
67     fit_params['D_%i' % iy].expr='D_1'
68 return minimize(objective,fit_params,args=(B,data))
69
70 def MovingDiff(data,slicelength=10):
71     '''Fitting for time-dependent diffusion + concentration data.
72     Input: pandas dataframe formatted as
73     B_0 IO_0 I1_0 ... In_0
74     B_1 IO_1 I1_1 ... In_1
75     ...
76     B_m IO_m I1_m ... In_m
77
78     '''
79
80 import numpy as np
81 import pandas as pd
82 from lmfit import minimize, Parameters, report_fit
83
84 npoints = data.shape[0]-slicelength
85 Dpoints = np.zeros((npoints))
86 I0points = np.zeros((npoints,data.shape[1]-1))
87 I0range = range(I0points.shape[1])
88 for i in range(npoints):
89     params = GlobalDiff(data.iloc[i:i+slicelength])
90     Dpoints[i] = params.params['D_1'].value
91     for j in I0range:
92         I0points[i,j] = params.params['IO_%i' % (j+1)].value
93
94 return Dpoints,I0points

```

```

91 def MovingDiff_csv(fname,slicelength=10):
92     '''A simple wrapper of MovingDiff() to act on .csv files'''
93     import pandas as pd
94     return MovingDiff(pd.read_csv(fname),slicelength)
95
96 def SeparateMovingDiffusion(data,slicelength=10):
97     '''Moving average diffusion processing for multiple separate chemical species.
98     Acts on a pandas dataframe containing a list of B-values in the first column, and corresponding peak
99     integrals in subsequent columns.
100    Returns a pair of pandas dataframes [D,I] containing the calculated diffusion coefficients and
101    concentrations for each peak present in the input array.'''
102    import pandas as pd
103    D = pd.DataFrame()
104    D,I = MovingDiff(data.iloc[:,[0,1]],slicelength=slicelength)
105    D = pd.DataFrame(D)
106    D.columns = [data.columns[1]]
107    I = pd.DataFrame(I)
108    I.columns = [data.columns[1]]
109    for i in range(2,data.shape[1]):
110        td,ti = MovingDiff(data.iloc[:,[0,i]],slicelength=slicelength)
111        td = pd.DataFrame(td)
112        ti = pd.DataFrame(ti)
113        td.columns = [data.columns[i]]
114        ti.columns = [data.columns[i]]
115        D = pd.concat([D,td],axis=1)
116        I = pd.concat([I,ti],axis=1)
117    return D, I
118 def SeparateMovingDiffusion_csv(fname,slicelength=10):
119     '''A wrapper of SeparateMovingDiffusion to act on .csv files'''
120     import pandas as pd
121     D,I = SeparateMovingDiffusion(pd.read_csv(fname),slicelength=slicelength)
122     return D,I
123
124 def MeOHTemp(dDelta):
125     '''Converts a methanol CH3-OH chemical shift separation (in ppm) into a temperature (in K).
126     See J. Magn. Reson. 1982, 46, 319-321'''
127     return 409-36.54*dDelta-21.85*dDelta**2
128
129 def MeOHDiff(dDelta):
130     '''Calculates the expected self-diffusion coefficient of methanol for a given OH-CH3 peak chemical
131     shift separation.
132     (This work)'''
133     import numpy as np
134     return 5.124e-7 * np.exp((-1601)/(MeOHTemp(dDelta)))

```

7.4 Additional References

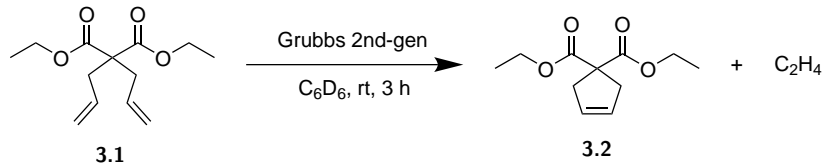
- [1] W. S. Price, P. W. Kuchel, *J. Magn. Reson.* **1991**, *94*, 133–139.
- [2] D. Bourissou, B. Martin-Vaca, A. Dumitrescu, M. Graullier, F. Lacombe, *Macromolecules* **2005**, *38*, 9993–9998.

Chapter 8

Appendix for ‘enhanced diffusion’ of molecular catalysts

8.1 Synthesis

8.1.1 Ring-closing metathesis (model reaction 1)

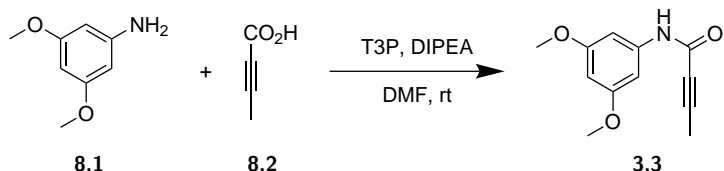


$\text{Cr}(\text{acac})_3$ (3.50 mg, 10 μmol) was dissolved in 500 μL C_6D_6 to make a 20 mM stock solution, then diluted in C_6D_6 to 1 mM before use.

Grubb’s 2nd-generation catalyst (1.27 mg, 1.5 μmol) was dissolved in 500 μL of stock solution (1 mM $\text{Cr}(\text{acac})_3$ in C_6D_6) and transferred to a standard 5 mm NMR tube with optional CH_3OH capillary (see Chapter 2^[1]), and used to lock, tune/match, and shim the NMR instrument. After a single-scan ^1H scan to check the lineshape, a long random-gradient diffusion experiment was prepared for acquisition. The sample was then removed from the instrument and diethyl diallyl malonate (**3.1**, 24 μL , 100 μmol) added by syringe to give a 200 mM solution. The sample was then quickly capped and rolled and shaken to mix, before returning it to the instrument and beginning acquisition as quickly as possible (typically 2–5 min from mixing).

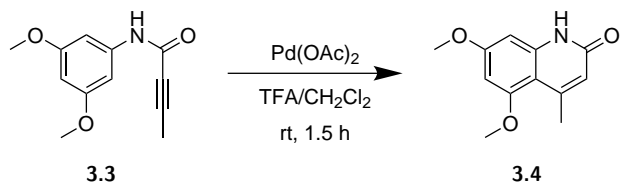
For experiments involving narrow 3 mm NMR tubes, mixing by rolling the NMR tube was ineffective and the reaction mixture was instead prepared in a small vial and subsequently transferred to the narrow tube. This meant that locking, shimming, and tuning/matching had to be performed after the reaction had already begun, and led to a longer delay of 5–10 min between initial mixing and acquisition of the first spectrum.

8.1.2 Synthesis of substrate for palladium-catalysed cyclisation



Tetrolic acid **8.2** (500 mg, 5.95 mmol, 1 eq) and 3,5-dimethoxyaniline **8.1** (1.0 g, 6.6 mmol, 1.1 eq) were combined in 5 mL DMF. Diisopropylethylamine (2.7 mL, 15 mmol, 2.5 eq) added, and reaction mixture cooled to 0 °C with stirring. Propylphosphonic anhydride (‘T3P’, 5.6 mL 50 wt% solution in DMF; 2.8 g, 8.8 mmol, 1.5 eq) added dropwise with stirring, and reaction mixture left to stir overnight. The reaction mixture was then diluted with ethyl acetate (100mL) and washed with NaHCO₃ solution (3 × 25 mL), water (25 mL), brine (25 mL), dried over MgSO₄, and concentrated under reduced pressure to give a brown solid. Recrystallisation from hot toluene/hexanes gave the pure **3.3** as a white amorphous solid in 65% yield. ¹H spectra (CDCl₃) were in accordance with those previously reported.^[2]

8.1.3 Palladium-catalysed arylation (model reaction 2)



Palladium acetate was dissolved in trifluoroacetic acid to make a 60 mM stock solution (13.6 mg/mL). Alkyne **3.3** (22 mg, 100 µmol) was dissolved in 500 µL 3:1 trifluoroacetic acid:CD₂Cl₂ to make a 200 mM solution and transferred to a standard 5 mm NMR tube and used to lock, tune/match, and shim the NMR instrument. After a single-scane ¹H experiment to check lineshape, a long random-gradient diffusion experiment was prepared. The sample was then removed from the instrument and Pd(OAc)₂ in TFA (25 µL of the 60 mM stock solution, 1.5 µmol Pd(OAc)₂) added to give a 3 mM solution of catalyst in the reaction mixture. The sample was then shaken and rolled to mix the solution, returned to the instrument and the diffusion experiment started as quickly as possible (2–5 min).

For experiments involving narrow 3 mm NMR tubes, mixing by rolling the NMR tube was ineffective and the reaction mixture was instead prepared in a small vial and subsequently transferred to the narrow tube. This meant that locking, shimming, and tuning/matching had to be performed after the reaction had already begun, and led to a longer delay of 5–10 min between initial mixing and acquisition of the first spectrum.

8.2 General NMR experimental, acquisition, and processing

NMR experiments were conducted using a 500 MHz Bruker Avance III spectrometer equipped with a TBI probe fitted with standard high-resolution gradient coils capable of generating

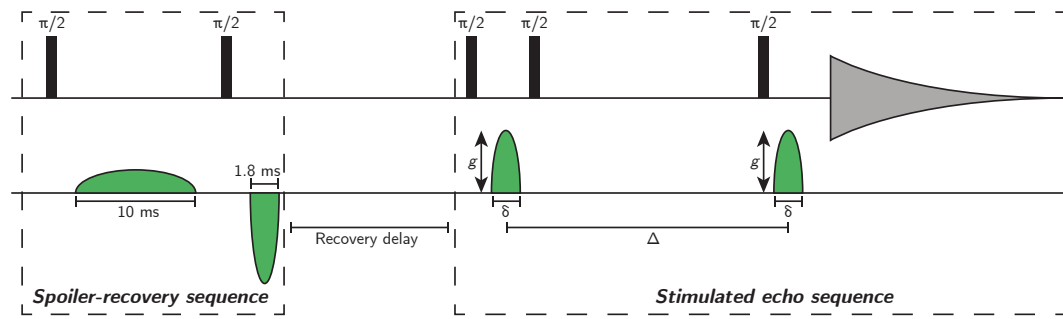


Figure 8.1. Pulsed gradient stimulated echo (PGSTE) sequence with spoiler-recovery sequence,^[3] used for rapid acquisition of diffusion data. A spoiler-recovery sequence consisting of two mismatched gradient pulses of +33% and -90% g_{max} was used to destroy residual magnetisation between experiments, allowing faster repetition rates.^[1]

gradient pulses up to 53.45 G cm^{-1} . Diffusion experiments were set up using the Bruker **diff5** utility and used the **diffSte** stimulated-echo pulse sequence Figure 8.1.

Time-resolved diffusion data were obtained using the methods previously described in Chapter 2,^[1] with diffusion spectra continually acquired using random gradient lists of 200–1000 gradients with $5\text{--}53.45 \text{ G cm}^{-1}$ gradient pulses. Typical experimental parameters for the Grubbs and Pd-catalysed cyclisation reactions with respective diffusion coefficients of 1–2 and $0.5\text{--}1 10^{-9} \text{ m}^2 \text{ s}^{-1}$ were $\Delta = 50 \text{ ms}$ and $\delta = 1.2 \text{ ms}$ or 1.8 ms , respectively. Gradient pulses were sine-shaped and ranged in amplitude from $0\text{--}53.45 \text{ G cm}^{-1}$. Spoiler gradient pulses with a 1.5 s delay to allow for recovery were used for fast acquisition of diffusion data. Representative examples of stacked random-gradient diffusion spectra for both reactions studied are shown in Figure 8.2.

8.3 Diffusion data for Grubbs metathesis reaction

8.3.1 Agreement of static diffusion coefficients with the literature

The diffusion coefficient of ^{14}C -labelled benzene at 298 K has been reported^[4] as $2.17 \times 10^{-9} \text{ m}^2 \text{ s}^{-1}$, which is in acceptable agreement with the diffusion coefficient of $2.03 \times 10^{-9} \text{ m}^2 \text{ s}^{-1}$ measured for benzene-d₅ in the absence of chemical reaction in this work. The at-rest diffusion coefficients for the other chemical species were measured as shown in Table 8.1 (500 MHz, 500 μL solution in C₆D₆, $\Delta = 50 \text{ ms}$, $\delta = 1.3 \text{ ms}$, ns = 8).

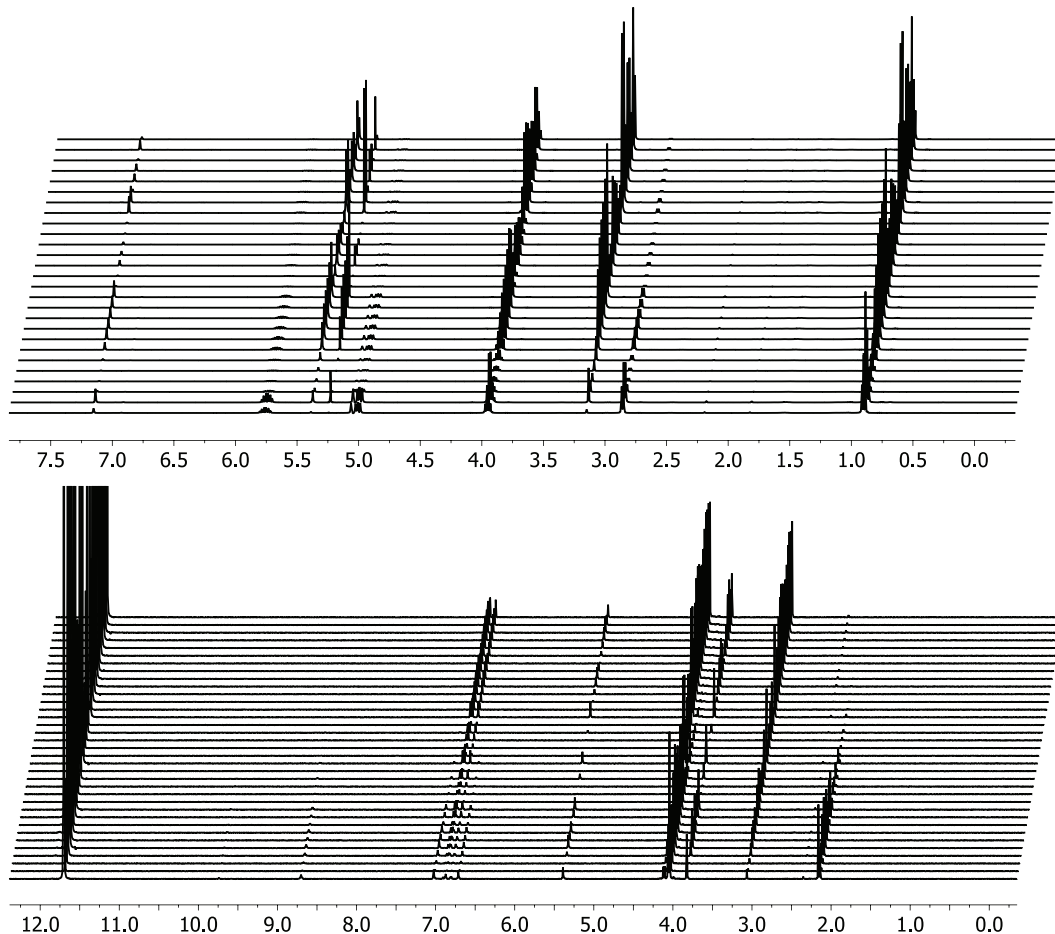


Figure 8.2. Stacked NMR spectra of representative random-gradient diffusion experiments. Top: Grubbs ring-closing metathesis (500 MHz, C₆D₆, 270 random gradient slices; 10× decimation for clarity). Bottom: Pd-catalysed cyclisation (500 MHz, TFA+CD₂Cl₂, 350 random gradient slices; 10× decimation

Table 8.1. At-rest diffusion coefficients measured by NMR (500 MHz, 500 µL solution in C₆D₆, Δ = 50 ms, δ = 1.3 ms, ns = 8).

Species	$D / 10^{-9} \text{ m}^2 \text{s}^{-1}$
Benzene ^[a]	2.03
DDM ^[a]	1.08
Reaction product ^[b]	1.16
Grubbs’ catalyst ^[c]	0.65
Dissolved ethylene ^[b]	3.46

[a] 200 mM DDM in C₆D₆, without added catalyst.

[b] Measured in reaction mixture long (>10 h) after reaction completion.

[c] Measured for 3 mM solution of Grubbs’ catalyst in C₆D₆ (no DDM or reaction product present)

8.3.2 Standard conditions: 200 mM DDM, 3 mM Grubbs catalyst

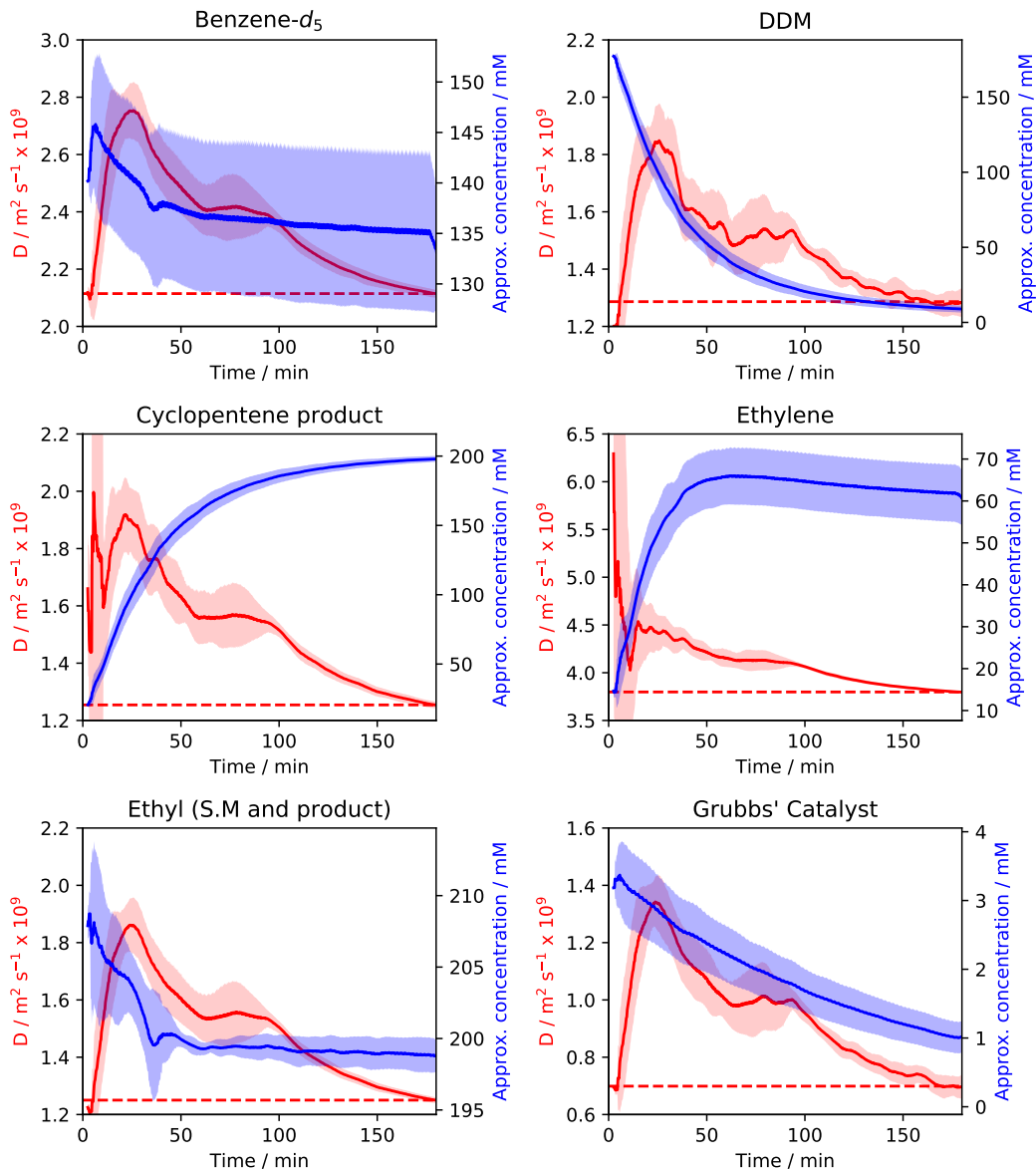


Figure 8.3. Concentration and diffusion changes for all chemical species during Grubbs metathesis (200 mM DDM, 3 mM Grubbs catalyst, C_6D_6 ; 1H , 500 MHz, $\delta = 1.3$ ms, $\Delta = 50$ ms). Red lines and shaded areas represent measured diffusion coefficients and associated error; blue lines and shaded areas respectively represent measured concentrations and associated error from eight experiments. Red dashed lines show measured diffusion coefficients on reaction completion. Concentrations calibrated from the ethyl protons as an internal standard at assumed 200 mM concentration.

8.3.3 Reduced catalyst loading: 200 mM DDM, 0.5 mM Grubbs catalyst

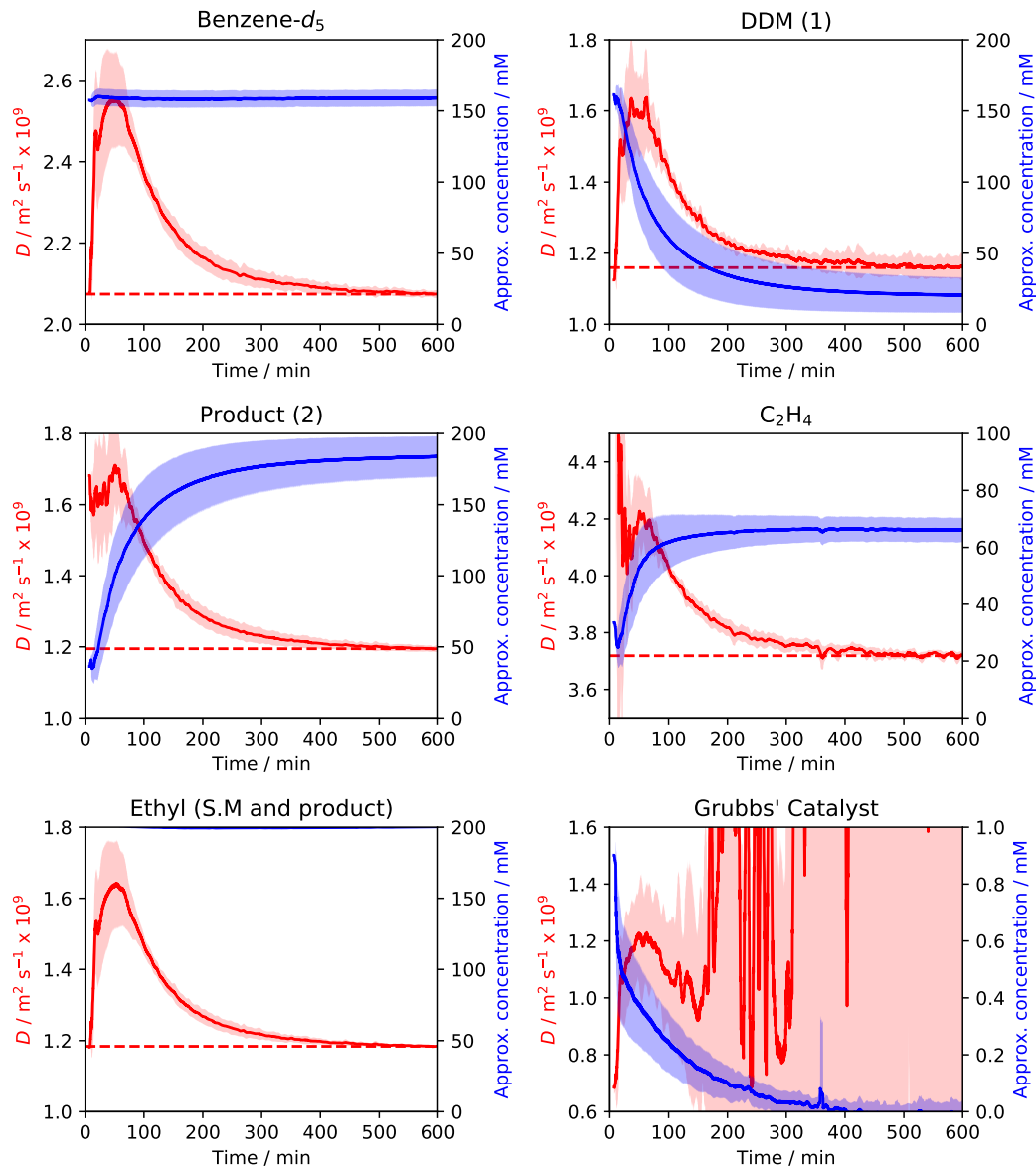


Figure 8.4. Concentration and diffusion changes for all chemical species during Grubbs metathesis (200 mM DDM, 0.5 mM Grubbs catalyst, C_6D_6 ; ^1H , 500 MHz, $\delta = 1.3$ ms, $\Delta = 50$ ms). Red lines and shaded areas represent measured diffusion coefficients and associated error; blue lines and shaded areas respectively represent measured concentrations and associated error from eight experiments. Red dashed lines show measured diffusion coefficients on reaction completion. Concentrations calibrated from the ethyl protons as an internal standard at assumed 200 mM concentration.

8.3.4 Reduced substrate loading: 100 mM DDM, 3 mM Grubbs catalyst

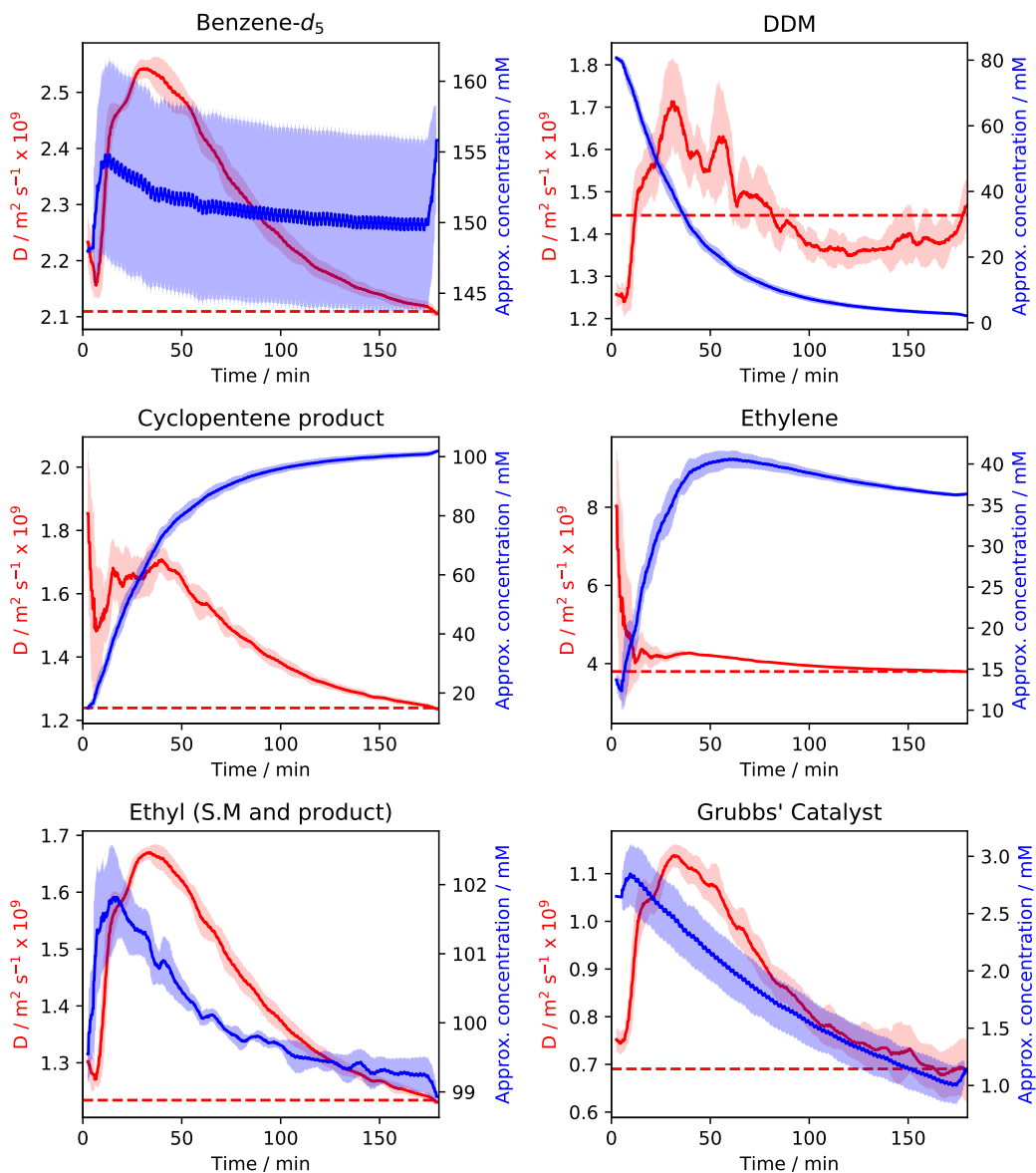


Figure 8.5. Concentration and diffusion changes for all chemical species during Grubbs metathesis (100 mM DDM, 3 mM Grubbs catalyst, C_6D_6 ; ^1H , 500 MHz, $\delta = 1.3$ ms, $\Delta = 50$ ms). Red lines and shaded areas represent measured diffusion coefficients and associated error; blue lines and shaded areas respectively represent measured concentrations and associated error from eight experiments. Red dashed lines show measured diffusion coefficients on reaction completion. Concentrations calibrated from the ethyl protons as an internal standard at assumed 100 mM concentration.

8.3.5 Convection studies: influence of measurement time Δ on measured diffusion

Varying Δ : $\Delta = 25$ ms, $\delta = 3.0$ ms, 200 mM DDM, 3 mM Grubbs catalyst

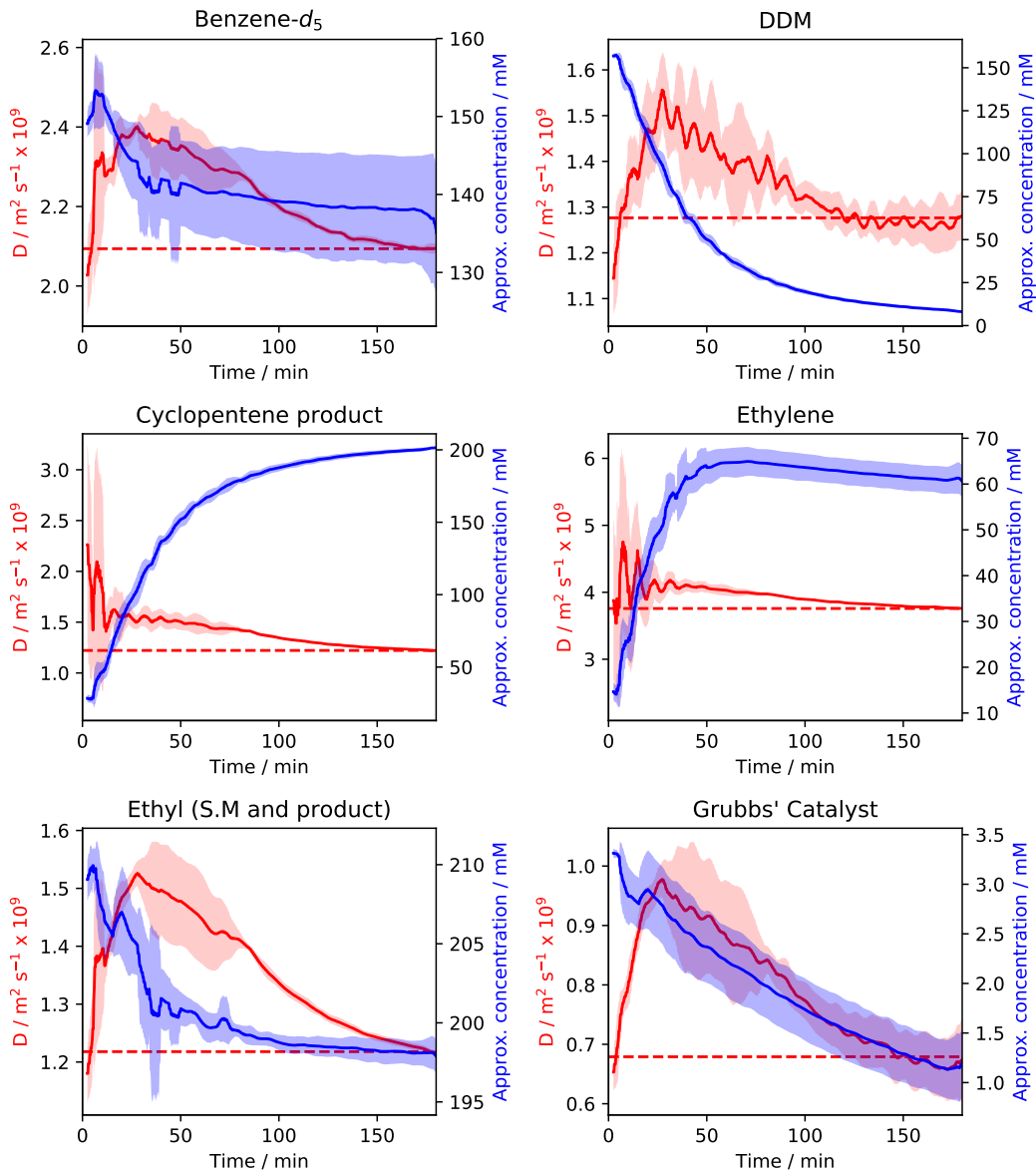


Figure 8.6. Concentration and diffusion changes for all chemical species during Grubbs metathesis (200 mM DDM, 3 mM Grubbs catalyst, C_6D_6 ; ^1H , 500 MHz, $\delta = 3.0$ ms, $\Delta = 25$ ms). Red lines and shaded areas represent measured diffusion coefficients and associated error; blue lines and shaded areas respectively represent measured concentrations and associated error from eight experiments. Red dashed lines show measured diffusion coefficients on reaction completion. Concentrations calibrated from the ethyl protons as an internal standard at assumed 100 mM concentration.

Varying Δ : $\Delta = 100$ ms, $\delta = 1.0$ ms, 200 mM DDM, 3 mM Grubbs catalyst

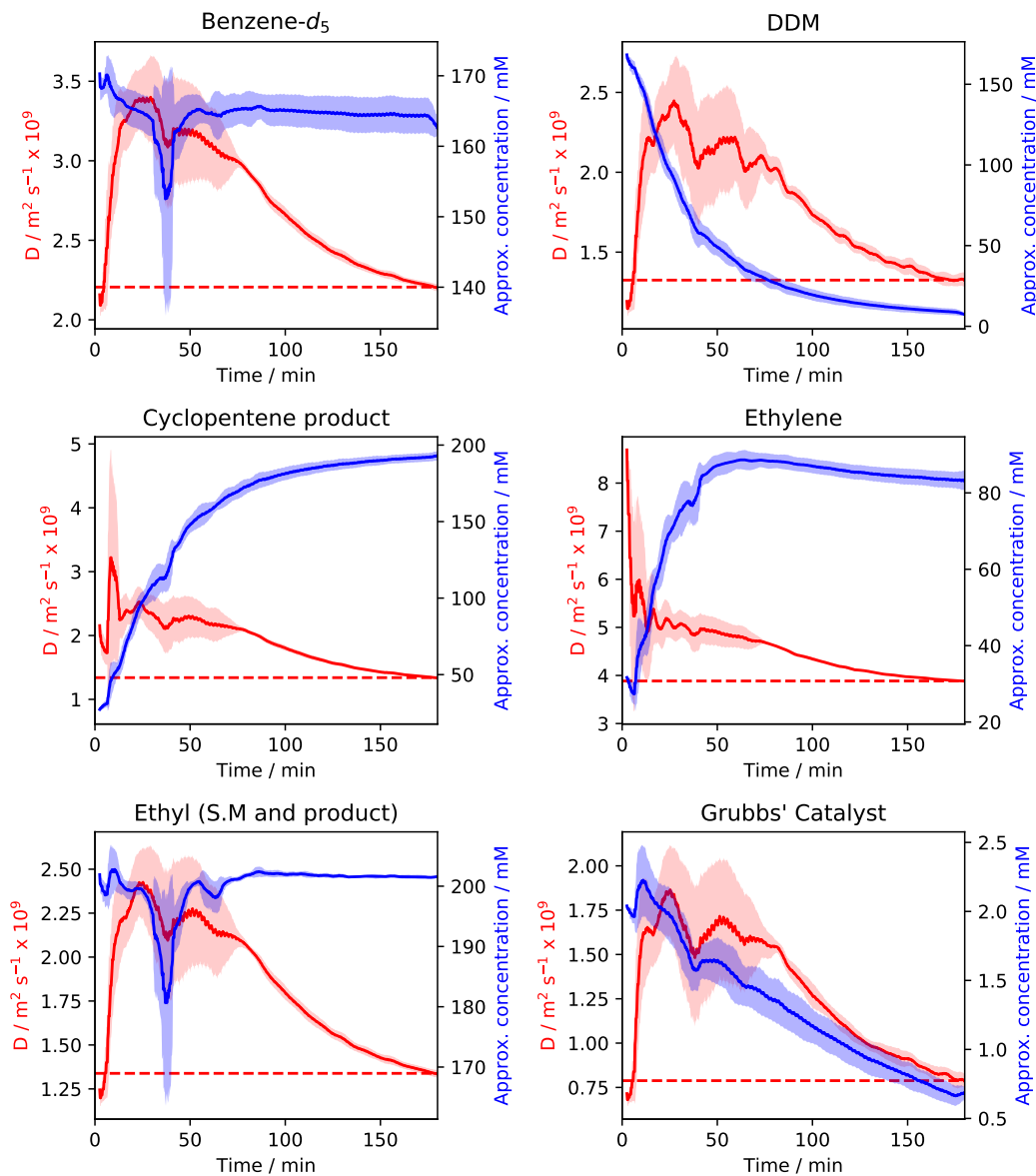


Figure 8.7. Concentration and diffusion changes for all chemical species during Grubbs metathesis (200 mM DDM, 3 mM Grubbs catalyst, C_6D_6 ; ^1H , 500 MHz, $\delta = 1.0$ ms, $\Delta = 100$ ms). Red lines and shaded areas represent measured diffusion coefficients and associated error; blue lines and shaded areas respectively represent measured concentrations and associated error from eight experiments. Red dashed lines show measured diffusion coefficients on reaction completion. Concentrations calibrated from the ethyl protons as an internal standard at assumed 100 mM concentration.

8.4 Diffusion data for palladium-catalysed cyclisation

8.4.1 Agreement of static diffusion coefficients with the literature

At-rest diffusion coefficients of chemical species under reaction conditions (before addition of Pd(OAc)₂ or long after reaction completion) were measured as shown in Table 8.2 (500 MHz, 500 µL solution, Δ = 50 ms, δ = 1.8 ms, ns = 8).

Table 8.2. The at-rest diffusion measured by NMR (500 MHz, 500 µL solution in C₆D₆, Δ = 50 ms, δ = 1.8 ms, ns = 8).

Species	$D / 10^{-9} \text{ m}^2 \text{s}^{-1}$
Trifluoroacetic acid (OH proton) ^[a]	1.5
CDHCl ₂ ^[a]	3.2
Alkyne 3 ^[a]	0.7
Quinolinone 4 ^[b]	0.7

^[a] 200 mM in 3:1 TFA:CD₂Cl₂, without catalyst added.

^[b] Measured in reaction mixture long (>10 h) after reaction completion.

8.4.2 Diffusion and concentration plots for palladium-catalysed cyclisation

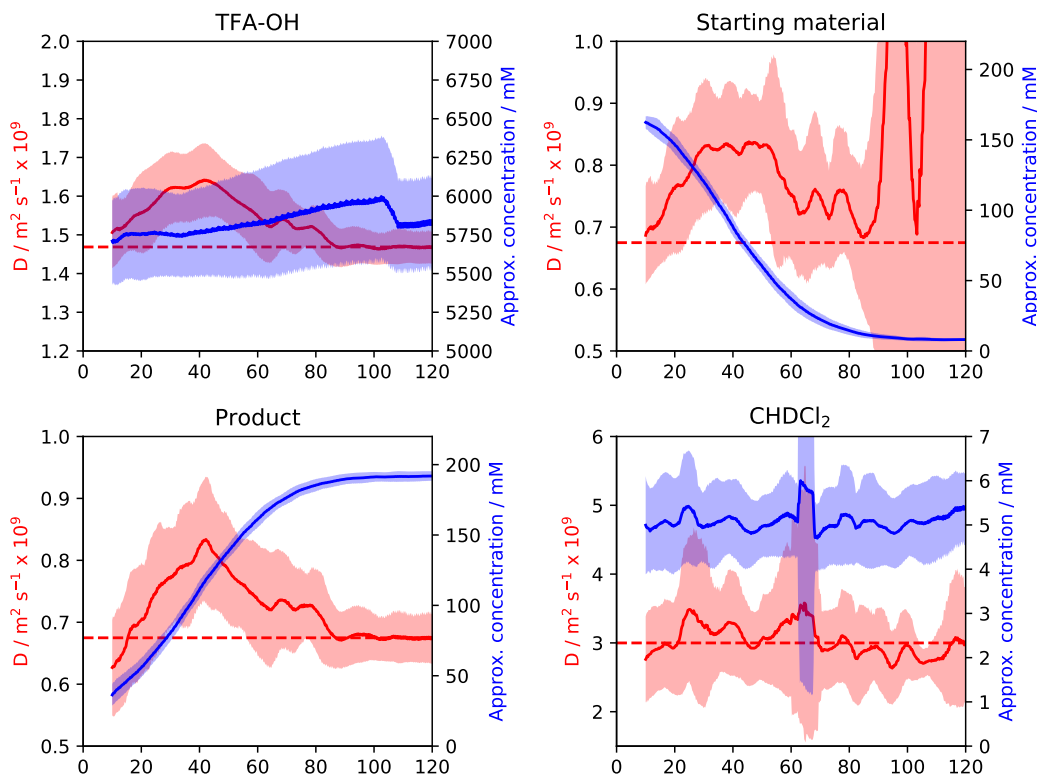


Figure 8.8. Concentration and diffusion changes for all chemical species during palladium-catalysed intramolecular cyclisation (200 mM substrate, 3 mM Pd(OAc)₂, 3:1 TFA:CD₂Cl₂; ${}^1\text{H}$, 500 MHz, $\delta = 1.8 \text{ ms}$, $\Delta = 50 \text{ ms}$). Red lines and shaded areas represent measured diffusion coefficients and associated error; blue lines and shaded areas represent measured concentrations and associated error. Concentrations calibrated from the sum of starting material and product at assumed 200 mM concentration.

8.4.3 Convection studies: influence of measurement time Δ on measured diffusion coefficients for Pd-catalysed cyclisation

Influence of stimulated echo delay Δ : $\Delta = 25 \text{ ms}$

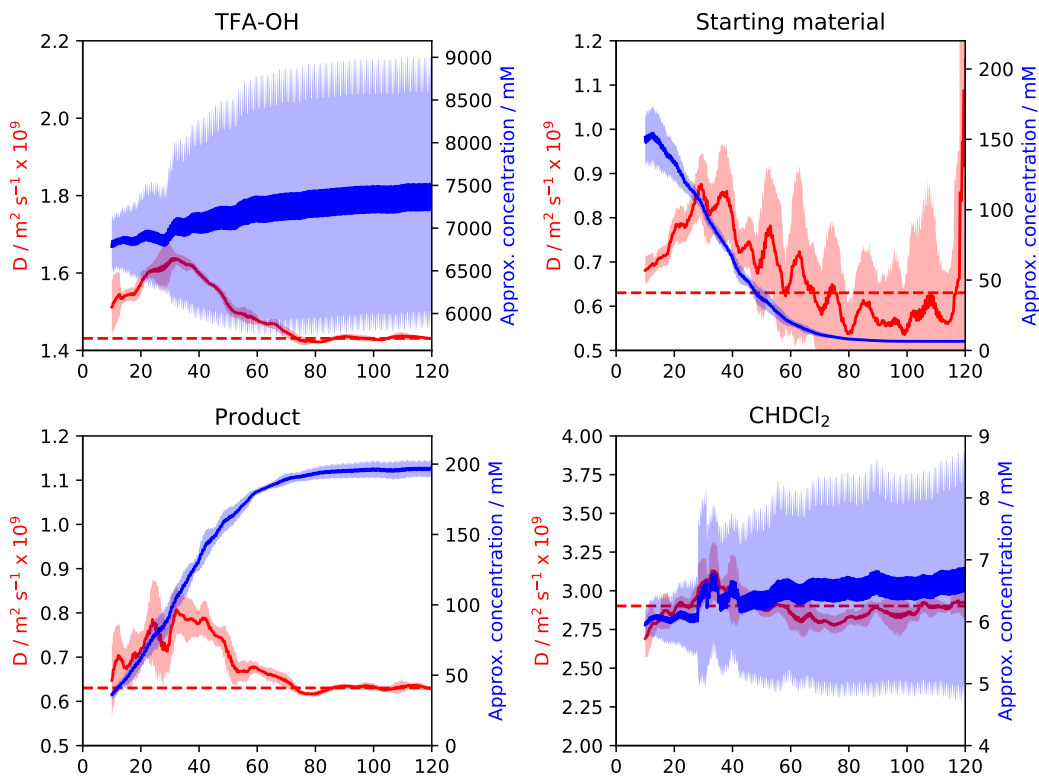


Figure 8.9. Concentration and diffusion changes for all chemical species during palladium-catalysed intramolecular cyclisation (200 mM substrate, 3 mM $\text{Pd}(\text{OAc})_2$, 3:1 TFA: CD_2Cl_2 ; ${}^1\text{H}$, 500 MHz, $\delta = 2.5 \text{ ms}$, $\Delta = 25 \text{ ms}$). Red lines and shaded areas represent measured diffusion coefficients and associated error; blue lines and shaded areas represent measured concentrations and associated error. Concentrations calibrated from the sum of starting material and product at assumed 200 mM concentration.

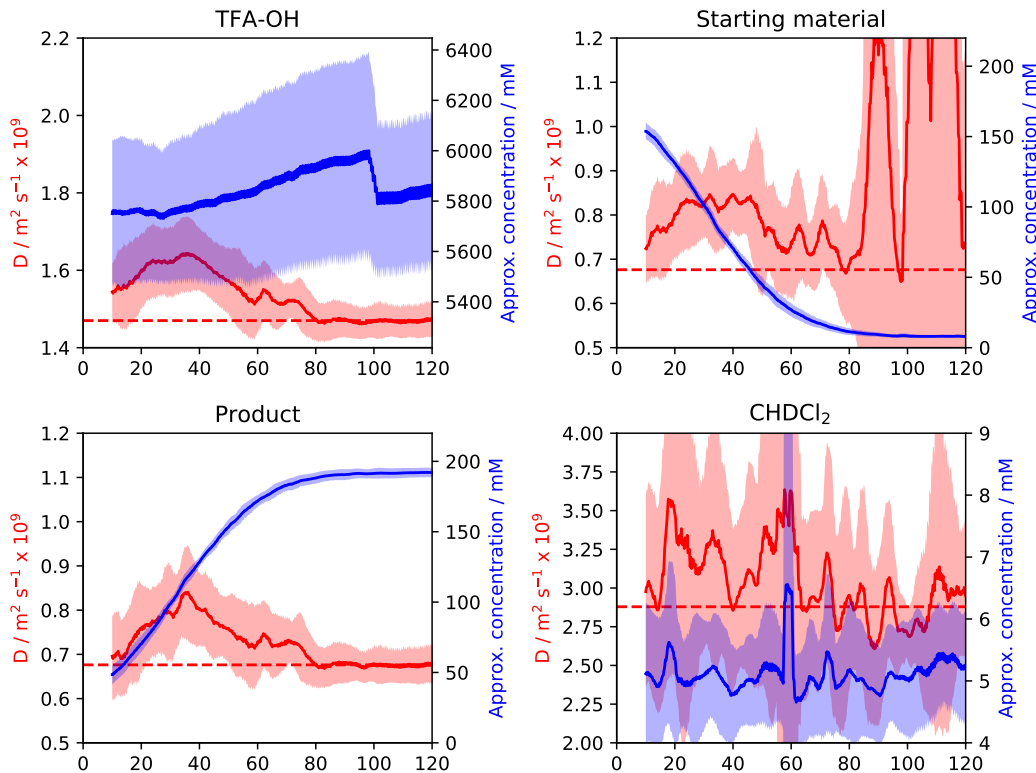
Influence of stimulated echo delay Δ : $\Delta = 50$ ms

Figure 8.10. Concentration and diffusion changes for all chemical species during palladium-catalysed intramolecular cyclisation (200 mM substrate, 3 mM $\text{Pd}(\text{OAc})_2$, 3:1 TFA:CD₂Cl₂; ^1H , 500 MHz, $\delta = 1.8$ ms, $\Delta = 50$ ms). Red lines and shaded areas represent measured diffusion coefficients and associated error; blue lines and shaded areas represent measured concentrations and associated error. Concentrations calibrated from the sum of starting material and product at assumed 200 mM concentration.

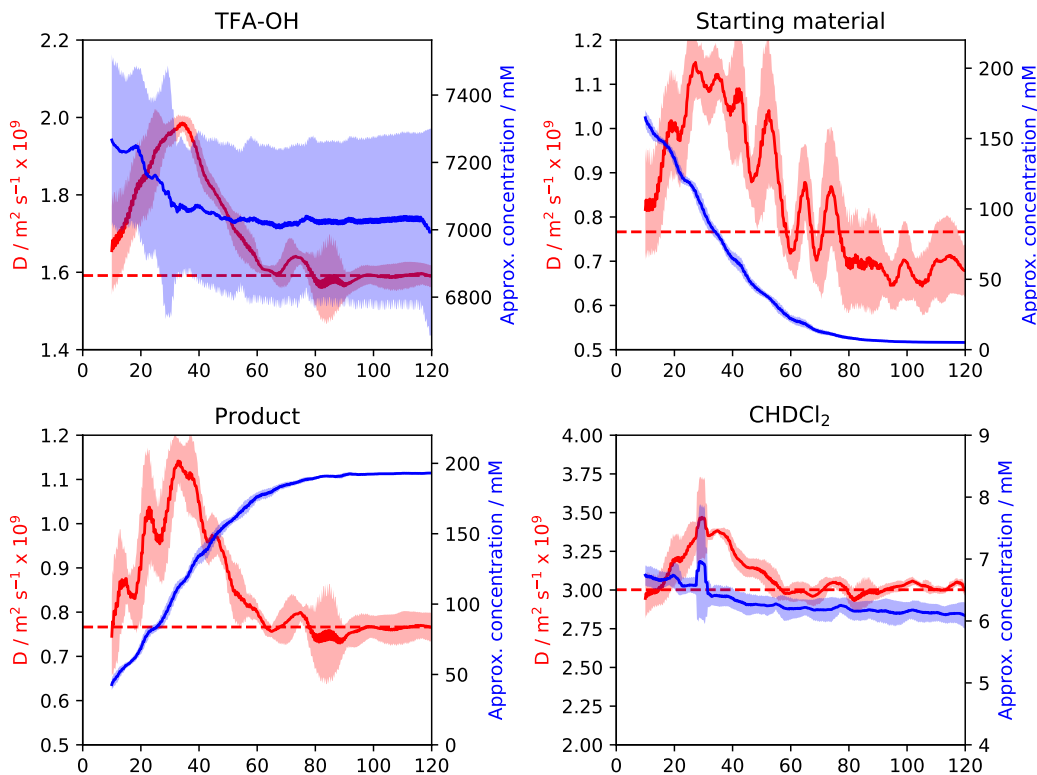
Influence of stimulated echo delay Δ : $\Delta = 100 \text{ ms}$ 

Figure 8.11. Concentration and diffusion changes for all chemical species during palladium-catalysed intramolecular cyclisation (200 mM substrate, 3 mM Pd(OAc)₂, 3:1 TFA:CD₂Cl₂; ¹H, 500 MHz, $\delta = 1.1 \text{ ms}$, $\Delta = 100 \text{ ms}$). Red lines and shaded areas represent measured diffusion coefficients and associated error; blue lines and shaded areas represent measured concentrations and associated error. Concentrations calibrated from the sum of starting material and product at assumed 200 mM concentration.

8.5 Influence of sample geometry on measured diffusion

8.5.1 Use of a restricted-volume Shigemi tube

As convection is known to depend substantially on sample geometry, diffusion behaviour was also investigated in a restricted volume Shigemi NMR tube. The palladium-catalysed arylation reaction was chosen as a model due to concerns regarding gas generation within the enclosed environment of a Shigemi tube, with results presented in Figure 8.12. A 100 ms Δ delay was used such that any bulk motion would be readily apparent, and while an increase in measured D was observed the increase was much less than that seen in the comparable experiment conducted with a standard 5 mm NMR tube (Figure 8.8). While the trifluoroacetic acid and starting material/product diffusion coefficients were previously observed to increase to approximately 2.0 and $1.1 \times 10^{-9} \text{ m}^2 \text{s}^{-1}$ respectively, under the confines of a restricted volume Shigemi tube smaller increases in diffusion coefficients to 1.5 and $0.75 \times 10^{-9} \text{ m}^2 \text{s}^{-1}$ were observed. This influence of sample geometry on observed diffusion coefficients is difficult to justify based on nano-scale dynamic coupling, but is consistent with convection.

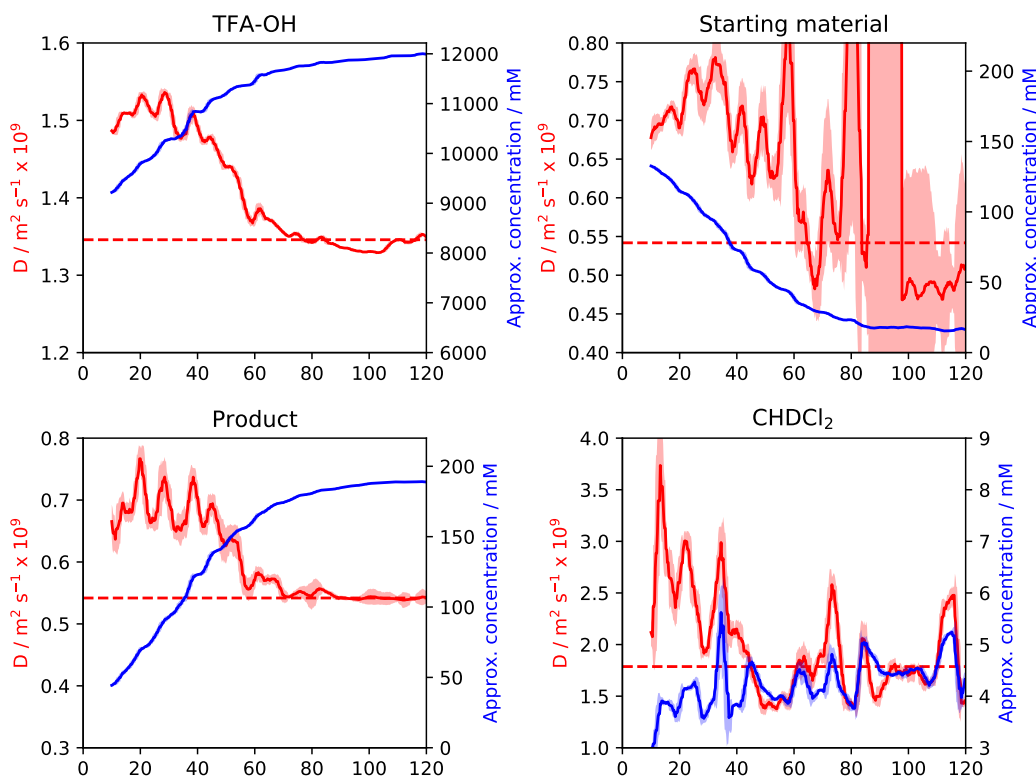


Figure 8.12. Concentration and diffusion changes for all chemical species during palladium-catalyzed intramolecular cyclisation (200 mM substrate, 3 mM Pd(OAc)₂, 3:1 TFA:CD₂Cl₂; ^1H , 500 MHz, $\delta = 1.1 \text{ ms}$, $\Delta = 100 \text{ ms}$) for 200 μL of reaction mixture in a 5 mm Shigemi NMR tube. Red lines and shaded areas represent measured diffusion coefficients and associated error; blue lines and shaded areas represent measured concentrations and associated error. Concentrations calibrated from the sum of starting material and product at assumed 200 mM concentration.

8.5.2 Data for Grubbs reaction in a narrow 3 mm NMR tube

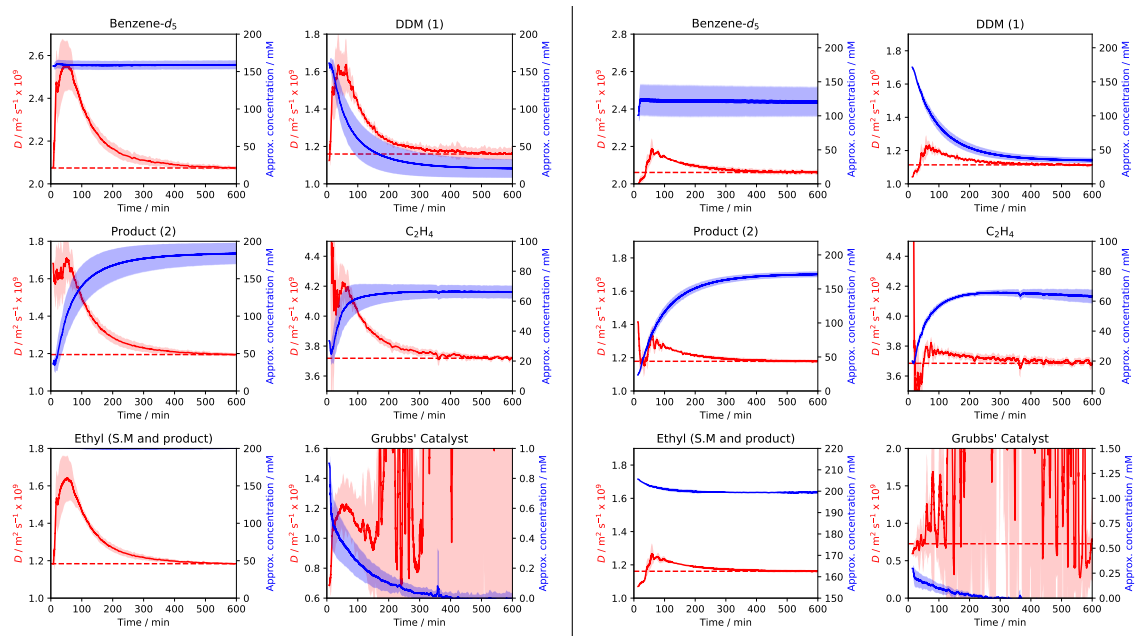


Figure 8.13. Concentration and diffusion changes for all chemical species during Grubbs metathesis (200 mM DDM, 0.5 mM Grubbs catalyst, C_6D_6 ; ^1H , 500 MHz, $\delta = 1.3$ ms, $\Delta = 50$ ms). Left plots: standard conditions in a 5 mm NMR tubes. Right plots: 200 μL of reaction mixture in a 3 mm diameter NMR tube. Red lines and shaded areas represent measured diffusion coefficients and error; blue lines and shaded areas represent measured concentrations and errors. Red dashed lines show measured diffusion coefficients on reaction completion. Data combined from two separate experiments, with concentrations calibrated from the ethyl protons as an internal standard at assumed 200 mM concentration.

8.5.3 Data for palladium-catalysed reaction in a narrow 3 mm NMR tube

The use of a 3 mm NMR tube for diffusion experiments led to an almost entirely flat time-dependent measurement of diffusion (i.e. no observed enhancement in diffusion), even with a long echo delay of $\Delta = 100$ ms. Comparing the results obtained using the 3 mm NMR tube (Figure 8.14) to those obtained using a 5 mm sample tube under otherwise identical conditions (Figure 8.8) the observed “enhanced diffusion” appears entirely dependent on sample geometry. This observation is incompatible with microscopic views of enhanced diffusion as driven by dynamic coupling or molecular interactions, but is entirely consistent with misinterpreted convection driven by temperature or other inhomogeneity across the bulk reaction solution.

8.6 Python code for processing diffusion data

After integration of peaks in MestreNova, moving-fit diffusion coefficients were calculated with simple Python scripts (Python 3.6), making use of the **numpy**, **pandas**, and **lmfit** modules. The scripts used are shown in Script 8.1.

Script 8.1 Python code used for moving-fit diffusion processing and gradient calibration from methanol.

```

1  '''Module for global fitting of (time-dependent) diffusion NMR data.
2  This module provides the following functions:
3
4  GlobalDiff(data)
5      Global nonlinear fitting of the S-T equation for an arbitrary number of gradients and chemical shift
6      environments.
7      Returns an lmfit parameters object containing fitted I0 intensities for all peaks, as well as a
8      single globally fitted D value.
9
10 MovingDiff(data,slicelength=10)
11     Global moving average fit for diffusion, using GlobalDiff to obtain a D value for each time point. S
12     Takes as input a pandas dataframe with the first column containing B values, and subsequent columns
13     containing integrals for the peaks of interest.
14     Slicelength sets the number of experiments used for each D(time) point. Slicetime sets the time (in
15     minutes) taken to acquire each gradient slice.
16     Returns (Dpoints, I0points,Derr,Ierr): four pandas dataframes, each with indices corresponding to
17     time. I0points and Ierr contain a column for each fitted NMR peak, while Dpoint and Der contain a
18     single column with globally fitted diffusion data.
19     For systems involving multiple chemical species, use SeparateMovingDiffusion to obtain individual
20     (non-globally fitted) diffusion coefficients.
21     Dpoints, I0points, Derr, and Ierr contain diffusion points, extrapolated intensities, and respective
22     errors for each from fitting.
23     MovingDiff_csv(fname,slicelength=10,slicetime=2/3)
24     A wrapper for MovingDiff to act on a similarly formatted .csv file.
SeparateMovingDiffusion(data,slicelength=10,slicetime=2/3)
    Returns (Dpoints, I0points,Derr,Ierr): four pandas dataframes, each with indexes corresponding to
    time and a column for each peak.
    Dpoints, I0points, Derr, and Ierr contain diffusion points, extrapolated intensities, and respective
    errors for each from fitting.
SeparateMovingDiffusion_csv(fname,slicelength=10,slicetime=2/3)
    Generates a pair of pandas dataframes [D,I] containing calculation time-dependent diffusion
    coefficients and unattenuated integrals.
    Acts on a .csv file with the first column containing B-values, and each subsequent column containing
    the corresponding integrals for a particular chemical shift.
MeOHTemp(dDelta)
    Calculates temperature from methanol OH-CH3 chemical shift separation (in ppm)
MeOHDiff(dDelta)

```

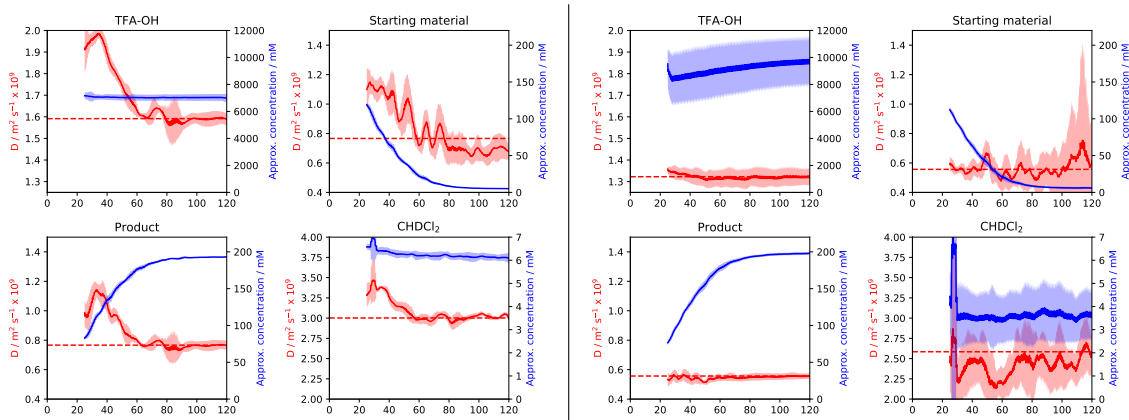


Figure 8.14. Concentration and diffusion changes for all chemical species during palladium-catalyzed intramolecular cyclisation (200 mM substrate, 3 mM Pd(OAc)₂, 3:1 TFA:CD₂Cl₂; ¹H, 500 MHz, δ = 1.1 ms, Δ = 100 ms). Left plots: standard conditions in a 5 mm NMR tube. Right plots: 200 μL of reaction mixture in a 3 mm diameter NMR tube. Data are combined from three separate experiments. Red lines and shaded areas represent measured diffusion coefficients and associated error; blue lines and shaded areas represent measured concentrations and associated error. Concentrations calibrated from the sum of starting material and product at assumed 200 mM concentration.

```

25     Calculates expected diffusion coefficient from methanol OH-CH3 chemical shift separation (in ppm)
26     ...
27
28 def GlobalDiff(data):
29     '''Function to globally fit a single diffusion coefficient to data from a list of peaks
30     Input: a pandas dataframe consisting of:
31
32     B_0 IO_0 I1_0 ... In_0
33     B_1 IO_1 I1_1 ... In_1
34     ...
35     B_m IO_m I1_m ... In_m
36     where B is the list of B-parameters for all experiments, and each column In_ contains the integrals
37     ↪ measured for a single peak.
38     The function returns a single lmfit Parameters object.
39     '''
40
41     import numpy as np
42     import pandas as pd
43     from lmfit import minimize, Parameters, report_fit
44
45     def STExp(B,IO,D):
46         IO,B,D = np.asarray(IO), np.asarray(B), np.asarray(D)
47         return IO*np.exp(-B*D)
48
49     def STExp_dataset(B,params,i):
50         IO = params['IO_%i' % (i+1)].value
51         D = params['D_%i' % (i+1)].value
52         return STExp(B,IO,D)
53
54     def objective(params,B,data):
55         dataT = np.array(data.T[1:])
56         ndata, nx = dataT.shape
57         resid = 0.0*dataT[:,]
58         #Residual per data set:
59         for i in range(ndata):
60             resid[i,:] = dataT[i,:]-STExp_dataset(B,params,i)
61         #Flatten to a 1d array:
62         return resid.flatten()
63
64     B = data.iloc[:,0]
65     dataT = np.array(data.T[1:])
66     fit_params = Parameters()
67     IOguesses = data.max()[1:]
68
69     for iy, y in enumerate(dataT):
70         fit_params.add('D_%i' % (iy+1), value = 1e-9, min = 1e-12, max = 1e-8)
71         fit_params.add('IO_%i' % (iy+1), value = IOguesses[iy], min = 1, max = 100*IOguesses[iy]) #Give
72         ↪ each IO parameter a unique guessed IO
73
74     for iy in range(2,len(dataT)+1):
75         fit_params['D_%i' % iy].expr='D_1'
76
77     return minimize(objective,fit_params,args=(B,data))
78
79 def MovingDiff(data,slicelength=10,slicetime=2/3):
80     '''Fitting for time-dependent diffusion + concentration data.
81     Input: pandas dataframe formatted as
82     B_0 IO_0 I1_0 ... In_0
83     B_1 IO_1 I1_1 ... In_1
84     ...
85     B_m IO_m I1_m ... In_m
86
87     ...
88
89     import numpy as np
90     import pandas as pd
91     from tqdm import tqdm_notebook as tqdm
92     from lmfit import minimize, Parameters, report_fit

```

```

83
84     npoints = data.shape[0]-slicelength
85     ipoints = np.arange(0,npoints)
86     tpoints = ipoints*slicetime+slicetime*slicelength/2
87
88     cols = data.columns[1:]
89     D = pd.DataFrame(index = tpoints,columns = [cols[0]])
90     Derr = pd.DataFrame(index = tpoints,columns = [cols[0]])
91     I0 = pd.DataFrame(index = tpoints,columns = cols)
92     I0err = pd.DataFrame(index = tpoints,columns = cols)
93
94     for i in tqdm(range(npoints),desc='Progress:',position=1,leave=False):
95         params = GlobalDiff(data.iloc[i:i+slicelength])
96         I0slice,I0errslice = [],[]
97         for Ival in range(0,len(cols)):
98             ParamName = 'I0_{}'.format(Ival+1)
99             #I0.insert(params.params[ParamName].value,index=i,col)
100            I0slice.append(params.params[ParamName].value)
101            I0errslice.append(params.params[ParamName].stderr)
102            D.loc[tpoints[i],cols[0]] = params.params['D_1'].value
103            Derr.loc[tpoints[i],cols[0]] = params.params['D_1'].stderr
104            I0.loc[tpoints[i],cols] = I0slice
105            I0err.loc[tpoints[i],cols] = I0errslice
106
107     return D,I0,Derr,I0err
108
109 def MovingDiff_csv(fname,slicelength=10,slicetime=2/3):
110     '''A simple wrapper of MovingDiff() to act on .csv files'''
111     import pandas as pd
112     return MovingDiff(pd.read_csv(fname),slicelength,slicetime)
113
114 def SeparateMovingDiffusion(data,slicelength=10,slicetime=2/3):
115     '''Moving average diffusion processing for multiple separate chemical species.
116     Acts on a pandas dataframe containing a list of B-values in the first column, and corresponding peak
117     integrals in subsequent columns.
118     Returns a pair of pandas dataframes [D,I] containing the calculated diffusion coefficients
119     and concentrations for each peak present in the input array. '''
120     import pandas as pd
121     import numpy as np
122     from tqdm import tqdm_notebook as tqdm
123     npoints = data.shape[0]-slicelength
124     ipoints = np.arange(0,npoints)
125     tpoints = ipoints*slicetime+slicetime*slicelength/2
126     D = pd.DataFrame(index = tpoints,columns=data.columns[1:])
127     I = pd.DataFrame(index = tpoints,columns=data.columns[1:])
128     Derr = pd.DataFrame(index = tpoints,columns=data.columns[1:])
129     Ierr = pd.DataFrame(index = tpoints,columns=data.columns[1:])
130
131     for peak in tqdm(data.columns[1:],desc='Peak-by-peak progress',position=2):
132         td,ti,tderr,tierr = MovingDiff(pd.concat([data.iloc[:,0],data[peak]],axis=1),
133                                         slicelength=slicelength,
134                                         slicetime=slicetime)
135         D[peak] = td
136         I[peak] = ti
137         Derr[peak] = tderr
138         Ierr[peak] = tierr
139
140     return D, I, Derr, Ierr
141 def SeparateMovingDiffusion_csv(fname,slicelength=10,slicetime=2/3):
142     '''A wrapper of SeparateMovingDiffusion to act on .csv files'''
143     import pandas as pd

```

```

142     return SeparateMovingDiffusion(pd.read_csv(fname),
143         slicelength=slicelength,
144         slicetime=slicetime)
145
146 def MeOHTemp(dDelta):
147     '''Converts a methanol CH3-OH chemical shift separation (in ppm) to a temperature (in K).
148     See J. Magn. Reson. 1982, 46, 319-321'''
149     return 409-36.54*dDelta-21.85*dDelta**2
150
151 def MeOHDiff(dDelta):
152     '''Calculates the expected self-diffusion coefficient of methanol for a given OH-CH3 peak chemical
153     shift separation. See MacDonald et al, ChemPhysChem 2019, 20, 926-9'''
154     import numpy as np
155     return 5.124e-7 * np.exp((-1601)/(MeOHTemp(dDelta)))

```

Script 8.2 Example processing schema for Grubbs metathesis data.

```

1  '''Processing of NMR integral data for Grubbs metathesis to obtain time-dependent diffusion information.
2  Outputs 'grubbs' as a tuple, with each tuple item made up of a tuple containing diffusion and
3  concentration data as generate by SeparateMovingDiffusion() function shown above.'''
4  import os
5  from tqdm import tqdm_notebook as tqdm
6  path = '5. NMR data\Grubbs Integrals' #Set path to directory containing all CSV files
7  grubbs = ()
8  for entry in tqdm(os.scandir(path)):
9      data = SeparateMovingDiffusion_csv(entry,
10         slicelength=10,
11         slicetime=2/3) #Moving-fit processing of every file in directory. Here, diffusion fits are conducted
12         #over a slice of 10 gradients (slicelength=10), each of which was acquired in 40 s (slicetime=2/3
13         #minutes).
14         for item in data:
15             item.name=entry.name[:-4] #Set the name of each dataset to the name of the corresponding .csv
16             #file
17             grubbs += (data,)
18
19
20 from scipy.optimize import curve_fit
21 def expkin(t,delt,I,k):
22     return I*(1-np.exp(-k*(t-delt)))
23 #Reset all indices to start from 0
24
25 for data in grubbs:
26     for j in range(len(data)):
27         data[j].index = data[j].index - data[j].index[0]
28
29 #Fit exponential kinetics to datasets, and add offsets to time indices such that product concentration is
30 #at t = 0
31 fig,ax = plt.subplots(2,1,figsize=(12,15),sharex=True)
32 for data in grubbs:
33     offsets = []
34     for curve in data[1].columns:
35         if np.average(data[1][curve].iloc[-5:]) / np.average(data[1][curve].iloc[:5]) > 1.2:
36             popt,pcov = curve_fit(expkin, np.array(data[1].index, dtype=float),
37             np.array(data[1][curve], dtype=float), p0=[1,max(data[1][curve]), 1])
38             corrfactor = data[1][curve][45:50].mean(axis=0)
39             ax[0].plot(data[1].index, data[1][curve]/corrfactor, label=curve)
40             ax[0].plot(data[1].index, expkin(data[1].index, popt[0], popt[1] / corrfactor, popt[2]))
41             #Plot uncorrected data and fit curves for each dataset
42             ax[1].plot(data[1].index-popt[0], expkin(data[1].index-popt[0], 0, popt[1] / corrfactor,
43             popt[2]))
44             ax[1].plot(data[1].index-popt[0], data[1][curve] / corrfactor, label=curve) #Plot corrected
45             #data and fit curves for each dataset

```

```
36         offsets.append(popt[0])
37     offset = np.median(offsets)
38     for j in range(len(data)):
39         data[j].index = data[j].index-offset #Add offset to indices of each dataset
40
41     ax[0].set_xlim(0,180)
42     ax[0].set_ylim(0,None)
43     plt.show() #Show all plots
```

8.7 Additional References

- [1] T. S. C. MacDonald, W. S. Price, J. E. Beves, *ChemPhysChem* **2019**, *20*, 926–930.
- [2] T. Vacala, L. P. Bejcek, C. G. Williams, A. C. Williamson, P. A. Vadola, *J. Org. Chem.* **2017**, *82*, 2558–2569.
- [3] T. Stait-Gardner, P. G. Anil Kumar, W. S. Price, *Chem. Phys. Lett.* **2008**, *462*, 331–336.
- [4] (a) A. F. Collings, R. Mills, *Trans. Faraday Soc.* **1970**, *66*, 2761–2766; (b) D. R. Falcone, D. C. Douglass, D. W. McCall, *J. Phys. Chem.* **1967**, *71*, 2754–2755.

Chapter 9

Appendix for switchable phosphate binding

9.1 Acid-base speciation of H_2PO_4^- in DMSO

Given the focus placed upon the dihydrogen phosphate anion, it is important to consider potential protonation-deprotonation that may occur under the conditions of wet DMSO. Acid-base properties in non-aqueous solutions are notoriously uncharacterised, but in this case we have access to a carefully-conducted recent study of the acid-base properties of H_2PO_4^- and CH_3CO_2^- in DMSO.^[1] That study also measured an association constant for antielectrostatic H_2PO_4^- dimerization of 180 M^{-1} in DMSO, but did not study indefinite association to form higher oligomers as is presented here.

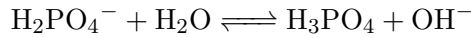
It has previously been shown that the deprotonation of H_2PO_4^- in DMSO is highly unfavorable.^[1] As such, we limit our consideration to the possibility of forming of phosphoric acid, H_3PO_4 , by protonation of H_2PO_4^- with water. Literature data for K^H , the acid association constant of a species, are given in Table 9.1.

Table 9.1. Literature acid-base association constants for phosphate,^[1] acetate,^[1] and water^[2] in DMSO.

Species	$\log K^H$ (DMSO)
$\text{H}_3\text{PO}_4^{[1]}$	10.8
$\text{CH}_3\text{CO}_2\text{H}^{[1]}$	12.8
$\text{H}_2\text{O}^{[2]}$	28

9.1.1 Speciation of phosphate in DMSO

Proton transfer from water to dihydrogen phosphate would occur as:



With the acid-base relationship and using the values in Table 9.1:

$$\frac{[\text{OH}^-][\text{H}_3\text{PO}_4]}{[\text{H}_2\text{PO}_4^-][\text{H}_2\text{O}]} = \frac{10^{-28}}{10^{-10.8}} = 10^{-17.2}$$

With 0.5% v/v H₂O, [H₂O]₀ = 280 mM. Considering the case for 50 mM H₂PO₄⁻ and setting x as the concentration [OH⁻], we can restate the above relationship as:

$$\frac{[\text{OH}^-][\text{H}_3\text{PO}_4]}{[\text{H}_2\text{PO}_4^-][\text{H}_2\text{O}]} = \frac{x^2}{([\text{H}_2\text{PO}_4^-]_0 - x)([\text{H}_2\text{O}]_0 - x)} = 10^{-17.2}$$

And then:

$$\begin{aligned} \frac{x^2}{(50 \times 10^{-3} - x)(280 \times 10^{-3} - x)} &= 10^{-17.2} \\ x &= 9.4 \times 10^{-9} \text{ M}^{-1} \end{aligned}$$

[H₃PO₄] is thus expected to be vanishingly small, and is not expected to play any role in the supramolecular assembly.

9.1.2 Speciation of acetate in DMSO

Following the same process as used above for H₂PO₄⁻/H₃PO₄:



And using the parameters given in Table 9.1:

$$\frac{[\text{OH}^-][\text{CH}_3\text{CO}_2\text{H}]}{[\text{CH}_3\text{CO}_2^-][\text{H}_2\text{O}]} = \frac{10^{-28}}{10^{-12.8}} = 10^{-15.2}$$

And solving for the extent of proton transfer as before:

$$\begin{aligned} \frac{x^2}{(50 \times 10^{-3} - x)(280 \times 10^{-3} - x)} &= 10^{-15.2} \\ x &= 9.4 \times 10^{-8} \text{ M}^{-1} \end{aligned}$$

While the formation of CH₃CO₂H is slightly more favourable than that of H₃PO₄, it is still expected to only be present at insignificant (nM) concentrations.

9.2 General experimental

Reagents were purchased from Combi-Blocks or Sigma-Aldrich and used as received. Deuterated NMR solvents were purchased from Cambridge Isotope Laboratories and used as received unless otherwise noted.

NMR experiments were conducted using a Bruker Avance III 500 MHz spectrometer equipped with a TBI (^{31}P) probe fitted with standard high-resolution gradient coils capable of generating gradient pulses up to 53.45 G cm^{-1} . Diffusion experiments were prepared and executed through the Bruker **diff5** utility and used the **diffSte** stimulated-echo pulse sequence. Typical parameters for ^1H diffusion experiments were $\Delta = 50 \text{ ms}$ and $\delta = 4 \text{ ms}$. Typical parameters for ^{31}P diffusion experiments were $\Delta = 100 \text{ ms}$ and $\delta = 7 \text{ ms}$. Gradient pulses were sine-shaped, and gradient lists typically consisted of 12 gradient strengths linearly increasing from $0\text{--}53.45 \text{ G cm}^{-1}$.

Spectra were automatically phased and baseline-corrected with MestReNova software 12.0, with peak integrals obtained using the built-in data analysis routines and exported as csv data for further processing.

Time-resolved diffusion data for *in situ* studies were obtained using the methods previously described in chapter 2,^[3] with diffusion spectra continually acquired using random gradient lists of 200–1000 gradients with $5\text{--}53.45 \text{ G cm}^{-1}$ gradient pulses. Typical experimental parameters were $\Delta = 50 \text{ ms}$ and $\delta = 4 \text{ ms}$. Gradient pulses were sine-shaped and ranged in amplitude from $0\text{--}53.45 \text{ G cm}^{-1}$.

9.3 Additional diffusion titration data

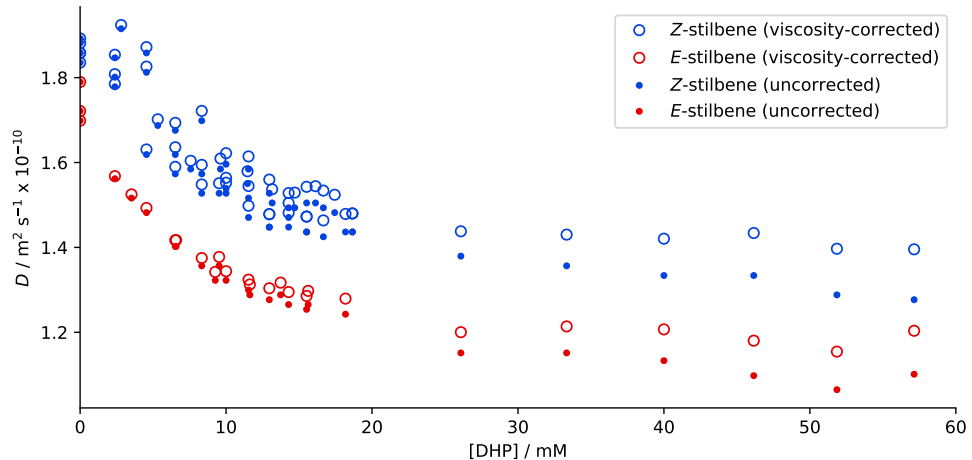


Figure 9.1. Diffusion of separate 5 mM solutions of pure *E*-**4.2** or *Z*-**4.2** titrated with H_2PO_4^- , presented on a single axis for clarity. Diffusion coefficients as-acquired are shown as solid points; diffusion coefficients corrected for changes in viscosity caused by increasing $[\text{H}_2\text{PO}_4]$ are shown as empty circles (linear correction from directly measured viscosities of TBA- H_2PO_4 solutions; see Figure 4.17). Each point represents one diffusion experiment. 500 MHz ^1H , $\Delta = 50$ ms, $\delta = 4$ ms, linear ramp of 12 gradients from $g = 0$ –53.45 G cm $^{-1}$

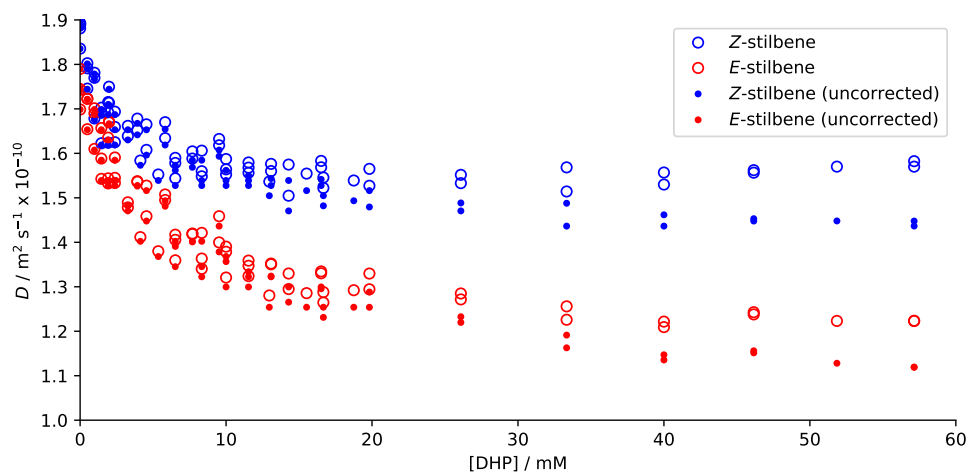


Figure 9.2. Diffusion of host **4.2** in 1 mM mixed solution (1:1 *E*-**4.2**:*Z*-**4.2**), in the presence of 0–70 mM H_2PO_4 . Diffusion coefficients as-acquired are shown as solid points; diffusion coefficients corrected for changes in viscosity caused by increasing $[\text{H}_2\text{PO}_4]$ are shown as empty circles (linear correction from directly measured viscosities of TBA- H_2PO_4 solutions; see Figure 4.17). Each point represents one diffusion experiment. 500 MHz ^1H , $\Delta = 50$ ms, $\delta = 4$ ms, linear ramp of 12 gradients from $g = 0$ –53.45 G cm $^{-1}$

9.3. ADDITIONAL DIFFUSION TITRATION DATA

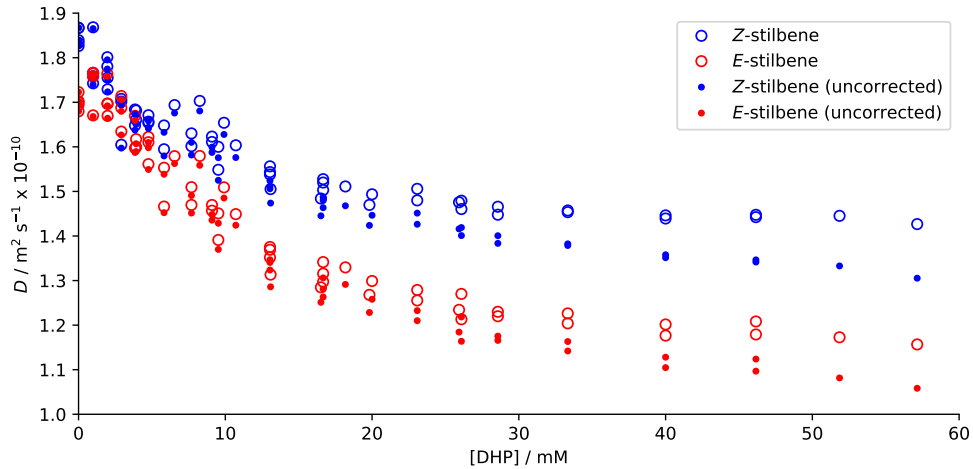


Figure 9.3. Diffusion of host **4.2** in 5 mM mixed solution (1:1 *E*-**4.2**:*Z*-**4.2**), in the presence of 0–70 mM H₂PO₄. Diffusion coefficients as-acquired are shown as solid points; diffusion coefficients corrected for changes in viscosity caused by increasing [H₂PO₄] are shown as empty circles (linear correction from directly measured viscosities of TBA-H₂PO₄ solutions; see Figure 4.17). Each point represents one diffusion experiment. 500 MHz ¹H, Δ = 50 ms, δ = 4 ms, linear ramp of 12 gradients from $g = 0$ –53.45 G cm^{−1}

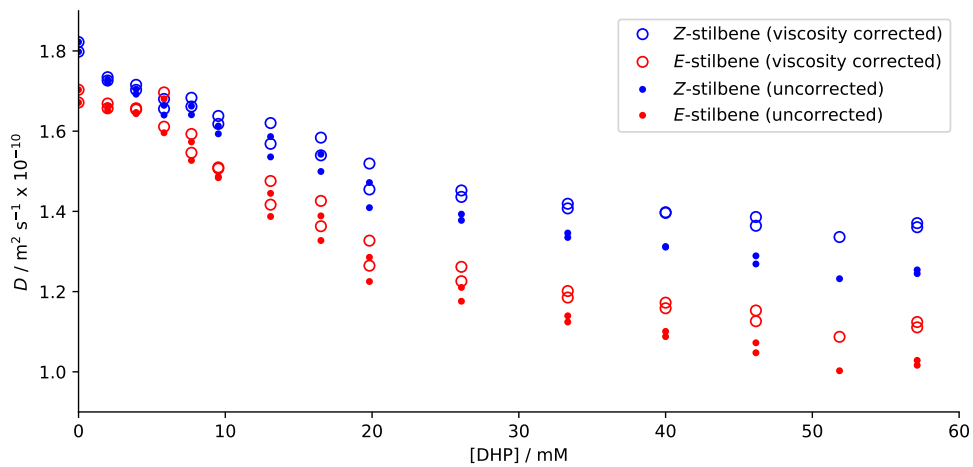


Figure 9.4. Diffusion of host **4.2** in 10 mM mixed solution (1:1 *E*-**4.2**:*Z*-**4.2**), in the presence of 0–70 mM H₂PO₄. Diffusion coefficients as-acquired are shown as solid points; diffusion coefficients corrected for changes in viscosity caused by increasing [H₂PO₄] are shown as empty circles (linear correction from directly measured viscosities of TBA-H₂PO₄ solutions; see Figure 4.17). Each point represents one diffusion experiment. 500 MHz ¹H, Δ = 50 ms, δ = 4 ms, linear ramp of 12 gradients from $g = 0$ –53.45 G cm^{−1}

9.4 Estimated diffusion coefficients of supramolecular host-guest complexes

To aid in comparing the sizes of proposed complexes, approximate molecular weights are shown in Table 9.2. As H_2PO_4^- oligomers have been modelled as forming with a continuous distribution of sizes, no single definitive molecular weight can be given for complexes involving oligomeric H_2PO_4^- . Instead, we provide molecular weights for the calculated median and mean oligomer sizes.

Table 9.2. Estimated diffusion coefficients for representative supramolecular structures of the form $[\text{H}_m\text{G}_n]$. Estimated diffusion coefficients for complexes (calculated using Equation 4.26) are shown in normal text. While a wide distribution of host-guest systems are expected to form in solution, the measured host diffusion coefficients at 5 mM host and 50 mM TBA- H_2PO_4^- suggest complexes of approximately 1.5–2.5 kDa in size under these conditions.

Complex	Median MW / kDa	Mean MW / kDa	$D_{\text{H}_2\text{PO}_4}$ ^[a] / $\text{m}^2 \text{s}^{-1} \times 10^{-10}$	D_E ^[a] / $\text{m}^2 \text{s}^{-1} \times 10^{-10}$	D_Z ^b / $\text{m}^2 \text{s}^{-1} \times 10^{-10}$
Free host $[\text{H}_1\text{G}_0]$		0.5	-	1.74 ^[a]	1.87 ^[a]
Oligo $[\text{H}_2\text{PO}_4^-]_n$ ^[c]	0.4	0.5	2.16 ^[b]		
Free H_2PO_4^-		0.1	3.39		
Host with monomeric phosphate ($D_{\text{H}_2\text{PO}_4} = 3.39$)					
$[\text{H}_1\text{G}_1]$		0.6		1.67	1.78
$[\text{H}_1\text{G}_2]$		0.7		1.61	1.70
Host with phosphate oligomers (50 mM, $D_{\text{H}_2\text{PO}_4} = 2.16$)					
$[\text{H}_1(\text{G}_n)_1]$	0.9	1.0		1.51	1.58
$[\text{H}_1(\text{G}_n)_2]$	1.3	1.5		1.37	1.42
$[\text{H}_2(\text{G}_n)_1]$	1.4	1.5		1.22	1.35
$[\text{H}_2(\text{G}_n)_2]$	1.8	2.0		1.20	1.26
$[\text{H}_2(\text{G}_n)_3]$	2.2	2.5		1.14	1.18
$[\text{H}_3(\text{G}_n)_2]$	2.4	2.6		1.09	1.15
$[\text{H}_3(\text{G}_n)_3]$	2.8	3.0		1.05	1.10
$[\text{H}_3(\text{G}_n)_4]$	3.1	3.5		1.01	1.05
5 mM host, 50 mM guest			<i>E-4.2:</i> 1.93 ^[b] <i>4.2:</i> 2.01 ^[b]	1.17 ^[a]	1.39 ^[a]

^[a] 202 MHz ^{31}P PGSTE, $\delta = 7$ ms, $\Delta = 100$ ms, $g = 0\text{--}53.45 \text{ G cm}^{-1}$.

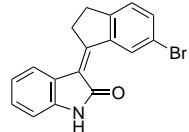
^[b] 500 MHz ^1H PGSTE, $\delta = 4$ ms, $\Delta = 50$ ms, $g = 0\text{--}53.45 \text{ G cm}^{-1}$.

^[c] Oligomeric H_2PO_4^- distribution at 50 mM H_2PO_4^- with $K_i = 120$.)

9.5 Experimental: oxindole-derived hemistilbenes

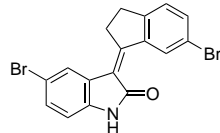
9.5.1 Synthesis

(Z)-3-(6-bromo-2,3-dihydro-1H-inden-1-ylidene)indolin-2-one 4.10



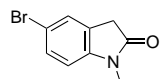
Oxindole (666 mg, 5 mol, 1.0 eq) and 6-bromoindanone (1.272 g, 6 mmol, 1.2 eq) combined in dry THF (10 mL), and pyridine (800 μ L, 10 mmol, 2 eq) added. $Ti(O^iPr)_4$ (4.45 mL, 15 mmol, 3 eq) added dropwise with stirring, and mixture stirred at room temperature overnight. Reaction mixture then quenched with aq. NH_4Cl solution, sonicated to form a fine suspension, and filtered. Solid repeatedly sonicated into acetone, filtered, and combined filtrate concentrated under reduced pressure to give the oxindole switch as a tan solid (720 mg, 44%). 1H NMR (400 MHz, DMSO- d_6) δ 10.62 (s, 1H), 9.83 (d, J = 1.9 Hz, 1H), 7.67 – 7.53 (m, 2H), 7.44 (s, 1H), 7.23 (t, J = 7.6 Hz, 1H), 7.02 (td, J = 7.7, 1.1 Hz, 1H), 6.87 (d, J = 7.7 Hz, 1H), 3.40 – 3.35 (m, 2H), 3.20 – 3.12 (m, 2H).

(Z)-5-bromo-3-(6-bromo-2,3-dihydro-1H-inden-1-ylidene)indolin-2-one 4.3



5-Bromooxindole (852 mg, 4 mol, 1.0 eq) and 6-bromoindanone (922 mg, 4.8 mmol, 1.2 eq) combined in dry THF (10 mL), and pyridine (640 μ L, 8 mmol, 2 eq) added. $Ti(O^iPr)_4$ (3.65 mL, 15 mmol, 3 eq) added dropwise with stirring, and mixture stirred at room temperature overnight. Reaction mixture then quenched with aq. NH_4Cl solution, sonicated to form a fine suspension, and filtered. Solid repeatedly sonicated into acetone, filtered, and combined filtrate concentrated under reduced pressure to give the oxindole switch as an insoluble tan solid (47 mg, 2%). 1H NMR (500 MHz, DMSO- d_6 , 70 °C) δ 10.60 (s, 1H), 9.81 (d, J = 1.9 Hz, 1H), 7.70 (d, J = 1.9 Hz, 1H), 7.64 (dd, J = 8.3, 2.0 Hz, 1H), 7.45 (d, J = 8.1 Hz, 1H), 7.41 (dd, J = 8.2, 1.6 Hz, 1H), 6.86 (d, J = 8.3 Hz, 1H), 3.40 (dd, J = 7.4, 4.2 Hz, 2H), 3.22 – 3.16 (m, 2H).

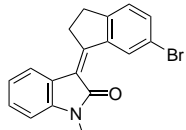
5-Bromo-N-methyloxindole 4.15



N-Methyloxindole (1.76 g, 12 mmol, 1.0 eq) and *N*-bromosuccinimide (2.35 g, 13.2 mmol, 1.1 eq) combined in 60 mL MeCN and stirred overnight at room temperature. Solvent

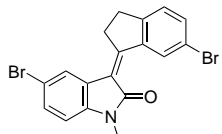
removed under reduced pressure, and crude dissolved in CH_2Cl_2 (100 mL). CH_2Cl_2 solution washed with aq. Na_2CO_3 (3×30 mL), water (30 mL), dried on MgSO_4 , and concentrated under reduced pressure to give the bromo oxindole as a tan solid (2.63 g, 99.5%). ^1H NMR (400 MHz, CDCl_3) δ 7.45 – 7.39 (m, 1H), 7.38 – 7.35 (m, 1H), 6.69 (d, $J = 8.2$ Hz, 1H), 3.52 (s, 2H), 3.19 (s, 4H).

(Z)-3-(6-bromo-2,3-dihydro-1H-inden-1-ylidene)-1-methylindolin-2-one 4.8



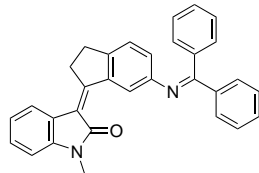
N-Methyloxindole (1.47 g, 10 mmol, 1.0 eq) and 6-bromoindanone (2.12 g, 10 mmol, 1.0 eq) combined in 20 mL dry THF, pyridine (2.5 mL, 30 mmol, 3 eq) added, and $\text{Ti}(\text{O}^i\text{Pr})_4$ (12.0 mL, 40 mmol, 4 eq) added dropwise with stirring. After overnight stirring at room temperature, reaction mixture quenched with aq. NH_4Cl solution and extracted with CH_2Cl_2 (3×50 mL). Combined organic phases washed with NH_4Cl solution and water and concentrated to dryness to give crude product as a yellow solid, which was recrystallised from \sim boiling toluene to give pure **4.8** as a crystalline yellow solid (2.22 g, 65%). ^1H NMR (400 MHz, CDCl_3) δ 9.86 (d, $J = 1.9$ Hz, 1H), 7.54 (d, $J = 7.7$ Hz, 1H), 7.49 (dd, $J = 8.1, 1.9$ Hz, 1H), 7.31 – 7.25 (m, 1H), 7.22 (d, $J = 8.1$ Hz, 1H), 7.07 (td, $J = 7.7, 1.1$ Hz, 1H), 6.82 (d, $J = 7.7$ Hz, 1H), 3.39 – 3.32 (m, 2H), 3.28 (s, 3H), 3.22 – 3.08 (m, 2H). ^{13}C NMR (101 MHz, CDCl_3) δ 157.32, 150.00, 143.02, 134.16, 133.10, 128.19, 126.08, 124.90, 124.90, 124.11, 121.83, 121.52, 120.71, 107.78, 35.60, 30.42, 26.08.

(Z)-5-bromo-3-(6-bromo-2,3-dihydro-1H-inden-1-ylidene)-1-methylindolin-2-one 4.9



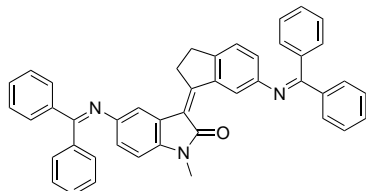
5-Bromo-*N*-methyloxindole **4.15** (2.26 g, 10 mmol, 1 eq) and 6-bromoindanone (2.12 g, 10 mmol, 1 eq) combined in 40 mL dry THF, pyridine (2.5 mL, 30 mmol, 3 eq) added, and $\text{Ti}(\text{O}^i\text{Pr})_4$ (12.0 mL, 40 mmol, 4 eq) added dropwise with stirring. After overnight stirring at room temperature, reaction mixture quenched with aq. NH_4Cl solution and extracted with CH_2Cl_2 (3×50 mL). Combined organic phases washed with NH_4Cl solution and water and concentrated to dryness to give crude product as a yellow solid, which was recrystallised from \sim 100 mL boiling toluene to give pure **4.9** as fine gold needles (2.52 g, 60%). ^1H NMR (400 MHz, CDCl_3) δ 9.84 (d, $J = 1.9$ Hz, 1H), 7.63 (d, $J = 1.9$ Hz, 1H), 7.52 (dd, $J = 8.1, 1.9$ Hz, 1H), 7.38 (dd, $J = 8.2, 1.8$ Hz, 1H), 7.29 – 7.22 (m, 3H), 6.70 (d, $J = 8.3$ Hz, 1H), 3.37 – 3.31 (m, 3H), 3.28 (s, 4H), 3.21 – 3.15 (m, 3H). ^{13}C NMR (101 MHz, CDCl_3) δ 168.88, 161.67, 152.97, 144.26, 143.45, 137.16, 135.74, 133.03, 129.30, 129.10, 128.68, 123.28, 122.94, 116.97, 111.49, 38.17, 32.93, 28.67.

(Z)-3-((diphenylmethylene)amino)-2,3-dihydro-1H-inden-1-ylidene)-1-methylindolin-2-one 4.11

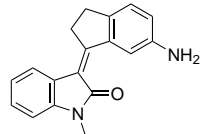


Bromo *N*-methyloxindole switch **4.8** (510 mg, 1.5 mmol, 1 eq), *t*BuXphos (57 mg, 0.135 mmol, 9 mol%), Pd₂dba₃ (42 mg, 0.045 mmol, 3 mol%), and K₃PO₄ (636 mg, 3.0 mmol, 2.0 eq) combined in a dry Schlenk flask and evacuated/backfilled three times. Dry dimethoxyethane (5 mL) added, benzophenone imine (360 μ L, 1.8 mmol, 1.2) added by syringe, and reaction mixture stirred at room temperature for 3 days. Reaction mixture diluted with water, and extracted 3 \times with CH₂Cl₂. CH₂Cl₂ portions washed with aq. NaHCO₃, water, dried on MgSO₄, and concentrated under reduced pressure to give a tacky brown solid. The solid was sonicated into Et₂O, and the insoluble imine product obtained by filtration as a tan solid (401 mg, 61 %). ¹H NMR (400 MHz, CDCl₃) δ 9.17 (d, *J* = 2.0 Hz, 1H), 7.88 – 7.74 (m, 2H), 7.55 (d, *J* = 7.8 Hz, 1H), 7.50 – 7.42 (m, 1H), 7.39 (dd, *J* = 8.2, 6.5 Hz, 3H), 7.26 (d, *J* = 2.8 Hz, 2H), 7.10 (d, *J* = 8.0 Hz, 1H), 7.05 (t, *J* = 7.6 Hz, 1H), 6.82 (d, *J* = 7.7 Hz, 1H), 6.68 (dd, *J* = 8.0, 2.0 Hz, 1H), 3.33 (dd, *J* = 7.6, 4.3 Hz, 3H), 3.28 (s, 4H), 3.13 – 2.95 (m, 3H).

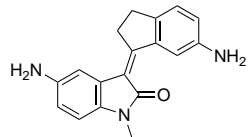
(Z)-5-((diphenylmethylene)amino)-3-((diphenylmethylene)amino)-2,3-dihydro-1H-inden-1-ylidene)-1-methylindolin-2-one 4.12



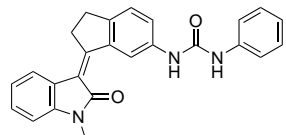
Dibromo *N*-methyloxindole switch **4.9** (838 mg, 2.0 mmol, 1 eq), *t*BuXphos (152 mg, 0.36 mmol, 9 mol% per Br), Pd₂dba₃ (110 mg, 0.12 mmol, 3 mol% per Br), and K₃PO₄ (1.70 g, 8.0 mmol, 2.0 eq per Br) combined in a dry Schlenk flask and evacuated/backfilled three times. Dry dimethoxyethane (12 mL) added, benzophenone imine (960 μ L, 4.8 mmol, 1.2 eq per Br) added by syringe, and reaction mixture stirred at room temperature for 3 days. Reaction mixture diluted with water, and extracted 3 \times with CH₂Cl₂. CH₂Cl₂ portions washed with aq. NaHCO₃, water, dried on MgSO₄, and concentrated under reduced pressure to give a tacky brown solid. The solid was sonicated into Et₂O, and the insoluble imine product obtained by filtration as a tan solid (280 mg, 23 %). ¹H NMR (400 MHz, CDCl₃) δ 9.14 (d, *J* = 2.0 Hz, 1H), 7.81 – 7.72 (m, 4H), 7.51 – 7.36 (m, 7H), 7.31 (dd, *J* = 4.5, 2.1 Hz, 3H), 7.25 – 7.16 (m, 7H), 7.07 (d, *J* = 8.0 Hz, 1H), 6.98 (s, 1H), 6.78 (d, *J* = 8.2 Hz, 1H), 6.66 (d, *J* = 8.5 Hz, 1H), 6.63 (d, *J* = 8.2 Hz, 1H), 3.21 (s, 3H), 3.02 – 2.94 (m, 2H), 2.94 – 2.89 (m, 2H).

(Z)-3-(6-amino-2,3-dihydro-1H-inden-1-ylidene)-1-methyl indolin-2-one 4.13

Imine **4.13** (400 mg, 0.91 mmol), hydroxylamine hydrochloride (114 mg, 1.64 mmol, 1.8 eq), and sodium acetate (anhyd., 179 mg, 2.18 mmol, 2.4 eq) combined in 10 mL dry methanol and stirred overnight at room temperature. Solvent was removed under reduced pressure, and the residue was taken up in CH₂Cl₂ (50 mL). After washing with aq. NaOH (1M, 3 × 15 mL) the solution was dried on MgSO₄, concentrated under reduced pressure, and purified by FCC (0–4% MeOH in CH₂Cl₂) to give **4.13** as a tan foam (175 mg, 70%). ¹H NMR (600 MHz, CDCl₃) δ 8.99 (d, *J* = 2.3 Hz, 1H), 7.52 (d, *J* = 7.8 Hz, 1H), 7.23 – 7.19 (m, 1H), 7.11 (d, *J* = 8.0 Hz, 1H), 7.00 (td, *J* = 7.7, 1.1 Hz, 1H), 6.78 (dd, *J* = 7.8, 1.1 Hz, 1H), 6.75 (dd, *J* = 8.0, 2.3 Hz, 1H), 3.72 (s, 2H), 3.34 – 3.29 (m, 2H), 3.25 (s, 3H), 3.08 – 3.03 (m, 2H). ¹³C NMR (151 MHz, CDCl₃) δ 167.00, 160.20, 145.17, 142.48, 142.26, 140.12, 127.37, 125.32, 125.01, 123.79, 121.56, 119.86, 119.66, 115.79, 107.44, 36.11, 29.85, 25.87.

(Z)-5-amino-3-(6-amino-2,3-dihydro-1H-inden-1-ylidene)-1-methyl indolin-2-one 4.14

Bisimine **4.12** (250 mg, 0.40 mmol), hydroxylamine hydrochloride (100 mg, 1.44 mmol, 3.6 eq), and sodium acetate (anhyd., 159 mg, 1.94 mmol, 4.8 eq) combined in 8 mL dry methanol and stirred for 16 h at room temperature. Solvent was removed under reduced pressure, and the residue was taken up in CH₂Cl₂ (50 mL). After washing with aq. NaOH (1M, 3 × 15 mL) the solution was dried on MgSO₄, concentrated under reduced pressure, and purified by FCC (0–4% MeOH in CH₂Cl₂) to give **4.14** as a red foam (105 mg, 90%). ¹H NMR (400 MHz, CDCl₃) δ 9.07 (d, *J* = 2.3 Hz, 1H), 7.17 (d, *J* = 8.1 Hz, 1H), 7.03 (s, 1H), 6.80 (dd, *J* = 8.1, 2.3 Hz, 1H), 6.64 (t, *J* = 1.0 Hz, 2H), 3.65 (s, 4H), 3.36 – 3.29 (m, 2H), 3.26 (d, *J* = 0.9 Hz, 3H), 3.13 – 3.06 (m, 2H).

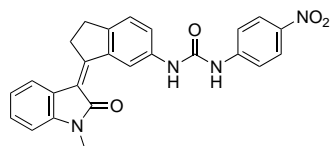
(Z)-1-(3-(1-methyl-2-oxoindolin-3-ylidene)-2,3-dihydro-1H-inden-5-yl)-3-phenyl urea 4.19

Amine **4.13** (20 mg, 72.5 μmol) combined with phenyl isocyanate (7.9 μL, 72.5 μmol, 1 eq) in 5 mL CH₂Cl₂ and stirred for 3 h at room temperature. Solvent removed under reduced

9.5. EXPERIMENTAL: OXINDOLE-DERIVED HEMISTILBENES

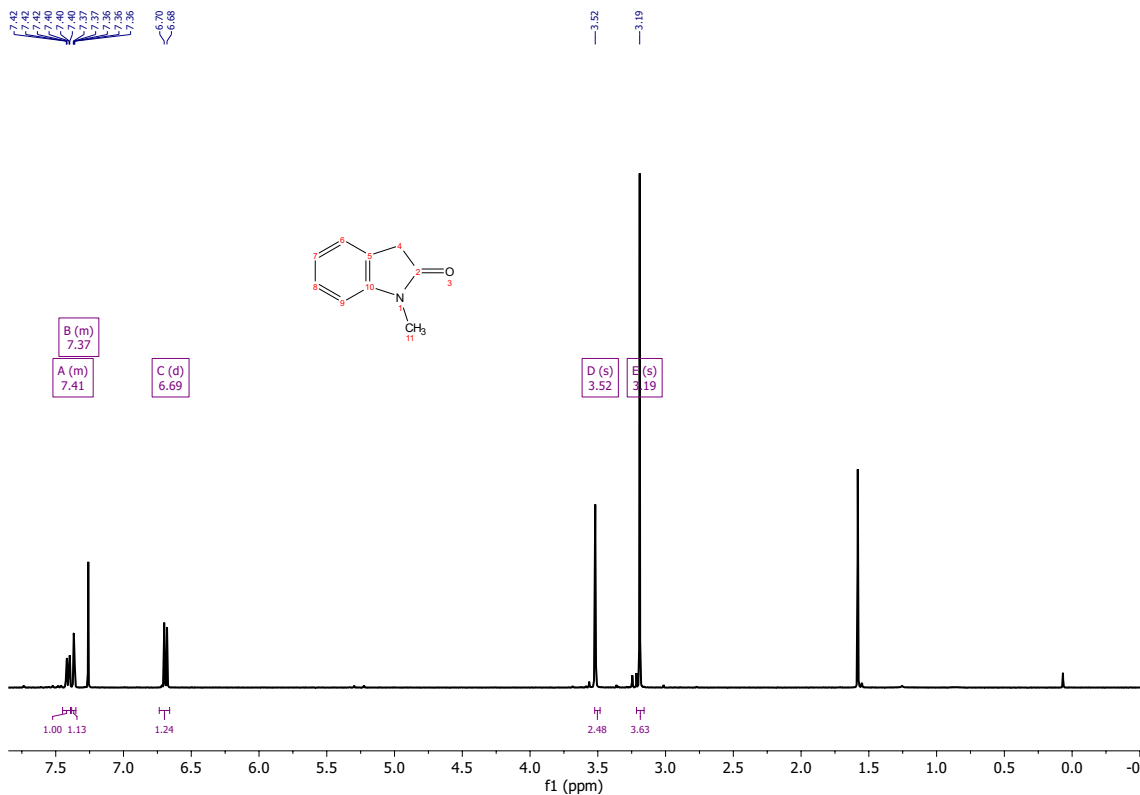
pressure to give an orange-brown solid (25 mg) containing a mixture of **4.19** and biphenylurea. ¹H NMR (600 MHz, CDCl₃ + CD₃OD) δ 9.02 (d, *J* = 2.1 Hz, 1H), 8.02 (dd, *J* = 8.3, 2.1 Hz, 1H), 7.53 (d, *J* = 7.7 Hz, 1H), 7.42 – 7.37 (m, 2H), 7.35 – 7.32 (m, 2H), 7.29 (d, *J* = 8.3 Hz, 1H), 7.04 (td, *J* = 7.7, 1.1 Hz, 1H), 6.94 (td, *J* = 7.3, 1.3 Hz, 2H), 6.82 (dd, *J* = 7.7, 1.1 Hz, 1H), 3.34 – 3.31 (m, 2H), 3.24 (s, 3H), 3.13 – 3.08 (m, 2H). ¹³C NMR (151 MHz, CDCl₃) δ 167.26, 160.56, 153.77, 146.43, 141.91, 139.17, 137.54, 128.79, 127.58, 125.06, 124.92, 122.77, 122.61, 122.10, 119.94, 119.82, 119.25, 107.78, 35.93, 30.00, 25.82.

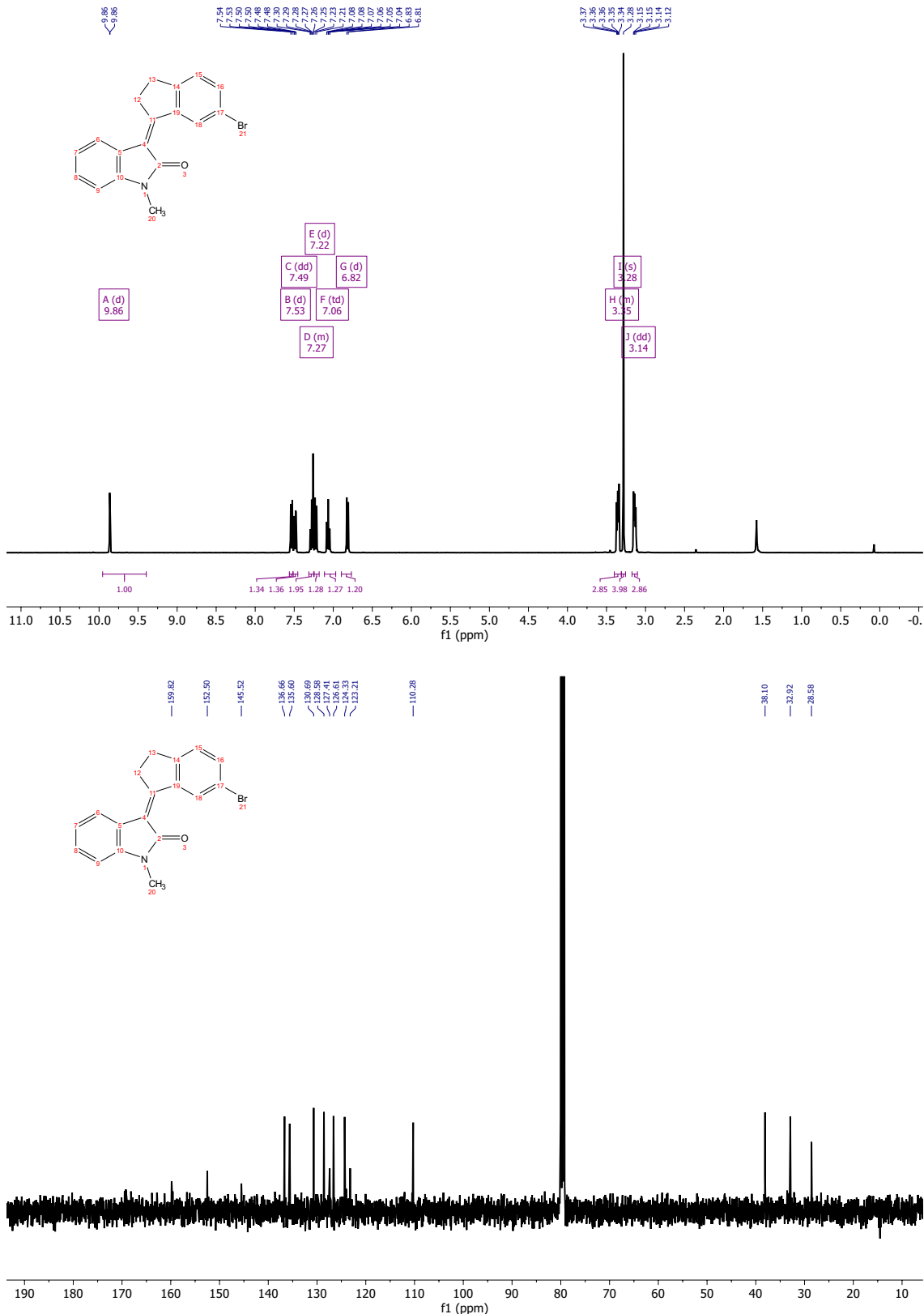
(Z)-1-(3-(1-methyl-2-oxoindolin-3-ylidene)-2,3-dihydro-1H-inden-5-yl)-3-(4-nitrophenyl)urea **4.18**



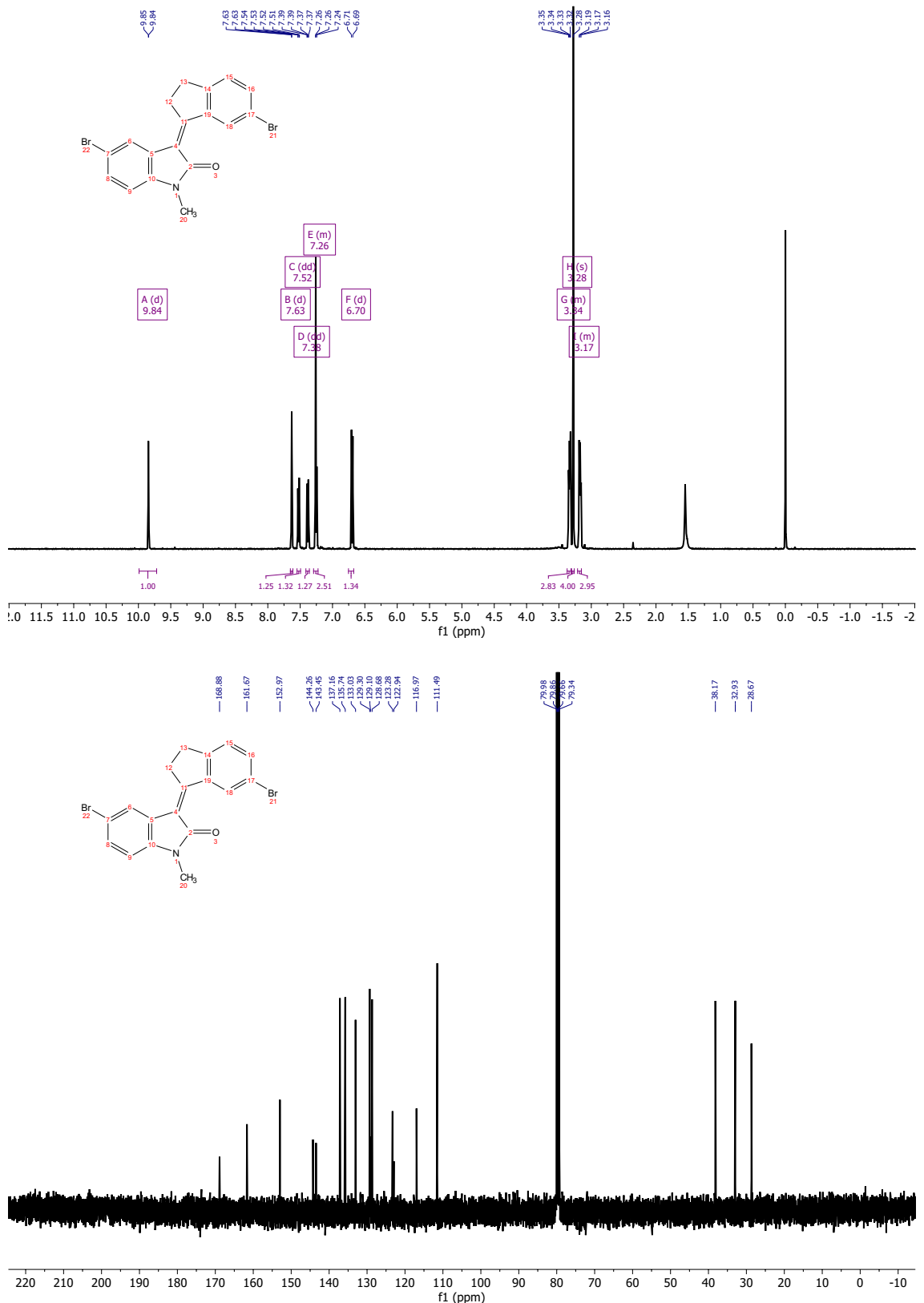
Amine **4.13** (50 mg, 0.18 mmol) and 4-nitrophénylisocyanate (33 mg, 0.2 mmol, 1.1 eq) stirred in 10 mL dry CH₂Cl₂ overnight. Product obtained by filtration (45 mg, 54%). ¹H NMR (400 MHz, DMSO-*d*₆) δ 10.35 (s, 2H), 9.54 (d, *J* = 2.1 Hz, 1H), 8.21 (d, *J* = 8.9 Hz, 2H), 7.91 (d, *J* = 8.9 Hz, 2H), 7.72 (d, *J* = 8.3 Hz, 1H), 7.65 (d, *J* = 7.8 Hz, 1H), 7.47 (d, *J* = 8.2 Hz, 1H), 7.32 (t, *J* = 7.7 Hz, 1H), 7.10 (t, *J* = 7.6 Hz, 1H), 7.03 (d, *J* = 7.8 Hz, 1H), 3.49 – 3.38 (m, 3H), 3.21 (m, 5H).

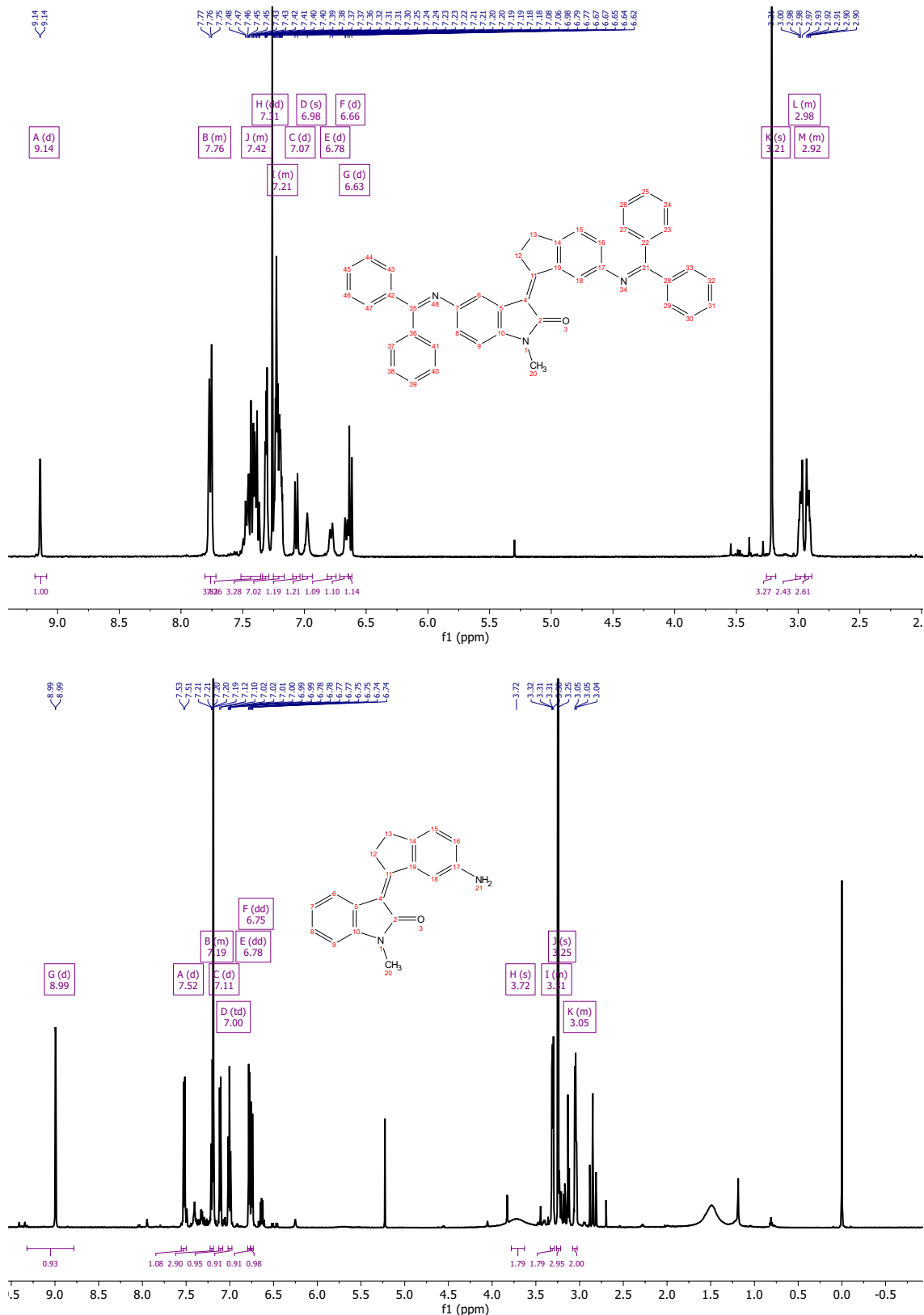
9.5.2 Oxindole NMR spectra



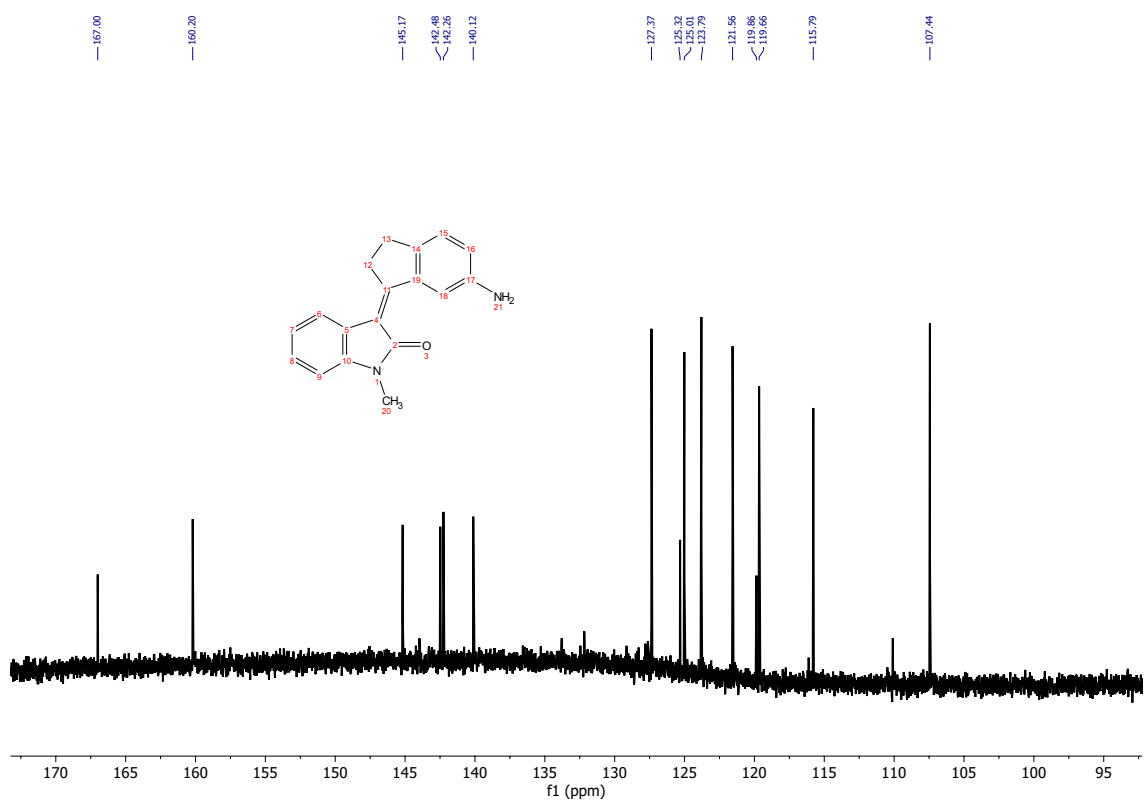


9.5. EXPERIMENTAL: OXINDOLE-DERIVED HEMISTILBENES





9.5. EXPERIMENTAL: OXINDOLE-DERIVED HEMISTILBENES



9.6 Experimental: stiff stilbene anion binders

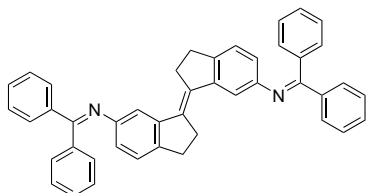
9.6.1 Synthetic details

E and *Z* dibromo stilbenes **E-4.20** and **Z-4.20**

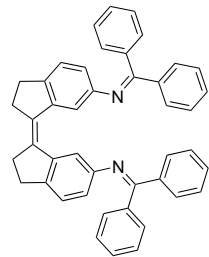


TiCl_4 (10.4 mL, 94.5 mmol, 2.0 eq) was added dropwise to a suspension of Zn powder (12.4 g, 189 mmol, 4.0 eq) in 95 mL dry THF, and heated at reflux for 3 h. After allowing the mixture to cool, 6-bromoindanone (10.0 g, 47.4 mmol, 1.0 eq) was added quickly and the mixture was returned to reflux for 16 h. On cooling, the reaction mixture was quenched with aq. NH_4Cl (500 mL) and extracted with CHCl_3 (3×70 mL). The combined organic portions were washed with NH_4Cl solution to remove suspended inorganics (grey; not the beige sparingly soluble *E* stilbene), washed with water, concentrated to approx. 30 mL under reduced pressure, and filtered to yield **E-4.20** (5.14 g, 56%, used without further purification). The filtrate was then concentrated under reduced pressure and purified by column chromatography (0 – 50% CH_2Cl_2 in hexanes) to give pure **Z-4.20** (1.83 g, 20%). NMR chemical shifts were consistent with those previously reported.^[4]

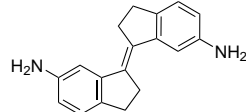
E-stilbene di(benzophenone imine) **E-4.21**



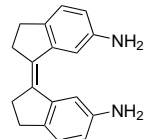
E-4.20 (1.01 g, 2.6 mmol, 1.0 eq), $\text{Pd}(\text{dppf})\text{Cl}_2$ (190 mg, 0.26 mmol, 5 mol% per site), sodium tert-butoxide (550 mg, 5.7 mmol, 1.1 eq per site), and benzophenone imine (1.03 g, 5.7 mmol, 1.1 eq per site) were combined in 15 mL dry degassed toluene and heated at 90 °C for 48 h. After cooling to room temperature, the reaction mixture was diluted with water (20 mL) and extracted with CHCl_3 (3×20 mL). The combined organic portions were reduced in volume to approximate 5 mL under reduced pressure, after which pure **E-4.21** was obtained as a tan solid by precipitation with cold Et_2O (1.22 g, 81%). NMR chemical shifts were consistent with those previously reported.^[4]

Z-stilbene di(benzophenone imine) Z-4.21

Z-4.20 (1.02 g, 2.6 mmol, 1.0 eq), Pd(dppf)Cl₂ (190 mg, 0.26 mmol, 5 mol% per site), sodium tert-butoxide (550 mg, 5.7 mmol, 1.1 eq per site), and benzophenone imine (1.03 g, 5.7 mmol, 1.1 eq per site) were combined in 15 mL dry degassed toluene and heated at 90 °C for 48 h. After cooling to room temperature, the reaction mixture was diluted with water (20 mL) and extracted with CHCl₃ (3 × 20 mL). The combined organic portions were washed with water and brine, dried on MgSO₄, and concentrated under reduced pressure to give a brown oil. Purification by chromatography (0.1% triethylamine in CH₂Cl₂) gave a **Z-4.21** as yellow oil that solidified to a waxy substance on refrigeration (1.43 g, 94%). NMR chemical shifts were consistent with those previously reported.^[4]

E-stilbene diamine E-4.22

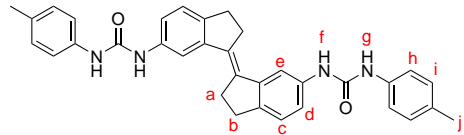
Diimine **E-4.21** (1.0 g, 1.7 mmol, 1.0 eq) was dissolved in mixture of THF (50 mL) and aq. HCl (2 M, 25 mL) and stirred at room temperature for 3 h. The mixture was then basified with sat. Na₂CO₃ and extracted with ethyl acetate (3 × 25 mL), with the combined organic portions dried over MgSO₄ and reduced in volume before precipitating **E-4.22** as a tan solid by the addition of Et₂O (420 mg, 94%). NMR chemical shifts were consistent with those previously reported.^[4]

Z-stilbene diamine Z-4.22

Diimine **Z-4.21** (2.14 g, 3.62 mmol) was suspended in mixture of THF (50 mL) and aq. HCl (2 M, 25 mL), and stirred at room temperature for 3 h. The reaction mixture was diluted with water (25 mL) and washed with Et₂O (3 × 25 mL; discarded) before being made basic with sat. Na₂CO₃. The aqueous solution was extracted with EtOAc (3 × 25 mL), with the ethyl acetate portions combined, dried on MgSO₄, and concentrated under reduced pressure

to give **Z-4.22** as a tan foam (400 mg, 42%). NMR chemical shifts were consistent with those previously reported.^[4]

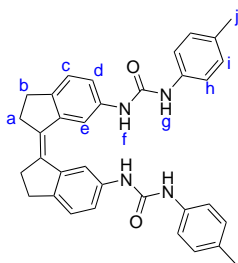
E-bis(4-tolyl)urea stilbene **E-4.2**



Diamine **E-4.22** (100 mg, 0.38 mmol, 1.0 eq) was suspended in 50 mL dry CH₂Cl₂, and *p*-tolylisocyanate (101 mg, 95 μ L, 1.0 eq per NH₂) added by syringe. The reaction mixture was stirred at reflux overnight, cooled to room temperature, and filtered to obtain crude **E-4.2**. The crude was washed with CH₂Cl₂ and aq. HCl (1 M), sonicated into a suspension in water, and collected by filtration as a fine beige solid (167 mg, 83%).

¹H NMR (600 MHz, DMSO-*d*₆) δ 8.70 (s, 2H, **H^f**), 8.57 (s, 2H, **H^g**), 7.89 (d, *J* = 1.9 Hz, 2H, **H^e**), 7.35 (d, *J* = 8.1 Hz, 4H, **H^b**), 7.26 – 7.20 (m, 4H, **H^{c,d}**), 7.09 (d, *J* = 8.1 Hz, 4H, **Hⁱ**), 3.11 (m, 4H, **H^a**), 3.04 (m, 4H, **H^b**), 2.25 (s, 6H, **H^j**). ¹³C NMR (151 MHz, DMSO-*d*₆) δ 152.80, 140.12, 138.37, 137.24, 135.08, 130.49, 129.15, 128.48, 124.82, 118.31, 117.58, 114.27, 31.66, 29.82, 20.35.

Z-bis(4-tolyl)urea stilbene **Z-4.2**



Diamine **Z-4.22** (100 mg, 0.38 mmol, 1.0 eq) was dissolved in 5 mL of dry CH₂Cl₂, and *p*-tolylisocyanate (101 mg, 95 μ L, 1.0 eq per NH₂) added by syringe. The reaction mixture was stirred at room temperature overnight and filtered to obtain crude **Z-4.2**. The crude was washed with CH₂Cl₂ and aq. HCl (1 M), sonicated into a suspension in water, and collected by filtration to give **Z-4.2** as a fine beige solid (152 mg, 75%).

¹H NMR (600 MHz, DMSO-*d*₆) δ 8.59 (s, 2H, **H^g**), 8.43 (s, 2H, **H^f**), 8.11 (s, 2H, **H^e**), 7.42 (dd, *J* = 8.2, 1.9 Hz, 2H, **H^d**), 7.29 (d, *J* = 8.0 Hz, 4H, **H^b**), 7.22 (d, *J* = 8.2 Hz, 2H, **H^c**), 6.88 (d, *J* = 8.0 Hz, 4H, **Hⁱ**), 2.89 (m, 4H, **H^b**), 2.77 (m, 4H, **H^a**), 2.11 (s, 6H, **H^j**). ¹³C NMR (151 MHz, DMSO-*d*₆) δ 152.71, 141.27, 140.05, 137.59, 137.28, 134.86, 130.20, 129.04, 125.10, 118.14, 117.71, 113.62, 34.45, 29.39, 20.22.

9.6.2 Host NMR spectra

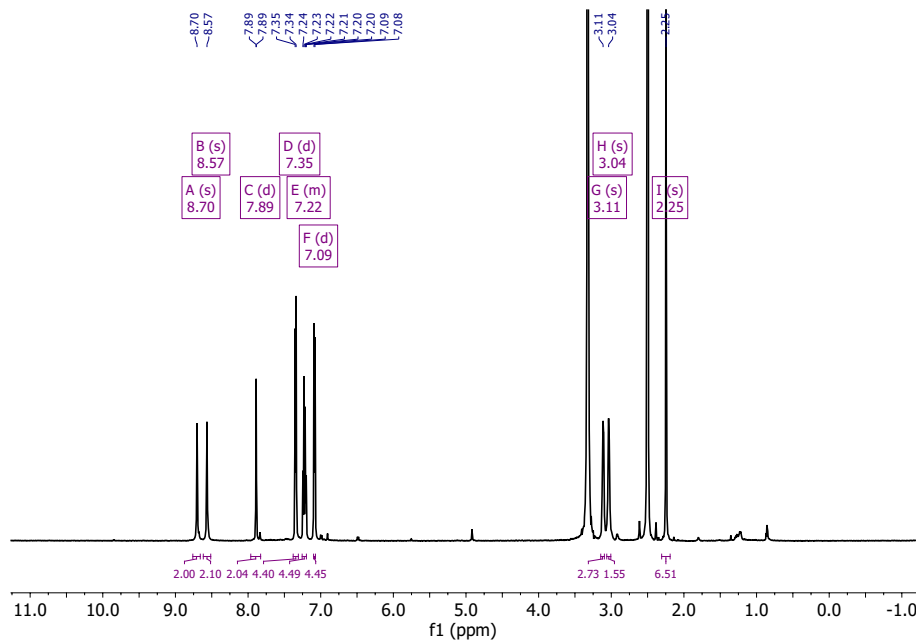


Figure 9.5. ^1H NMR spectrum of *E*-4.2 (600 MHz, $\text{DMSO}-d_6$).

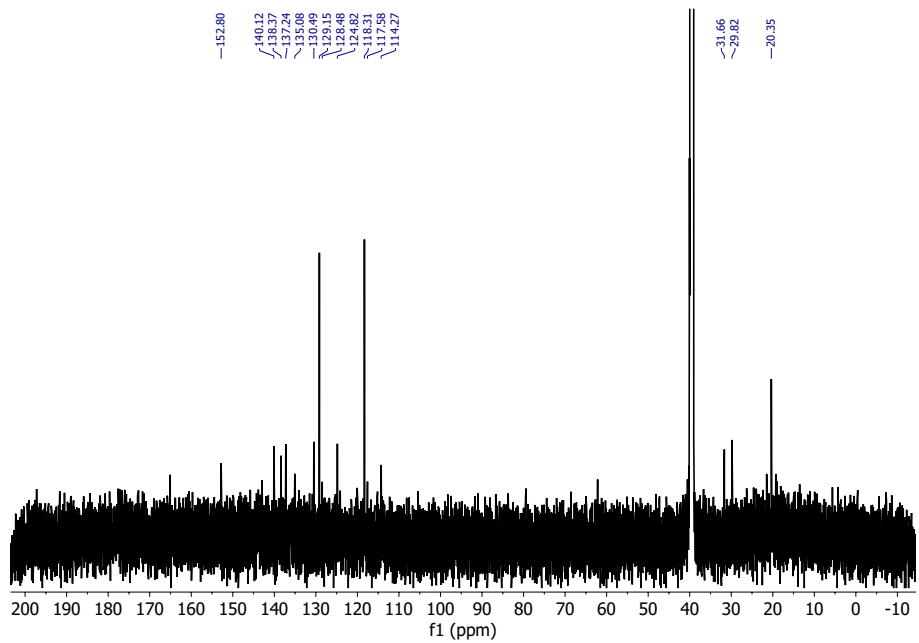


Figure 9.6. ^{13}C NMR spectrum of *E*-4.2 (150 MHz, $\text{DMSO}-d_6$). Low signal-to-noise due to poor solubility of *E*-4.2 in the absence of guest

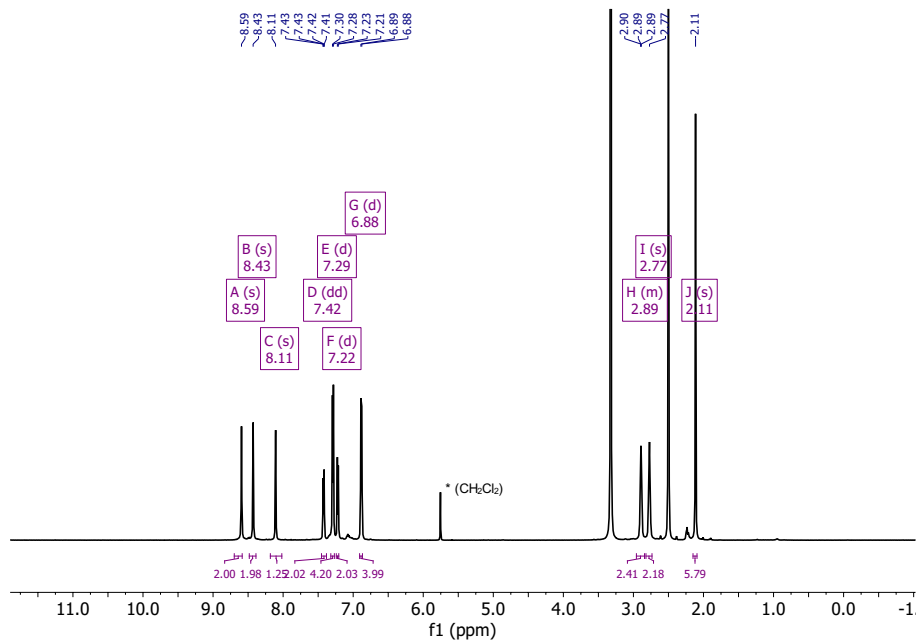


Figure 9.7. ¹H NMR spectrum of *Z*-4.2 (600 MHz, DMSO-*d*₆).

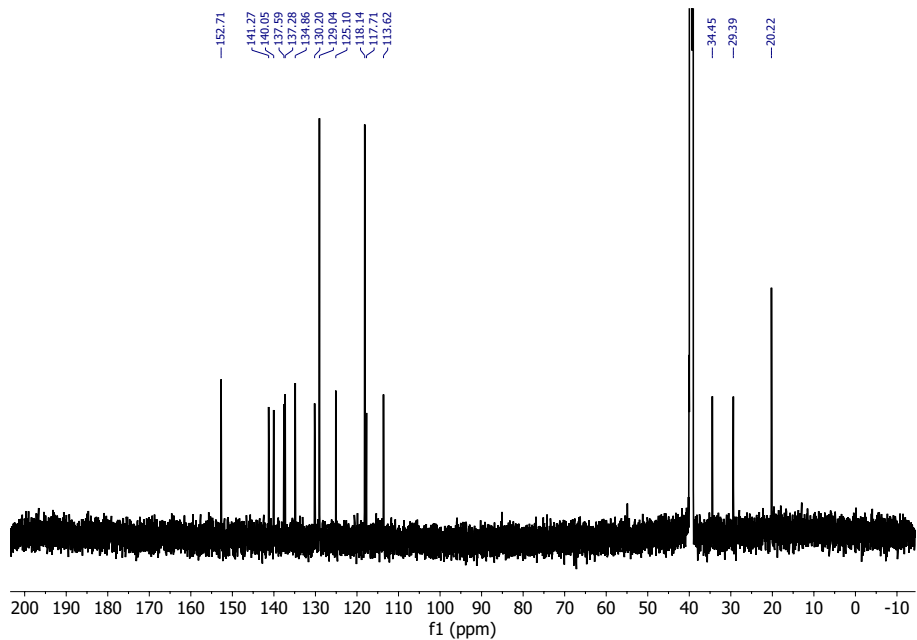


Figure 9.8. ¹³C NMR spectrum of *Z*-4.2 (150 MHz, DMSO-*d*₆).

9.7 Scripts used for data processing

NMR spectra were processed using MestreNova for baseline correction, phasing, etc. Moving-fit diffusion coefficients were calculated with the Python scripts given in previous chapters (7.3, 8.6).

Script 9.1 Python scripts for fitting of host-guest association data. Mathematical models used are from the literature.^[5]

```

1 import pandas as pd
2 import numpy as np
3 import scipy.optimize
4 import matplotlib.pyplot as plt
5 from lmfit import minimize, Parameters, report_fit
6 import itertools
7 import matplotlib.cm as cm
8 import seaborn as sns
9
10
11 #Global fit for 2:1 H:G complex data
12
13 '''Global analysis of NMR chemical shift data for fitting 2:1 host-guest association data.
14
15 This function calculates association constants from NMR titration data as a Pandas dataframe with the
16    ↪ following columns
17      [Host concentration / Molar] [Guest concentration / Molar] [Peak 1 / ppm] [ Peak 2 / ppm]...
18      ...for an arbitrary number of peaks. If desired, this can be called from the clipboard using
19      ↪ pd.read_clipboard(), eg: item
20 Binding parameters are calculated using a global nonlinear least-squares fit over all provided peaks.
21
22 data: a pandas dataframe containing host concentrations in the first column, guest concentrations in the
23    ↪ second column, and NMR chemical shifts for different peaks in the subsequent columns.
24 figsize: tuple containing (width,height) for generated matplotlib plot
25
26 Global12 returns a tuple (result,fig), where result contains fitted association data and fig contains a
27    ↪ matplotlib figure.
28 '''
29 def Global21(data,figsize=(8,6)):
30     '''Fitting function for 2:1 Host:Guest stoichiometry.
31
32     '''
33     def H21(G0,H0,K1,K2):
34         '''H21 calculate the concentration of free host, [H], given G0 (total guest concentration), H0
35             (total host concentration), K1 (H + G <=> [HG] association constant), and K2 (H + [HG] <=>
36             [H2G] association constant).
37
38         '''
39         G0,H0,K1,K2 = np.asarray(G0), np.asarray(H0), np.asarray(K1), np.asarray(K2)
40         try:
41             length = len(G0)
42             coeffs = np.zeros((length,4))
43             for i in range(length):
44                 coeffs[i] = [K1*K2, K1*(2*K2*G0[i] - K2*H0[i] + 1), K1*(G0[i]-H0[i])+1, -H0[i]]
45             roots = np.zeros(len(G0),3)
46             R = np.zeros(len(G0))
47             for i in range(len(G0)):
48                 roots[i] = np.roots(coeffs[i])
49                 R[i] = min(roots[i][roots[i] >= 0])
50
51         return R

```

```

44     except TypeError:
45         coeffs = [K1*K2, K1*(2*K2*G0 - K2*H0 + 1), K1*(G0-H0)+1, -H0]
46         R = np.roots(coeffs)
47         return min(R[R >= 0])
48
49 def nmr21(X,K1,K2,delHG,delHG2):
50     '''nmr21: calculates chemical shift difference delDel for a given peak from the free host
51     chemical shift as a function of X = H0, G0, K1, K2, delHG = chemical shift difference on
52     first association, delHG2 = chemical shift difference on second association.'''
53     H0, G0 = X
54     H = H21(G0,H0,K1,K2)
55     delDel = (delHG*K1*G0*H + 2*delHG2*G0*K1*K2*H**2)/(H0*(1+K1*H+K1*K2*H**2))
56     return delDel
57
58 def nmr21_dataset(X,params,i):
59     '''Given X = H0, G0 and params = lmfit parameters element for multiple peaks, calculates
60     chemical shifts for each peak, for each [G0, H0] pairing'''
61     K1 = params['K1_%i' % (i+1)].value
62     K2 = params['K2_%i' % (i+1)].value
63     delHG = params['delDHG1_%i' % (i+1)].value
64     delHG2 = params['delDHG2_%i' % (i+1)].value
65     return nmr21(X,K1,K2,delHG,delHG2)
66
67 def objective(params, X, data):
68     """Calculate total residual for fits to several data sets"""
69     dataT = np.array(data.T[2:])
70     ndata, nx = dataT.shape
71     resid = 0.0*dataT[:,]
72     # make residual per data set
73     for i in range(ndata):
74         dataT[i] = dataT[i] - dataT[i][0]
75         resid[i, :] = dataT[i, :] - nmr21_dataset(X,params,i)
76     # now flatten this to a 1D array, as minimize() needs
77     return resid.flatten()
78
79 X = data.iloc[:,0],data.iloc[:,1]
80
81 dataT = np.array(data.T[2:])
82 fit_params = Parameters()
83 for iy, y in enumerate(dataT):
84     fit_params.add('K1_%i' % (iy+1), value=1000, min=0.0, max=1e6)
85     fit_params.add('K2_%i' % (iy+1), value=100, min=0.0, max=1e4)
86     fit_params.add('delDHG1_%i' % (iy+1), value=1.0, min=-4.0, max=4.0)
87     fit_params.add('delDHG2_%i' % (iy+1), value=-1.0, min=-4.0, max=4.0)
88
89 for iy in range(2,len(dataT)+1):
90     fit_params['K1_%i' % iy].expr='K1_1'
91     fit_params['K2_%i' % iy].expr='K2_1'
92
93 result = minimize(objective, fit_params, args=(X, data), nan_policy='omit')
94 #report_fit(result.params)
95
96 palette = itertools.cycle(sns.color_palette())
97 fig, (ax1, ax2, ax3) = plt.subplots(3,1,sharex=True,figsize=figsize)
98 plt.rcParams["lines.markeredgewidth"] = 1.5
99 interp = np.linspace(min(X[1]),max(X[1]),1000)
100 Xinterp = (interp*0.0+X[0][0]), interp
101
102 K1, K2 = result.params['K1_1'].value, result.params['K2_1'].value

```



```

156     roots = np.zeros((len(G0),3))
157     R = np.zeros(len(G0))
158     for i in range(len(G0)):
159         roots[i] = np.roots(coeffs[i])
160         R[i] = min(roots[i][roots[i] >= 0])
161     return R
162 except TypeError:
163     coeffs = [K1*K2, K1*(2*K2*H0 - K2*G0 + 1), K1*(H0-G0)+1, -G0]
164     R = np.roots(coeffs)
165     return min(R[R >= 0])
166
167 def nmr12(X,K1,K2,delHG,delHG2):
168     H0, G0 = X
169     G = G12(G0,H0,K1,K2)
170     delDel = (delHG*K1*G + delHG2*K1*K2*G**2)/(1+K1*G+K1*K2*G**2)
171     return delDel
172
173 def nmr12_dataset(X,params,i):
174     K1 = params['K1_%i' % (i+1)].value
175
176     K2 = K1*params['alpha_%i' % (i+1)].value/4
177
178     delHG = params['delDHG1_%i' % (i+1)].value
179     delHG2 = params['delDHG2_%i' % (i+1)].value
180     return nmr12(X,K1,K2,delHG,delHG2)
181
182 def objective(params, X, data):
183     """ calculate total residual for fits to several data sets"""
184     dataT = np.array(data.T[2:])
185     ndata, nx = dataT.shape
186     resid = 0.0*dataT[:,]
187     # make residual per data set
188     for i in range(ndata):
189         dataT[i] = dataT[i] - dataT[i][0]
190         resid[i,:] = dataT[i, :] - nmr12_dataset(X,params,i)
191     # now flatten this to a 1D array, as minimize() needs
192     return resid.flatten()
193
194 X = data.iloc[:,0],data.iloc[:,1]
195
196 dataT = np.array(data.T[2:])
197 fit_params = Parameters()
198 for iy, y in enumerate(dataT):
199
200     if alpha == None:
201         fit_params.add('alpha_%i' % (iy+1), value=1, min=0.0, max=10)
202     else:
203         fit_params.add('alpha_%i' % (iy+1), value=alpha,vary=False)
204     if K1 == None:
205         fit_params.add('K1_%i' % (iy+1), value=1000, min=0.0, max=1e5)
206     else:
207         fit_params.add('K1_%i' % (iy+1), value=K1, vary=False)
208
209     fit_params.add('delDHG1_%i' % (iy+1), value=1.0, min=-4.0, max=4.0)
210     fit_params.add('delDHG2_%i' % (iy+1), value=-1.0, min=-4.0, max=4.0)
211
212 for iy in range(2,len(dataT)+1):
213     fit_params['K1_%i' % iy].expr='K1_1'
214     fit_params['alpha_%i' % iy].expr='alpha_1'
215

```

```

216     result = minimize(objective, fit_params, args=(X, data), nan_policy='omit')
217     #report_fit(result.params)
218
219     palette = iterools.cycle(sns.color_palette())
220     fig, (ax1, ax2, ax3) = plt.subplots(3,1,sharex=True,figsize=figsize)
221     plt.rcParams["lines.markeredgewidth"] = 1.5
222     interp = np.linspace(min(X[1]),max(X[1]),1000)
223     Xinterp = (interp*0.0+X[0][0]), interp
224
225     K1 = result.params['K1_1'].value
226     K2 = K1*result.params['alpha_1'].value/4
227
228     Ginterp = G12(Xinterp[1],Xinterp[0],K1,K2)
229     Hinterp = Xinterp[0]/(1+K1*Ginterp + K1*K2 * Ginterp * Ginterp)
230     HGinterp = K1*Ginterp * Hinterp
231     HG2interp = K2 * HGinterp * Ginterp
232
233     for i in range(len(dataT)):
234         c = next(palette)
235         y_fit = nmr12_dataset(X, result.params, i)
236         Yinterp = nmr12_dataset(Xinterp, result.params, i)
237         ax1.plot(X[1]/X[0], dataT[i, :]-dataT[i,0], 'o', color=c, markerfacecolor='None')
238         ax1.plot(Xinterp[1]/Xinterp[0], Yinterp, '--', color=c)
239         ax2.plot(X[1]/X[0], dataT[i,:]-dataT[i,0]-y_fit, fmt,color=c,markerfacecolor='None')
240         ax1.set_ylabel('Δδ')
241         ax2.set_ylabel('Residual')
242
243         ax2.axhline(y=0,color='k')
244         ax3.plot(Xinterp[1]/Xinterp[0], Hinterp/Xinterp[0],label='[H]')
245         ax3.plot(Xinterp[1]/Xinterp[0], HGinterp/Xinterp[0],label='[HG]')
246         ax3.plot(Xinterp[1]/Xinterp[0], HG2interp/Xinterp[0],label='[HG2]')
247         ax3.legend(loc='best',frameon=True,framealpha=0.5)
248         ax3.set_xlabel('Guest equiv ([G]0 / [H]0)')
249         ax3.set_ylabel('Molfraction')
250         safeVal = lambda x: "ERROR" if result.params[x].value==None else result.params[x].value
251         safeErr = lambda x: "ERROR" if result.params[x].stderr==None else result.params[x].stderr
252         ax1.set_title("K1: {:.0f} +/- {:.0f}\n K2: {:.0f}, alpha: {:.2f} +/-  

253         → {:.2f}.format(safeVal("K1_1"), safeErr('K1_1'), safeVal("K1_1")*safeVal("alpha_1")/4,  

254         → safeVal("alpha_1"), safeErr("alpha_1")))
255         plt.tight_layout()
256         fig.align_labels()
257         plt.show()
258         return result, fig
259
260     '''Global analysis of NMR chemical shift data for fitting 1:1 host-guest association data.
261
262     data: a pandas dataframe containing host concentrations in the first column, guest concentrations in the
263     → second column, and NMR chemical shifts for different peaks in the subsequent columns.
264     figsize: tuple containing (width,height) for generated matplotlib plot
265     plotaxis: type of x axis for plotting. Can be 'eq' (plotting guest equivalents per host) or 'abs'
266     → (plotting absolute guest concentration)
267     fmt: matplotlib format for plotting. Defaults to 'o--', eg solid datapoints linked by dashed lines.
268
269     Global11 returns a tuple containing (results,fig), where results contains fitted association data and fig
270     → contains a matplotlib figure.
271
272     def Global11(data,figsize=(8,6),plotaxis='eq',fmt='o--'):
273         import seaborn as sns
274         def HG11(G0,H0,K):
275             return 0.5*(G0 + H0 + 1/K - np.sqrt((G0-H0-1/K)**2 + 4*G0/K))

```

```

271     def nmr11(X,K,delDHG):
272         HO, GO = X
273         HG = HG11(GO,HO,K)
274         out = delDHG*HG/HO
275         return out
276     def nmr11_dataset(X,params,i):
277         K = params['K_%i' % (i+1)].value
278         delDHG = params['delDHG_%i' % (i+1)].value
279         return nmr11(X,K,delDHG)
280
281     def objective(params, X, data):
282         """ calculate total residual for fits to several data sets"""
283         dataT = np.array(data.T[2:])
284         ndata, nx = dataT.shape
285         resid = 0.0*dataT[:,]
286         # make residual per data set
287         for i in range(ndata):
288             dataT[i] = dataT[i] - dataT[i][0]
289             resid[i, :] = dataT[i, :] - nmr11_dataset(X,params,i)
290         # now flatten this to a 1D array, as minimize() needs
291         return resid.flatten()
292
293     X = data.iloc[:,0],data.iloc[:,1]
294
295     dataT = np.array(data.T[2:])
296     fit_params = Parameters()
297     for iy, y in enumerate(dataT):
298         fit_params.add('K_%i' % (iy+1), value=200, min=0.0, max=1e6)
299         fit_params.add('delDHG_%i' % (iy+1), value=0.4, min=-4.0, max=4.0)
300     for iy in range(2,len(dataT)+1):
301         fit_params['K_%i' % iy].expr='K_1'
302
303
304     result = minimize(objective, fit_params, args=(X, data), nan_policy='omit')
305     #report_fit(result.params)
306
307
308     import matplotlib.cm as cm
309     import seaborn as sns
310     palette = itertools.cycle(sns.color_palette())
311     plt.rcParams["lines.markeredgewidth"] = 1.5
312     fig, (ax1, ax2, ax3) = plt.subplots(3,1,sharex=True,figsize=figsize)
313
314     interp = np.linspace(min(X[1]),max(X[1]),1000)
315     Xinterp = (interp*0.0+X[0][0]), interp
316
317     HGinterp = HG11(Xinterp[1],Xinterp[0],result.params['K_1'].value)
318     Hinterp = Xinterp[0] - HGinterp
319
320     for i in range(len(dataT)):
321         c = next(palette)
322         y_fit = nmr11_dataset(X, result.params, i)
323         Yinterp = nmr11_dataset(Xinterp, result.params, i)
324         if plotaxis == 'eq':
325             ax1.plot(X[1]/X[0], dataT[i, :]-dataT[i,0], 'o', color=c,markerfacecolor='None')
326             ax1.plot(Xinterp[1]/Xinterp[0], Yinterp, 'r-', color=c)
327             ax2.plot(X[1]/X[0],dataT[i,:]-dataT[i,0]-y_fit, fmt,color=c,markerfacecolor='None')
328         elif plotaxis == 'abs':
329             ax1.plot(X[1], dataT[i, :]-dataT[i,0], 'o', color=c,markerfacecolor='None')
330             ax1.plot(Xinterp[1], Yinterp, 'r-', color=c)

```

```

331         ax2.plot(X[1],dataT[i,:]-dataT[i,0]-y_fit, fmt,color=c,markerfacecolor='None')
332     if plotaxis == 'eq':
333         ax3.plot(Xinterp[1]/Xinterp[0],Hinterp/Xinterp[0],label = '[H]')
334         ax3.plot(Xinterp[1]/Xinterp[0],HGinterp/Xinterp[0],label = '[HG]')
335         ax3.set_xlabel('Guest equiv ([G]0 / [H]0)')
336     elif plotaxis == 'abs':
337         ax3.plot(Xinterp[1],Hinterp/Xinterp[0],label = '[H]')
338         ax3.plot(Xinterp[1],HGinterp/Xinterp[0],label = '[HG]')
339         ax3.set_xlabel('Guest concentration / M')
340     ax3.legend(loc='best',frameon=True,framealpha=0.5)
341     ax1.set_ylabel('Δδ')
342     ax2.set_ylabel('Residual')
343
344     ax2.axhline(y=0,color='k')
345     ax3.set_ylabel('Molfraction')
346     safeVal = lambda x: "ERROR" if result.params[x].value==None else result.params[x].value
347     safeErr = lambda x: "ERROR" if result.params[x].stderr==None else result.params[x].stderr
348     ax1.set_title("Ka: {} +/- {}".format(safeVal('K_1'),safeErr('K_1')))
349     plt.tight_layout()
350     fig.align_labels()
351     plt.show()
352     return result, fig

```

9.8 Additional References

- [1] D. Barišić, V. Tomišić, N. Bregović, *Anal. Chim. Acta* **2019**, *1046*, 77–92.
- [2] K. Izutsu, T. Adachi, T. Fujinaga, *Electrochim. Acta* **1970**, *15*, 135–145.
- [3] T. S. C. MacDonald, W. S. Price, J. E. Beves, *ChemPhysChem* **2019**, *20*, 926–930.
- [4] S. J. Wezenberg, B. L. Feringa, *Org. Lett.* **2017**, *19*, 324–327.
- [5] P. Thordarson, *Chem. Soc. Rev.* **2011**, *40*, 1305–1323.

Chapter 10

Appendix for photoswitch-fluorescence feedback

10.1 Bifurcation conditions

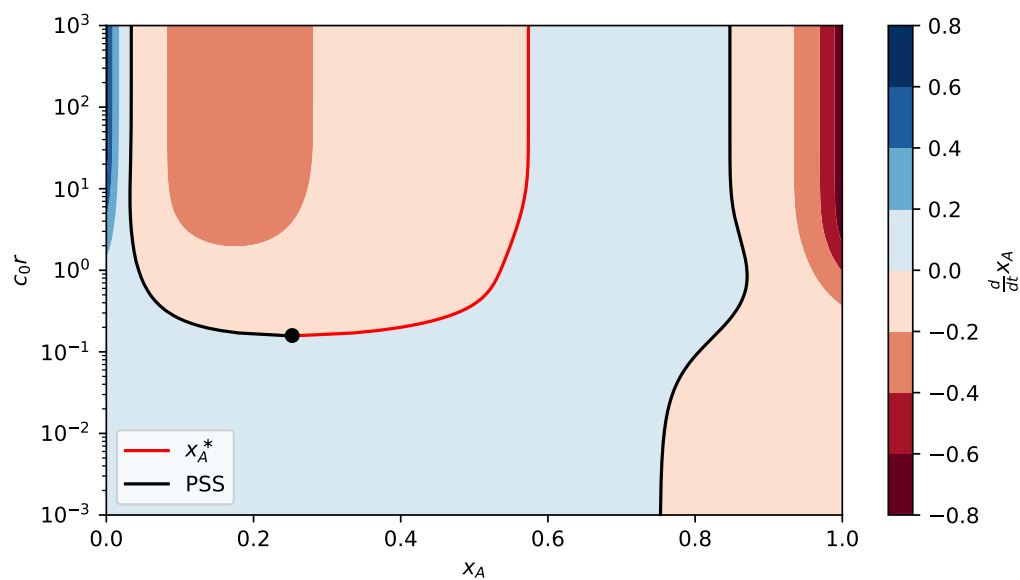


Figure 10.1. Change in $\frac{d}{dt}x_A$ as a function of c_0r for a wide range of c_0r . When c_0r is small bifurcation does not occur and there is a single unique photostationary state (black line), but above some critical optical density (here $c_0r > 0.16$) bifurcation occurs at composition x_A^* (red line). x_A^* increases with c_0r from $x_A^* = 0.34$ at the onset of bifurcation and eventually stabilises at $x_A^* = 0.57$ at high c_0r .

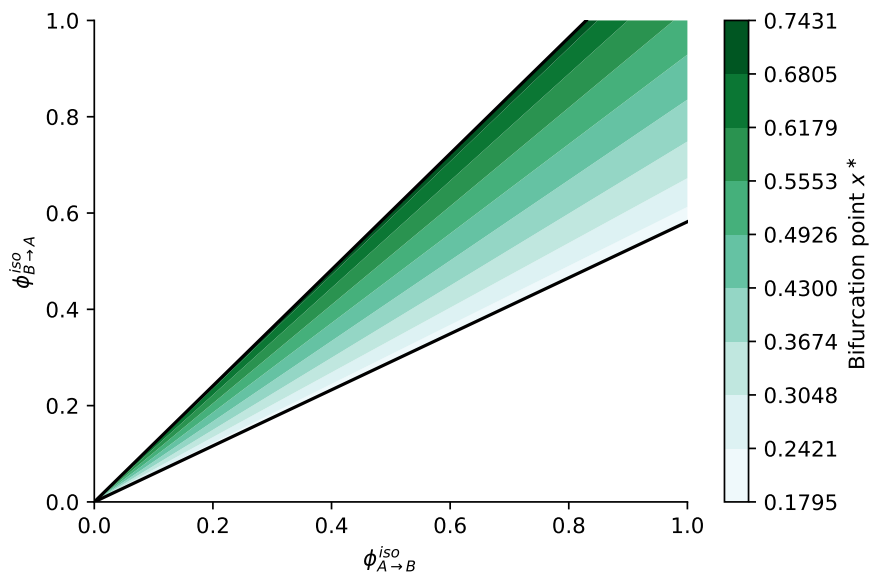
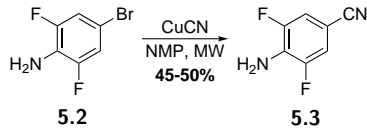


Figure 10.2. Relationship between $\phi_{A \rightarrow B}^{iso}$ and $\phi_{B \rightarrow A}^{iso}$ for bifurcation. With all other parameters fixed as the parameters given in Figure 5.5, the bifurcation point x^* appears to depend linearly on the ratio $\phi_{A \rightarrow B}^{iso}/\phi_{B \rightarrow A}^{iso}$. For these parameters, bifurcation only occurs if both isomers have similar photoisomerisation quantum yields: here, the requirement for bifurcation is $0.829 < \phi_{A \rightarrow B}^{iso}/\phi_{B \rightarrow A}^{iso} < 1.72$.

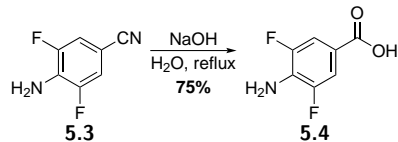
10.2 Reaction experimental

4-Cyano-2,6-difluoroaniline 5.3



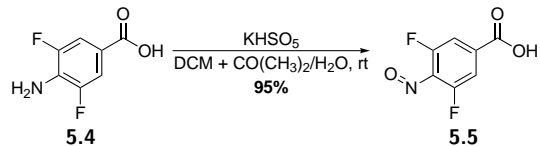
Bromo-2,6-difluoroaniline **5.2** (5 mmol, 1.04 g) and CuCN (580 mg, 6.5 mmol) combined in 5 mL of *N*-methylpyrrolidone, and heated to 220 °C for 20 mins under microwave irradiation (5 minute ramp time). On cooling to room temperature, the mixture was diluted with 10 mL of ice water. The white precipitate formed was collected by filtration, dissolved in ethyl acetate with sonication, and washed with aqueous ammonia until washings ran clear. The crude product was then obtained *via* removal of ethyl acetate under reduced pressure and purified by re-crystallisation from hot ethanol to acquire **5.3** in 45–50% yield. NMR shifts were consistent with those previously reported.^[1]

4-Amino-1,3-difluorobenzoic acid 5.4



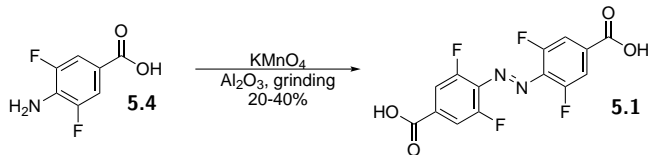
Aniline **5.3** (4.6 mmol, 705 mg) was suspended in aqueous NaOH (1 M, 25 mL) and heated at reflux for 14 h. After cooling to rt, aqueous HCl (1 M) was added to precipitate the benzoic acid. The solution was extracted with ethyl acetate after which organic portions were combined and dried over MgSO₄ and concentrated under reduced pressure to give **5.4**. NMR shifts were consistent with those previously reported.^[1]

4-Nitroso-1,3-difluorobenzoic acid 5.5



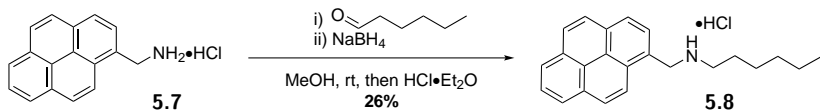
Carboxylic acid **5.4** (1.16 mmol, 200 mg) was dissolved in a mixture of CH₂Cl₂ (3 mL) and acetone (0.6 mL). Oxone (2 KHSO₅ · KHSO₄ · K₂SO₄ triple salt; 1.07 g, 1.75 mmol, 1.5 eq) was dissolved into 1.5 mL water and added to the solution, which was stirred vigourously overnight. The layers were separated, with the organic layer washed with water and concentrated under reduced pressure to give nitroso **5.5**.

Unfortunately, this compound could not be successfully coupled with **5.4** under TFA/AcOH Mills conditions to give azobenzene **5.1**. NMR shifts were consistent with those previously reported.^[2]

4,4'-Dibenzoic acid tetrafluoro azobenzene 5.1

Carboxylic acid **5.4** (3 mmol, 520 mg) and KMnO_4 (6 mmol, 950 mg, 2 eq) combined on neutral alumina (6 g) and ground by hand in a pestle and mortar for 30–60 minutes. The powdered solid was suspended in aqueous NaOH (1 M, 10 mL), sonicated, and filtered through Celite. The aqueous filtrate was gradually acidified with aq. HCl (1 M) until a bright red colour developed, and then extracted with ethyl acetate. The organic portions were combined, dried over MgSO_4 , filtered, and concentrated under reduced pressure to give **10.1** as a brick-red solid (20–40%). NMR shifts were consistent with those previously reported.^[1]

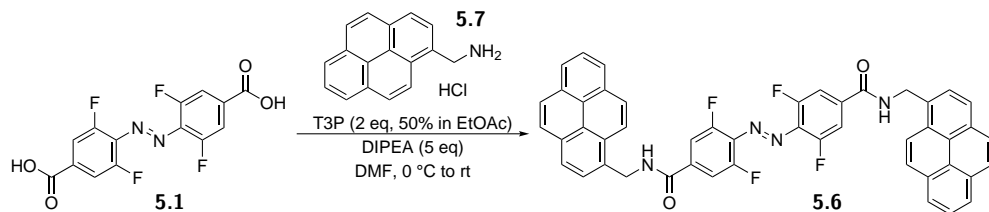
^1H NMR (600 MHz, DMSO-d_6) δ = 7.80 (d, J = 10.2 Hz, 4H), 2.50 (s, 3H). ^{19}F NMR (565 MHz, DMSO-d_6) δ = -120.23 (d, J = 10.4 Hz).

Hexylation of pyrenemethylamine 5.1 5.8

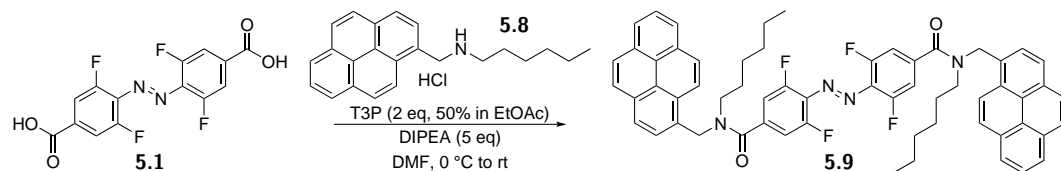
Pyrenemethylamine hydrochloride (1.05 mmol, 280 mg) dissolved in 5 mL ethyl acetate, washed with NaHCO_3 solution, and evaporated to dryness. Hexanal (1.0 mmol, 100 mg) and methanol (5 mL) added, and reaction stirred at room temperature for 2 hours. NaBH_4 (1.6 mmol, 61 mg) added, reaction stirred for an additional 10 minutes, and then quenched with 1 M aq. NaOH . The reaction mixture was extracted with diethyl ether, the ethereal portions were combined, dried with brine and MgSO_4 , and concentrated to dryness to give a tacky brown crude product. This crude was taken up in a small volume of diethyl ether from which **5.8** was precipitated as the hydrochloride salt on addition of ethereal HCl^* . The crude hydrochloride was then recrystallised from hot ethanol to give pure **5.8** in 26% yield.

^1H NMR (600 MHz, DMSO-d_6) δ = 9.08 (s, 2H), 8.56 (d, J = 9.2 Hz, 1H), 8.42–8.35 (m, 4H), 8.30–8.26 (m, 2H), 8.23 (d, J = 8.9 Hz, 1H), 8.14 (t, J = 7.6 Hz, 1H), 4.92 (s, 2H), 3.18–3.07 (m, 2H), 1.71 (ddd, J = 12.2, 9.9, 6.6 Hz, 2H), 1.39–1.24 (m, 6H), 0.91–0.83 (m, 3H).

*Prepared by shaking 5 mL conc. HCl with 50 mL ether and drying over MgSO_4

Amide coupling to give azobenzene bis-pyrenemethylamide 5.6

Azobenzene diacid **5.1** (0.25 mmol, 85 mg) and pyrenemethylamine hydrochloride (0.5 mmol, 133 mg, 1 eq) were dissolved in 3 mL DMF and cooled to 0 °C on ice. Diisopropyl ethylamine (2.5 mmol, 0.44 mL, 5 eq) was added, followed by the slow addition of T3P (propylphosphonic anhydride; 1 mmol, 0.6 mL of 50 wt% solution in ethyl acetate). The reaction mixture was stirred for 18 h while warming to room temperature. The reaction mixture was then diluted with ethyl acetate (10 mL), washed with NaHCO₃ solution, water, and brine; dried over MgSO₄ and concentrated under reduced pressure to give **5.6**.

Amide coupling to give hexylated azobenzene bis-pyrenemethylamide 5.9

Azobenzene diacid **5.1** (0.073 mmol, 25 mg) and hexylated pyrenemethylamine hydrochloride (0.15 mmol, 53 mg, 1 eq) were dissolved in 2 mL DMF and cooled to 0 °C on ice. Diisopropyl ethylamine (0.75 mmol, 125 µL, 5 eq) was added, followed by the slow addition of T3P (propylphosphonic anhydride; 0.3 mmol, 180 µL of 50 wt% solution in ethyl acetate). The reaction mixture was then stirred for 18 h while warming to room temperature. The reaction mixture was then diluted with ethyl acetate (5 mL), washed with NaHCO₃ solution, water, and brine; dried over MgSO₄ and concentration under reduced pressure to give **5.9** (67 mg, 91%) which was then purified by column chromatography (CH₂Cl₂/silica). ¹H NMR too broad to assign (see Figure 10.5). ¹⁹F NMR (565 MHz, CDCl₃) δ = -116.93, -117.02, -118.56 (d, J = 9.1 Hz), -118.65 (d, J = 9.8 Hz) (mixture of *E*-**5.9** and *Z*-**5.9**: *Z*-**5.9** at δ ≈ -117 ppm, *E*-**5.9** at δ ≈ -119 ppm).

10.3 NMR Spectra

10.3.1 Pyrenemethyl hexylammonium chloride 5.8

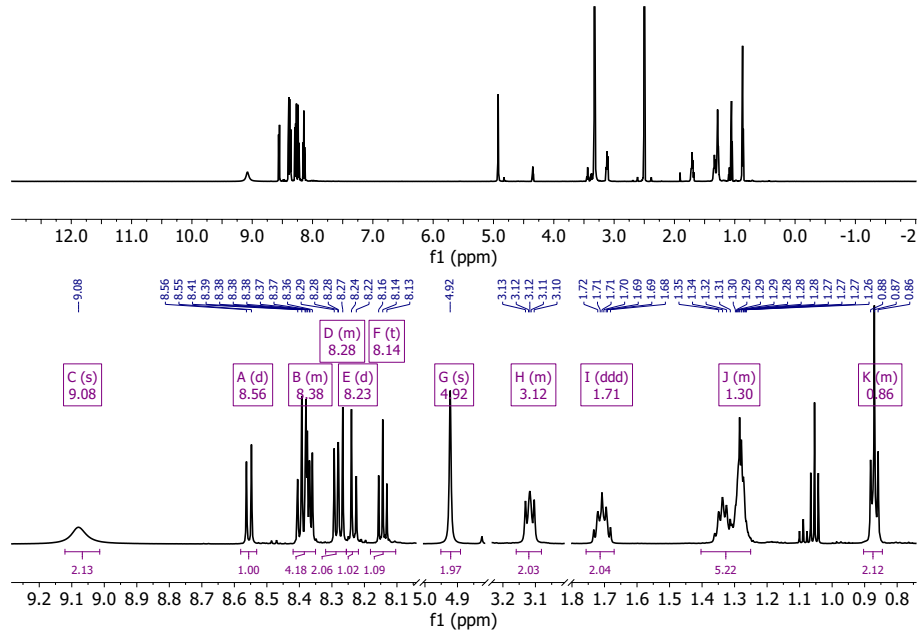


Figure 10.3. ¹H NMR (600 MHz, DMSO-*d*₆) of pyrenemethyl hexylamine **5.8** as its hydrochloride salt.

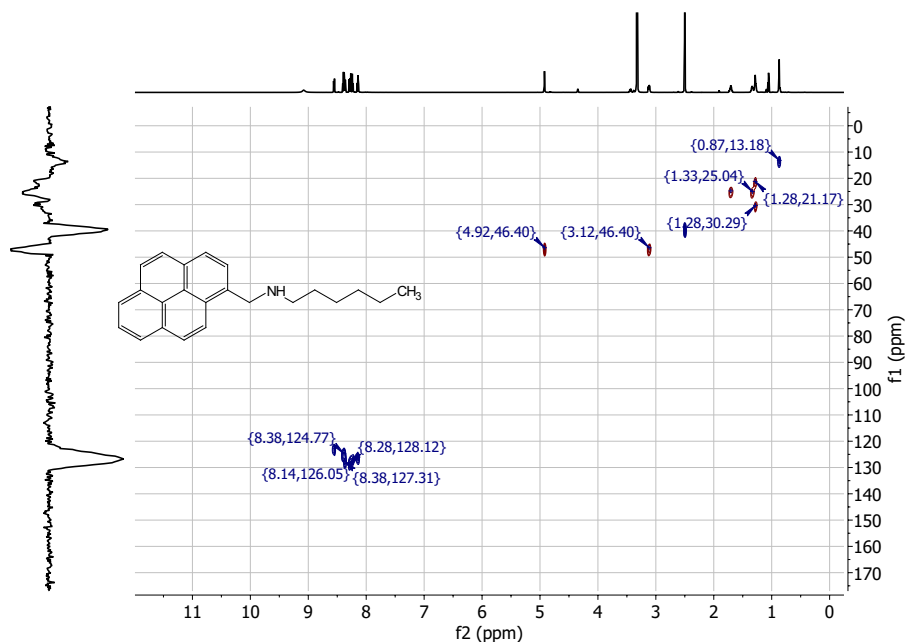


Figure 10.4. HSQC NMR (600 MHz ¹H, DMSO-*d*₆) of pyrenemethyl hexylamine **5.8** as its hydrochloride salt.

10.3.2 Pyrene-azobenzene conjugate 5.9

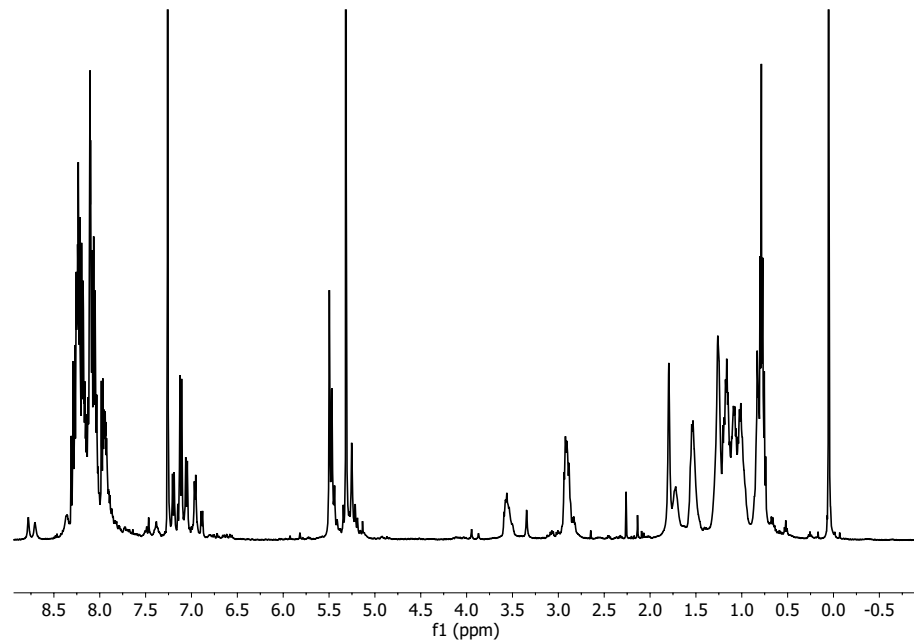


Figure 10.5. ^1H NMR (600 MHz, CDCl_3 , -35°C) of pyrenemethyl hexylamine **5.8**.

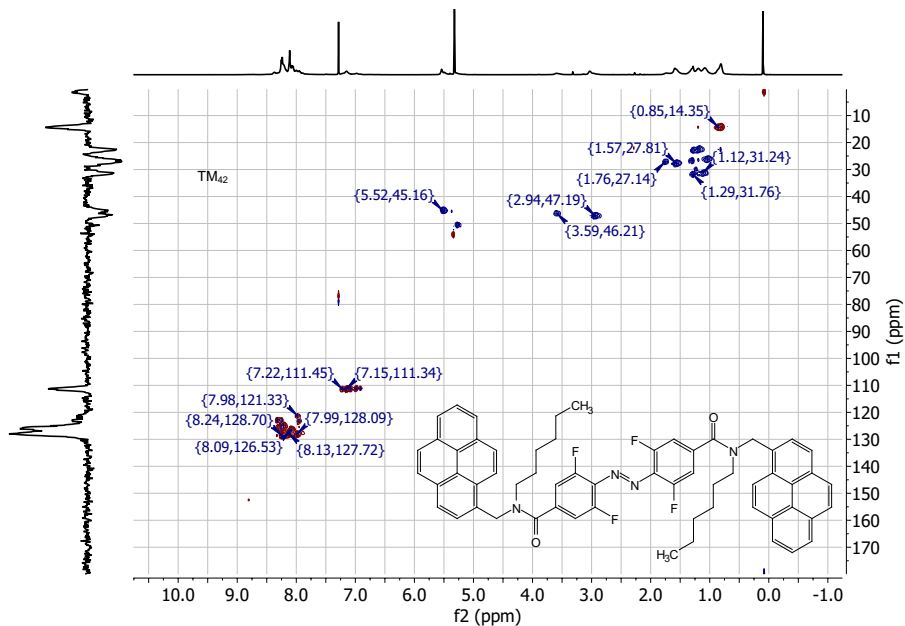


Figure 10.6. HSQC NMR (600 MHz ^1H , CDCl_3 , -35°C) of pyrene-azobenzene conjugate **5.9**.

10.4 Additional References

- [1] B. Heinrich, K. Bouazoune, M. Wojcik, U. Bakowsky, O. Vázquez, *Org. Biomol. Chem.* **2019**, *17*, 1827–1833.
- [2] C. Knie, M. Utecht, F. Zhao, H. Kulla, S. Kovalenko, A. M. Brouwer, P. Saalfrank, S. Hecht, D. Bléger, *Chem. Eur. J.* **2014**, *20*, 16492–16501.

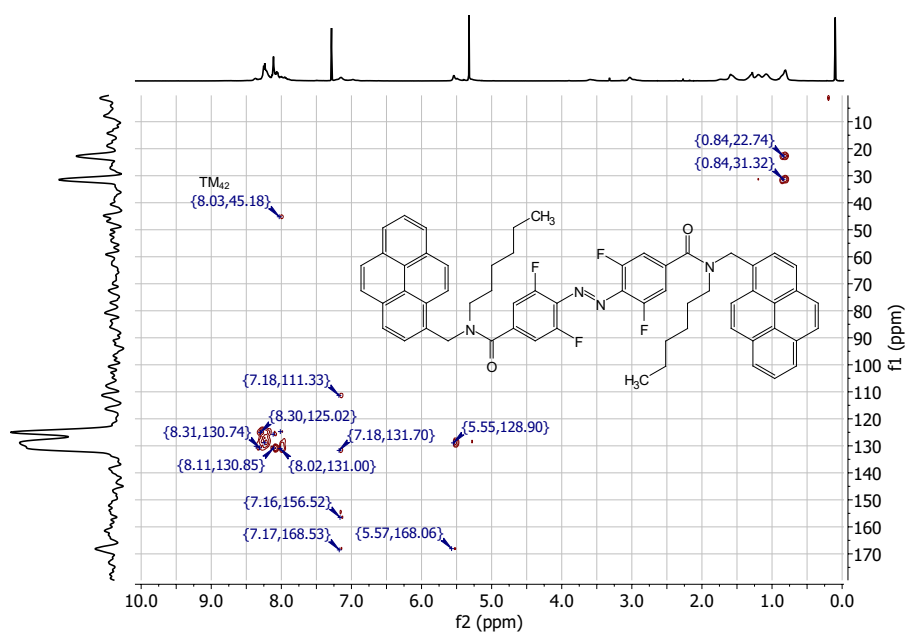


Figure 10.7. HMBC NMR (600 MHz ^1H , CDCl_3 , -35°C) of pyrene-azobenzene conjugate **5.9**.